Synthesis, characterisation and electrocatalytic behaviour of three series of Metal Organic Frameworks

A thesis submitted in fulfilment of the requirements for the degree

Of

DOCTOR OF PHILOSOPHY

Of

Rhodes University

By

Tafadzwa Wendy Murinzi

Dedication

This work is dedicated to my family; Mum, Ronnie, Marcia and my late father, Dominic. You complete me.

Abstract

Metal organic frameworks (MOFs) have received a lot of attention over the past few years due to their vast range of interesting properties and applications, such as catalysis, environmental sensing and storage. This wide range of potential applications is afforded by careful selection and manipulation of the components chosen in assembling of MOFs. In this study, three series of MOFs were synthesized from Co(II), Cu(II) and Mo(VI) polyoxometallates with either 1,3,5-benzenetricarboxylic acid, 1,2,4,5-benzenetetracarboxylic acid or 2,6-pyridinedicarboxylic acid as the ligands. In series 1, the common 1,3,5-benzenetricarboxylic acid MOF, HKUST-1, and POM modified HKUST-1 compounds involving encapsulation and encorporation of the POM were utilised. In series 2, flexible cobalt(II) benzenepolycarboxylate MOFs which investigated the effect of varying the degree of carboxylate substituent were utilised. In series 3, flexibly reduced heterocyclic polycarboxylate MOFs using 2,6-pyridine dicarboxylate were utilised.

Solvothermal and slow evaporation synthesis conditions were employed. Where single crystals of good quality were produced, single crystal X-ray diffraction (SC-XRD) was employed for structural elucidation. In the absence of such crystals, a combination of elemental analysis, inductively coupled plasma optical emission spectrometry (ICP-OES) and powder X-ray diffraction (PXRD) was used. Characterization of the MOFs was done by Fourier transform infrared spectrometry (FTIR) and thermal methods, namely thermogravimetric analysis (TGA) and differential scanning calorimetry (DSC).

The electrocatalytic potential of the compounds in the oxidation of L-cysteine was then investigated using a variety of techniques. Cyclic voltammetry was used for L-cysteine detection whilst chronoamperometry and differential pulse voltammetry were used to determine the nanoprobes' sensitivity, rate constants and detection limits. Electrochemical impedence spectroscopy was used to investigate the charge transfer resistance (R_{CT}) and electron transfer kinetics.

Of the three, series 3 gave the best signals and sensitivities for electrocatalysis of L-cysteine followed by series 2 and lastly series 1. Series 2 showed the highest stability and series 1 required the least overpotential. The results highlight the effects of different metal centres and ligands on electrocatalysis. The application of MOFs in electrochemistry is a relatively new field making the findings of this study a significant addition to the body of knowledge.

Acknowledgements

I would like to express my deepest gratitude to my supervisor Prof. Gareth M. Watkins, for his commitment, patience and guidance throughout the research. His continued support led me the right way and allowed me to grow.

I would also like to extend my appreciation to my colleagues in the F12 laboratory; "you made it an interesting journey".

My sincere appreciation is extended to Dr. Munyaradzi Shumba (senior postgraduate student for Prof Nyokong, Rhodes University) for his invaluable support and advise in electrochemistry and to Dr Eric Hosten (Nelson Mandela Metropolitan University) for his help immeasurable assistance with SC-XRD.

Special thanks goes to Midlands State University for affording me this grand opportunity. Without them, I would not have had a chance to be at Rhodes University.

I would also like to extend my deepest gratitude to my family. Without their encouragement and support, I would not have made it through the dark times. I'm forever indebted to you.

Publications

The following work has been published from this study:-

1. T. W. Murinzi, E. Hosten, G. M. Watkins, Synthesis and characterization of a cobalt-2,6-pyridinedicarboxylate MOF with potential application in electrochemical sensing, *Polyhedron* **2017**, *137*, 188–196.

Table of Contents

List of Abbreviations

H_4B4C	Benzenetetracarboxylic acid
H_3BTC	Benzenetricarboxylic acid
2,6-pydc	2,6-pyridinedicarboxylic acid
2,3-pydc	2,3-pyridinedicarboxylic acid
acac	acetylacetonate
dpm	dipyridin
bpp	1,3-bis(4-pyridyl)propane
DPV	Differential pulse voltammetry
DSC	Differential scanning calorimetry
EIS	Electrochemical impedence spectroscopy
FTIR	Fourier transform infrared spectroscopy
MOF	Metal organic framework
PSM	Post synthetic modification
PBU	Primary building unit
POM	Polyoxometallate
SBU	Secondary building units
TGA	Thermogravimetric analysis

List of Figures

List of Schemes

List of Tables

Chapter One

This chapter describes the development of metal organic frameworks as a branch of coordination chemistry. It looks at the properties and resulting applications of MOFs, specifically those of copper, cobalt and molybdenum metals. The chapter also has the aims of the thesis.

1. Introduction

1.1 Coordination compounds

The period between the 18th and 19th century saw the dawn of a new era, which later became known as the industrial revolution. During this period, theories of electromagnetism (Michael Faraday), thermodynamics (James Prescott Joule) and John Dalton's Atomic theory were developed. Albert Werner developed the basis for coordination chemistry with his work on structural and geometric isomerisation leading to the first Nobel prize to be awarded to an inorganic chemist (1913) [1]. Some of the greatest scientific inventions of our time such as electric light bulbs, fossil and steam powered engines also emerged during this era [2–4]. Since that time, scientists have made numerous other discoveries which have greatly benefitted trade and commerce as well as overall human livelihood.

The 20th century saw an increase in environmental awareness as scientists noticed the detrimental effects of industrialization on the environment and human health [5]. Medical scientists also realized the importance of easy and regular monitoring of various conditions in an effort to improve the quality of life and keep diseases at bay [6]. Since then, there has been a movement towards the development of cheaper, more environmentally friendly alternatives. As a result, the 21st century has seen the emergence of new foci, ranging from energy sources, green synthesis routes and portable biosensors, to name a few [7–10]. These developments would not have been possible had scientists not dedicated themselves to studying the chemistry of compounds and getting a better understanding of the elements and how they work together.

Coordination chemistry is the study of complexes formed between metals and non-metal atoms (or groups of atoms), known as ligands, to give coordination compounds [3]. These compounds have various properties such as porosity [11,12], isomerism [13], magnetism [14,15], optical [16] and redox activities. This has made them suitable for various applications such as antimicrobial studies [17], sorption [18,19] and catalysis [20]. Some examples of this in literature include the use of transition metal complexes such as Copper [$Cu(C_{12}H_23N_3)_4Br_2{\cdot}2H_2O$] and Cobalt (RGO/$[Co(NH_3)_6]^{3+}$) complexes, both of which have shown great potential for use as electrochemical sensors for hydrogen peroxide and nitrates at low potentials [21–23]. Despite the success of coordination compounds, there are however some issues with the selectivity, stability and efficiency [16]. This led to the development of new branches of coordination compounds, one of which is Metal Organic Frameworks (MOFs) [24–26].

1.1.1 Nomenclature in coordination chemistry

Since MOFs and coordination compounds are interdisciplinary fields, there has been a lot of confusion over terminology used to describe them. Naming compounds is a complex task which requires careful analysis and an understanding of the structure [27]. The International Union of Pure and Applied Chemistry (IUPAC) is a body that often helps by setting guidelines for nomenclature. In 2013, an IUPAC task team led by Professor Lars Öhrström came up with the following;

A coordination polymer is coordination compound with repeating coordination entities extending in 1-, 2- or 3- dimensions. A coordination network is a coordination compound extending, through repeating coordination entities, in 1-dimension, but with cross-links between two or more individual chains, loops or

spiro-links. In simpler terms, it is a coordination compound extending through repeating coordination entities in 2- or 3- dimensions [28,29].

From these definitions, it is apparent a coordination network is a subgroup of coordination polymers. In both, a prerequisite is the presence of repeating coordination entities to form 1-, 2- or 3- dimensional structures. However in coordination networks, the presence of crosslinks between at least two of the chains are essential for this classification. A more recent subgroup has emerged from the branch of coordination polymers in recent years and this is the branch of Metal Organic Frameworks (MOFs). A MOF is a metal coordination network with organic ligands containing potential voids [28]. This definition makes it a subset within the coordination networks defined above.

Scheme 1.1 below shows how coordination compounds and coordination polymers are made by varying the ligands employed. When acetylacetonate is combined with cobalt, a tetrahedral coordination compound is formed, $[Co(acac)_2]$, via chelating bonds. Upon the introduction of dipyrrin, the compound changes to an octahedron. These chelated coordination compounds now have the formula $[Co(acac)(dpm)_2]$. Further introduction of nodes (Co and Cd) and ligands, leads to extension of the compound into a coordination network structure [13].

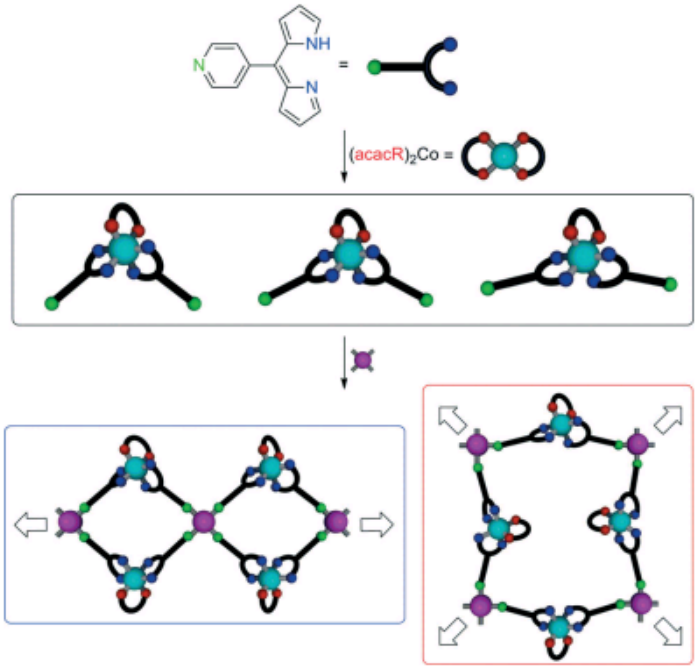

Scheme 1. 1: Schematic representation, featuring different possible arrangements in the formation of coordination polymers [13].

A Metal Organic Framework is a metal coordination network with organic ligands containing potential voids [29]. MOF synthesis involves combining metal centres or clusters with an organic ligand. Depending on synthesis factors like metal to ligand ratio, temperature and solvent system, different products with different properties can be formed from the same starting materials [26,30] (Scheme 1.2). There is a wide range of techniques which can be used in MOF synthesis [25] as shown in Figure 1.1 [31]. Of these however, the most popular are solvothermal and hydrothermal, both of which use a combination of high temperatures and pressures [32].

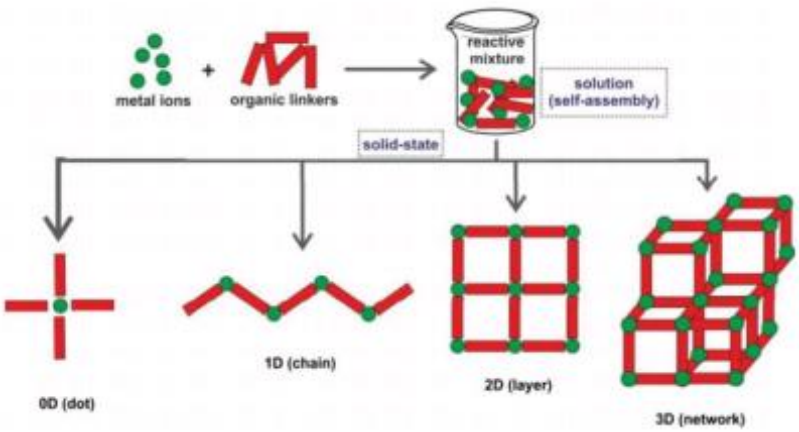

Scheme 1. 2: Schematic representation of the formation of MOFs with different dimensionalities (1D, 2D and 3D) from the same primary building units [30].

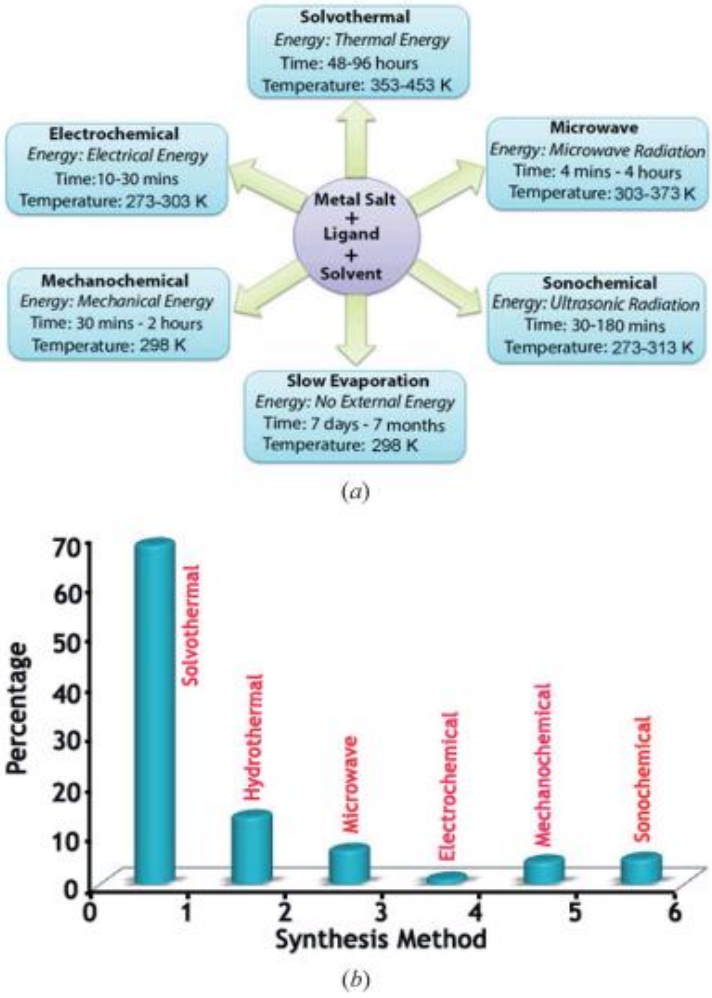

Figure 1. 1: Synthesis methods used for MOFs (a) and the frequency of use over the past two decades (b)[31].

1.1.2 Crystal engineering/designing of MOFs

By careful selection of both the primary building units (PBU), that is the metal and ligand, the properties of the resulting MOF can be tuned to suit a particular application [33–35]. The design of a MOF can also be influenced by the use of secondary building units (SBU). This is when additional molecules such as metal carboxylate clusters, metal oxy or hydroxyl clusters are used. They may form around solvent templates creating the framework [36]. Once the framework is formed, the solvent can be evacuated creating potential voids. Studies have shown that the chemical environment within the potential void is often the reason for their activity in the different applications like sensing and catalysis [30,37,38]. This activity can also be induced by functionalization of the MOF, through doping of the final product or modifying the PBU prior to MOF synthesis [39–41].

1.2 Organic ligands

The nature of organic ligands employed in synthesis has a direct bearing on the structure and properties of the final coordination compound. In MOFs for example, the ligand acts as a spacer/linker between the metal nodes and hence has a deciding effect on the size of the potential voids [42]. The chemical properties of ligands also influence the chemical properties of the final product. An example of this is when polar moieties are used and induce the same polarity in the coordination compound. Aromatic ligands introduce rigidity into the molecule due to steric hinderance associated with the ring structures. This helps in reduction of incidences of the structure collapsing upon changes in the environment of the coordination compound. Aromatic groups also allow π--π stacking which can be an advantage depending on the end-use of the network.

Due to this, a number of aromatic based ligands have been employed in synthesis of these compounds [43–46]. Functionalization of the ligand by incorporating of acidic carboxylic groups and basic amine groups has seen a wide range of compounds with interesting properties formed. Carboxylic groups result in the creation of multiple bonding modes due to flexibility of this group and its ability to act as both a hydrogen bond acceptor or donor [47]. The existence of multiple denticities results in an increase in binding sites for a particular ligand and hence a vast range of products become possible. Reactions of divalent metals with polydentate ligands like 1,2,4,5-benzenetetracarboxylic acid (H_4B4C) have shown a high tendency towards formation of 2- or 3- dimensional networks [47,48]. When multiple carboxylic acid groups are included, as is the case with benzene-1,3,5-tricarboxylic acid (H_3BTC) 3-dimensional products can form [49–51].

Formation of heterocyclic chelate rings by incorporation of a nitrogen atom results in a reduction in this flexibility and thus allows for a better ability to predict the possible structural conformations with higher accuracy. This has been observed when working with ligands like substituted pyridines. The combination of both *COOH* and N- groups in an aromatic ring results in a wider range of possible conformations and properties. This behaviour has been exhibited by various 3 dimensional coordination compounds like [*Cu*(2,3-pydc)(bpp)]·2.5H_2O and [*Cd*(2,3-pydc)(bpp)(H_2O)]·3H2O (where 2,3-pydc = pyridine-2,3-dicarboxylic acid and bpp = 1,3-bis(4-pyridyl)propane) [52], which are different from the homocyclic dicarboxylic products and which tend to form discrete compounds and chains [53–57].

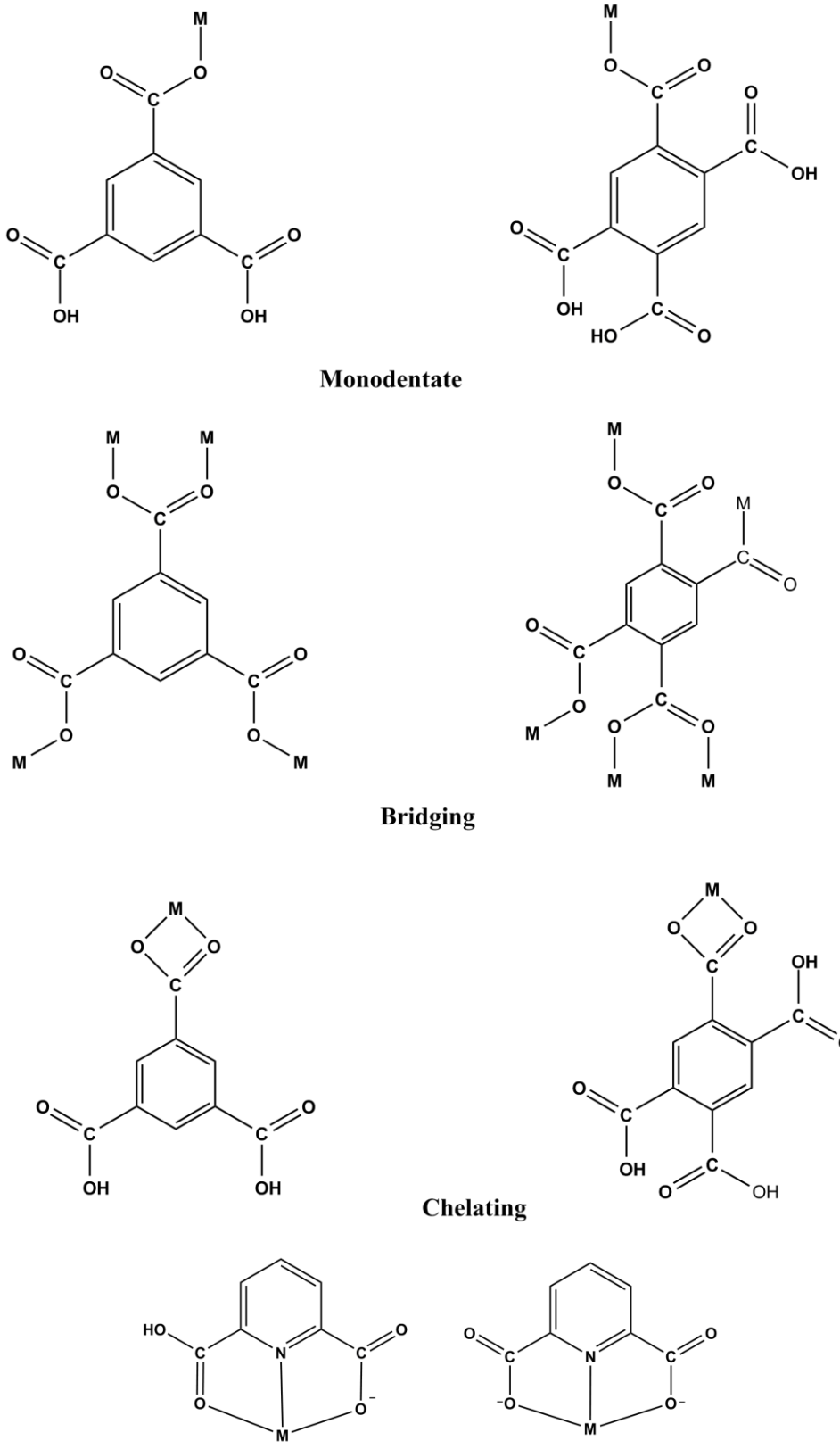

Figure 1. 2: Coordination modes of H_3BTC, H_4B4C and pyridine 2,6-dicarboxylic acid.

Figure 1.2 shows some of the common bonding modes exhibited by benzene-1,3,5-tricarboxylic acid (H_3BTC), benzene-1,2,4,5-tetracarboxylic acid (H_4B4C) and 2,6-pyridinedicarboxylate (2,6-pydc) with different metal nodes (Figure 1.2). The different ligation modes of each ligand moiety result in possible different supramolecular structures with different properties.

In addition to all these possibilities for interesting product synthesis in coordination compounds, there are other equally important factors (such as ligand to metal ratio and nature of bonding) which affect the formation and properties of the final product. In this work, the following aromatic homocyclic and heterocyclic ligands were employed; H_3BTC, H_4B4C and 2,6-pydc, with copper, cobalt and molybdenum metal salts in the formation of a variety of metal organic framework compounds for electrocatalysis.

1.3 Copper benzenepolycarboxylates

Perhaps the most popular copper benzene polycarboxylate MOF to have been studied in literature is that of Hong Kong University of Science and Technology, HKUST-1; also known as MOF 199. The SBU unit of HKUST-1 is formed by Cu^{2+} dimers coordinating to oxygen from four BTC^{3-} linkers and two water molecules, forming a paddle wheel [58]. It was first synthesized by Chui *et al* [59] using solvothermal methods. HKUST-1 crystallizes in a three dimensional network with bimodal pores forming channels. It is thermal stable upto 280 °C and this porosity and thermal stability has seen its application in a wide range of areas [60–62]. By altering the synthetic method and conditions used (temperature,

reaction time, solvent systems), different forms of HKUST-1, all with the general structure $Cu_3(BTC)_2 \cdot nH_2O$ can be formed [63].

HKUST-1 crystallizes in the face-centred crystal lattice with Fm-3m symmetry. It forms cubic or octahedral shaped turquoise crystals with a specific surface area of 1055 m^2/g and large pores of size 9x9 $Å^2$ [60] (Figure 1.3). The main reasons for its citing and use by different researchers are its ease of synthesis, stability and large surface area.

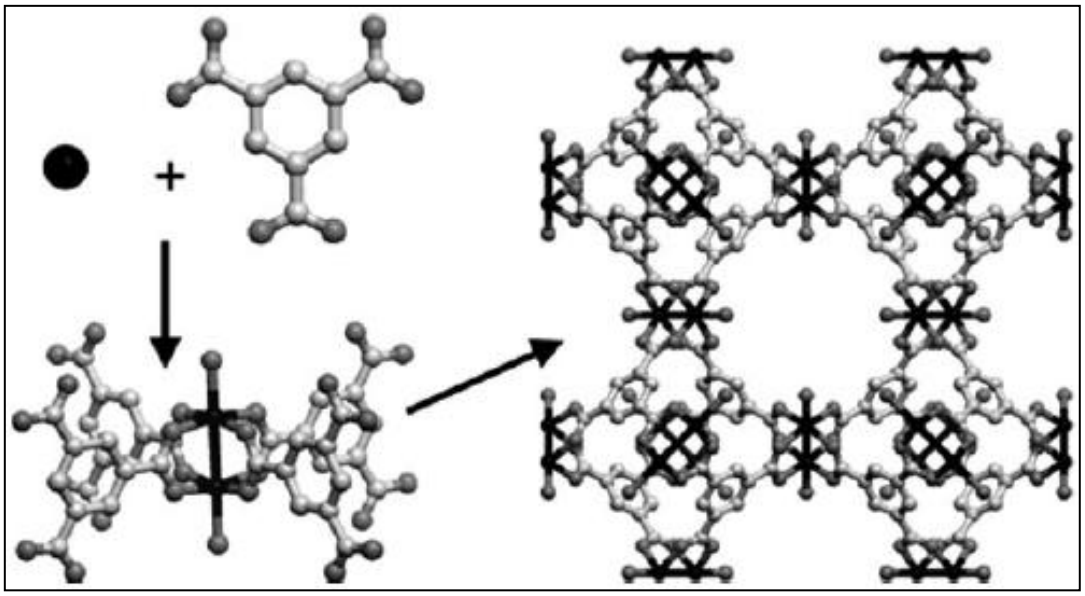

Figure 1. 3: Schematic illustration of HKUST-1 synthesis (by Bordiga *et al*) [60].

Most Cu^{2+} compounds with benzene polycarboxylates tend to exhibit either square pyramidal or square planar structures. Unlike H_3BTC and terepthalic acid, the COOH groups in H_4B4C cannot achieve coplanarity with the ring due to steric hinderance, resulting in distortion in the sheet structure. Clegg *et al* [64] worked with Cu^{2+} and H_4B4C and observed a number of possible complexes all in the triclinic or monoclinic crystal systems giving rise to 2- dimensional sheets.

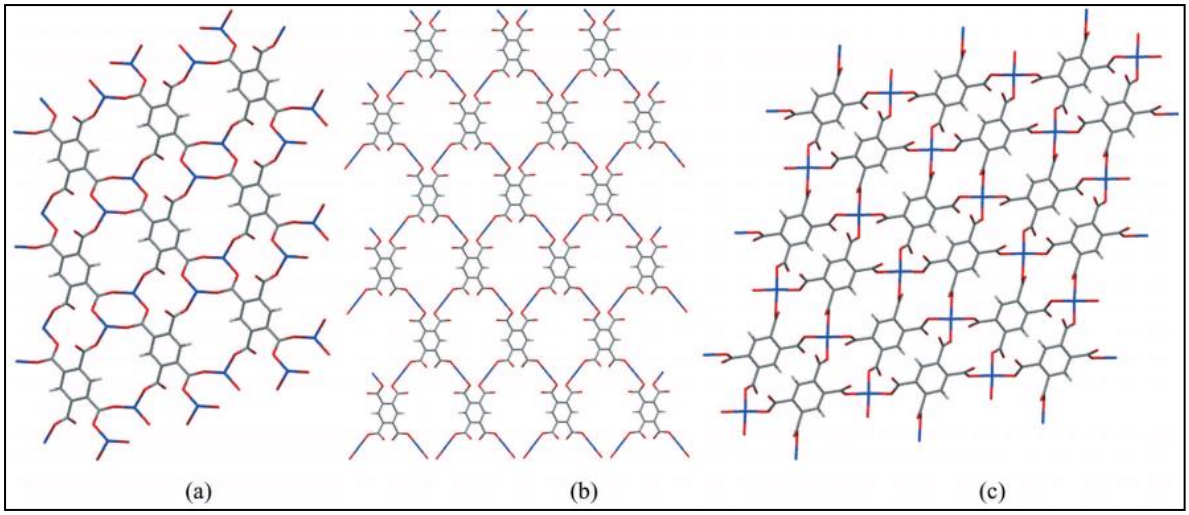

Figure 1. 4: 2-dimensional sheets (by Clegg et al) [64].

In the presence of terpyridine, Wang *et al* [65] obtained very different complexes when employing H_3BTC and H_4B4C ligands. In the first instance, a helical structure was formed by bridging two carboxyl groups from H_3BTC with the opposing terpyridine molecule. When H_4B4C was used instead of H_3BTC, a ladder like conformation was observed instead of the more common square pyramidal conformation.

By comparing the products of different benzenepolycarboxylates and Cu^{2+}, it was observed that the number of COOH groups on the benzene ring and the inclusion of an additional ligand (mixed ligands), has an effect on both the structural conformation (2D vs 3D) and the behaviour of the final coordination compound. When combined with H_3BTC as opposed to H_4B4C, products display better catalytic activity due to the larger number of coordinately unsaturated Cu^{2+} sites [60].

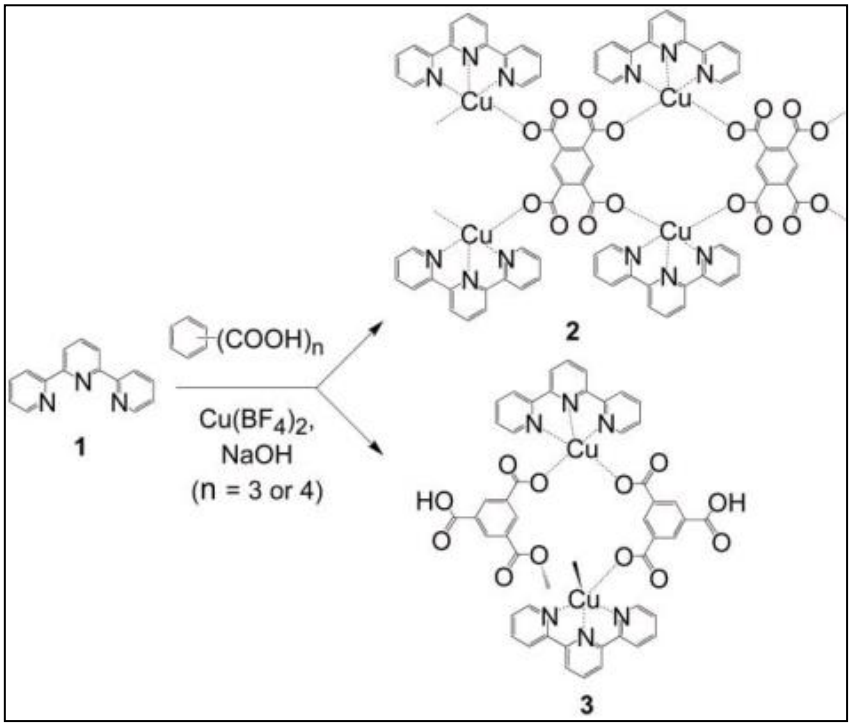

Figure 1. 5: Chemical structure of repeat units in ladder-like and helical conformations (by Wang *et al*) [65].

1.4 Cobalt benzenepolycarboxylates

The effect of metal centres in coordination compounds can be observed by looking at the different properties and resulting applications of similar or isostructural compounds upon changing the metal. In the previous section, we discussed a number of copper coordination compounds with polycarboxylate ligands. When cobalt replaces copper as the metal node, despite both metals having the same valency, different characteristics are observed.

Yaghi and co-authors [66] experimented with Co and H_3BTC, and were able to yield a 1-dimensional zig-zag chain, with the subsequent chains being held in a tight 3-dimensional form by hydrogen bonding and π--π interactions (Figure 1.6). $Co_3(BTC)_2{\cdot}H_20$ crystallises as red rods, in the monoclinic space group, C2. It has elliptically shaped pores which have a diameter of 4x5 Å and extend throughout the structure as channels. Yaghi's product has the chemical fomula $Co_3(BTC)_2{\cdot}H_20$, which bears close resemblance to HKUST-1. Upon closer inspection however, it is clear that this is where the resemblance ends. Unlike the paddlewheel SBU of HKUST-1, in Yaghi's [66] product two of the carboxyl groups on BTC bind to two Co^{2+} (Co2 and Co2A) ions in a unidentate mode, whilst the third carboxyl group binds to a third Co2+ ion (Co1) in a bidentate bonding mode.

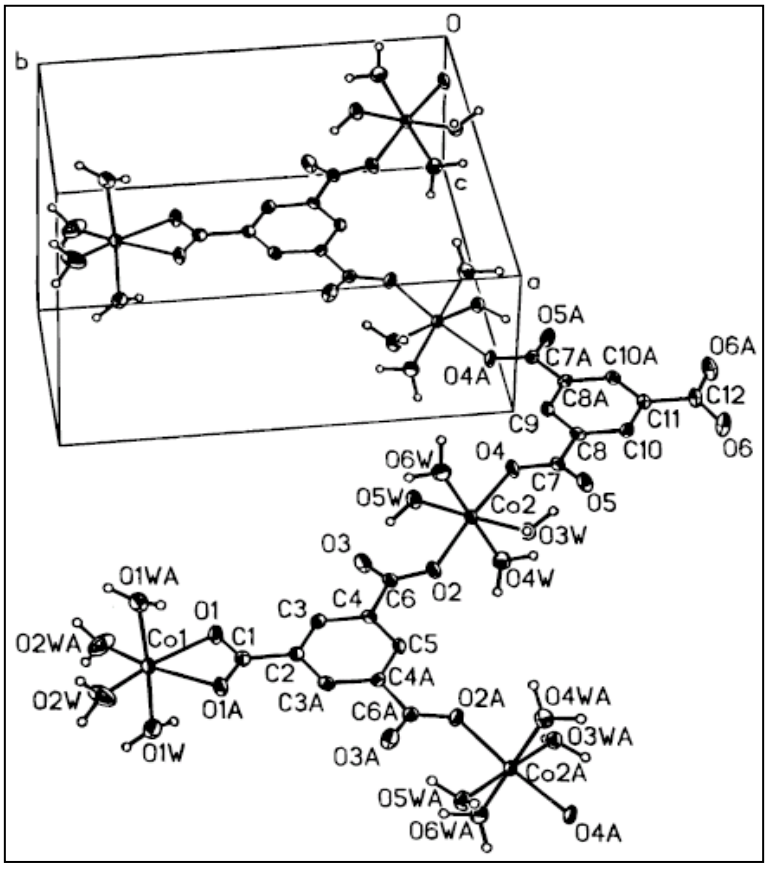

Figure 1. 6: The zigzag $Co_3(BTC)_2$ chain and asymmetric unit by Yaghi *et al* [66].

Camara *et al* [67] worked with Co and H4B4C and observed the formation of a 2-dimensional square grid (Figure 1.7). Two Co^{2+} ions are each situated on an inversion centre and each is coordinated to four water O atoms and two COOH groups from two B4C, in a distorted octahedron. The framework is held together by hydrogen-bonding interactions involving the coordinated water molecules, the carboxylate groups and lattice water, leading to the formation of a three-dimensional network.

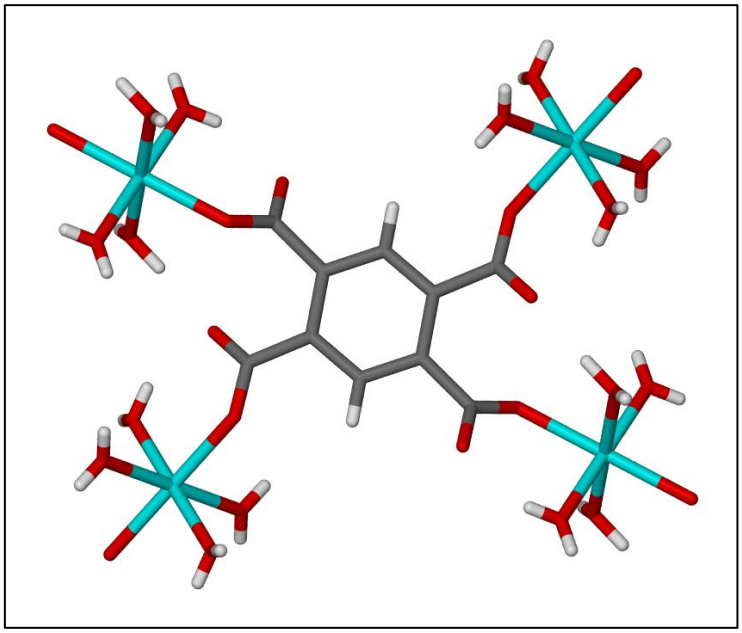

Figure 1. 7: 2-dimensional CoB4C square grid (by Camara) [67].

In a mixed ligand synthesis using pyridine and H_3BTC, Kamarka and Oliver *et al* [68] produced a 2-dimensional sheet by using the carboxyl groups on H_3BTC to bridge Co^{2+} ions in the 101 plane. The Co^{2+} exists in 2 chemical environments (Figure 1.8). Co1 is coordinated to two pyridines and two water molecules in the orthogonal plane, and also to two BTC^{3-} via monodentate bridging coordination modes, forming an octahedron. Co2 it is coordinated to two BTC^{3-} via monodentate bridging coordination modes and a third BTC^{3-} via bidentate

coordination mode. It is also coordinated to two pyridines, forming a distorted octahedron. The product, $[Co_{1.5}\cdot(C_9H_3O_6)\cdot(C_5H_5N)_3\cdot H_2O]\cdot CH_3OH$ $0.26H_2O$, crystallizes in the triclinic space group P1 and is stabilized by hydrogen bonding and π--π stacking.

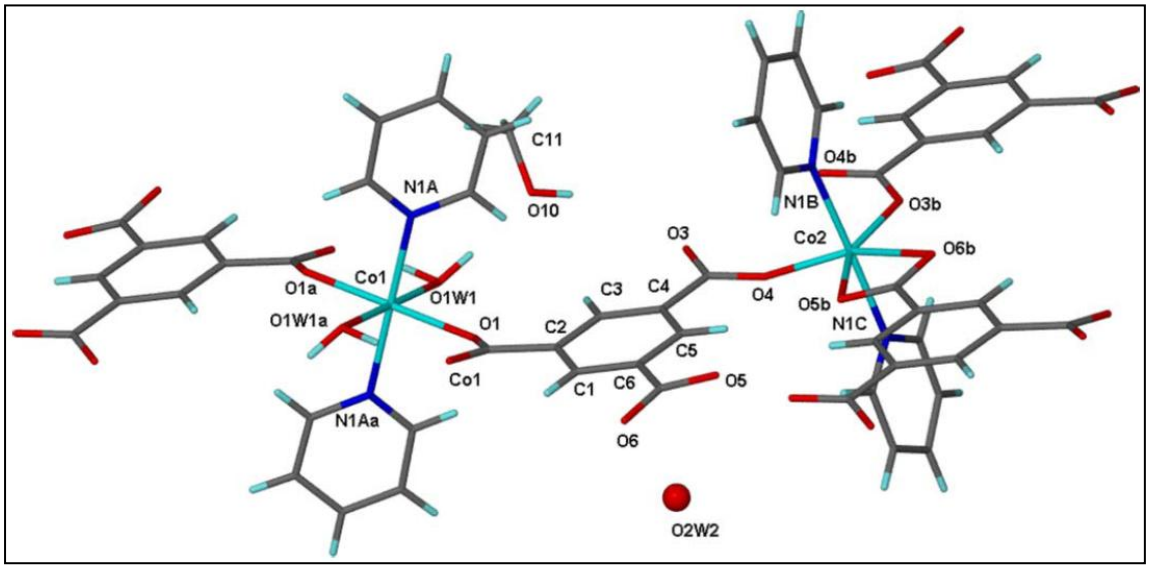

Figure 1. 8: Coordination environment of Co^{2+} ions (by Kamarkar and Oliver) [68].

Upon reaction with H_4B4C in the presence oxalate, Li *et al* [47] discovered that cobalt forms a 3-dimensional structure through interpenetration of 2-dimensional sheets. The single crystal data revealed that cobalt ions exist in two crystallographically unique environments. Co1 is monodentate coordinated to four carboxyl groups from four B4C ligands through the oxygen atoms. It is also coordinated to two oxygen atoms from two waters forming a distorted octahedron (Figure 1.9A). The Co2 and Co2A centres are each coordinated to three oxygens from three B4C carboxyl groups, two oxygens from one oxalate ion and lastly to one oxygen from a bridging water molecule. This creates a distorted octahedron. The resulting three $\{CoO_6\}$ octahedra are connected to form a trinuclear linear chain by sharing edges. Two bonding modes are

displayed by the carboxyl groups on each B4C ion. Two carboxyl groups act as bidentate ligands bridging two cobalt centres. The other two carboxyl groups display unusual dentate behaviour and link three cobalt centres, forming polyhedral secondary building units. This coordination behaviour leads to interpenetration of the 2-dimensional structures (Figure 1.9B) creating a 3-dimensional product [47].

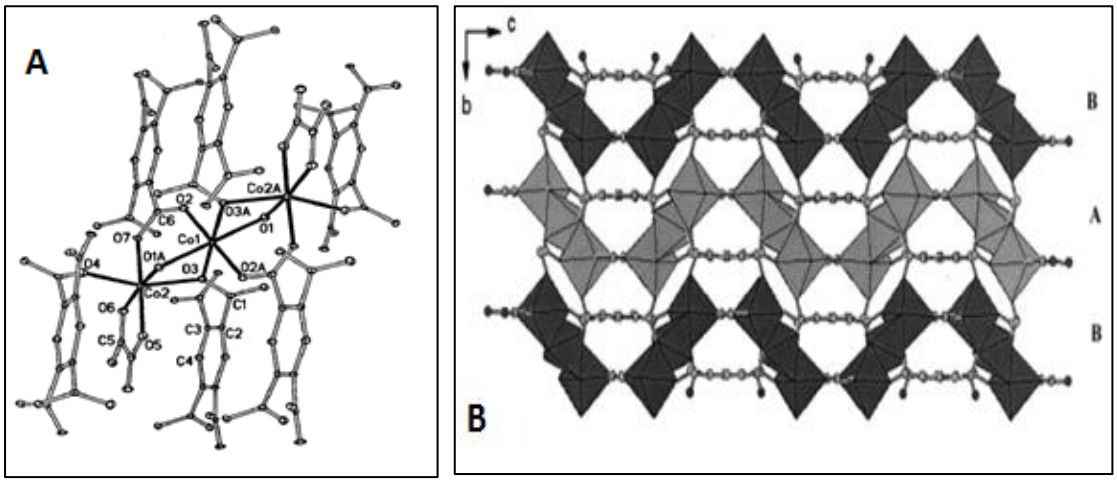

Figure 1. 9: Coordination environment of Co ions (A) and polyhedral representation of the 3-D metal-organic framework of compound **1** viewed along the *a* axis; the light and dark colours represent two 2-D interpenetrating layers with different extending directions, respectively (B) (by Li *et al*) [47].

A comparison of the products of Co with various benzenepolycarboxylates, shows that these compounds have the potential to form 1-, 2- and 3-dimensional structures, with the latter often being a result of hydrogen bonding. In mixed ligand systems, the metal centres often exist in different chemical environments and exhibit different bonding modes. These differences in coordination numbers and geometries lead to significant differences in polymeric structure. Both Co^{2+} and Co^{3+} often favour six coordinate octahedral geometries. In benzenepolycarboxylates the dimensionality of the resulting

coordination framework topology is largely dependent on the deprotonation level of the COOH groups [69]. This results in a wide range of possible different applications, from sorption [66] to catalysis [70–72]. Thus, the selection of both primary and secondary building units has a marked effect on the structure, properties and potential applications of MOFs.

1.5: Molybdenum polyoxometalate (POMs) polycarboxylates

Molybdenum cations often exist as polyatomic oxoanions which are formed by bridging three or more metal centres through terminal oxygens to form a 3-dimensional structure [73]. A number of structural motifs can be formed depending on the number of metals in the cluster unit. POMs can either be of made up of one metal (eg. Lindqvist hexamolybdate) or mixed metal clusters (eg. Keggin phosphomolybdate). Both the iso- and hetero- POMs have been seen to possess good redox properties owning to their existence in strong Bronsted acidity [74] and high oxidation states.

Reactions of the Mo POM, $[Mo_6O_{18}(O_3AsPh)_2]$, with various Cu-bis(triazole) ligands under solvothermal conditions yielded some very interesting structures [75]. The Cu adopts a T-type geometry and is coordinated to two N atoms from two trans-positioned ligands, resulting in S-shaped 1-dimensional chains. These chains are then bridged through Cu-O (from the POMs) links to give 2-dimensional sheets. The S-shaped chains penetrate the parallel sheets to give a 3-dimensional framework. Liu *et al* [75] also realized that the POMs exhibited different coordination modes ranging from bidentate to octadentate, resulting

in a wide range of structures with significant chemical and physical properties (Figure 1.10)

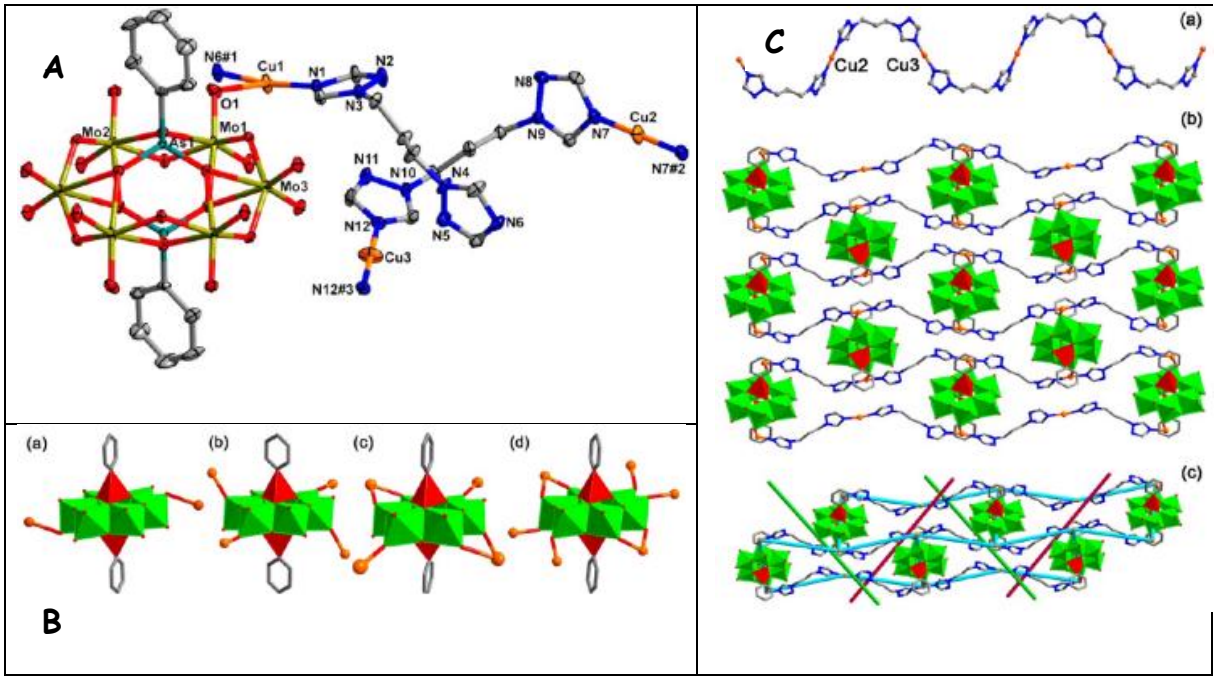

Figure 1. 10: A view of the (A) coordination environments of the Cu(I) centres in 1, (B) coordination modes of As_2Mo_6 polyoxoanions and (C) 1-D S-shaped chains in 1(a); 2-D highly undulated layer (b); 3-D polypseudo-rotaxane array constructed by 1D S-shaped chains and 2D undulated layer [75].

Sun *et al* [74] made a series of POM-MOFs by via one pot hydrothermal synthesis with the general structure; $[Cu_2(BTC)_{4/3}(H_2O)_2]_6[H_nXM_{12}O_{40}]\cdot(C_4H_{12}N)_2$ (where X =Si, Ge, P, As and M = W, Mo). The resulting host framework was isostructural to HKUST-1 but had guest POM ions with different charges encapsulated as shown in Figure 1.11. The framework has two kinds of pores, A and B, both with cuboctahedral shapes (a polyhedron with 8 triangular faces and 6 square faces). Pore A has a large free diameter of 13 Å and hosts the POM anions whilst pore B has a free diameter of 10 Å due to coordinated waters directed inside the pores [74].

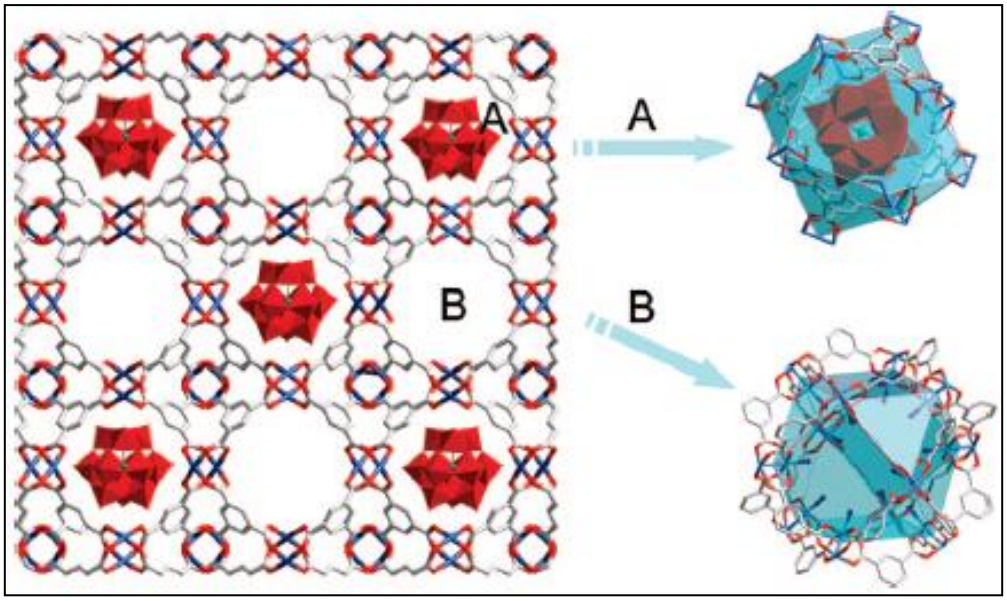

Figure 1. 11: The Cu-BTC framework and Keggin polyanions (by Sun *et al*) [74].

Each of these scenarios indicates that POMs have a dual potential in MOF synthesis, they can either be encapsulated within a framework or they can be encorporated in the framework structure. In both cases, they still contribute significantly to the properties and hence possible applications of the POM-MOFs.

1.6 Applications of Mo-POMs, Co and Cu benzene polycarboxylates

These materials have found a wide range of application in various fields such as storage, sensing and catalysis as shown in Table 1.1. Bordiga *et al* [60] synthesized HKUST-1 at lower temperatures and investigated its gas sorption properties using small molecules (NO, NO_2, CO, CO_2 and H_2). The range of molecular adsorption ranged from 3mmol/g for NO to 11.6mmol/g for H_2. This sorption was mainly attributed to the formation of Cu^{2+}···gas adducts upon evacuation of the water from the MOF. Dehydration had the effect of creating

more coordinately unsaturated Cu^{2+} dimers and hence improving attraction between the MOFs and adsorbates [60].

Table 1. 1: Applications of MOFs

MOF	Application	Reference
HKUST-1	Adsorption (eg.CO, NO, N_2, H_2)	[60,76]
HKUST-1/CF, UiO-66(NH_2)	Catalyst (H_2O_2 & phenol oxidation)	[77,78]
$[Co_3(btec)(C_2O_4)(H_2O)_2]_n$,Cu(btec)(pyz)	Magnetism	[47,69]
$\{[Co_4(FcDCA)_4(bpy)_4(H_2O)_6]\cdot 11H_2O\}_n$	Supercapacitors, dye adsorption	[79]
$Cu(I)_n$(bis(1,2,4-triazol-1yl)$_n Mo_6O_{18}$ $(O_3AsPh)_2$	Photocatalysis (dyes), electrocatalytic reduction of nitrates	[75]
$Co_2(pm)(bib)_{0.5}(H_2O)_{0.5}$	Luminescence	[48]
C/Al-MIL-53-$(OH)_2$	Electrochemical detection of dopamine	[80]
$\{[Cu_2(HL)_2(\mu_2\text{-}OH)_2(H_2O)_5]H_2O\}_n$	Ascorbic acid electrochemical detection	[81]
Au-SH-SiO_2@Cu-MOF	Electrochemical detection of L-cysteine	[82]
$Al_2(OH)_2$TCPP-Co	Electrocatalytic reduction of CO_2	[83]
$[Co_3(oba)_3(O)$ $(Py)_{0.5}]n\cdot 4DMF\cdot Py$	Oxidative desulphurization catalysts	[84]

Lin *et al* [76] calcined HKUST-1 at 160 and 200 °C before investigating its potential for the storage of hydrogen gas. They reported a 0.47 weight% uptake at 303 K and 35 bars pressure. Improvements on these figures are reported for electro-synthesised HKUST-1 (4.71 weight% uptake at 298 K and 1.2 bars pressure) [85].These conditions are relatively close to the conditions required for commercial hydrogen storage. The United States Department of Energy has the recommended that by 2017 Hydrogen storage materials meet the following; high gravimetric storage capacity of 5.5 weight%, operating temperatures of not more than 333 K and maximum pressure of 100 bars [86].

The HKUST-1 counterpart synthesized by Yaghi [66] and co authors using cobalt, was also successfully applied to the absorption and desorption of ammonia and water after it had been activated by dehydration at 110 °C, showing the success of these materials in storage applications.

On their own, POMs are known to have good catalytic activity. However the efficiency is greatly reduced due to their tendency to aggregate and hence reduce access to active sites [74]. In order to circumvent this, a suitable porous support, such as a zeolite, for the POM could be used. For example, Shahram Tangestaninejad *et al* [87] supported $MoO_2(acac)_2$ catalyst on silica and observed an increase in the catalytic activity and reusability in alkene epoxidation. Tang *et al* [78] also observed similar results for olefin oxidation, when the $MoO_2(acac)_2$ was loaded on the Zr-MOF, (UiO-66(NH_2)) via post synthetic modification of the MOF.

A more recent approach involves the integration of MOF and POM unit creating POM-MOFs. These have been seen to be particularly good catalysts due to the afore-mentioned properties of MOFs [88-90]. Abednatanzi [91] applied post synthetic modification to HKUST-1 pores via incorporation of molybdenum oxodiperoxo Schiff bases for applications in catalysis (Figure 1.12). The epoxidation of olefins and allylic alcohols was most efficient in the presence of TBHP oxidant and chlorinated solvents like $CHCl_3$ with very high percentage conversions of 99% achieved after 1 hr [91].

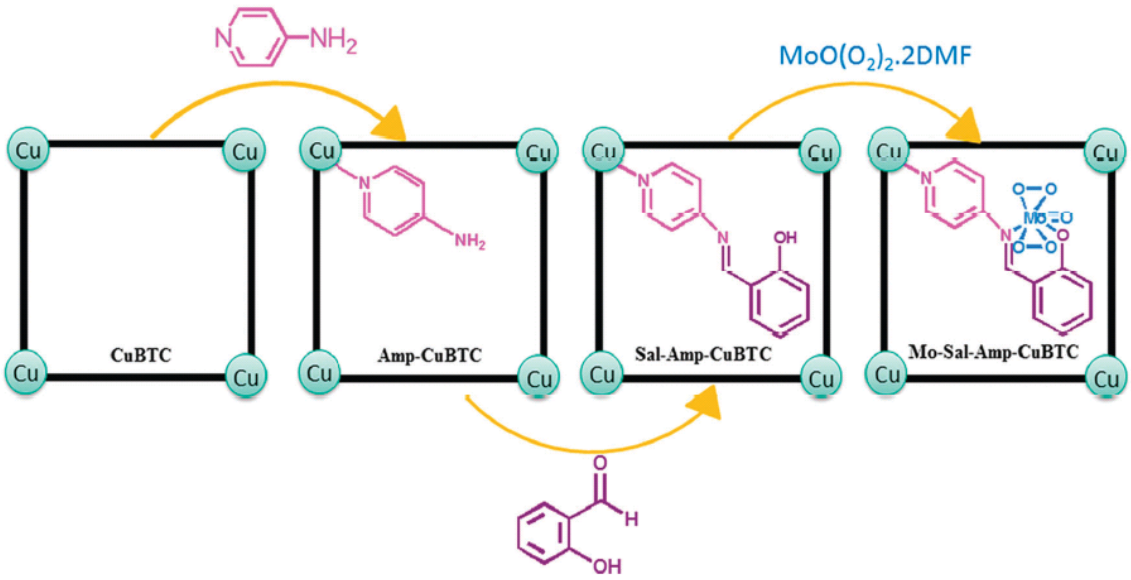

Figure 1. 12: Schematic illustrating PSM of HKUST-1 (by Abednatanzi *et al*) [81].

The $[Cu(I)_n(bis(1,2,4\text{-triazol-1yl})_nMo_6O_{18}(O_3AsPh)_2]$ POM-MOFs synthesized by Liu *et al* [75] is another such example of this success. These compounds showed photocatalytic activity against methyl blue as well as electrocatalytic activity for the reduction of nitrates [75].

1.7 Catalysis

Catalysis is the increase in the rate of a chemical reaction by use of a catalyst. By definition, a catalyst is a substance that increases the rate of a chemical reaction without itself undergoing any permanent chemical change [92]. In catalytic reactions, the catalyst works by providing an alternative route which requires a lower activation energy. This results in a higher reaction rate under the same experimental conditions. A typical catalytic mechanism starts with a reaction between the substrates and the catalyst to form an intermediate structure in which everything is adsorbed on the catalyst. The second phase then involves a reaction between the substrates whilst both are still attached

to the catalyst. The third stage involves desorption of the now reacted molecules to form desired products, leaving a free catalytic active site to react with new molecules [93].

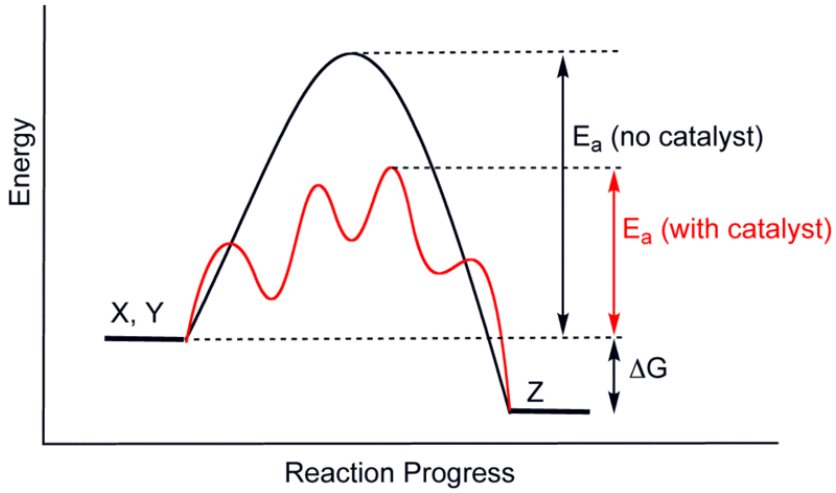

Figure 1. 13: Energy profile of catalytic reactions.

A good catalyst should have a number of characteristics including good stability. This however does not mean it cannot be poisoned but simply implies that it should be able to undergo a number of cycles before fouling occurs. Fouling reduces the catalysts efficiency creating a need for recycling or replacement. A catalyst should be unchanged at the end of the reaction such that it can facilitate further reactions. A good catalyst should also be efficient in small quantities and be selective for a group of reactants. Catalytic activity is also improved by employing optimum reaction conditions such as temperature and pH.

Catalysis can be classified into four broad groups; biocatalysis, homogeneous, heterogeneous and electrocatalysis [92,94]. Biocatalysts are normally employed in biochemical systems. Examples of these are enzymes. Homogeneous catalysts

are in the same phase as the reactants and heterogeneous catalysts are in a different phase from the reactants. Heterogeneous catalysts are usually solid materials which are supported on another solid matrix to increase efficiency and reduce costs. The difference in phases often makes it easier to separate the catalyst from products [92,95]. Electrocatalysis involves employing electrical energy to drive the reaction at the electrode surface. These electrochemical reactions occur as a result of charge transfer, which in turn is due to the movement of electrons or holes (in electrodes) and of ions (electrolyte) [96,97].

1.7.1 MOFs in electrocatalysis

The most structurally important feature of any catalyst is the active site. Because of this, it is important to avail as much of the potential active sites to the reaction mixture as possible. This increases efficiency and reaction rates. MOFs have been used in various catalytic reactions in literature [62,77,98]. Through proper choice of primary and secondary building units, MOFs which target specific reactions can be synthesized.

For catalysis to occur, access to the active sites needs to be improved as this results in shorter reaction times. Mo compounds have already been used as competitive electrocatalysts [88]. Zinc POM-MOFs catalysts with the general formula $(TBA)_3[PMoV_8Mo(VI)_4O_{36}(OH)_4Zn_4][C_6H_3(COO)_3]_{4/3}\cdot nH_2O(\varepsilon(trim)_n)$ were synthesized using the Mo keggin POM, ammonium molybdate tetrahydrate and employed in electrocatalytic Hydrogen evolution reaction detection. A turnover number of $1.2x10^5$ was obtained within 5 hours. The high oxidation states of Mo compounds make the metal a good platform for charge transfer and candidate for other electrocatalytic processes.

The combination of Co-Mo complexes has also successfully been used for various catalytic reactions [99]. Previous research has shown that higher catalytic efficiencies are observed with longer chains [100]. However, unless properly dispersed on a suitable support, activity is greatly reduced. The major disadvantage with supports like alumina and silica is that they take up about 80% of the weight of the final product without adding any catalytic activity. Using MOFs made of the catalytically active PBUs plays a dual role of support as well as providing catalysis active sites [99].

Other combinations such as Cu-Mo have also shown promising results in other fields of electrocatalysis. Keita and co-authors [101] studied the electrochemical properties of a series of Dawson-type hetero-POMs including α_2-$K_8[Cu(OH_2)P_2W_{15}Mo_2O_{61}]$ and α_2-$K_7[Fe(OH_2)P_2W_{15}Mo_2O_{61}]$ by cyclic voltammetry (CV). The POM substituted materials showed electrocatalytic activity towards the reduction of nitrates, dioxygen and hydrogen peroxides. The results indicate a cooperative effect between the Mo and Cu centers within these POMs [101].

L-cysteine is an amino acid that is important for various biological processes such as protein synthesis and metabolism [82]. It is important to monitor physiological molecules as they are indicators of the health of individuals. There are various techniques which can be used to detect the L-cysteine; very few however have to do with the use of MOFs in electrochemistry [102]. Compared to other nanomaterials, the area of MOFs in electrocatalysis is still relatively unexplored [103]. MOFs have the potential to be used as catalysts due to their porosity and high charge transfer abilities [37]. They have already demonstrated ability to form positive cooperative effects with other metals making them good

candidates for other catalytic fields [101]. POMs have been successfully used as electrocatalysts due to the high oxidation states of the metals [104].

The current study is an attempt at using polyoxomolybdates (Mo_6) incorporated into HKUST-1 MOF (Mo_6–CuBTC POM-MOF), Cu and Co benzenepolycarboxylate MOFs as electrochemical sensors for L-cysteine.

1.8 Aims of this study

The aims of the study were to:

- Synthesize novel coordination compounds (MOFs and POM-MOFs).
- Characterize the compounds using single crystal X-ray diffraction (SC-XRD), X-ray powder diffraction (PXRD), Fourier transform infrared spectroscopy (FTIR), thermogravimetric analysis (TGA), differential scanning calorimetry (DSC), elemental analysis and scanning electron microscopy (SEM).
- Electrocatalysis of L-cysteine using the synthesized compounds:-
    - To investigate the difference in electrocatalytic behaviour depending on encapsulation vs encorporation of Mo-POMs in HKUST-1.
    - To investigate the difference in electrocatalytic behaviour depending on coordination of a flexible benzenepolycarboxylate based MOF.
    - To investigate the difference in electrocatalytic behaviour depending on coordination of a reduced heterocyclic polycarboxylate MOF.

References

[1] K. Bowman-james, *Acc. Chem. Res.* **2005**, *38*, 671–678.

[2] M. S. Ridenour, *A Brief History of Chemistry, Research Institute for Waldorf Education*, AWSNA Publications, ISBN 9781365376016, **2004**.

[3] T. Poulsen, *Introduction to Chemistry*, Open Education Group, ISBN 147829860X, **2010**.

[4] J. Hudson, in *Hist. Chem.*, Springer US, Boston, MA, **1992**, pp. 1–15.

[5] S. K. Ghosh, *Res. J. Chem. Environ. Sci.* **2015**, *3*, 44–47.

[6] R. A. Mazzocchi, *ACS Sensors* **2016**, 1167–1170.

[7] P. T. Anastas, M. Kirchhoff, *Acc. Chem. Res* **2002**, *35*, 686–694.

[8] J. Yang, T.-J. Kwak, X. Zhang, R. Mcclain, W.-J. Chang, S. Gunasekaran, *Sci. Technol. Adv. Mater.* **2016**, 1–9.

[9] T. Li, X. Wang, L. Zhou, J. An, J. Li, N. Li, H. Sun, Q. Zhou, *ACS Sensors* **2016**, *1*, 1374–1379.

[10] J. B. Raoof, R. Ojani, H. Beitollahi, *Electroanalysis* **2007**, *19*, 1822–1830.

[11] K. Uemura, R. Matsuda, S. Kitagawa, *J. Solid State Chem.* **2005**, *178*, 2420–2429.

[12] Y. Kubota, M. Takata, T. C. Kobayashi, S. Kitagawa, *Coord. Chem. Rev.* **2007**, *251*, 2510–2521.

[13] A. Béziau, S. A. Baudron, M. W. Hosseini, D. Rasoloarison, M. W. Hosseini, *CrystEngComm* **2014**, *16*, 4973–4980.

[14] A. F. Williams, *Chem. Met. Alloy.* **2009**, *2*, 1–9.

[15] D. E. C. Ferreira, H. F. Dos Santos, W. B. De Almeida, G. M. A. Junqueira, *J. Brazillian Chem. Soc.* **2007**, *18*, 1379–1387.

[16] J. Qin, D. Liu, C. Dai, C. Chen, B. Wu, C. Yang, *Coord. Chem. Rev.* **1999**, *188*, 23–34.

[17] A. T. Çolak, F. Çolak, O. Z. Yesilel, D. Akduman, F. Yilmaz, M. Tümer, *Inorg. Chim. Acta* **2010**, *363*, 2149–2162.

[18] O. K. Farha, A. M. Spokoyny, K. L. Mulfort, S. Galli, J. T. Hupp, C. A. Mirkin, *Small* **2009**, *5*, 1727–1731.

[19] S. Bureekaew, S. Shimomura, S. Kitagawa, *Sci. Technol. Adv. Mater.* **2008**, *9:1*, 12pp.

[20] M. E. Van der Boom, D. Milstein, *Chem. Rev.* **2003**, *103*, 1759–1792.

[21] R.-R. Zhuang, F.-F. Jian, K. Wang, *Sci. Technol. Adv. Mater.* **2009**, *10*, 045001.

[22] A. Ramdass, V. Sathish, E. Babu, M. Velayudham, P. Thanasekaran, S. Rajagopal, *Recent Developments on Optical and Electrochemical Sensing of Copper (II) Ion Based on Transition Metal Complexes Tiruvedagam*, **2017**.

[23] T. Kokulnathan, S. Sakthinathan, S.-M. Chen, R. Kartik, T.-W. Chiu, *Inorg. Chem. Front.* **2018**, DOI 10.1039/c8qi00055g.

[24] R. J. Kuppler, D. J. Timmons, Q.-R. Fang, J.-R. Li, T. A. Makal, M. D. Young, D.-Q. Yuan, D. Zhao, W.-J. Zhuang, H.-C. Zhou, *Coord. Chem. Rev.* **2009**, *253*, 3042–3066.

[25] J. Lei, R. Qian, P. Ling, L. Cui, H. Ju, *Trends Anal. Chem.* **2014**, *58*, 71–78.

[26] H. Furukawa, K. E. Cordova, M. O. Keeffe, O. M. Yaghi, *Science, 80.* **2013**, *341*, 974–986.

[27] L. Öhrström, *Crystals* **2015**, *5*, 154–162.

[28] S. R. Batten, N. R. Champness, X.-M. Chen, J. Garcia-Martinez, S. Kitagawa, L. Öhrström, M. O. Keeffe, M. P. Suh, J. Reedijk, *Pure Appl. Chem.* **2013**, *85*, 1715–1724.

[29] S. R. Batten, N. R. Champness, X.-M. Chen, J. Garcia-Martinez, S. Kitagawa, L. Ohrstrom, M. O. Keeffe, M. P. Suh, J. Reedijk, *CrystEngComm* **2012**, *14*, 3001–3004.

[30] R. F. Mendes, F. A. A. Paz, *Inorg. Chem. Front.* **2015**, *2*, 495–509.

[31] C. Dey, T. Kundu, B. P. Biswal, A. Mallick, R. Banerjee, *Acta Cryst.* **2014**, *B70*, 3–10.

[32] S. T. Meek, J. A. Greathouse, M. D. Allendorf, *Adv. Mater.* **2011**, *23*, 249–267.

[33] N. Stock, S. Biswas, *Chem. Rev.* **2012**, *112*, 933–969.

[34] D. Tanaka, S. Kitagawa, *Chem. Mater.* **2008**, *20*, 922–931.

[35] M. Bosch, M. Zhang, H.-C. Zhou, *Adv. Chem.* **2014**, 8pp.

[36] P. Kumar, A. Deep, K.-H. Kim, *Trends Anal. Chem.* **2015**, *73*, 39–53.

[37] L. E. Kreno, K. Leong, O. K. Farha, M. Allendorf, R. P. Van Duyne, J. T. Hupp, *Chem. Rev.* **2012**, *112*, 1105–1125.

[38] S. Ma, G. A. Goenaga, A. V Call, D.-J. Liu, *Chem. Eur. J.* **2011**, *17*, 2063–2067.

[39] X. Hu, Y. Lu, F. Dai, C. Liu, Y. Liu, *Micropor. Mesopor. Mat.* **2013**, *170*, 36–44.

[40] P. C. Banerjee, D. E. Lobo, R. Middag, W. K. Ng, M. E. Shaibani, M. Majumder, *Appl. Mater. Interfaces* **2015**, *7*, 3655–3664.

[41] Y. Ren, M. Wang, X. Chen, B. Yue, H. He, *Materials.* **2015**, *8*, 1545–1567.

[42] J. Xu, D. Chu, J. Yu, T. Wang, A. Tang, *Sci. China Ser. B Chem.* **2004**, *47*, 10–16.

[43] I. H. Choi, Y. Kim, D. N. Lee, S. Huh, *Polyhedron* **2016**, *105*, 96–103.

[44] Y. Xie, Z. Yu, X. Huang, Z. Wang, L. Niu, M. Teng, J. Li, *Chem. - A Eur. J.* **2007**, *13*, 9399–9405.

[45] H. Hahm, K. Yoo, H. Ha, M. Kim, *Inorg. Chem.* **2016**, *55*, 7576–7581.

[46] C. Zhang, D. Ma, X. Zhang, J. Ma, L. Liu, X. Xu, *J. Coord. Chem.* **2016**, *69*, 985–995.

[47] Y.-G. Li, N. Hao, E.-B. Wang, Y. Lu, C.-W. Hu, L. Xu, *Eur. J. Inorg. Chem.* **2003**, *3*, 2567–2571.

[48] C.-L. Ming, Y.-N. Zhao, B.-Y. Yu, K. Van Hecke, G.-H. Cui, *Bull. Korean Chem. Soc* **2014**, *35*, 3349–3352.

[49] L. Xu, E. Y. Choi, Y. U. Kwon, *Inorg. Chem. Commun.* **2008**, *11*, 1190–1193.

[50] M. J. Manos, E. E. Moushi, G. S. Papaefstathiou, A. J. Tasiopoulos, *Cryst. Growth Des.* **2012**, *12*, 5471–5480.

[51] M.-S. Chen, Y.-Q. Yang, C.-H. Zhang, D.-Z. Kuang, Y.-F. Deng, Z.-M. Chen, *Inorg. Chem. Commun.* **2011**, *14*, 444–446.

[52] G.-H. Wang, Z.-G. Li, H.-Q. Jia, N.-H. Hu, J.-W. Xu, *CrystEngComm* **2009**, *11*, 292–297.

[53] J. Xie, Z. Han, W. Pei, Y. Zou, X. Ren, *Inorg. Chem. Commun.* **2011**, *14*, 1266–1270.

[54] J. Kim, S.-H. Kim, S.-T. Yang, W.-S. Ahn, *Micropor. Mesopor. Mat.* **2012**, *161*, 48–55.

[55] M. J. Plater, M. R. S. J. Foreman, T. Gelbrich, M. B. Hursthouse, *Inorg. Chim. Acta* **2001**, *318*, 171–174.

[56] C. Merz, M. Desciak, C. O. Brien, R. L. Laduca, R. C. Finn, R. S. Rarig, J. A. Zubieta, *Inorg. Chim. Acta* **2004**, *357*, 3331–3335.

[57] M. J. Plater, M. R. S. J. Foreman, R. A. Howie, J. M. S. Skakle, *Inorg. Chim. Acta* **2001**, *318*, 175–180.

[58] S. Loera-Serna, M. A. Oliver-Tolentino, M. D. L. López-Núñez, A. Santana-Cruz, A. Guzmán-Vargas, R. Cabrera-Sierra, H. I. Beltrán, J. Flores, *J. Alloys Compd.* **2012**, *540*, 113–120.

[59] S.-Y. Chui, M.-F. Lo, J. P. H. Charmant, A. G. Orpen, D. I. Williams, I. D. Williams, *Science 80.* **1999**, *283*, 1148–1150.

[60] S. Bordiga, L. Regli, F. Bonino, E. Groppo, C. Lamberti, B. Xiao, P. S. Wheatley, R. E. Morris, A. Zecchina, *Phys. Chem. Chem. Phys.* **2007**, *9*, 2676–2685.

[61] K. Peikert, L. J. McCormick, D. Cattaneo, M. J. Duncan, F. Hoffmann, A. H. Khan, M. Bertmer, R. E. Morris, M. Fröba, *Micropor. Mesopor. Mat.* **2015**, *216*, 118–126.

[62] J. M. Zamaro, N. C. Perez, E. E. Miro, C. Casado, B. Seoane, C. Tellez, J. Coronas, *Chem. Eng. J.* **2012**, *195–196*, 180–187.

[63] M. Schlesinger, S. Schulze, M. Hietschold, M. Mehring, *Micropor. Mesopor. Mat.* **2010**, *132*, 121–127.

[64] W. Clegg, J. M. Holcroft, N. C. Martin, *CrystEngComm* **2015**, *17*, 2857–2871.

[65] P. Wang, G. R. Newkome, M. Panzer, C. N. Moorefield, *Chem. Commun.* **2005**, 465–467.

[66] O. M. Yaghi, H. Li, T. L. Groy, *J. Am. Chem. Soc.* **1996**, *118*, 9096–9101.

[67] M. Camara, M. Tine, C. Daiguebonne, O. Guillou, T. Roisnel, *Acta Cryst.* **2014**, *E69*, m680–m681.

[68] A. Karmakar, C. L. Oliver, *Z.Kristallogr.* **2013**, *288*, 330–334.

[69] A. Majumder, V. Gramlich, G. M. Rosair, S. R. Batten, J. D. Masuda, M. S. El Fallah, J. Ribas, J.-P. Sutter, C. Desplanches, S. Mitra, *Cryst. Growth Des.* **2006**, *6*, 2355–2368.

[70] D. Dey, A. B. Roy, A. Ranjani, L. Gayathri, C. Saravanan, D. Dhanasekaran, A. M. Akabarsha, C.-Y. Shen, H.-L. Tsai, M. Maji, et al., *J. Chem. Sci.* **2015**, *127*, 649–661.

[71] M. Kumar, P. M. Kozlowski, *Angew. Chem. Int. Ed.* **2011**, *50*, 8702–8705.

[72] S. Meghdadi, M. Amirnasr, M. H. Habibi, A. Amiri, V. Ghodsi, A. Rohani, R. W. Harrington, W. Clegg, *Polyhedron* **2008**, *27*, 2771–2778.

[73] K. C. Dey, V. Sharma, *Int. J. Chem. Tech. Res.* **2010**, *2*, 368–375.

[74] C.-Y. Sun, S.-X. Liu, D.-D. Liang, K.-Z. Shao, Y.-H. Ren, Z.-M. Su, *J. Am. Chem. Soc.* **2009**, *131*, 1883–1888.

[75] B. Liu, J. Yang, G.-C. Yang, J.-F. Ma, *Inorg. Chem.* **2013**, *52*, 84–94.

[76] K.-S. Lin, A. K. Adhikari, C.-N. Ku, C.-L. Chiang, H. Kuo, *Int. J. Hydrogen Energy* **2012**, *37*, 13865–13871.

[77] T. Granato, F. Testa, R. Olivo, *Micropor. Mesopor. Mat.* **2012**, *153*, 236–246.

[78] J. Tang, W. Dong, G. Wang, Y. Yao, L. Cai, Y. Liu, X. Zhao, J. Xu, L. Tan, *RSC Adv.* **2014**, *4*, 42977–42982.

[79] R. Rajak, M. Saraf, A. Mohammad, S. M. Mobin, *J. Mater. Chem. A Mater. energy Sustain.* **2017**, *5*, 17998–18011.

[80] Y. Wang, H. Ge, G. Ye, H. Chen, X. Hu, *J. Mater. Chem. B* **2015**, *3*, 3747–3753.

[81] X.-Q. Wu, J.-G. Ma, H. Li, D.-M. Chen, W. Gu, G.-M. Yang, P. Cheng, *Chem. Commun.* **2015**, *51*, 9161–9164.

[82] H. Hosseini, H. Ahmar, A. Dehghani, A. Bagheri, A. Tadjarodi, A. Reza, *Biosens. Bioelectron.* **2013**, *42*, 426–429.

[83] N. Kornienko, Y. Zhao, C. S. Kley, C. Zhu, D. Kim, S. Lin, C. J. Chang, O. M. Yaghi, P. Yang, *J. Am. Chem. Soc.* **2015**, 7p.

[84] M. Y. Masoomi, M. Bagheri, A. Morsali, *Inorg. Chem.* **2015**, *54*, 11269–

11275.

[85] W. W. Lestari, M. Adreane, H. Suwarno, *J. Math. Fundam. Sci.* **2017**, *49*, 213–224.

[86] US Department of Energy, in *Targets Onboard Hydrog. Storage Syst. Light. Veh.*, **2009**, pp. 1–22.

[87] S. Tangestaninejad, M. Moghadam, V. Mirkhani, I. Mohammadpoor-Baltork, K. Ghani, *J. Iran. Chem. Soc.* **2008**, *5*, s71-79.

[88] B. Nohra, H. El Moll, L. M. R. Albelo, P. Mialane, C. Mellot-Draznieks, M. O'Keeffe, R. N. Biboum, J. Lemaire, B. Keita, L. Nadjo, et al., *J. Am. Chem. Soc.* **2011**, *133*, 13363–13374.

[89] X. Hu, Y. Lu, F. Dai, C. Liu, Y. Liu, *Micropor. Mesopor. Mat.* **2013**, *170*, 36–44.

[90] S. Ribeiro, A. D. S. Barbosa, A. C. Gomes, M. Pillinger, I. S. Gonçalves, L. Cunha-Silva, S. S. Balula, *Fuel Process. Technol.* **2013**, *116*, 350–357.

[91] S. Abednatanzi, A. Abbasi, M. Masteri-Farahani, A. Abbasi, *New J. Chem.* **2015**, *39*, 5322–5328.

[92] G. Rothenberg, *Catalysis: Concepts and Green Applications*, Wiley-VCH Verlag GmbH & Co. KGaA, **2008**.

[93] I. Chorkendorff, J. W. Niemantsverdriet, *Concepts of Modern Catalysis and Kinetics*, Wiley-VCH Verlag GmbH & Co. KGaA, **2007**.

[94] A. J. Bard, L. R. Faulkner, *Eectrochemical Methods; Fundamentals and Applications*, John Wiley & Sons, Inc., New York, **2001**.

[95] E. Farnetti, R. Di Monte, J. Kašpar, *Inorg. Bio-inorganic Chem.* **1999**, *II*, 1–10.

[96] E. Herrero, J. M. Feliu, A. Aldaz, in *Encycl. Electrochem.*, Wiley-VCH Verlag GmbH & Co. KGaA, **2007**.

[97] C. Sánchez, E. Leiva, in *Handb. Fuel Cells*, John Wiley & Sons, Ltd, Published Online, **2010**, p. accessed 22/08/16.

[98] Q. Han, B. Qi, W. Ren, C. He, J. Niu, C. Duan, *Nat. Commun.* **2015**, *6*, 10007.

[99] H. Gomez-Bernal, L. Cedeno-Caero, A. Gutierrez-Alejandre, *Catal. Today*

2009, *142*, 227–233.

[100] J. Qiu, G. Wang, D. Zeng, Y. Tang, M. Wang, Y. Li, *Fuel Process. Technol.* **2009**, *90*, 1538–1542.

[101] B. Keita, E. Abdeljalil, L. Nadjo, R. Contant, R. Belghiche, *Langmuir* **2006**, *22*, 10416–10425.

[102] W. Liu, X.-B. Yin, *Trends Anal. Chem.* **2016**, *75*, 86–96.

[103] H. Hosseini, H. Ahmar, A. Dehghani, A. Bagheri, A. R. Fakhari, M. M. Amini, *Electrochim. Acta* **2013**, *88*, 301–309.

[104] S.-S. Wang, G.-Y. Yang, *Chem. Rev.* **2015**, *115*, 4893–4962.

Chapter Two

This chapter outlines the synthetic methods used in making MOFs and coordination compounds. The techniques used for characterization and structural elucidation of the compounds are also outlined.

2. Experimental section

This chapter gives a brief overview of the methodology employed in this research. It also gives a background on the instrumentation and nature of results that can be obtained from the different techniques.

2.1 Materials

All chemicals were purchased from Sigma Aldrich and used as supplied. The metal salts used were copper nitrate hexahydrate ($CuNO_3{\cdot}6H_2O$), cobalt chloride hexahydrate ($CoCl_2{\cdot}6H_2O$), ammonium heptamolybdate tetrahydrate ($(NH_4)_6Mo_7O_{26}{\cdot}4H_2O$) and ammonium phosphomolybdate tetrahydrate ($(NH_4)_3PMo_{12}O_{40}{\cdot}4H_20$). All electrochemical studies were conducted with potassium chloride (KCl) as an electrolyte, L-cysteine, potassium ferricyanide (lll) $K_3Fe(CN)_6$ and potassium hexacyanoferrate trihydrate (lV) $K_4Fe(CN)_6$. All the above were technical grade and had a purity of 98% or higher.

The organic ligands used were benzene-1,3,5-tricarboxylic acid, benzene-1,2,4,5- tetracarboxylic acid, pyridine and 2,6-pyridine dicarboxylic acid, all with a purity of 97% or higher and being technical reagent grade.

The solvents used were pyridine, ethanol, dimethylformamide (DMF) and Millipore water. The solvents were of technical reagent grade and the Millipore water was dispensed by MilliQ systems.

2.2 General synthetic procedures

All compounds used in this work were made by solvothermal or slow evaporation techniques. The synthetic procedures involved dissolving the metal salt in water or ethanol and the ligand in water or DMF, then combining the solutions by

sonication. The solution mix was placed in a glass tube, sealed and heated in an autoclave at a specific temperature for a particular length of time as described in the relevant chapters to follow. In the case of slow evaporation, the mix would be covered with parafilm and left at room temperature until crystals formed. Detailed synthetic procedures for the different compounds are given in the relevant chapters.

2.3 Fourier transform infrared spectroscopy (FTIR)

FTIR is very useful in studying the functional groups in a material as well as the chemical environment in which these groups exist. Infrared radiation is electromagnetic radiation found between 14000 - 10 cm^{-1}. It is further subdivided into three regions; the Far Infrared found between 400 - 10 cm^{-1}, the Mid Infrared found between 4000 - 400 cm^{-1}, and the Near Infrared found between 14000 - 4000 cm^{-1} [1]. FTIR works by passing an infrared beam through a sample. The transmitted energy is passed through a detector and used to generate an interferogram. This is then subjected to Fourier transformations and a spectrum showing the interaction of the bonds in the material with the applied radiation is generated. Absorption bands produced in the Mid Infrared region tend to be characteristic of specific functional groups and relatively independent of the composition of the rest of the molecule whereas those in the Far Infrared region are affected by the molecular structure of the whole molecule. The Far IR spectra is characterized by bands which are unique to a specific molecule (eg. a fingerprint) and can be used for identification of unknowns [2]. The analyst can then interpret the spectrum by comparing against frequency tables and deduce the bonds present in the material as well as their chemical environments.

FTIR is a very fast and easy to use technique which requires minimal or no sample preparation, for example, when using attenuated total reflection (ATR) techniques [3-5]. In this work, the technique was mainly employed in monitoring the changes in ligand coordination mode (COO and NH), which in turn gave an indication as to the occurrence and nature of coordination. In coordination chemistry FTIR can be used to ascertain bonding ligands and none bonding ones through the vibrational shifts in these functional groups [6]. For example, conjugated C=O bands are often observed at lower frequencies (1600 - 1650 cm^{-1}) while non bonding ligands appear at higher frequencies (1700 - 1760 cm^{-1}). The nature of the chemical environment also affects band position, with aromatic bound carbonyls often appearing at lower wavenumbers than free carbonyls. In coordination chemistry, FTIR has been used to study ligand vibrations, skeletal vibrations and the coupled vibrations characteristic of complex coordination compounds. By studying the afore-mentioned vibrations, FTIR was used to characterize the products and starting materials used in this work. It was also used in conjunction with other techniques (TGA, Elemental analysis) to aid in the identification of unknown synthesized compounds. A PerkinElmer Spectrum 400 FTIR/FIR with an (ATR) attachment was employed in these studies for the range 4000 - 650 cm^{-1}. KBr discs were used over for the range 650 – 250 cm^{-1} [4,5]. The FTIR regions were determined by instrumental parameters. In the case of ATR attachments, no sample preparation was done and samples where analysed as-synthesized. For KBr discs, samples were ground with a mortar and pestle, mixed with nujol to form a mull and a placed between KBr discs. Specific details are described in chapters 3, 4 and 5.

2.4 Electrochemistry

Electrochemistry deals with the phenomena that result from combined chemical and electrical effects [7]. It covers 2 main areas;

1. Reactions in which chemical changes occur as a result of passing electrical current.

2. Reactions that result in production of electrical energy.

An electrochemical cell consists of 3 electrodes; anode(-), cathode(+) and a reference electrode, all immersed in electrolyte. Electrochemical reactions occur at the electrodes as a result of charge transfer. Charge transfer occurs as a result of movement of electrons or holes (in electrodes) and of ions (electrolyte) [8]. In an electrochemical cell, the reference electrode has a constant makeup and fixed potential therefore any changes in the cell are ascribed to the working electrode. The energy of the electrons within the working electrode is controlled by connecting a power supply to the cell. By driving the electrode to more negative potentials, the energy of the electrons can reach a level high enough to transfer into vacant electronic states on species in the electrolyte. In such cases, a flow of electrons occurs from electrode to solution and a reduction current is observed (Figure 2.1a) [9]. Similarly, the energy of the electrons can be lowered by imposing a more positive potential, and this causes electrons on solutes in the electrolyte to transfer to lower energy levels on the electrode. This is results in an oxidation current (Figure 2.1b). The critical potentials at which these processes occur are related to the standard potentials, E°, for the specific chemical substances in the system. The sum of these reactions give the reaction of the cell whilst the direction of movement and thermodynamics, determines which species is oxidized or reduced.

Electrochemical reactions are affected by electrode, external, electrical, mass transfer and solution variables. Electrode reaction kinetics are mainly affected by the electrode surface and chemical make-up. The electrode surface morphology, microstructure and geometry should allow maximum contact with the analyte so as to increase reaction rates and also enhance charge transfer [10]. This is often achieved by electrode modification. In this work, a glassy carbon electrode (GCE) surface was modified using different MOFs with the aim of improving the electrode reaction kinetics. L-cysteine was oxidized on the MOF-modified electrode surfaces and not the bare GCE suggesting that the desired outcomes were achieved (shown in following chapters).

External variables such as temperature and time also affect the reaction. In electrocatalysis, temperature increase to an optimum can lead to increased reaction rates as well as increased kinetic energy for motion of charge carriers and the analyte to the electrode surface. Allowing the reaction to run for a longer time also tends to allow more reactants to be converted to products at the electrode surface [11,12].

There are three modes by which mass is transferred in electrochemical systems; diffusion, convection and migration. Diffusion is when movement aided by a concentration gradient, convection is due to stirring and migration is the movement of a charged body under the influence of an electric field. The method of mass transfer employed in a system affects the rate of turnover and hence efficiency of an electrochemical system [13,14].

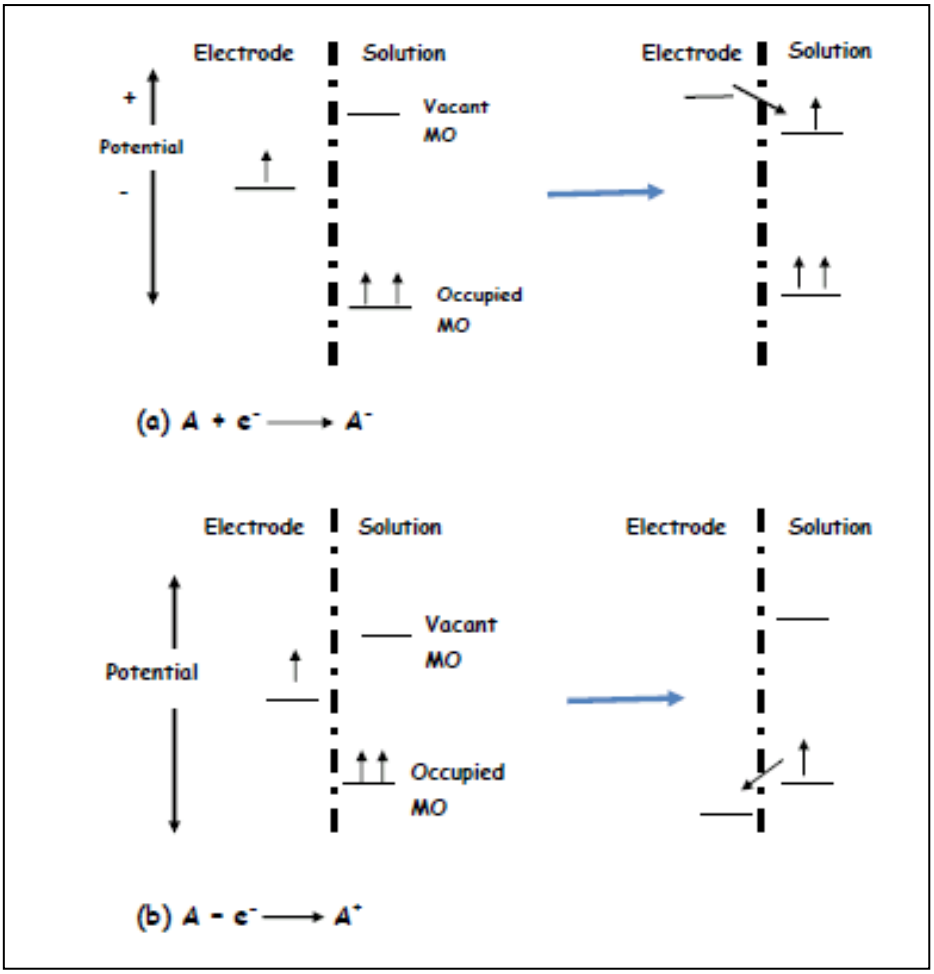

Figure 2. 1: Representation of reduction (a) and oxidation (b) in electrochemical cells [11]. .

All electrochemical experiments were performed using BAS-CV 50, Bioanalytical Systems Inc (USA). A platinum wire (cross-sectional area 0.02 cm^2) was used as the counter electrode, a silver-silver chloride wire as the reference electrode and a glassy carbon electrode as the working electrode. The glassy carbon electrode was modified using the drop-dry method with the synthesized materials (2 mg suspended in 1 mL of DMF) and used in electrocatalytic detection of L-cysteine. The electrochemical reactions occurring at the electrode surface were monitored using a combination of sweep and step electrochemical techniques such as cyclic voltametry (CV), differential pulse

voltammetry (DPV), chronoamperometry and electrochemical impedence (EIS) [8,10,15]. The sensing abilities, kinetic parameters, rate constants, sensitivity and limits of detection were also investigated. Specific details are described in chapters 3, 4 and 5.

2.5 X-ray diffraction

2.5.1 Single crystal X-ray diffraction

Whenever synthesis yielded single crystals, gravity filtration was employed to separate crystals from mother liquor. The crystals were rinsed in reaction solvent system, air dried and then good quality single crystals were hand-picked for SC-XRD. SC-XRD is a non-destructive analytical technique which provides detailed information about the internal lattice of crystalline substances, as well as unit cell dimensions, bond-lengths, bond-angles, and details of site-ordering. The data generated from the x-ray analysis is interpreted and refined to obtain the crystal structure [16]. The process involves generating x-rays using a cathode tube and producing electrons which then bombard the target element (eg. Molybdenum) and dislodge inner shell electrons. This results in production of characteristic x-rays which are collimated and directed at the sample to be analysed. Only diffracted rays of the correct orientation for the configuration are then collected by the detector and processed into a signal [17].

Single crystal structure determination was performed using Bruker Kappa Apex-II diffractometer (by Dr Eric Hosten, Nelson Mandela Metropolitan University). All measurements were made at 200 K, using graphite monochromated Mo-K_α radiation (λ=0.71073Å). Data collection was performed using the APEX-II and structure refinement was performed using SAINT [18].

Non-hydrogen atoms were refined with anisotropic thermal parameters where possible. Hydrogen atoms were introduced to calculated positions and refined isotropically. Carbon-bound hydrogen atoms were placed in calculated positions and were included in the refinement in the riding model approximation, with U_{iso}(H) set to 1.2U_{eq}(C). The H atoms of the hydroxyl groups were allowed to rotate with a fixed angle around the C – O bond to best fit the experimental electron density, with U_{iso}(H) set to 1.5 U_{eq}(O) [19]. The relevant crystallographic data are presented in appropriate chapters, while the selected bond lengths and angles are in supporting information.

2.5.2 Powder X-ray diffraction (PXRD)

PXRD was used for characterization, structural determination and identification of material. The PXRD diffractogram can be used to determine whether a material is crystalline or amorphous. It also helps us identify the phases present and their purity. Concentrated monochromatic radiation is directed towards a sample, interacts with the sample and produces constructive interference if Bragg's law is satisfied. The sample is scanned through a range of 2θ angles and all possible diffraction X-rays are attained; then detected, processed and converted to d-spacings. Comparison with a reference sample allows for identification of the unknown crystal because each crystal has a set of unique d-spacings. Powdered samples were used in their as-synthesized form with slight grinding and homogenization where necessary. The samples were lightly packed in the sample holder and data was collected in the range 2θ = 10° to 60°, scanning at 0.010° min^{-1} and 192 s per step, for at least two hours [20]. PXRD spectra were performed on a Bruker D8 Discover diffractometer (by Dr Jonathan Britton, Rhodes University), equipped with a LynxEye detector, under Cu-Ka radiation (l = 1.5405 Å).

2.6 Elemental analysis

Carbon, hydrogen and nitrogen elemental analysis was carried out using the as-synthesized products (by Mr Francis Chindeka, Rhodes University). Elemental analysis works on the principle that when atoms are exposed to high temperatures, in an oxygen rich environment, they are easily converted to oxides; carbon burns to form carbon dioxide, hydrogen forms water and nitrogen forms nitric oxides. Through a series of calculations, the analyst can then determine the relative percentages of these three elements as well as those of the remaining elements and predict the empirical formula of the sample. The instrument employed in this work was an Elementar Vario Micro cube with a Thermal Conductivity detector (TCD), employing temperatures of 1150 °C in the combustion tube and 850 °C in the reduction tube. Helium (1200-1350 mbar) and oxygen (17 mbar) were used as the gases [21,22].

Analysis of metals was carried out using an ICP-OES, Thermo Fischer ICAP 6000. Calibration standards for the range (0-100 ppm) were prepared and analysed. Approximately 2 mg of sample was dissolved in a few drops of concentrated nitric acid and made up to the mark with distilled water in a 20 mL volumetric flask. The solution heated and stirred until a clear solution was obtained. After acid digestion, the solution was cooled and analyzed [23–25].

2.7 Thermal analysis

Thermal analysis techniques have to do with monitoring the decomposition behavior of compounds when subjected to heat and a constant pressure. Two main techniques were employed, thermogravimetric analysis (TGA) and differential scanning calorimetry (DSC) [26].

2.7.1 Thermogravimetric analysis (TGA)

TGA is a technique in which the mass of a substance is monitored as a function of temperature or time as the sample specimen is subjected to a controlled temperature program in a controlled atmosphere [27]. TGA can quantify loss of water, loss of solvent, loss of plasticizer, decarboxylation, pyrolysis, oxidation, decomposition, amount of metallic residue remaining and weight % ash. Depending on the desired outcome, either an inert gas or a reactive gas can be used. For this work, TGA was used for decomposition studies with nitrogen as the sample purge gas, a process called pyrolysis. Pyrolysis is the chemical decomposition of organic materials by heating in the absence of oxygen or any other reagents. This is done so the sample only reacts to temperature during decomposition. All TGA studies were conducted using a PerkinElmer TGA 4000 was used. Between 2.5-5.0 mg of sample was placed in a ceramic crucible and loaded in the TGA furnace. The sample was heated under a nitrogen atmosphere to 30 °C, held for 1 minute and then heated from 30 – 800 °C at a rate of 10 °C/minute. The changes in sample mass were monitored during this phase and the losses identified and quantified [28,29].

2.7.2 Differential scanning calorimetry (DSC)

The DSC measures the changes in the energy of a system with time. Calorimetry allows the identification of phase changes such as melting and crystallization as well as the decomposition which occurs within a sample. DSC measures these changes in heat flow of the sample, both radiated and absorbed, against those in the reference sample [30,31] employing either heat flux or as in this case power consumption techniques [27]. The DSC monitors both exothermic and endothermic changes in the sample and records these changes as a function of the programmed temperature. Strict control of both heating and cooling rates

is essential to allow for reproducibility and modeling of data [32]. Inert gases like Nitrogen and Argon are the most common purge gases used in DSC due to their better heat conductivity except when oxidative studies are being conducted, and then oxygen rich atmospheres are used. Analysis of the resulting thermogram gives information on the solid state transitions such as phase changes, crystallization, degradation, loss of solvents and chemical reactions.

In this work, DSC was used in conjunction with TGA to gain a more comprehensive understanding of the thermal behaviour of samples. All samples were used as synthesized with no prior preparation. DSC was performed on a PerkinElmer DSC 6000. Between 2.5 - 5 mg of sample was loaded into alumina pans and heated with a ramp rate of 10 °C/min from 30 – 445 °C under a nitrogen atmosphere.

2.8 Scanning electron microscopy (SEM)

SEM is a high resolution magnification technique which is used to study the surface morphology and topographical information of samples through three dimensional images [33,34]. This is achieved by focusing a high energy electron beam on the surface of the sample. This interaction produces secondary electrons and x-rays which are detected and processed into images reflecting the surface structure of the sample. Samples were sparsely spread on a piece of double-sided tape and coated with a thin film of gold in a vacuum chamber. The other side was afixed to the sample holder. SEM images were obtained using a TESCAN Vega TS 5136LM Electron microscope.

2.9 Conclusion

This chapter covers the techniques that were collectively used for characterization of the starting materials and products. General descriptions of the exact instrumentation and methodologies employed were given. The importance of each technique as well as information obtained from the analysis of expected results were also discussed. An appreciation of these issues is important for good quality analysis of results.

References

[1] ThermoScientific, *Introduction to FT-IR Sample Handling*, **2013**, 1–8.

[2] K. Nakamoto, *Infrared Raman Spectra Inorg. Coord. Compd. Part A Theory Appl. Inorg. Chem. Sixth Ed.* **2008**, 1–419.

[3] J. S. Gaffney, N. A. Marley, D. E. Jones, in *Charact. Mater.*, **2002**, pp. 1–33.

[4] B. H. Stuart, in *Infrared Spectrosc. Fundam. Appl.* (Ed.: D.J. Ando), **2004**, pp. 15–45.

[5] B. C. Smith, in *Fundam. Fourier Transform Infrared Spectrosc.*, CRC Press, Boca Raton, **2011**, pp. 129–140.

[6] Y. Chen, C. Zou, M. Mastalerz, S. Hu, C. Gasaway, X. Tao, *Int. J. Mol. Sci.* **2015**, *16*, 30223–30250.

[7] F. Scholz, *Electroanalytical Methods: Guide to Experiments and Applications*, **2010**.

[8] G. Li, P. Miao, in *Electrochem. Anal. Proteins Cells*, SpringerBriefs In Molecular Science., **2013**, pp. 5–15.

[9] A. J. Bard, L. R. Faulkner, *Eectrochemical Methods; Fundamentals and Applications*, John Wiley & Sons, Inc., New York, **2001**.

[10] D. A. C. Brownson, C. E. Banks, in *Handb. Graphene Electrochem.*, Springer-Verlag London Ltd., **2014**, pp. 23–77.

[11] T. Abe, T. Yoshida, S. Tokita, F. Taguchi, H. Imaya, M. Kaneko, *J. Electroanal. Chem.* **1996**, *412*, 125–132.

[12] A. J. Arvia, R. C. Salvarezza, W. E. Triaca, *J. New Mater. Electrochem.*

Syst. **2004**, *7*, 133–143.

[13] E. Vieil, *J. Electroanal. Chem. Interfacial Electrochem.* **1991**, *297*, 61–92.

[14] T. Subbaiah, S. C. Das, R. P. Das, *Hydrometallurgy* **1993**, *33*, 153–163.

[15] K. Habib, F. Al-Sabti, *Opt. Lasers Eng.* **2001**, *35*, 225–232.

[16] Pavan M. V., RajaAndrew, R. Barron, in *Phys. Methods Chem. Nano Sci.*, **2019**, p. 27839.

[17] A. S. Batsanov, *Encycl. Spectrosc. Spectrom.* **1999**, 2106–2115.

[18] E. Hosten, T. Gerber, R. Betz, *Acta Cryst.* **2011**, *2*, 1–11.

[19] Z. R. T. Adeniyi S. Ogunlaja, Eric Hosten, Richard Betz, *RSC Adv.* **2016**, *6*, 39024–39038.

[20] M. Shumba, T. Nyokong, *Electrochim. Acta* **2016**, *196*, 457–469.

[21] manual-vario-micro-e.pdf,Elemental Analysis. **2008**. www.elementar.de

[22] V. P. Fadeeva, V. D. Tikhova, O. N. Nikulicheva, *J. Anal. Chem.* **2008**, *63*, 1094–1106.

[23] A. Montaser, J. A. McLean, H. Liu, in *Inductively Coupled Plasma Mass Spectrom.*, John Wiley & Sons, Inc., **1998**, pp. 2–28.

[24] J. Nölte, *ICP Emission Spectrometry*, John Wiley & Sons, Inc., **2003**.

[25] B. J. Alloway, in *Heavy Met. Soils*, Blackie, **1990**, pp. 291–296.

[26] T. Hatakeyama, F. X. Quinn, *Thermal Analysis: Fundamentals and Applications to Polymer Science*, Wiley-VCH Verlag GmbH & Co. KGaA, **1999**.

[27] M. E. Brown, in *Introd. to Therm. Anal. Tech. Appl.*, Springer Netherlands, Dordrecht, **1988**, pp. 23–49.

[28] Perkin Elmer, *Thermogravim. Anal. A Beginner's Guid.* **2010**, 1–19.

[29] M. Carrier, A. Loppinet-Serani, D. Denux, J.-M. Lasnier, F. Ham-Pichavant, F. Cansell, C. Aymonier, *Biomass and Bioenergy* **2011**, *35*, 298–307.

[30] G. Bruylants, J. Wouters, C. Michaux, *Curr. Med. Chem.* **2005**, 2011–2020.

[31] P. Gill, T. T. Moghadam, B. Ranjbar, *J. Biomol. Tech.* **2010**, *21*, 167–193.

[32] G. Höhne, W. F. Hemminger, H. J. Flammersheim, *Differential Scanning Calorimetry*, Springer Berlin Heidelberg, **2013**.

[33] C. Thompson, N. . Champness, A. N. Khlobystov, C. J. Roberts, M.Schroder, S. J. B. Tendler, M. J. Wilkinson, *J. Microsc.* **2004**, *214*, 261–271.

[34] K. Odziomek, D. Ushizima, P. Oberbek, K. J. Kuzydloski, T. Puzyn, M. Haranczyk, *J. Microsc.* **2016**, 1–17.

Chapter Three

In this chapter, three structures were assembled from Cu(II), Mo(VI) POMs ions and H_3BTC via modification of the HKUST-1 MOF. The synthetic procedures are described. The synthesized products were characterized using FTIR, CHN elemental analysis, SEM, PXRD, TGA and DSC. They were also employed as catalysts in electroxidation of L-cysteine.

3. Compounds of Cu, Mo and benzenetricarboxylic acid.

In this chapter, two MOFs (HKUST-1 and Mo1) and 1 coordination compound (Mo2) were assembled from Cu(II), Mo(VI) POMs ions and H_3BTC to give three compounds. HKUST-1 is a well documented Cu-BTC MOF; Mo1 and Mo2 are POM-MOFs made by modifying HKUST-1 with the polyoxometallate ammonium heptamolybdate tetrahydrate. The detailed synthetic procedures and chemical formula are described later in the chapter. All three products were characterized using FTIR, CHN elemental analysis, SEM, PXRD, TGA and DSC. The compounds were then employed as catalysts in detection of L-cysteine.

3.1 Synthesis

3.1.1 Synthesis of HKUST-1:$[Cu_3(BTC)_2(H_2O)_3]$.

HKUST-1 was synthesized under solvothermal conditions, as detailed below in accordance with literature [1]. Copper nitrate trihydrate (0.6 g, 2.48 mmols) was dissolved in 10 mL of distilled water. H_3BTC (0.4 g, 1.9 mmols) was dissolved in 10 mL of a 1:1 mixture of ethanol and distilled water in a separate beaker. The two solutions were combined and placed in an ultrasonicater until a gelatinous blue substance was formed. The gel was placed in a glass vial, sealed and placed in an autoclave. The autoclave was heated to 120 °C, maintained at this temperature for 24 hrs, then cooled to room temperature, at which point turquoise blue HKUST-1 crystals had formed. The crystals were filtered off, washed with 20 mL of a 1:1 ethanol: water solution and dried in an oven for 12 hrs at 60 °C. The drying in the oven produces the desolvated form of HKUST-1.

3.1.2 Post-synthetic modification (PSM) of HKUST-1 to form Mo1.

The HKUST-1 samples were modified via impregnation. Impregnation was achieved by sonicating HKUST-1 (0.2g) with ammonium heptamolybdate tetrahydrate (0.6g, 0.485 mmols) in 20 mL ethanol for 30 minutes, filtering and drying the precipitate in an oven at 60 °C for 12 hrs. The resulting green-blue crystals are here after referred to as Mo1.

3.1.3 One-step solvothermal synthesis of Mo2

Copper nitrate trihydrate (0.6 g, 2.48 mmols) and H_3BTC (0.4 g, 1.9 mmols) was dissolved in 10 mL of a 1:1 mixture of ethanol and millipore water. Ammonium heptamolybdate tetrahydrate (0.6 g, 0.485 mmols) was placed in 10 mL millipore water and heated with stirring until it dissolved. The two solutions were combined and sonicated until a gelatinous blue substance was formed. The gel was placed in an autoclave at 180 °C for 24 hrs. The resulting grey crystals were slowly cooled to room temperature, filtered off, washed with 20 mL of a 1:1 mixture of ethanol and water. The product, hereafter referred to as Mo2, was dried in an oven at 60 °C.

3.2 Elemental analysis

The elemental analysis for HKUST-1, Mo1 and Mo2 all showed a close agreement between the observed and deduced results (Tables 1-3). Through a series of calculations, the empirical formula was determined and this in turn used to deduce the molecular formula of each product. Calculations for the deduced percentage compositions were based on this molecular formula. From the obtained results, we suggested the following molecular formulae; $Cu_3(BTC)\cdot 3H_2O$

for the HKUST-1 MOF, $\{Cu_3(BTC)_2(H_2O)_3\}\cdot 3\frac{1}{2}[(NH_4)_6Mo_7O_{24}\cdot\frac{1}{2}H_2O]$ for the Mo1 POM-MOF and $Cu_{5½}(BTC)\cdot((NH_4)_6Mo_7O_{28})\cdot 5H_2O$ for the Mo2 POM-MOF. This suggests that the Mo-POMs are encapsulated in Mo1 and encorporated in Mo2. The most definitive way to confirm the structure would be SC-XRD, however in this case crystals were too small for this technique. A series of other techniques (PXRD, FTIR, SEM, TGA and DSC) were hence employed in an attempt to confirm the proposed molecular formulae.

Table 3. 1: Elemental analysis of HKUST-1: $Cu_3(BTC)_2\cdot 3H_2O$.

Element	Expected %	Observed %	Difference	% Error
Carbon	33.745	33.250	+0.495	0.015
Hydrogen	0.0205	0.018	+0.003	0.146
Copper	29.758	30.080	-0.647	0.099

Table 3. 2: Elemental analysis of Mo1:$\{Cu_3(BTC)_2\cdot 3H_2O\}\cdot 3\frac{1}{2}[(NH_4)_6Mo_7O_{24}\cdot\frac{1}{2}H_2O]$.

Element	Expected %	Observed %	Difference	% Error
Carbon	4.535	4.250	+0.285	0.063
Hydrogen	2.090	1.891	+0.199	0.095
Nitrogen	6.172	5.920	+0.252	0.041
Copper	4.00	3.878	+0.122	0.031
Molybdenum	49.356	49.720	-0.364	0.007

Table 3. 3: Elemental analysis of Mo2: $Cu_{5\frac{1}{2}}(BTC)\cdot(NH_4)_6Mo_7O_{28}\cdot 5H_2O$.

Element	Expected %	Observed %	Difference	% Error
Carbon	5.763	5.550	+0.213	0.037

Hydrogen	1.974	1.801	+0.173	0.088
Nitrogen	4.482	4.299	+0.183	0.041
Copper	18.650	18.880	-0.23	0.012
Molybdenum	35.837	36.001	-0.164	0.005

3.3 Characterization by PXRD.

The MOF HKUST-1 has been reported before in literature [2-4] and characterization was performed to confirm that synthesis was successful. A lower temperature of 120 °C (vs 180 °C [1]) was used to avoid the formation of Cuprous oxides in the potential voids [2,5,6]. The crystals had the characteristic turquoise blue colour and the PXRD pattern is in accordance with published literature [2,7,8]. For comparison, Chui's PXRD pattern was downloaded from the Cambridge Structural Database (CSD 112934) and used as the calculated HKUST-1 (Figure 3.1A). The most notable similarities are the high intensity peaks at 2θ = 11° , 13°, 17° and 29° [1]. Slight differences in crystallinity were also noted, such as the presence of broad peaks in the synthesized HKUST-1. These have been attributed to defects or dislocations occurring within the bulk crystals [9] during crystal growth. Based on the match in PXRD patterns, synthesis of HKUST-1 was assumed to have been successful.

When HKUST-1 is modified to Mo1 via PSM, there is a reduction in crystallinity, shown by the amorphous character of the region from 2θ = 10 - 30° (Figure 3.1B). Similar changes in diffraction peaks in this region have been observed before for other HKUST-1-Mo-POM MOFs [10]. This indicates an expansion in the framework possibly due to the Molybdenum POMs encapsulated in the voids, showing that impregnation was successful and also resulted in partial distortion

of the HKUST-1 crystals [11]. Despite partial distortion, Mo1 is still isostructural to HKUST-1 as shown by the existence of matching peaks, such as those at 2θ = 27°, 29°and 36° (Figure 3.1B). Mo2 displays a shift in 2 theta values, confirming successful encorporation of the POMs. The pattern is characterized by intense sharp peaks at 22°, 23°, 24° and 33° (all absent in HKUST-1), suggesting that a new product results which has its own unique crystal structure, different from HKUST-1.

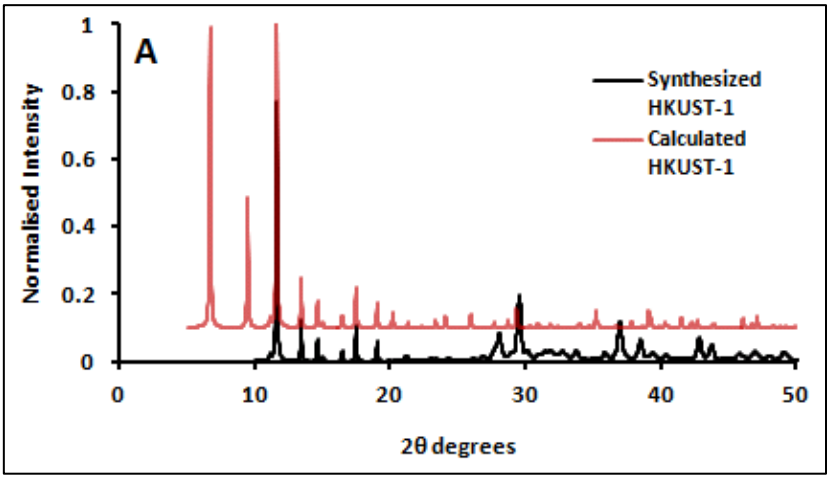

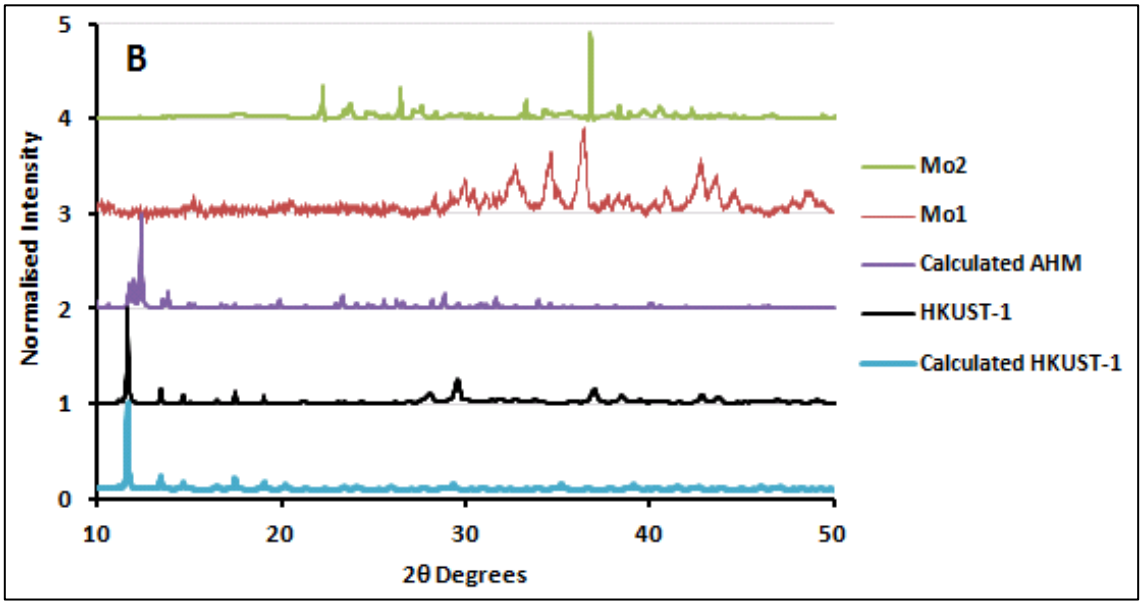

Figure 3.1: PXRD spectra of HKUST-1 calculated and the as-synthesized HKUST-1 (A) and pxrd spectra of HKUST-1, Mo1, Mo2 and calculated HKUST-1 and AHM (B).

To aid in confirmation of successful guest inclusion via encorporation or encapsulation, comparison of the products PXRD with that of the guest is often conducted [12]. For this work, the calculated PXRD for pure ammonium heptamolybdate tetrahydrate (AHM) was downloaded from the CSD (deposit number 1592851) and used for comparison [13]. From Figure 3b, both Mo2 and Mo1 display characteristic peaks at 22°, 23°, 24°, 28°, 31° and 32° which are also observed in with pure AHM [14]. This suggests the POM structure is maintained in both Mo1 and Mo2.

3.4 Characterization by FTIR

FTIR was used to further investigate the effects of modification on HKUST-1. MOFs of polybenzoic acids tend to display peaks in the carbonyl region. The as-synthesized HKUST-1 displays bands associated with carboxylate stretches in the region between 1700 cm^{-1} – 1400 cm^{-1} (Figure 3.2), which is in good agreement with published literature on HKUST-1 [2,6,15–18]. The significant bands were at 1611 cm^{-1}, 1585 cm^{-1}, 1484 cm^{-1}, 1438 cm^{-1} and 1400 cm^{-1} for the asymmetric and symmetric carboxylates. It also had a broad band at 3072 cm^{-1} which could be ascribed to absorbed water.

For pure MoO_3, the fundamental Mo-O symmetric stretches normally occur in the region between 1000 cm^{-1} and 400 cm^{-1} [19–21]. The bands around 990 - 957 cm^{-1} are normally ascribed as ν_{as}Mo=O stretching vibrations, those around 876 cm^{-1} and 818 cm^{-1} are the stretching vibrations of the oxygen atoms in a Mo-O-Mo entity and the complex band centred at about 600 cm^{-1} involves the stretching vibrations of the oxygen atoms linked to three metal atoms [19,22–25]. This behaviour is also observed in the infrared section of both Mo1 and Mo2. Mo1 shows strong bands at 970 cm^{-1}, 913 cm^{-1} and 836 cm^{-1} whilst Mo2 shows

bands at 913 cm^{-1} and 819 cm^{-1}, confirming the presence of the fundamental Mo POM stretches in both compounds. The slight differences in their values and shifts to lower wavenumbers suggest that the POMs are in different chemical environments and that there may be reduced Mo centres bound to ligands [26].

The spectra for the two Mo doped-HKUST-1 products are very similar between 1700 – 1400 cm^{-1} but show differences below 1100 cm^{-1}. Mo1 and Mo2 both show broad bands (3157 cm^{-1}, 2996 cm^{-1} and 3076 cm^{-1}) which suggests the presence of water in both the complexes. When working with pure ammonium heptamolybdate POMs bands for weakly bonded and structurally intercalated ammonium ions were observed between 3291 – 3176 cm^{-1} and their corresponding bonding vibrations in the region 1458 – 1401 cm^{-1} [25]. Mo1 and Mo2 show bands at 3179 cm^{-1} and 3205 cm^{-1} respectively, which we ascribed to ammonium ions.

Mo1 shows shifts to higher wavenumbers for the asymmetric stretch and lower wavenumbers for the symmetric stretch in the carbonyl region (from 1611 to 1615 cm^{-1}, 1438 to 1403 cm^{-1}) suggesting a change in coordination has occurred. Most of the bands in this region have reduced intensity or are masked by the prominent bands from the ammonium bending vibrations [25], such as those at 1585, 1507 and 1484 cm^{-1}, suggesting a change in structure. The shift also suggests a reduction in bond strength between the copper and BTC due to interactions with the Molybdenum POMs. Despite differences in intensity, characteristic bands for HKUST-1 are also seen in Mo1, and this has been taken by previous researchers as an indication that POMs are encapsulated in the host material [27].

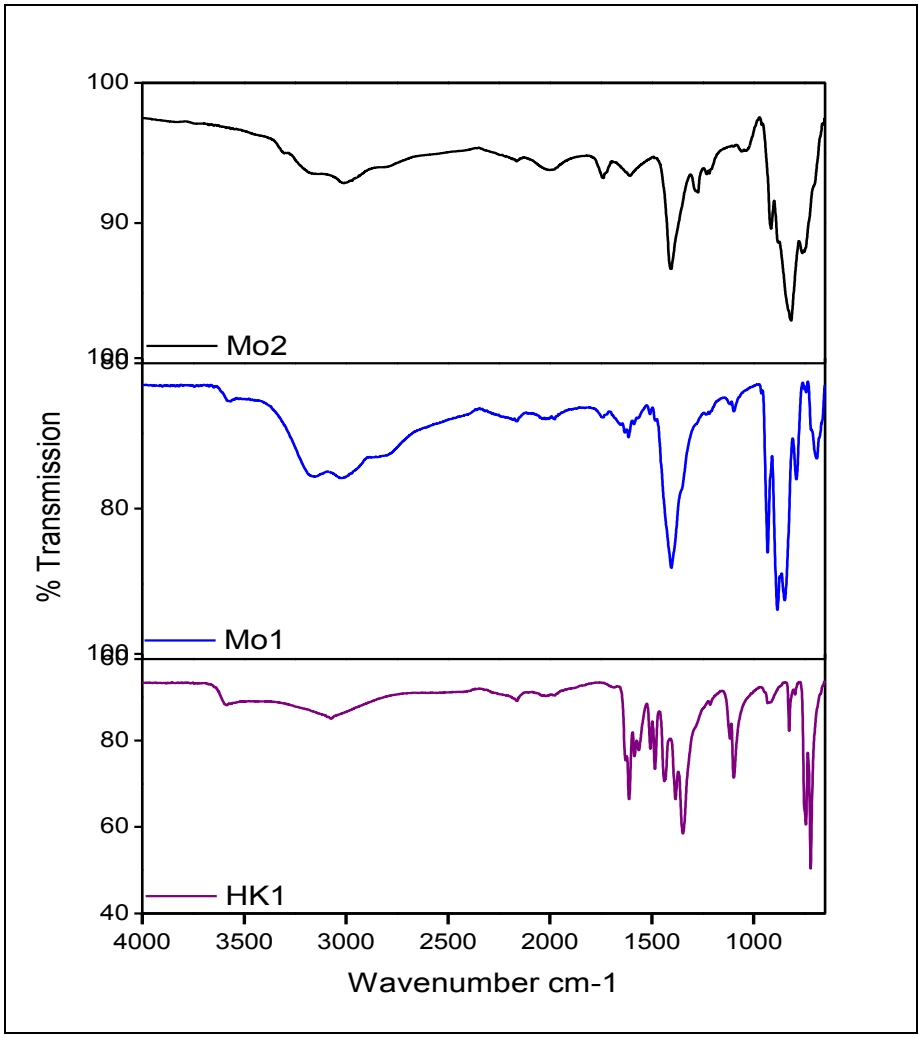

Figure 3. 2: FTIR spectra of HKUST-1, Mo1 and Mo2.

Mo2 displays similar shifts as Mo1 but to lower wavenumbers for both the asymmetric and symmetric carbonyl stretches (from 1611 to 1608 cm^{-1}, from 1400 to 1383 cm^{-1}, 1098 to 1032 cm^{-1}), suggesting stronger coordination in the solvothermal product. The presence of a band at 1098 cm^{-1} in HKUST-1 and Mo1 (as a shoulder) but which is absent in Mo2, suggests that the POMs are integrated differently in the HKUST-1.

3.5 Characterisation by SEM

The surface morphologies that emanate from the MOFs and POM-MOFs were examined by scanning electron microscopy (Figure 3.3). HKUST-1 shows well defined octahedral crystals, with a smooth surface and particle sizes in the range 6-15 μm (Figure 3.3C), as is expected from literature [3,11,28]. After post-synthetic modification to Mo1, the octahedral shape of HKUST-1 is still maintained but with "cauliflower-like" particles adhered to the surface (insert Figure 3.3A). Such changes in surface decoration have been seen previously by other researchers [27,28]. This behaviour was taken to represent successful modification.

In contrast, Mo2 shows a total loss of the octahedral shape characteristic of HKUST-1 and the appearance of rectangular blocks with very fine particles on its surface (Figure 3.3B). There is also a marked reduction in size from about 12 μm to 100 μm for the width of the blocks. This change in shape and size is consistant with phase changes observed in ammonium heptamolybdate exposed to such temperatures [25,29]. The SEM images show that PSM by impregnation resulted in preservation of the HKUST-1 octahedral shape whilst the one-pot approach forms a totally different crystal shape.

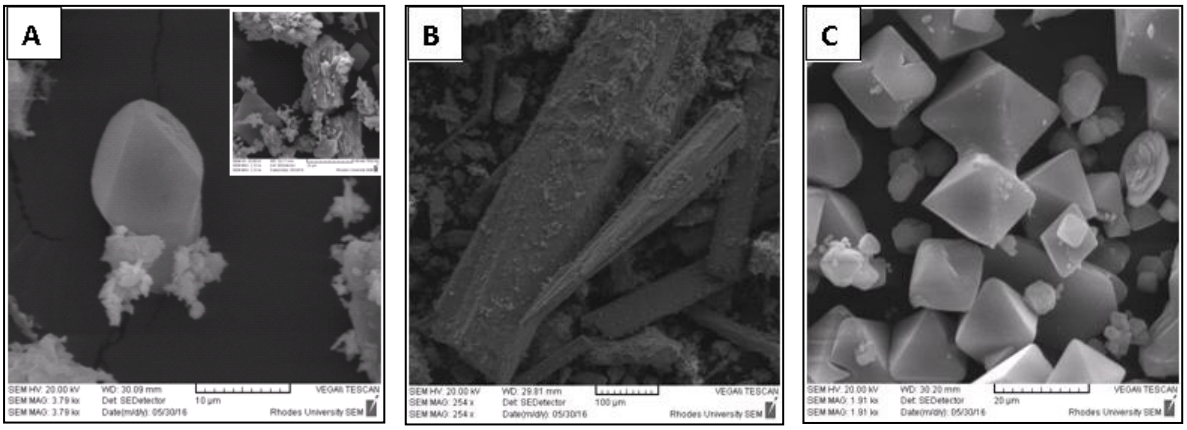

Figure 3.3: SEM images of Mo1 (A), Mo2 (B) and HKUST-1(C).

3.6 Thermal analysis

Upon exposure to the atmosphere, the HKUST-1 increased its water content by absorption to 12.19%. These results suggest that the as-synthesized HKUST-1 is not fully solvated as a fully hydrated MOF can contain up to 22% water [2]. It however is consistent with literature for a HKUST-1 MOF with an assumed structure of $Cu_3(BTC)_2(H_2O)_3 \cdot xH_2O$ [28], and the extent of uptake is dependent on the method of production. The thermal stability of HKUST-1 was investigated via thermo-gravimetric studies (Figure 3.4 A). The first weight loss of 3,74%; equivalent to one water (calculated 4.1%), was observed between 50 - 100 °C and is associated with desolvation, due to lose of lattice water. The second loss occurs between 150 - 230 °C and is due to coordinated waters. From the TGA the first mass loss (DTG 1 = 3.72%; calculated 4.1%) is due to loss of one water whilst the second two-step mass loss (DTG 2 and 3 = 8.45%; calculated 8.42%) could be due to loss of two coordinated waters. The two step mass loss is accompanied by a broad endotherm over this temperature range in the DSC. This results in a total water loss of approximately 12% (calculated 12.5%). This phenomenon has been observed by previous researchers when conducting HKUST-1 sorption studies [1,8].

The third mass loss (DTG 4 and 5 = 34.5%; calculated 33.75) occurs between 280 - 400 °C and is due to the framework breaking down, possibly triggered by the loss of the third coordinated water [30]. This is reflected by a twin endotherm in the DSC. The decomposition of the benzenepolycarboxylate framework at such temperatures is often accompanied by decarboxylation producing carbon dioxide and/or carbon monoxide [28,30], triggered by loss of solvent involved in hydrogen bonding within the lattice [30].

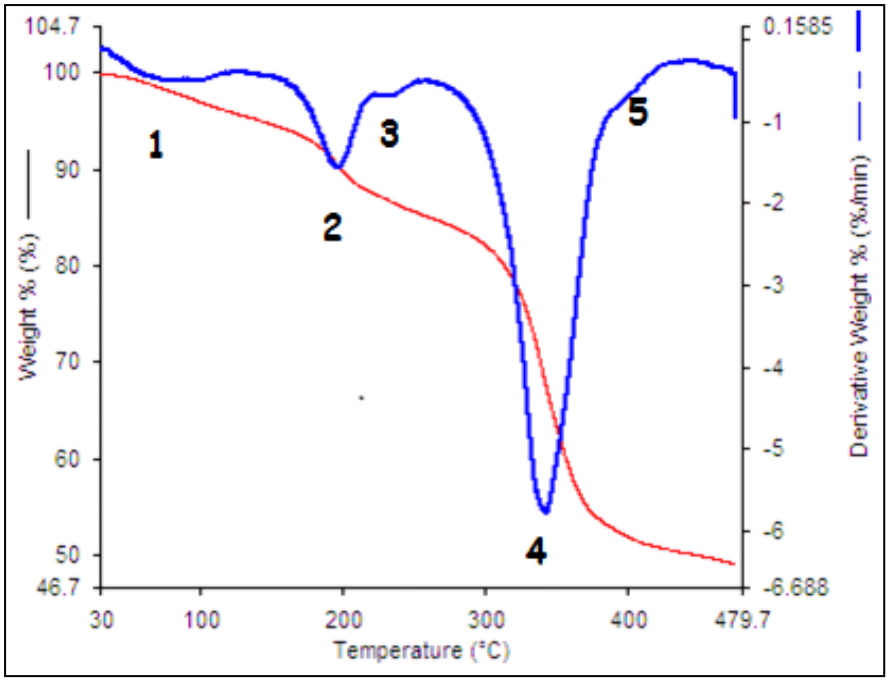

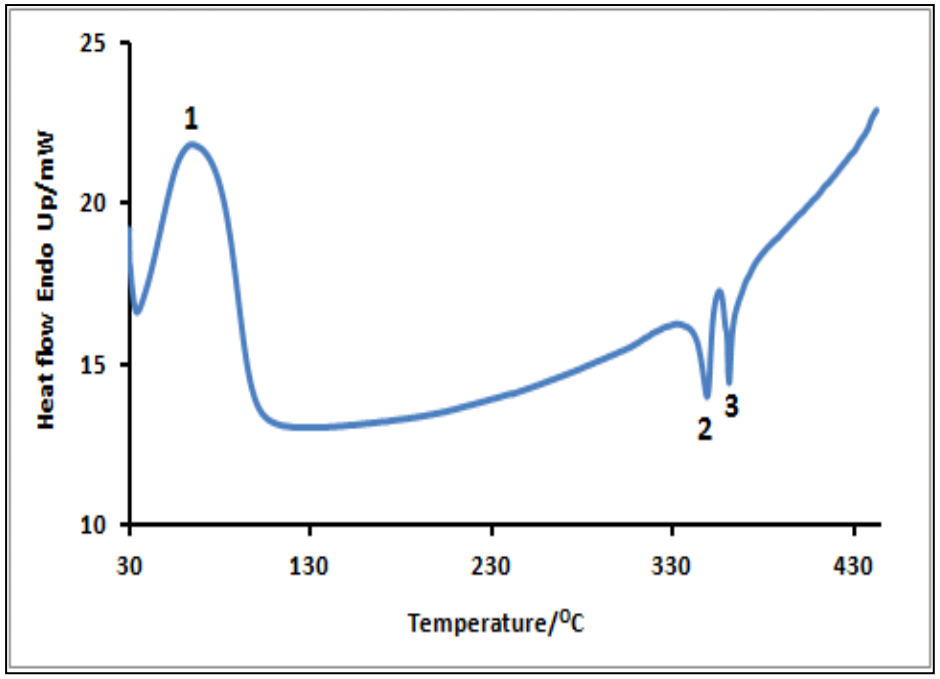

Figure 3.4: TGA/DTG and DSC curves for HKUST-1.

Since TGA was run under nitrogen, complete decarboxylation was not possible and a mixture of carbon residues and various carbon oxides were probably formed. A sure way to confirm the products would have to have been able to run evolved gas analysis [31]. Beyond this temperature, no further losses occur and the thermogram tappers off to approximately 48%. We suggest that this is due to mixed copper oxide residues (CuO/Cu_2O) and possibly amorphous carbon [30,32], given the calculated mass of the copper oxides (CuO= 49.84%; Cu_2O= 44.81%).

The TGA of Mo1 (Figure 3.5) shows a multi-step decomposition with a lot of these steps overlapping as shown by the derivative (DTA), making a complete thermal decomposition mechanism difficult to fully interprete. The complex mechanism may be suggestive of encapsulation. It is tentatively suggested that the first decomposition is the loss of ammonia (7.3%; calculated 7.9%), produced from the NH_4^+ cations. This occurs as multistep decomposition between 50 - 200 °C. This is followed by the loss of lattice and coordinated waters (2.1%; calculated 1.8%) in sequential steps between 150 and 250 °C (steps 1-4 DTG). The total loss of water and ammonia is 9.4 % (calculated 9.73%).

Between 250 - 380 °C (DTG steps 5-7) the framework starts to breakdown as the BTC is destroyed (total 14.41; calculated BTC loss 4.53%). Upon decomposition, the carbon is oxidized to carbon oxides during decarboxylation, as explained above for HKUST-1. The carbon framework breakdown is coupled with the breakdown of the Mo POMs (accounting for difference in observed loss vs calculated loss).

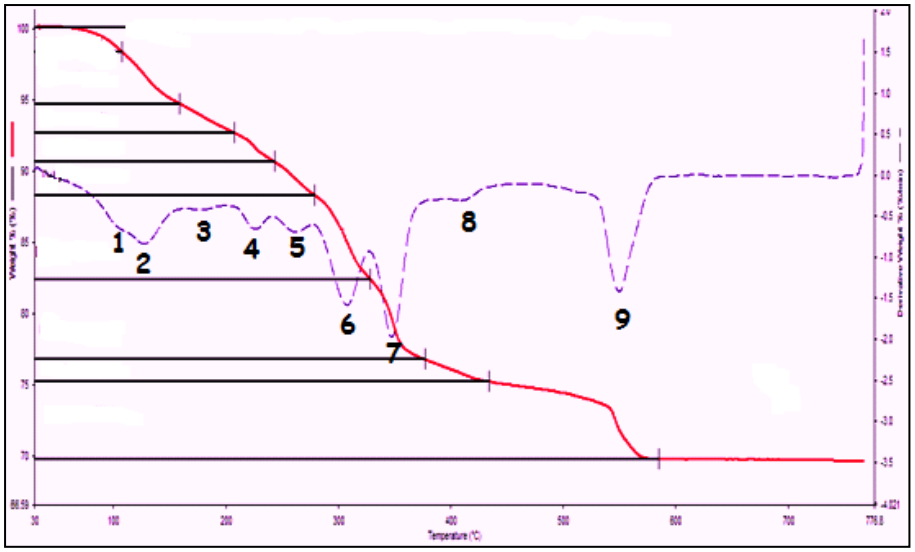

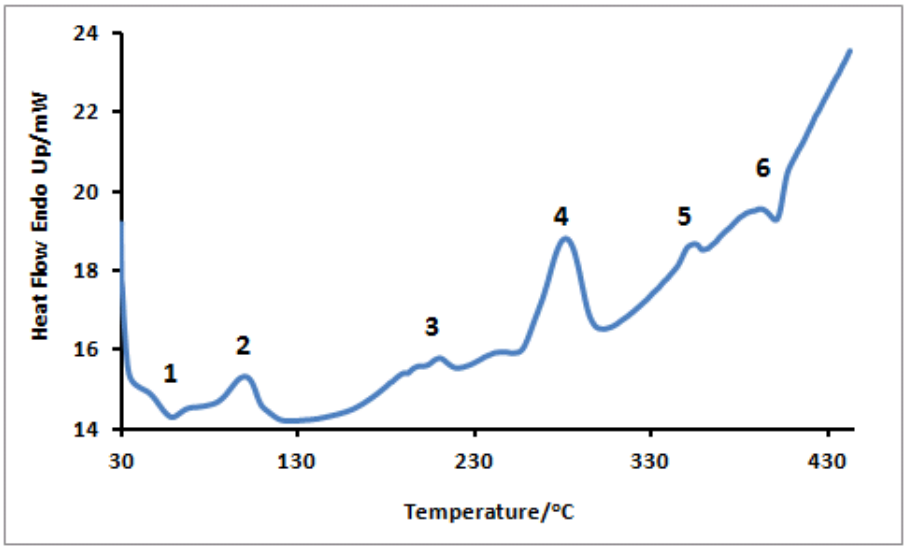

Figure 3. 5: TGA/DTG and DSC for Mo1.

Based on the thermal stability of HKUST-1, it is tentatively suggested that this is reflected by the DSC-4 peak at 280 °C, indicating no structural change to the HKUST-1 framework in Mo1; evidence for encapsulation. This overlapping of decomposition patterns has been observed with other Cu-Mo complexes like Mo-Sal-Amp-CuBTC [11]. Between 380-450 °C a mass loss of 1.56% is observed as a shoulder in the DTG (step 8). This value is assigned to possibly the loss of Mo POMs via sublimation. Previous researchers have observed the conversion from $[Mo_7O_{24}]^{6-}$ to a-MoO_3 at 420 °C [25,29,33] as well as sublimation of molybdenum oxides from 450 °C.

The final mass loss (5.42%) occurs between 550-600 °C (DTG step 9) and this is assigned to further loss of remaining structurally intercalated ammonium ions and crystalline water. The TGA tappers off to a final mass of 69.74%. At this point, we expect metal oxides (molybdenum and copper oxides) and amorphous carbon (the calculated mass of Mo without sublimation is 49.36% whilst that of Cu is 4.00%). The observed mass is higher than the calculated loss due to the possibility of the metals partially existing as oxides. This increase in mass on thermograms upon oxidation has been observed by previous researchers [31,34,35].

According to a recent study by Chithambararaj *et al* [25], the loss of water and ammonium ions from ammonium heptamolybdate tetrahydrate occurs in five steps from 180-580 °C. This is because there are two main mechanisms by which both molecules are found in this POM; structurally intercalated and weakly bonded. Changing the chemical environment of the POM also changes the nature and strength of bonding (as we have done by combining it with HKUST-1) and

this is evident in the changes at which thermal decomposition occurs. Such multistep decomposition behavior has been exhibited by other POM systems in different environments [36,37].

The DSC thermogram for Mo1 shows a combination of exothermic and endothermic peaks. It mirrors the same complexities as the TGA confirming the multistep decomposition. The first three endothermic peaks (at 54 °C, 95 °C and 210 °C) may correspond to the loss of ammonia and water molecules. Between 50-75 °C, a phase transition from the monoclinic $[NH_4]_6Mo_7O_{24}.4H_2O$ phase to monoclinic $[NH_4]_4(Mo_8O_{24.8}\ (O_2)_{1.2}\ (H_2O)_2)(H_2O)_4$ phase has been observed [25], which may account for the first transition.

The fourth endothermic peak (277 °C) has been ascribed to phase changes in the Mo-POM structure, to an intermediate anorthic phase $[NH_4]_4[Mo_8O_{26}]$ [25]. It is also associated with the loss of ammonia and crystalline water. The phase changes and removal of these molecules (H_2O, NH_3) trigger the decomposition of the framework at 350 °C (peak five). The sixth peak (395 °C) could be due to the Mo POM phase change described in the TGA above.

Mo2 shows a simpler decomposition than that for Mo1 (Figure 3.4 C). When heated to 100 °C, it exhibits an almost negligible weight loss of 0.644%, probably due to loss of surface moisture. The TGA curve shows a two-step decomposition, the first mass loss of 8.41% occurs between 250 – 300 °C, which is possibly due to breakdown of the carbon framework (calculated 5.76%) coupled with the loss of coordinated waters (calculated 4.81). The second decomposition step occurs between 420 – 460 °C and involves a mass loss of 6.19%.

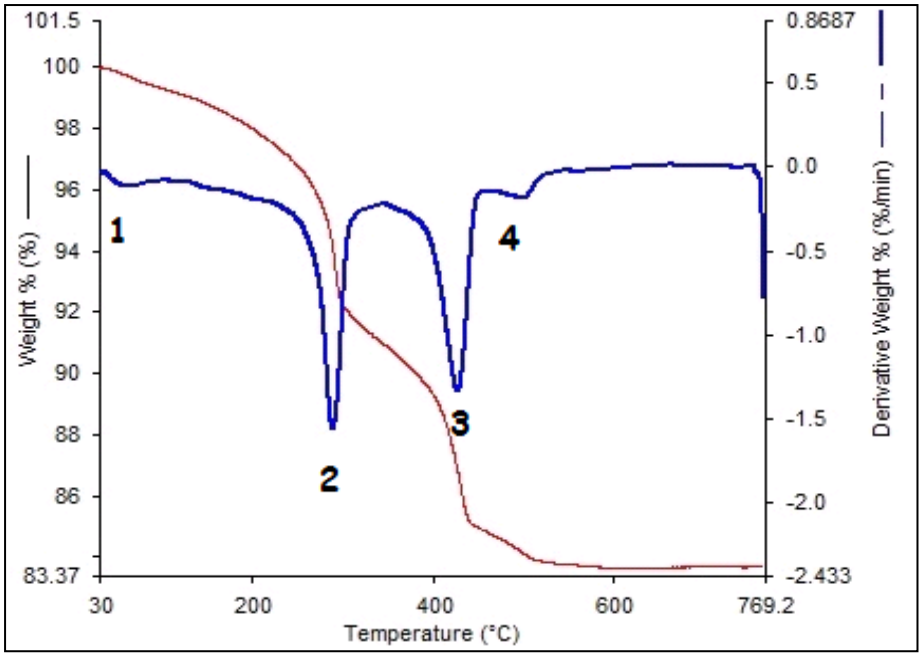

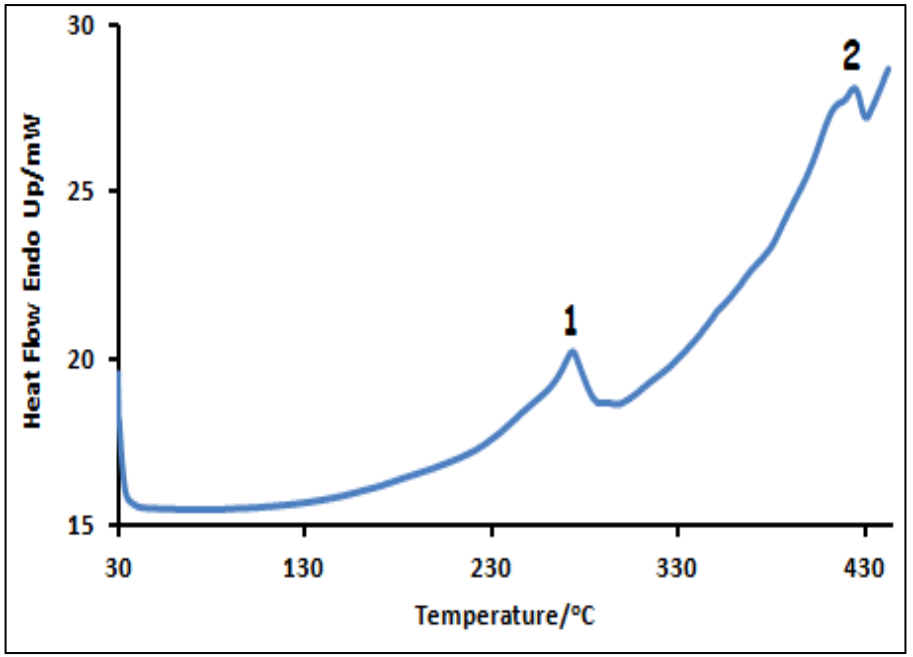

Figure 3. 6: TGA/DTG and DSC curves for Mo2.

Similar to Mo1, this loss could be due to the breakdown of Molybdenum POMs [11,29]. Between 450-500 °C, a mass loss of 0.92% occurs, seen as a shoulder in the derivative curve. This could be due to loss of molybdenum oxides via sublimation. Beyond 500 °C there are no significant decomposition steps and the thermogram levels off (at 83.8%) suggesting that mixed copper oxides, mixed molybdenum oxide residue and amorphous carbon are left (this is much higher than the sum of the calculated values for elemental copper and molybdenum (54.5%), indicating that they exist as mixed oxides).

The DSC for Mo2 (Figure 3.6) shows simple 2-step decomposition (two multistepped endothermic peaks), similar to the TGA. The first peak (270 °C) has been ascribed to the breakdown of the carbon framework. The 10 °C lowering in the DSC of this compared with that of HKUST-1 suggest a change in the framework indicating encorporation. The second peak (420 °C) and the slight shoulder (414 °C) have been ascribed to the phase changes of Mo POMs and their sequential breakdown, as already explained in Mo1.

3.7 Electrochemical characterization of modified electrodes

Electrochemical characterization was performed to study the electrochemical behavior of the synthesized materials under various electrochemical conditions. This process is done so as to gain insight into the interfacial electrochemical behavior between the electrode and the electrolyte in an electrochemical cell [38]. Characterization involves measuring of the basic electrochemical signals (potential, charge and current) and using these relationships to deduce chemical reactivity. In this chapter three MOFs were synthesized with the aim of

applying them in the electrocatalytic detection of L-cysteine. Each of these MOFs was used to modify a glassy carbon electrode and then characterized using cyclic voltammetry so as to evaluate their various electrochemical behaviours. Specific details to follow in forthcoming sections.

3.7.1 Electrode modifications

A glassy carbon electrode (GCE) was used as the working electrode, a silver/silver chloride electrode was used as the reference electrode and a platinum wire was used as the counter electrode. The GCE was polished on a Buehler-felt pad using alumina (<10 μm). Between each polishing step, impurities were removed by sonicating for 5 min in Millipore water. The electrode was rinsed in Millipore water, dried and modified using the dip dry method. For each of the MOFs, an optimized mass of 2 mg was suspended in 1 mL of DMF and the suspension sonicated for 30 min before the electrode was dipped in the solution and dried in an oven at 70 °C before use. The electrodes are designated as HK-GCE, Mo1-GCE and Mo2-GCE respectively. A complete list of the electrodes is shown in Table 3.4.

3.7.2 Cyclic voltammetry

Figure 3.7A shows cyclic voltammograms for the modified and unmodified electrodes in 1 mM $Fe(CN)_6^{3-/4-}$ in 0.1 M KCl in the range -0.3 to 0.5 V. The peak potential separation (ΔE) for a reversible system such as $Fe(CN)_6^{3-/4-}$ is a good measure of the electron transfer ability of the electrode with lower values depicting a good electron transfer ability [39,40]. In addition to the $Fe(CN)_6^{3-/4-}$ redox system being highly reversible, it is also very stable and more surface

sensitive to carbonaceous electrode materials [41]. The modified POM MOF electrodes follow the following order of ease of electron transferability for ΔE: HK-GCE (0.226 V) > Mo2-GCE (0.132 V) > Mo1-GCE (0.110 V) > Bare GCE (0.078 V) (Table 3.4).

From the obtained results, modifying the electrode reduced the electrodes' electron transfer ability compared to that of the Bare GCE electrode, probably because diffusion through MOFs tends to be slower than in solution [42], due to surface barriers [43]. POM-MOF modified electrodes had a lower ΔE compared to the MOF modified electrode, suggesting that Mo doping improved electron transfer.

Table 3. 4: Electrochemical parameters for the bare and modified electrodes.

GCE Modifier	ΔEp for $Fe(CN)_6^{3-/4-}$ in 0.1 M KCl	E/V (L-Cysteine) oxidation pH 4 buffer	Surface roughness	Eff. Area	Γ (mol. cm^{-2})	Background corrected oxidation currents/μA in pH 4 buffer
Bare GCE	0.078	-	-	-	-	-
HK-GCE	0.226	0.283	7.5075	0.533	5.51E-11	39.75
Mo1-GCE	0.110	0.205	16.8168	1.194	1.40E-11	31.40
Mo2-GCE	0.132	0.328	8.5886	0.609	2.45E-11	58.60

The surface roughness factors for the modified electrodes were determined using $[Fe(CN)_6]^{3-/4-}$ redox system and applying Randles–Sevcik equation [39] (Eq. 1) for reversible systems:

$$I_p = 2.69 \times 10^5 \, n^{3/2} \, ACD^{1/2} \, v^{1/2} \quad (1)$$

where Ip, n, A, C, D and v are the peak current, the number of electrons involved, the electrode surface area, the concentration of $[Fe(CN)_6]^{3-/4-}$, the diffusion coefficient of $[Fe(CN)_6]^{3-/4-}$, and the scan rate, respectively.

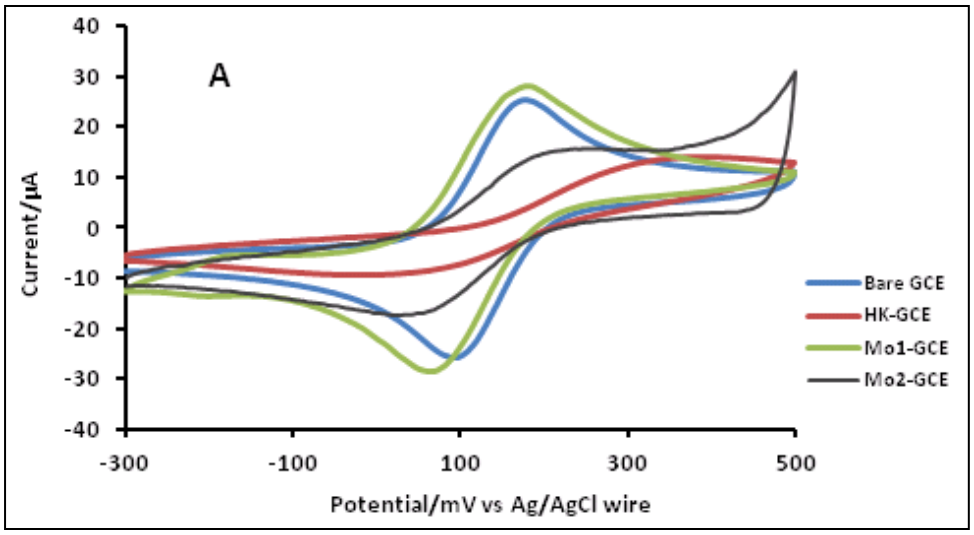

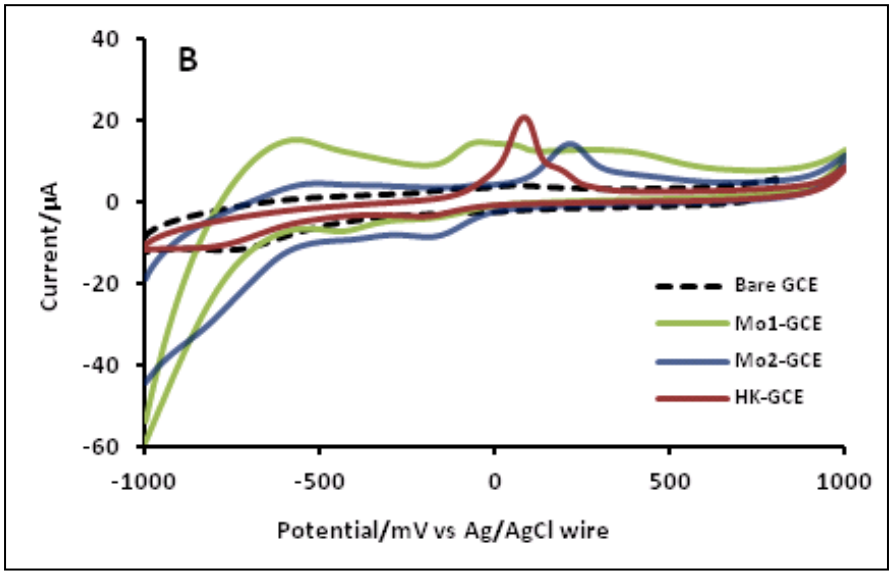

Figure 3. 7: Cyclic voltammograms of the bare and modified electrodes in 1 mM $[Fe(CN)_6]^{3-/4-}$ (A) and pH 4 buffer (B) at Scan rate 100 mV/s.

From the D value for $K_3[Fe(CN)_6]$ = 7.6 x 10^{-6} cm^2 s^{-1} and n = 1, the surface roughness factors (ratio of I_{pa} experimental/I_{pa} theoretical; shown in Table 3.4) were determined for all the probes and the corresponding effective electrode areas {roughness factor x theoretical surface area (0.071 cm^2)} were determined and used for the calculation of surface coverage, (Eq. 2) [39]. The theoretical Ipa was calculated by assuming the geometrical area of the electrode in Eq. 1.

$$\Gamma = \frac{Q}{nFA} \qquad (2)$$

where: Γ is the film surface coverage, Q is the charge under the oxidation peak in the supporting electrolyte, n is the number of transferred electrons, F is the Faraday constant, and A is the effective area of the electrode.

The surface coverage follows the order Mo1-GCE > Mo2-GCE > HK-GCE.

Figure 3.7 B shows the CVs for the bare and modified GCE electrodes in an optimised pH 4 buffer solutions. At this pH, the bare GCE displays no peak. Upon modification, HK-GCE and Mo2-GCE both display well resolved peaks in the range 195-60 mV with the highest signal at 20 μA, belonging to the HK-GCE. Mo1-GCE has a less defined peak in buffer.

3.7.3 L-cysteine detection

L-cysteine is classified as a non-essential amino acid that is important for protein synthesis, detoxification and metabolism in biological systems [44]. It contains a highly reactive sulfhydryl group which in turn plays a vital role in

biological activities like enzyme catalysis [45], detoxification and antioxidant activity [46]. By monitoring concentrations of physiological molecules like L-cysteine, there can be an improvement in human health and this can be achieved via biological sensors [28]. Numerous attempts have been made to detect the L-cysteine using various techniques; very few however have to do with the use of MOFs in electrochemistry [39,47,48].

MOFs are characterized by a highly porous surface morphology which can increase the surface area of the electrodes. This may result in subsequent improvement of electrocatalytic properties of the electrodes modified by MOFs. HKUST-1 on its own is a moderate electrocatalyst, however studies have shown that when modified with other materials, its performance improves [49-51]. Copper MOFs have been successfully used for electrochemical sensing of nitrates [52]. The combination of Cu and Mo centers in an electrocatalyst for the reduction of nitrate has been successful for the small oxomolybdate ($P_2W_{15}Mo_2O_{61}$) [53]. POMs have been successfully used as electrocatalysts due to the high oxidation states of the metals [54]. The current study is an attempt at using the larger polyoxomolybdates (Mo_6) incorporated into HKUST-1 MOF to give Mo_6–CuBTC POMMOF hybrids as biosensors for L-cysteine. HKUST-1, Mo1 and Mo2 were used in this analysis.

3.7.3.1 Cyclic voltammetry

The bare GCE did not show a peak whilst all the modified electrodes exhibited electrocatalytic oxidation of L-cysteine with good signal strengths (Figure 3.8 and Table 3.4). The observed oxidation peak potential window was 0.205 V - 0.328 V, which is characteristic for L-cysteine oxidation [55]. In terms of

oxidation potential, the electrodes followed the order Mo2-GCE (0.328 V) > HK-GCE (0.283 V) > Mo1-GCE (0.205 V). Since the bare GCE did not exhibit a peak, it can be concluded that modification with HKUST-1, Mo1 and Mo2 resulted in electrodes with an ability to detect L-cysteine. Mo1-GCE was able to do this at the lowest potential whilst Mo2-GCE gave the highest signal (almost twice that of HK-GCE).

L-cysteine can be oxidized to cystine via the following reaction (Eq. 3) [45,56];

$$2RSH \Leftrightarrow RSSR + 2H^+ + 2e^- \quad (3)$$

where RSH = L-cysteine and RSSR = cystine.

Electrocatalytic oxidation can either be due to interaction with the cavity or the framework [52]. HKUST-1 has coordinatively unsaturated Cu^{2+} sites [57] that are available for oxidation of L-cysteine. It is proposed that during L-cysteine oxidation, the mechanism involves reduction of Cu^{2+} to Cu^0. This normally occurs at E^0=0.34 V, however according to Giri and Sarkar [58], this value can also be as low as E^0=0.25 V in very alkaline solutions suggesting that pH affects electrode potentials [59]. In this work, we propose that reduction of Cu^{2+} to Cu^0 occurred at E^0=0.283 V.

When Mo is incorporated, there is an increase in available metal centers (Mo_6-POM). We propose that here the Mo is reduced from Mo^{6+} to Mo^{4+} instead of Mo^{5+} (due to the absence of the dark blue colour associated with Mo-blues). POMs have also been reported to easily and rapidly undergo one or two electron reductions reversibly in electrocatalysis [54].

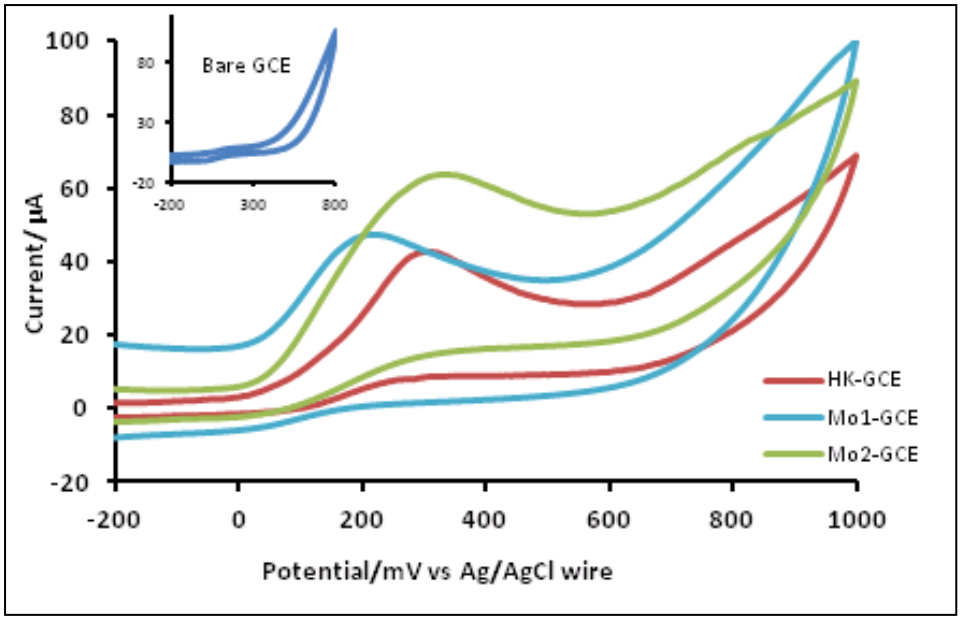

Figure 3. 8: Cyclic voltammograms of the modified electrodes (and Bare GCE (insert)) in 10 mM L-cysteine at 100 mV/s scan rate. pH 4 buffer.

It is noted that the modification method used has a direct bearing on the efficiency of the catalyst as can be seen from the different oxidation potentials. The following is proposed:-

1. A one pot solvothermal approach reduces the number of available active sites, possibly because there is saturation of the metal coordination sites (Mo^{6+} and Cu^{2+}) in formation of the framework. This results in electron transfer occurring at higher potentials (Compare HK-GCE (0.283 V) to (Mo2-GCE (0.328 V)).
2. PSM at room temperature results in an increase in catalytic sites (Compare HK-GCE (0.283 V) to (Mo1-GCE (0.205 V)).

The electrode behaviour suggests that PSM allows for both cavity (encapsulated Mo) and framework (Cu) mechanisms to be employed, hence resulting in the observed lower potential for Mo1-GCE. The electroreduction of L-cysteine is usually difficult suggesting that the reaction is irreversible.

Reversibility can be either chemical or electrochemical in nature. Chemical irreversibility occurs when products rapidly transform or decompose into another form and prohibit return to original materials[60,61]. Electrochemical irreversibility is often due to the kinetics of electron transfer being slow. This means that the reversibility of the reaction depends on the speed of the reaction at the electrode surface, the slower the reaction, the more irreversible the reaction becomes [40]. We propose that irreversibility could have been due to either chemical or electrochemial means. L-cysteine has been known to rapidly transform to the oxidized species by undergoing an irreversible chemical reaction, a phenomenon suggested by other researchers [56]. It could also be due to the high energy requirements for oxidation of MoO_2 (Eq. 4) back Mo^{6+}, making the reaction almost irreversible [62]. For such reactions, an overpotential has to be applied to overcome the activation barrier of the slow electron transfer reaction [63].

$$MoO_4^{2-} + 2H_2O + 2e^- \leftrightarrow MoO_2 + 4OH^- \qquad E^o = -0.818V \qquad (4)$$

3.7.3.2 Electrode stability

Electrode stability was investigated by running 20 successive cyclic voltammograms in 10 mM L-cysteine (Figure 3.9 A-C). The Mo2-GCE and HK-GCE are fairly stable and continue to detect L-cysteine, with good signal strength after 20 cycles. Mo1-GCE is not as stable and losses its ability to detect with consistency after about 10 cycles.

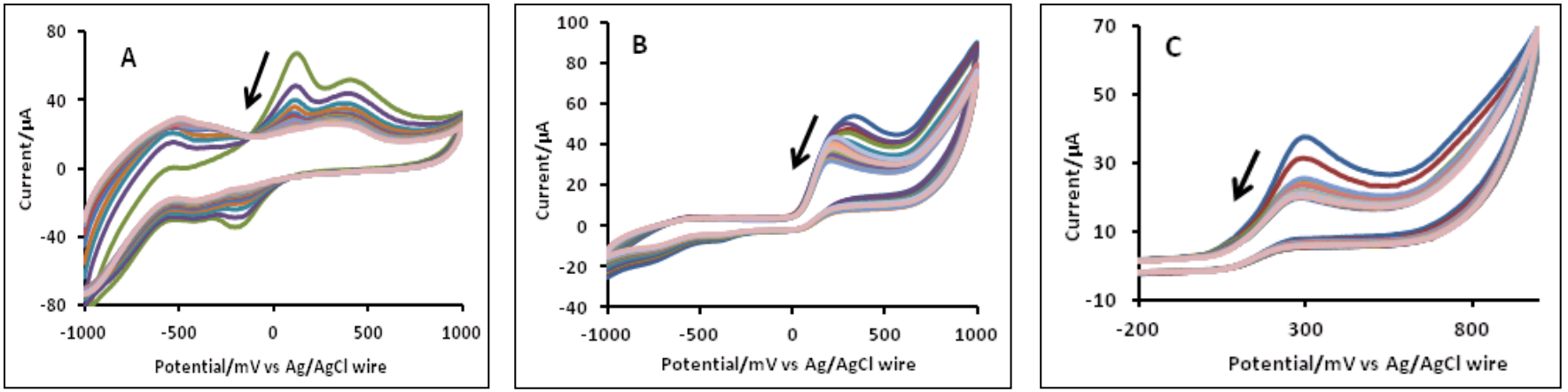

Figure 3. 9: Cyclic voltammogrammes (20 successive scans) of Mo1-GCE (A), Mo2-GCE (B), HK-GCE (C), in 10 mM L-cysteine. Scan rate of 100 mV/s. pH = 4 buffer.

3.7.3.3 Kinetic studies

The effect of scan rates on the modified electrodes was investigated in L-cysteine. The change in the scan rate is accompanied by a shift in peak potential which is suggestive of an irreversible reaction during oxidation of L-cysteine on the modified electrode surface (Figure 3.10). The relationship between oxidation peak potential and log of scan rate, Figure 3.10, for an irreversible diffusion-controlled process is given by (Eq. 5) [39],

$$E_p = \frac{2.303RT}{2(1-\alpha)n_\alpha F}\log \nu + K \qquad (5)$$

where α is the transfer coefficient, n_α is the number of electrons involved in the rate determining step, ν is the scan rate, K is a constant, R is the universal gas constant and T is the temperature (298 K).

From Figure 3.10, peak current increases linearly with the square root of scan rate ($v^{1/2}$) for Mo2-GCE suggesting that the electrochemical processes are diffusion controlled for all the modified electrodes [39]. The plots for HK-GCE and Mo1-GCE (Figure 3.8) however, show slight deviations from linearity suggesting either electrochemical quasi-reversibility or that electron transfer is occurring via surface adsorbed species [64]. For an electrochemical quasi-reversible process, a shift is observed in peak-to-peak separation with scan rate, whereas for surface absorbed species, there is no observable shift. Analysis of the plots of current vs scan rate all show shifts and this suggest the deviations from linearity observed for HK-GCE and Mo1-GCE are as a result of the process being electrochemically quasi-reversible.

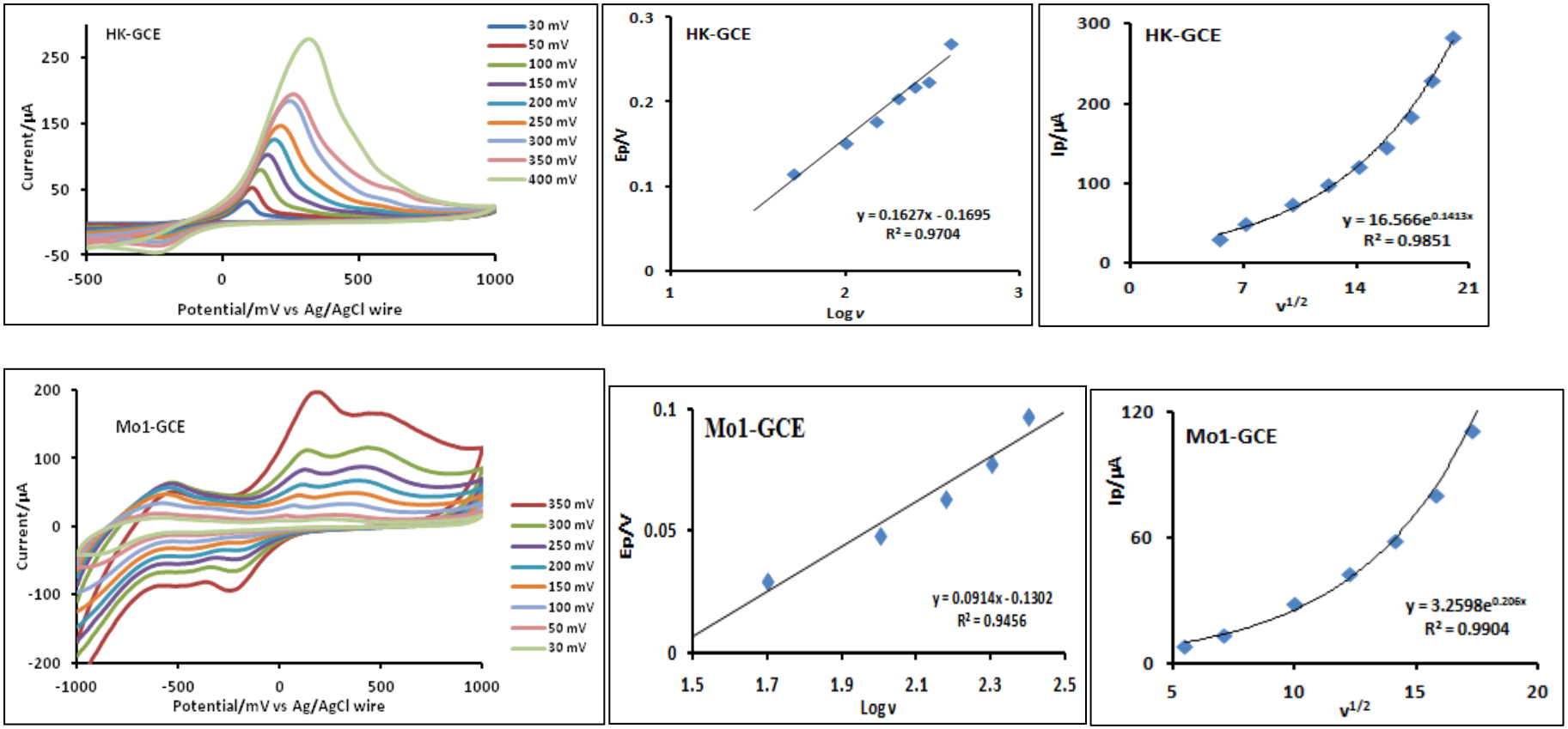

Figure 3. 10: Cyclic voltammograms of the detection of L-cysteine at different scan rates, their corresponding plots of oxidation Ep vs. log V and of oxidation Ip vs. $V^{1/2}$ scan rate in 10 mM L-cysteine of different electrodes, pH 4 buffer (continued next page).

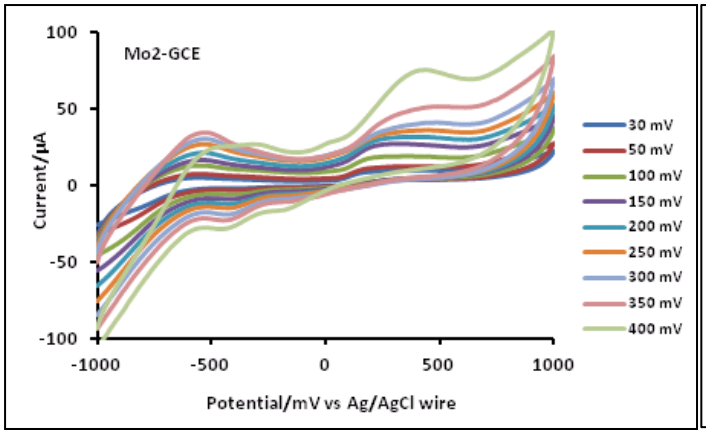
Mo2-GCE
Current/µA
Potential/mV vs Ag/AgCl wire
30 mV
50 mV
100 mV
150 mV
200 mV
250 mV
300 mV
350 mV
400 mV

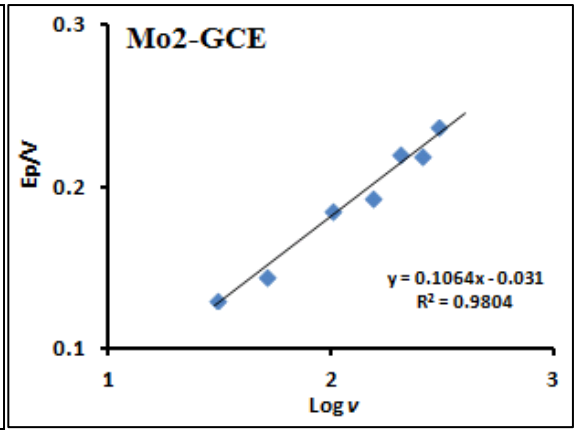
Mo2-GCE
Ep/V
Log v
y = 0.1064x - 0.031
R² = 0.9804

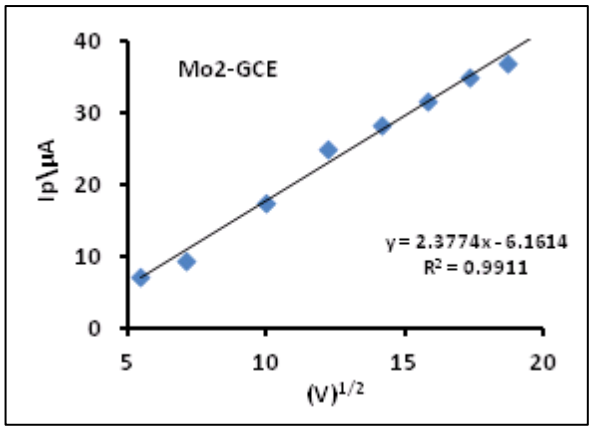
Mo2-GCE
Ip\µA
(V)1/2
y = 2.3774x - 6.1614
R² = 0.9911

In order to determine the Tafel slopes, equation 6 [65,66] for irreversible systems was used.

$$E_p = \frac{b}{2}\log v + k \qquad (6)$$

where ν is the scan rate and b is the Tafel slope.

Plots of Ep vs log ν (Figure 3.10) were drawn and used to determine the Tafel slopes. The Tafel slopes (2 x slope of the plot of Ep vs. log ν) for HK-GCE, Mo1-GCE and Mo2-GCE all gave high values (326 mV/decade, 183 mV/decade and 213 mV/decade respectively). This indicates to adsorption complications which can be caused by the presence of either the products or intermediates on the modified electrode surface [67]. Such high Tafel slopes, much greater than the normal 30–120 mV/decade have also been linked to chemical reactions coupled to electrochemical steps or electrode passivation. Materials with very high surface area to volume ratios, like activated carbon [68], metal nanoparticles [69] and MOFs [70] have been seen to give high Tafel slopes hence this is not surprising since the current study deals with POM-MOFs.

3.7.3.4 Chronoamperometry

Chronoamperometry was used to determine the nanoprobe sensitivity, rate constants and the detection limits. Within the first 0.1 seconds (on average), the catalytic current is dominated by electro oxidation of L-cysteine in this work (Figure 3.11) before it reaches steady-state. The sensitivity (in μA/mM) of the probes followed the order Mo1-GCE (4.4919) < HK-GCE (6.1439) < Mo2-GCE (25.329) (Figure 3.11).

According to literature [66], the rate constant can be evaluated using the Eq. (7);

$$\frac{I_{cat}}{I_{buf}} = \frac{\gamma^{1/2}(\pi^{1/2}\mathrm{erf}(\gamma^{1/2})+\exp(-\gamma))}{\gamma^{1/2}} \quad (7)$$

where I_{cat} and I_{buf} are the currents on the modified GCE in the presence and absence of L-cysteine, respectively, and $\gamma = kC_o t$ (Co is the bulk concentration of L-cysteine) and erf is the error function.

In cases where $\gamma > 2$, the error function is almost equal to 1, (Eq. 7) can be reduced to (Eq. 8) below.

$$\frac{I_{cat}}{I_{buf}} = \gamma^{½}\pi^{½} = \pi^{½}(kC_o t)^{½} \quad (8)$$

where k is the catalytic rate constant, Co is the bulk concentration of L-cysteine and t is time elapsed in seconds.

Figure 3.11 shows the plots of I_{cat}/I_{buf} vs $t^{1/2}$ (Eq 9) for L-cysteine oxidation. The plots were used to calculate the rate constants and these are represented by equations 9 a-c for HK-GCE, Mo1-GCE and Mo2-GCE respectively. The slope is equal to πk where k is the rate constant.

$$y=0.0384[\text{L-cysteine}]\left(\frac{s^{-1}}{mM}\right)-0.0948s^{-1},\ R^2=0.9671 \quad (9a)$$

$$y=0.0697[\text{L-cysteine}]\left(\frac{s^{-1}}{mM}\right)-0.0563s^{-1},\ R^2=0.9430 \quad (9b)$$

$$y=0.0182[\text{L-cysteine}]\left(\frac{s^{-1}}{mM}\right)-0.0539s^{-1},\ R^2=0.9694 \quad (9c)$$

The rate constants were found to be 1.22×10^1 $M^{-1}s^{-1}$, 2.2×10^1 $M^{-1}s^{-1}$ and 5.8 $M^{-1}s^{-1}$ for HK-GCE, Mo1-GCE and Mo2-GCE respectively. This compares well with those obtained in literature [39,56]. The electrocatalytic oxidation peak current of L-

cysteine showed a linear dependence on the L-cysteine concentration obtained in the range 0 to $1.0x10^{-2}$ M.

Table 3. 5: Comparative LODs for electrochemical oxidation of L-cysteine using different catalytic systems

Electrode	pH	LOD	Reference
Mo1-GCE	4	$3.07x10^{-7}$ M	This work
Mo2-GCE	4	$3.47x10^{-7}$ M	This work
HK-GCE	4	$3.03x10^{-7}$ M	This work
Boron-doped CNT-GCE	7.4	$2.6x10^{-7}$ M	[56]
Pt-CNT	7.4	$3.0x10^{-7}$ M	[71]
Ferrocenedicarboxylic acid-CPE	8	$2.6X10^{-5}$ M	[67]

Limits of detection (LOD) values were calculated using the 3σ notation, and using the Calibration curves (Figure 3.11). LODs followed the order HK-GCE< Mo1-GCE< Mo2-GCE. All the values are within the range often found in biological fluids (0.5-680 μM) such as urine and plasma [72]. Compared to HK-GCE though, both Mo1-GCE and Mo2-GCE LODs were slightly higher suggesting that molybdenum decreased the sensitivity of the electrodes for L-cysteine detection.

3.7.3.5 Selectivity and interferences

Selectivity of L-cysteine detection on other electrodes has been shown to be affected by the presence of sulphur containing amino acids like Methionine. However, this occurs when the oxidation potentials are in the same range [71,73] and concentrations of interferences are very high (above 200-fold) [74,75]. Other non-sulphur amino acids like L-serine, L-histidine, D-glutamic acid and L-alanine

have also been reported to have very little interference [56]. Amongst compounds like glucose, citric acid, urea, oxalic acid and ascorbic acid which often exist in the biological matrix, only ascorbic acid has been known to cause interference when in concentrations of at least 200 fold that of L-cysteine [74,76]. Hosseini et al [44] worked with a similar HKUST-1 modified electrode and observed no interference on the signals of L-cysteine in the presence of 10.0 μM interfering substance (biological matrix) and 5.0 μM L-cysteine with a deviation below 5.0%. Based on this, we recommend further studies on biological matrix but expect similar results for the electrodes used in this work.

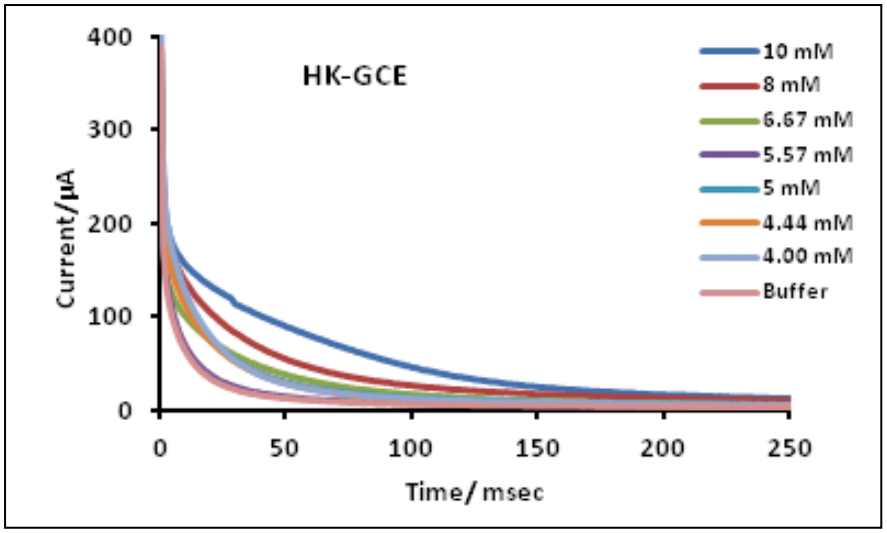

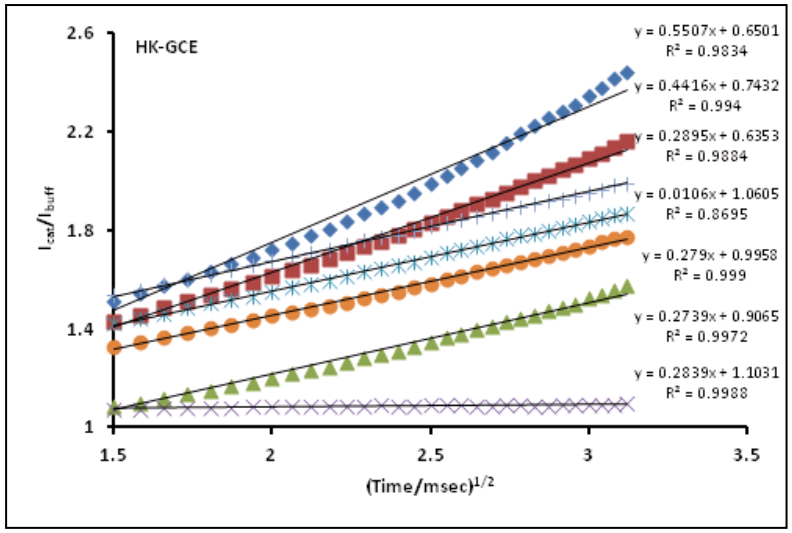

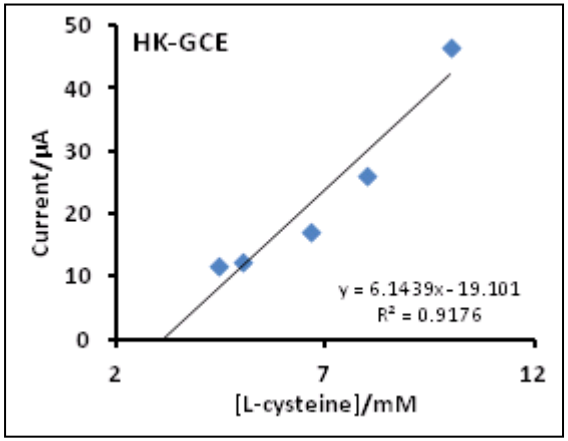

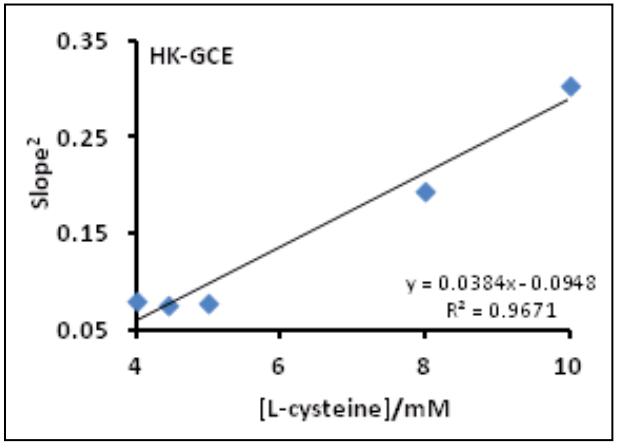

Figure 3. 11: Chronoamperograms, plots of Icat/Ibuf versus $t^{1/2}$ (10 mM, 8.0 mM, 6.67 mM, 5.71 mM, 5.0 mM, 4.44 mM, 4.0 mM and at 3.64 mM) determined using chronoamperometry for the POM-MOF GCE.(continued next 2 pages)

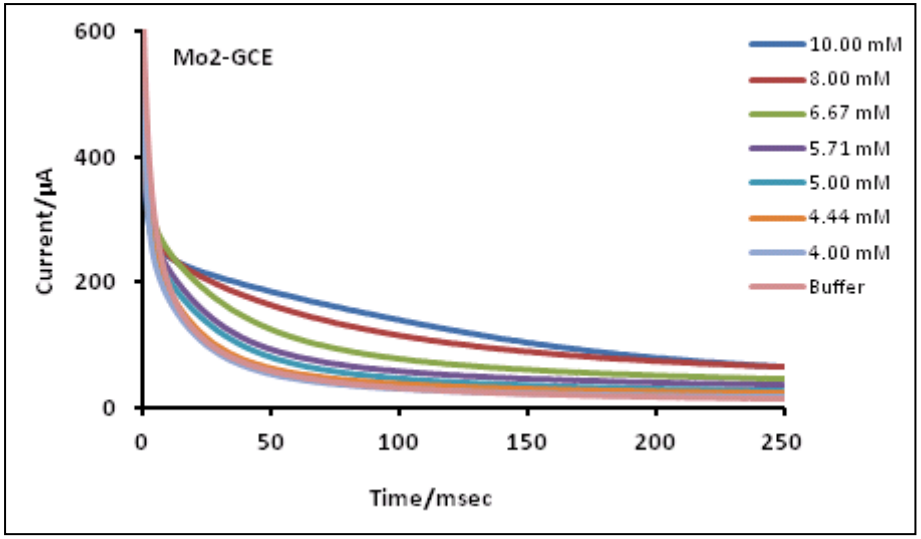
Mo2-GCE
Current/µA
Time/msec
10.00 mM
8.00 mM
6.67 mM
5.71 mM
5.00 mM
4.44 mM
4.00 mM
Buffer

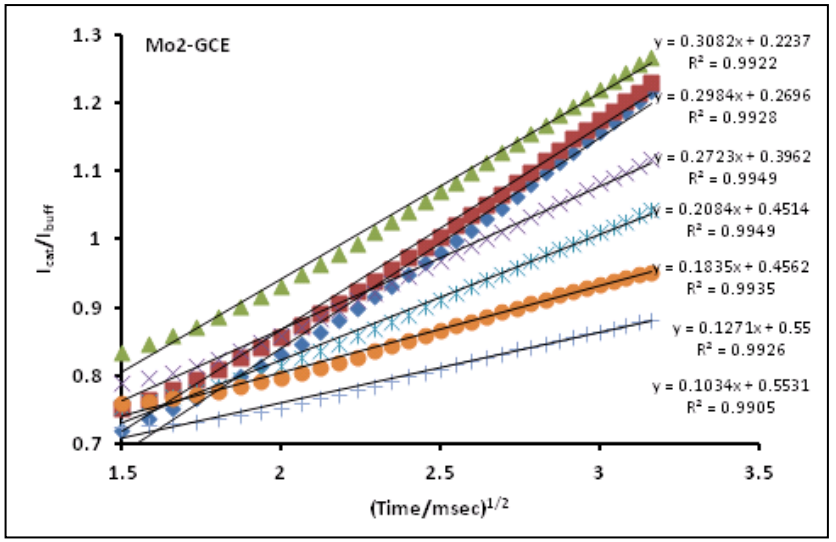
Mo2-GCE
I_{cat}/I_{buff}
(Time/msec)$^{1/2}$
y = 0.3082x + 0.2237
R² = 0.9922
y = 0.2984x + 0.2696
R² = 0.9928
y = 0.2723x + 0.3962
R² = 0.9949
y = 0.2084x + 0.4514
R² = 0.9949
y = 0.1835x + 0.4562
R² = 0.9935
y = 0.1271x + 0.55
R² = 0.9926
y = 0.1034x + 0.5531
R² = 0.9905

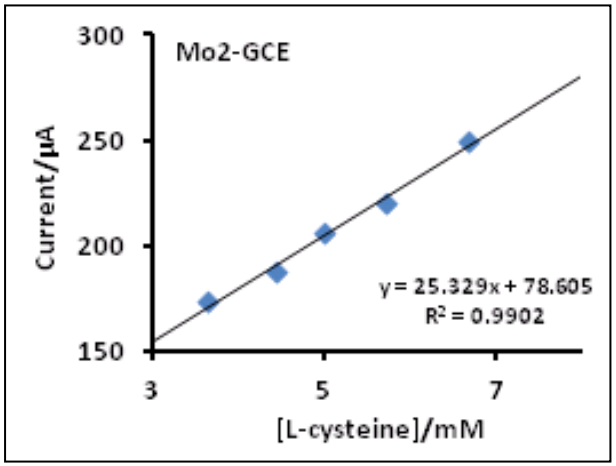
Mo2-GCE
Current/µA
[L-cysteine]/mM
y = 25.329x + 78.605
R² = 0.9902

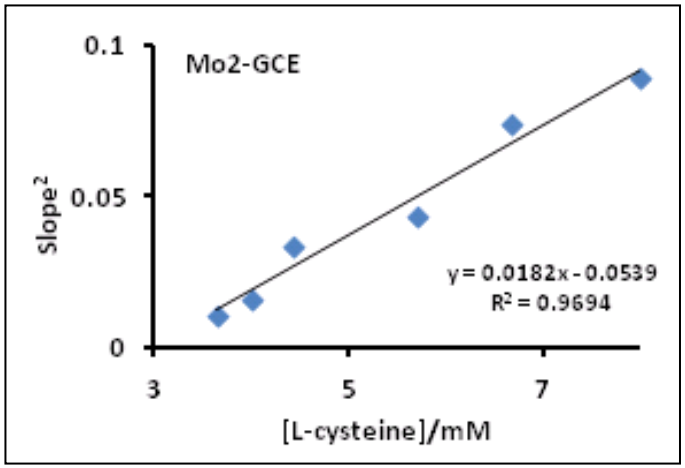
Mo2-GCE
Slope²
[L-cysteine]/mM
y = 0.0182x - 0.0539
R² = 0.9694

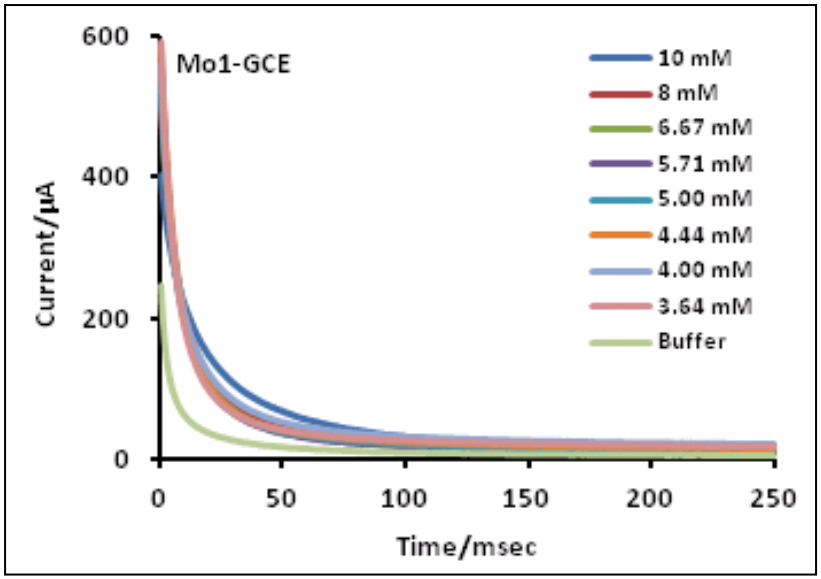
Mo1-GCE
10 mM
8 mM
6.67 mM
5.71 mM
5.00 mM
4.44 mM
4.00 mM
3.64 mM
Buffer
Current/µA
Time/msec
600
400
200
0
0
50
100
150
200
250

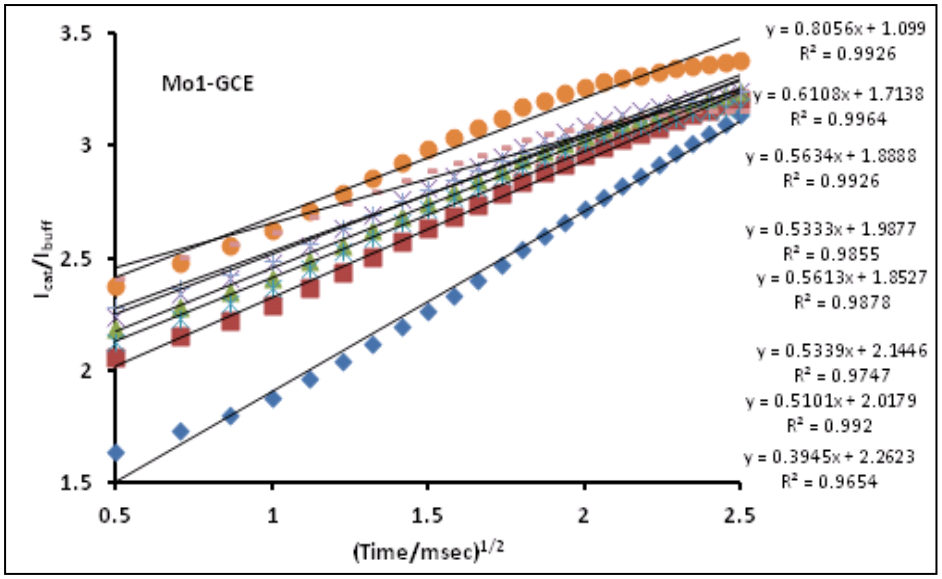
Mo1-GCE
y = 0.8056x + 1.099
R² = 0.9926
y = 0.6108x + 1.7138
R² = 0.9964
y = 0.5634x + 1.8888
R² = 0.9926
y = 0.5333x + 1.9877
R² = 0.9855
y = 0.5613x + 1.8527
R² = 0.9878
y = 0.5339x + 2.1446
R² = 0.9747
y = 0.5101x + 2.0179
R² = 0.992
y = 0.3945x + 2.2623
R² = 0.9654
I_{cat}/I_{buff}
$(Time/msec)^{1/2}$
3.5
3
2.5
2
1.5
0.5
1
1.5
2
2.5

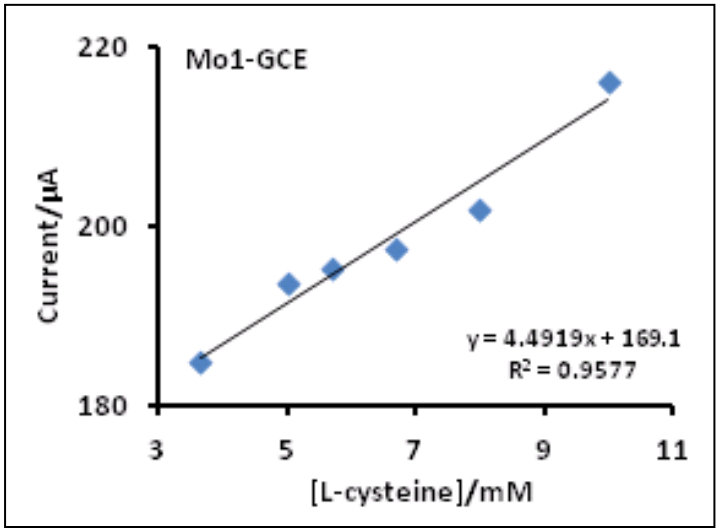
Mo1-GCE
y = 4.4919x + 169.1
R² = 0.9577
Current/µA
[L-cysteine]/mM
220
200
180
3
5
7
9
11

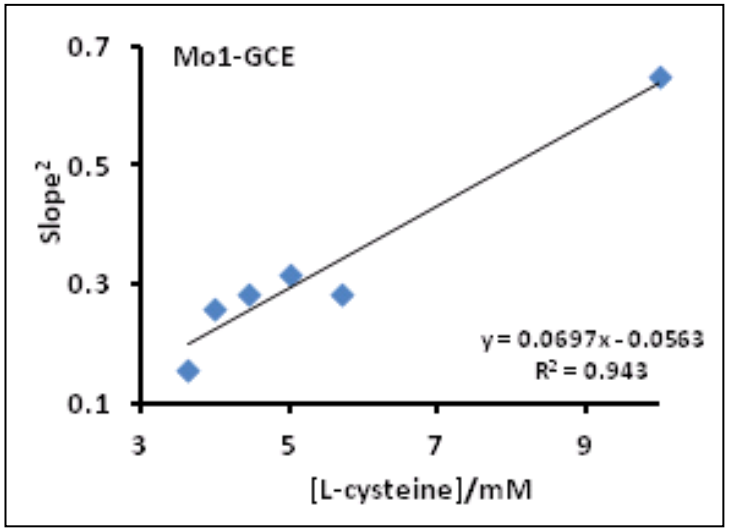
Mo1-GCE
y = 0.0697x - 0.0563
R² = 0.943
$Slope^2$
[L-cysteine]/mM
0.7
0.5
0.3
0.1
3
5
7
9

3.7.3.5 Conclusions

Glassy Carbon Electrodes modified with HKUST-1, Mo1 and Mo2 were employed for the detection of L-cysteine. Mo1-GCE gave the best catalytic activity with a rate constant of 2.2 $X10^4$ M^{-1} s^{-1} and relatively low detection limits of $3.07x10^{-7}$ M. The low detection limits and wide range of linearity points to these probes as a promising platform for L-cysteine sensing.

References

[1] S.-Y. Chui, M.-F. Lo, J. P. H. Charmant, A. G. Orpen, D. I. Williams, I. D. Williams, *Science .* **1999**, *283*, 1148–1150.

[2] K.-S. Lin, A. K. Adhikari, C.-N. Ku, C.-L. Chiang, H. Kuo, *Int. J. Hydrogen Energy* **2012**, *37*, 13865–13871.

[3] J. Kim, S.-H. Kim, S.-T. Yang, W.-S. Ahn, *Micropor. Mesopor. Mat.* **2012**, *161*, 48–55.

[4] R. J. Kuppler, D. J. Timmons, Q.-R. Fang, J.-R. Li, T. A. Makal, M. D. Young, D.-Q. Yuan, D. Zhao, W.-J. Zhuang, H.-C. Zhou, *Coord. Chem. Rev.* **2009**, *253*, 3042–3066.

[5] T. Granato, F. Testa, R. Olivo, *Micropor. Mesopor. Mat.* **2012**, *153*, 236–246.

[6] H. Yang, S. Orefuwa, A. Goudy, *Micropor. Mesopor. Mat.* **2011**, *143*, 37–45.

[7] M. Schlesinger, S. Schulze, M. Hietschold, M. Mehring, *Micropor. Mesopor. Mat.* **2010**, *132*, 121–127.

[8] Y. Li, R. T. Yang, *Am. Inst. Chem. Eng.* **2008**, *54*, 269–279.

[9] P. M. Shafi, A. C. Bose, *AIP Adv.* **2015**, *5*, 057137.

[10] H.-B. Wu, B.-Y. Xia, L. Yu, X.-Y. Yu, W.-X. D. Lou, *Nat. Commun.* **2015**, *6*, 1–12.

[11] S. Abednatanzi, A. Abbasi, M. Masteri-Farahani, A. Abbasi, *New J. Chem.* **2015**, *39*, 5322–5328.

[12] K. G. Desai, C. Liu, H. J. Park, *J. Microencapsulation,* **2006**, *23*, 79–90.

[13] H. T. Evans, B. M. Gatehouse, P. Leverette, *J. Chem. Soc. Dalt. Trans* **1975**, *6*, 505–514.

[14] J. Wienold, R. E. Jentoft, T. Ressler, *Eur. J. Inorg. Chem.* **2003**, 1058–1071.

[15] J. L. Zhuang, D. Ceglarek, S. Pethuraj, A. Terfort, *Adv. Funct. Mater.* **2011**, *21*, 1442–1447.

[16] J. M. Zamaro, N. C. Perez, E. E. Miro, C. Casado, B. Seoane, C. Tellez, J. Coronas, *Chem. Eng. J.* **2012**, *195–196*, 180–187.

[17] Y. Chen, X. Huang, X. Feng, J. Li, Y. Huang, J. Zhao, Y. Guo, X. Dong, R. Han, P. Qi, et al., *Chem. Commun. (Camb).* **2014**, *50*, 8374–8377.

[18] G. Mahalakshmi, V. Balachandran, *Spectrochim. Acta Part A Mol. Biomol. Spectrosc.* **2014**, *124*, 535–547.

[19] L. Seguin, M. Figlarz, R. Cavagnat, J. C. Lassegues, *Spectrochim. Acta Part A* **1995**, *51*, 1323–1344.

[20] G. Tsilomelekis, S. Boghosian, *J. Phys. Chem. C* **2011**, *115*, 2146–2154.

[21] S. M. K. G Ravikumar, S. Rajaraman, *Proc. indian Natl. Sci. Acad.* **1984**, *51*, 368–373.

[22] Y.-G. Li, L.-M. Dai, Y.-H. Wang, X.-L. Wang, E.-B. Wang, Z.-M. Su, L. Xu, *Chem. Commun.* **2007**, 2593–2595.

[23] S. Tangestaninejad, M. Moghadam, V. Mirkhani, I. Mohammadpoor-Baltork, K. Ghani, *J. Iran. Chem. Soc.* **2008**, *5*, s71-79.

[24] R. Thouvenot, M. Fournier, R. Franck, C. Rocchiccioli-Deltcheff, *Inorg. Chem.* **1984**, *23*, 598–605.

[25] A. Chithambararaj, D. Bhagya Mathi, N. Rajeswari Yogamalar, A. Chandra Bose, *Mater Res Express* **2015**, *2*, 055004–055014.

[26] G. Nagaraju, C. N. Tharamani, G. T. Chandrappa, J. Livage, *Nanoscale Res Lett* **2007**, *2*, 461–468.

[27] J. Juan-Alcaniz, M. G. Goesten, E. V Ramos-fernandez, J. Gascon, F. Kapteijn, *New J. Chem.* **2012**, *36*, 977–987.

[28] C. Wei, X. Li, F. Xu, H. Tan, Z. Li, L. Sun, Y. Song, *Anal. Methods* **2014**, *6*, 1550–1557.

[29] X.-W. Lou, H.-C. Zeng, *Chem. Mater.* **2002**, *14*, 4781–4789.

[30] E. Lamprecht, G. M. Watkins, M. E. Brown, *Thermochim. Acta* **2006**, *446*, 91–100.

[31] M. E. Brown, in *Introd. to Therm. Anal. Tech. Appl.*, Springer Netherlands, Dordrecht, **1988**, pp. 23–49.

[32] S. Loera-Serna, M. A. Oliver-Tolentino, M. D. L. López-Núñez, A. Santana-Cruz, A. Guzmán-Vargas, R. Cabrera-Sierra, H. I. Beltrán, J. Flores, *J. Alloys Compd.* **2012**, *540*, 113–120.

[33] K. Ma, J. Yin, Q. Zhang, J. Xie, *Phase Transitions* **2017**, *90*, 342–350.

[34] B. Mu, K. S. Walton, *J. Phys. Chem. C* **2011**, *115*, 22748–22754.

[35] T. Hatakeyama, F. X. Quinn, *Thermal Analysis: Fundamentals and Applications to Polymer Science*, Wiley-VCH Verlag GmbH & Co. KGaA, **1999**.

[36] Y.-F. Song, H. Abbas, C. Ritchie, N. McMillian, D.-L. Long, N. Gadegaard, L. Cronin, *J. Mater. Chem.* **2007**, *17*, 1903–1908.

[37] X. Dai, M. Liu, Z. Li, A. Jin, Y. Ma, X. Huang, H. Sun, H. Wang, X. Zhang, *J. Phys. Chem. C* **2016**, *120*, 12539–12548.

[38] Y. S. Choudhary, L. Jothi, G. Nageswaran, *Electrochemical Characterization*, Elsevier Inc., **2017**.

[39] M. Shumba, T. Nyokong, *Electrochim. Acta* **2016**, *196*, 457–469.

[40] A. J. Bard, L. R. Faulkner, *Eectrochemical Methods; Fundamentals and Applications*, John Wiley & Sons, Inc., New York, **2001**.

[41] R. L. McCreery, *ChemInform* **2008**, *39*, 2646–2687.

[42] W. Zhou, C. Wöll, L. Heinke, *Materials (Basel).* **2015**, *8*, 3767–3775.

[43] L. Heinke, Z. Gu, C. Wöll, *Nat. Commun.* **2014**, *5*, 1–6.

[44] H. Hosseini, H. Ahmar, A. Dehghani, A. Bagheri, A. Tadjarodi, A. Reza, *Biosens. Bioelectron.* **2013**, *42*, 426–429.

[45] L. H. Wang, W. S. Huang, *Sensors* **2012**, *12*, 3562–3577.

[46] N. C. Plaza, M. R. Gracia-Galbis, R. M. Martinez-Espinosa, *Molecules* **2018**, *23*, 1–13.

[47] M. P. Motaung, P. A. Ajibade, *Int. J. Electrochem. Sci.* **2015**, *10*, 8087–8096.

[48] W. Liu, X.-B. Yin, *Trends Anal. Chem.* **2016**, *75*, 86–96.

[49] J. Du, J. Wang, L. Ji, X. Xu, Z. Chen, *ACS Appl. Mater. Interfaces* **2016**, *8*,

30205–30211.

[50] W. Zhou, J. Jia, J. Lu, L. Yang, D. Hou, G. Li, S. Chen, *Nano Energy* **2016**, *28*, 29–43.

[51] M. H. Yap, K. L. Fow, G. Z. Chen, *Green Energy Environ.* **2017**, *2*, 218–245.

[52] B. Yuan, J. Zhang, R. Zhang, H. Shi, X. Guo, Y. Guo, X. Guo, S. Cai, D. Zhang, *Int. J. Electrochem. Sci* **2015**, *10*, 4899–4910.

[53] B. Keita, E. Abdeljalil, L. Nadjo, R. Contant, R. Belghiche, *Langmuir* **2006**, *22*, 10416–10425.

[54] S.-S. Wang, G.-Y. Yang, *Chem. Rev.* **2015**, *115*, 4893–4962.

[55] A. Nisar, Y. Lu, J. Zhuang, X. Wang, *Angew. Chemie - Int. Ed.* **2011**, *50*, 3187–3192.

[56] C. Deng, J. Chen, X. Chen, M. Wang, Z. Nie, S. Yao, *Electrochim. Acta* **2009**, *54*, 3298–3302.

[57] S. Bordiga, L. Regli, F. Bonino, E. Groppo, C. Lamberti, B. Xiao, P. S. Wheatley, R. E. Morris, A. Zecchina, *Phys. Chem. Chem. Phys.* **2007**, *9*, 2676–2685.

[58] S. D. Giri, A. Sarkar, *J. Electrochem. Soc.* **2016**, *163*, H252–H259.

[59] S. M. A. el Haleem, B. G. Ateya, *J. Electroanal. Chem. Interfacial Electrochem.* **1981**, *117*, 309–319.

[60] M. V. Mirkin, S. Amemiya, *Nanoelectrochemistry*, **2015**.

[61] F. A. Armstrong, J. Hirst, *Proc. Natl. Acad. Sci.* **2011**, DOI 10.1073/pnas.1103697108.

[62] C.-Y. Sun, S.-X. Liu, D.-D. Liang, K.-Z. Shao, Y.-H. Ren, Z.-M. Su, *J. Am. Chem. Soc.* **2009**, *131*, 1883–1888.

[63] F. Scholz, *Electroanalytical Methods: Guide to Experiments and Applications*, **2010**.

[64] N. Elgrishi, K. J. Rountree, B. D. McCarthy, E. S. Rountree, T. T. Eisenhart, J. L. Dempsey, *J. Chem. Educ.* **2018**, *95*, 197–206.

[65] T. Mugadza, T. Nyokong, *Polyhedron* **2011**, *30*, 1820–1829.

[66] S. Nyoni, T. Mugadza, T. Nyokong, *Electrochim. Acta* **2014**, *128*, 32–40.

[67] J. B. Raoof, R. Ojani, H. Beitollahi, *Electroanalysis* **2007**, *19*, 1822–1830.

[68] Z. Hu, M. P. Srinivasan, *Microporous Mesoporous Mater.* **2001**, *43*, 267–275.

[69] J. N. Sharma, D. K. Pattadar, B. P. Mainali, F. P. Zamborini, *Anal. Chem.* **2018**, acs.analchem.8b01905.

[70] G. Mehlana, S. A. Bourne, G. Ramon, *CrystEngComm* **2014**, *16*, 8160.

[71] S. Fei, J. Chen, S. Yao, G. Deng, D. He, Y. Kuang, *Anal. Biochem.* **2005**, *339*, 29–35.

[72] C. Xiao, J. Chen, B. Liu, X. Chu, L. Wu, S. Yao, *Phys. Chem. Chem. Phys* **2011**, *13*, 1568–1574.

[73] X.-Q. Wu, J.-G. Ma, H. Li, D.-M. Chen, W. Gu, G.-M. Yang, P. Cheng, *Chem. Commun.* **2015**, *51*, 9161–9164.

[74] A. Nezamzadeh-Ejhieh, H.-S. Hashemi, *Talanta* **2012**, *88*, 201–208.

[75] Y. Wang, H. Ge, G. Ye, H. Chen, X. Hu, *J. Mater. Chem. B* **2015**, *3*, 3747–3753.

[76] A. Abbaspour, A. Ghaffarinejad, *Electrochim. Acta* **2008**, *53*, 6643–6650.

Chapter Four

In this chapter, three structures were assembled from Co(II) ions and either H_3BTC or H_4B4C as ligands. The synthetic procedures are described. The synthesized products were characterized using microanalysis, SC-XRD, FTIR, TGA and DSC. Their potential as electrocatalysts in oxidative detection of L-cysteine was then investigated.

4. Compounds of Co, H_3BTC and H_4B4C

The synthetic procedures of the products from Co(II) and either H_3BTC or H_4B4C are described. The synthesized procedures, characterization (microanalysis, SC-XRD, FTIR, TGA and DSC) and electrocatalytic behaviour are discussed below. The initial synthetic procedure was designed to synthesize a cobalt POM-MOF, analogues of the encapsulated and encorporated POM-MOFs described in Chapter 3. The cobalt products proved to contain no molybdates (with the exception of CoB4C-POM) and the focus of the study was then extended to investigating the effect of different benzenepolycarboxylates as ligands for production of Co MOFs. Previous researchers have observed that varying the numbers of carboxylic acids on the ligands has a structure defining effect on the final product; for example 1D ladders vs 2D layers [1], rigid vs flexible structures [2]. The different ligation modes afforded by varying ligands result in numerous possibilities for supramolecular structures all with different properties [3–5]. The aim of the study in this chapter is to investigate the effect of H_3BTC or H_4B4C on the structure and properties of Co MOFs, especially on L-cysteine electrocatalysis. The identification of the product Co-B4C-POM as either an encapsulated or encorporated POM-MOF was determined by microanalysis and by the very high decomposition patterns observed in the TGA and DSC (Appendix B3). As a mixed metal system it was not pursued in the study.

4.1 Synthesis

Three compounds were synthesized using solvothermal methods at the same temperature. The duration for synthesis was either 5 or 10 days, depending on formation of products.

4.1.1 Synthesis of CoBTC

Exactly 4.5 mmol (1.071 g) of cobalt chloride hexahydrate, 1 mmol (0.210 g) of H_3BTC and 1 mmol (1.235 g) of $(NH_4)_6Mo_7O_{24}.4H_2O$ were each placed in separate beakers. To each beaker 10 mL of Millipore water were added and the mixture stirred for about 30 minutes with gentle heating, until a clear solution was obtained. All three solutions were mixed, sonicated for five minutes, placed in a glass vial and sealed. The vial was placed in an autoclave, heated to 120 °C and maintained at this temperature for 10 days. The autoclave was cooled to room temperature at which point dark pink sheet-like crystals had formed. These were named CoBTC. (Yield: 0.89 g, 78 % based on Co).

CAUTION: Hydrothermal synthesis employing $(NH_4)_6Mo_7O_{24}.4H_2O$) at temperatures above 120 °C may result in explosion due to the formation of NH_3.

4.1.2 Synthesis of CoB4C and CoB4C-2

From experience within the group, synthesis of MOFs using H_4B4C often produces a mixture of compounds that need to be separated. Exactly 5 mmol (1.190 g) of cobalt chloride hexahydrate, 1 mmol (0.254 g) of H_4B4C and 1 mmol (1.235 g) of

$(NH_4)_6Mo_7O_{24}.4H_2O$ were all added to 10 mL of Millipore water each and stirred for about 30 minutes with gentle heating, until a clear solution was obtained. All three solutions were mixed, sonicated for a few minutes, placed in a glass vial and sealed. The vial was placed in an autoclave, heated to 120 °C and maintained at this temperature for 5 days. The autoclave was cooled to room temperature at which point light pink sheet-like crystals and a purple powder had formed. The mixture was separated by hand, using tweezers to pick the pink crystals. The major pink product was named CoB4C ($CoH_{13}C_5O_{10}$ Yield: 0.98 g, 67.7 % based on Co). The purple product, the minor product, was named $CoB4C_p$. Preliminary infrared spectrum indicated it was a complex containing only the benzenepolycarboxylate. Since it was the minor component, it was not pursued further in the study.

In order to improve the yield of either one or the other product, the same mixture was prepared and placed in an autoclave at 120 °C for 10 days. After cooling very thin orange-pink sheets were collected and named CoB4C-2. (Yield: 1.08 g, 62.0 % based on Co). The crystals were contaminated by a very fine purple powder which was named CoB4C-POM. Attempts to improve the yield utilizing temperatures higher than 120 °C resulted in explosion.

4.2 SC-XRD and microanalysis

4.2.1 Microanalysis for CoBTC

The elemental analysis for CoBTC showed a close agreement between the observed and theoretical results. From the obtained results, the following empirical formula;

$Co_3(BTC)_2{\cdot}4H_2O{\cdot}5.5NH_3$; Mr 761.799 is proposed. A similar MOF for CoBTC was obtained by Yaghi *et al*[6] however their MOF had the ability to include more guest NH_3 molecules (proposed formula $Co_3(BTC)_2{\cdot}4H_2O{\cdot}15NH_3$). The most definitive way to confirm the structure would be to run SC-XRD, however in this case the crystals were too small for this technique. A series of additional techniques (FTIR, TGA and DSC) were employed in an attempt to confirm the suggested molecular formula.

Table 4. 1: Microanalysis for CoBTC: proposed formula ($Co_3(BTC)_2{\cdot}4H_2O{\cdot}5.5NH_3$).

Element	Expected	Observed	Difference	% Error
Carbon	28.380	28.447	+0.067	0.236
Hydrogen	4.036	4.010	-0.026	0.644
Nitrogen	10.113	10.021	-0.092	0.910

4.2.2 SC-XRD for CoB4C

Single crystal X-ray diffraction revealed that the compound crystallizes in the triclinic space group P-1 (number 2). Each unit cell contained four Co cations ($Co(H_2O)_4$) bound to two $B4C^{4-}$ ligands (Figure 4.1A) to form a three dimensional MOF (Figure 4.1C). Within the MOFs channels are four guest waters. The structure consists of two crystallographically independent networks held together by π---π stacking and hydrogen bonds.

The asymmetric unit contains two cobalt cations ($Co(H_2O)_2$) bound to half a $B4C^{4-}$ ligand unit ($C_5H_1O_4$) and two free waters (Figure 4.1B). Each cobalt centre is

coordinated to two $B4C^{4-}$ ligands and four waters; two Co-O=C bonds (from the ligand) occupy both the axial positions and the equatorial positions are occupied by coordinated water molecules. Each $B4C^{4-}$ unit is bound to four Co centres via monodentate coordination of the oxygens of the carboxylate groups. Each $B4C^{4-}$ is fully deprotonated and thus displays one bonding mode (through the carboxylate group) as shown in scheme 4.1. Full SC-XRD (ga280) is given in Appendix B1).

The structure has been reported before by Fabelo *et al* [7] for his compound 2 ($[Co_2(C_{10}H_2O_8)(H_2O)_8]\cdot 4H_2O$), a polymorph of his compound 1 (Table 4.2). Where Fabelo employed slow diffusion using a gel technique for this polymorph, we used a solvothermal approach. The corresponding Co-O bond lengths are in the range 2.0337(11) Å – 2.1292(10) Å for this work which is very close to the range for compound 2, 2.0430(10) Å – 2.1414(11) Å. Similar behaviour is observed for the O-Co-O bond angles which are in the range 86.12 ° - 93.88 ° and 87.05 ° - 93.76 ° for CoB4C (Appendix B1, Table S5) and compound 2, respectively. It would seem that contrary to their reports [7], under the conditions employed here, the solvothermal approach produced crystals of similar structure to the gel technique.

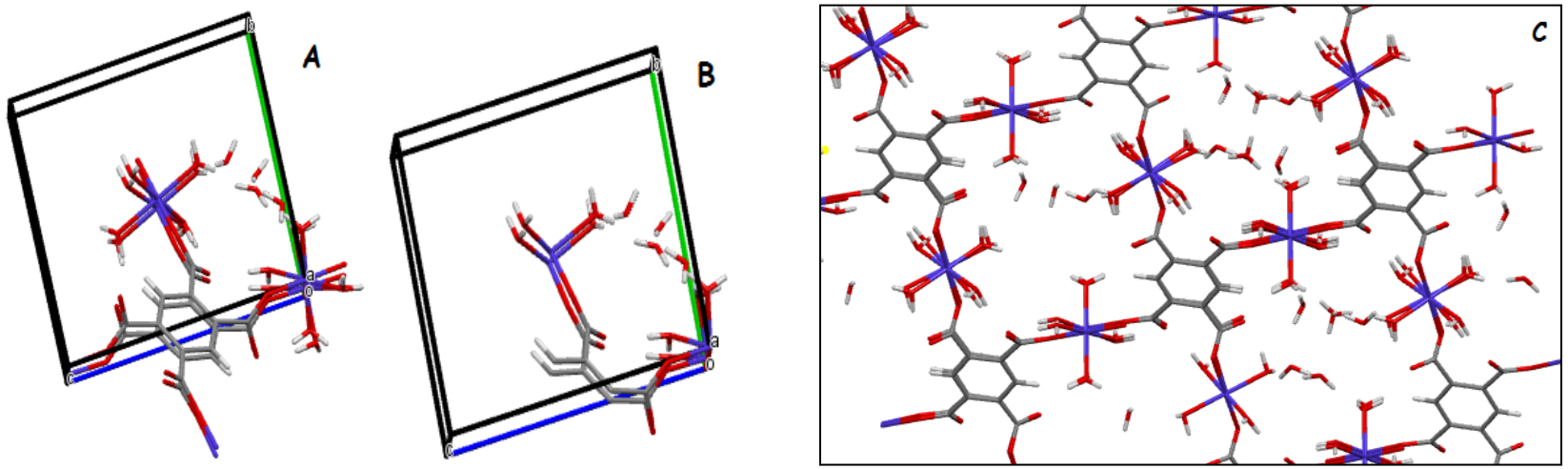

Figure 4. 1: Packing in CoB4C (A), asymmetric unit (B) and repeat unit (C). Interchain hydrogen bonding not shown for clarity.

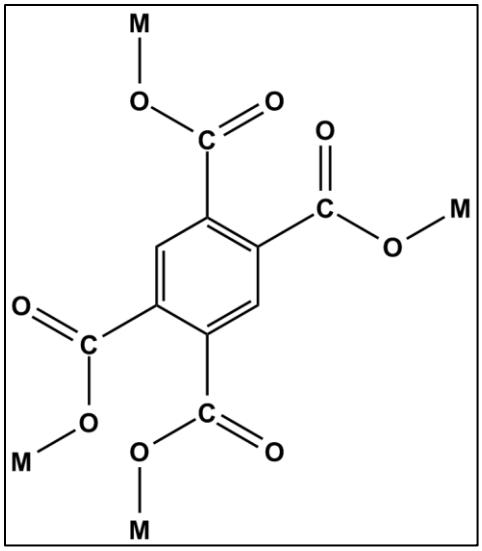

Scheme 4. 1: Monodentate bonding modes of $B4C^{4-}$.

Camara *et al* [8] made a similar compound but with more guest water; $[Co_2(C_{10}H_2O_8)(H_2O)_8]\cdot 8H_2O$. The synthesis method was the same as that by Fabelo *et al* [7], gel technique. The product however had almost the same cell parameters (angles, unit cell size) as Fabelo's compound 1 [7] (Table 4.3). A pictorial comparison of the structures is shown in Figure 4.2.

Table 4. 2: Comparison of SC-XRD data for CoB4C complexes.

	CoB4C-This work	Fabelo 1[2]	Fabelo 2[2]	Camara[3]
Empirical formula	$CoH_{13}C_5O_{10}$	$CoH_{13}C_5O_{10}$	$Co_2H_{26}C_{10}O_{20}$	$Co_2H_{34}C_{10}O_{24}$
Formula weight	292.08	292.08	584.17	656.22
Crystal system	Triclinic	Triclinic	Triclinic	Triclinic
Space group	P-1 (No. 2)	P-1	P-1	P-1
a /(Å)	10.8209(6)	5.4287(11)	10.847(2)	5.4371(1)
b/ (Å)	11.1168(7)	9.8286(16)	11.107(2)	9.8496(3)
c/(Å]	11.4713(6)	10.230(3)	11.483(2)	10.2564(3)
V /($Å^3$)	1079.84(11)	542.10(2)	1082.70(4)	545.48(3)
Alpha	82.892(2)	96.453(16)	82.93(3)	96.445(1)
Beta	62.852(2)	91.23(2)	63.02(3)	91.232(1)
Gamma	62.257(2)	91.339(14)	62.12(3)	91.328(1)
Z	4	2	2	1
D(calc) [g/cm^3]	1.797	1.789	1.792	-
μ (mm^{-1})	1.630	1.624	1.626	1.64
F(000)	600	-	-	-
Crystal Size [mm]	0.37 x 0.42 x 0.43	-	-	0,10 x 0.09 x 0.06
R(int)	0.017	-	-	0.025
Observed Data [I > 2.0 sigma(I)]	4671	-	-	-
R, wR2,	0.0259, 0.0703	-	-	-
S	1.08	-	-	-
Min. and Max. Resd. Dens. ($e/Å^{-3}$)	-0.38, 0.40	-	-	-

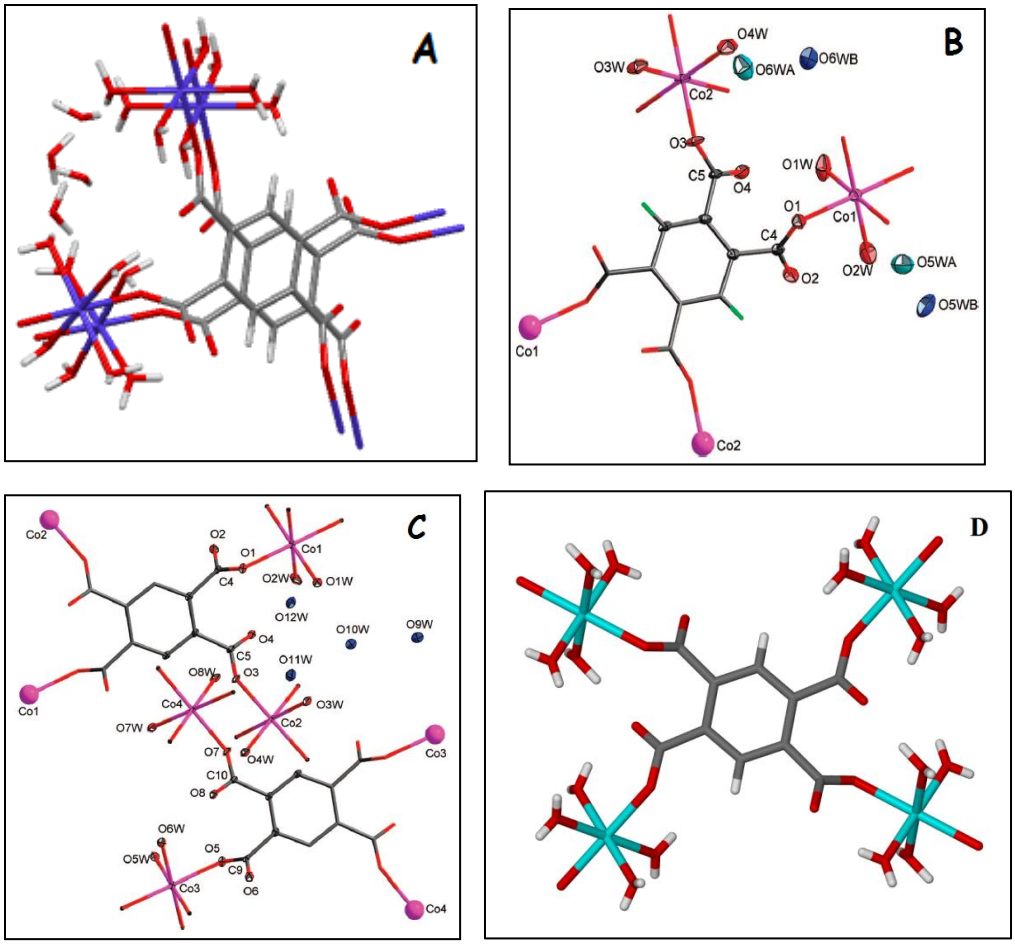

Figure 4. 2: Comparison of CoB4C (A), Fabelo 1 [2] (B), Fabelo 2 [2] (C) and Camara [3] (D) crystal structures.

The microanalysis showed a close agreement between the observed and theoretical results (Table 4.3). Based on its previous reporting in literature, extensive characterization was not pursued and microanalysis and SC-XRD for CoB4C were deemed sufficient confirmation.

Table 4. 3: Microanalysis for CoB4C: ($[Co_2(C_{10}H_2O_8)(H_2O)_8]\cdot 4H_2O$).

Element	Expected	Observed	Difference	% Error
Carbon	20.177	20.299	+0.122	0.60
Hydrogen	4.487	4.540	+0.053	1.18

4.2.2 SC-XRD for CoB4C-2

Single crystal X-ray diffraction revealed that the MOF CoB4C-2, exhibited twinned crystals and hence does not have a simple diffraction pattern due to its poor crystallinity. Though SC-XRD is a known technique for giving "irrefutable" structures, it is also dependant on the quality of the selected crystal [9,10]. Since the crystal was twinned, the water hydrogen atoms could not be located in the difference Fourier map. The data has been refined with only the hydrogens bound to the ring being fixed. Such twinned behaviour is not uncommon when dealing with SC-XRD [6]. From what could be obtained, the following deductions were made. CoB4C-2 crystallizes in the triclinic space group P-1 (number 2). The coordination environment of the Co centres is depicted in Figure 4.3. The asymmetric unit contains one cobalt cation moiety (CoO_3), (viz. coordinated to half a $B4C^{4-}$ ligand moiety ($C_5H_1O_4$) via the monodentate carboxyl group and two coordinated waters), as well as containing a second different CoO_3 moiety, (vis. half a cobalt hexaaqua cation).

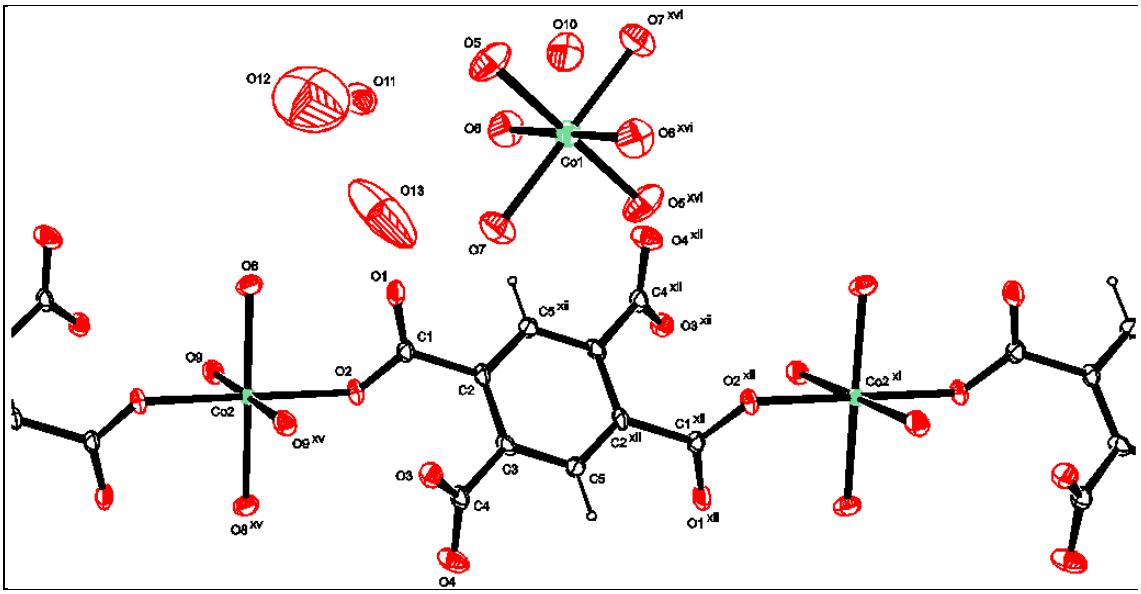

Figure 4. 3: Coordination environment of the Co centres with atomic labels in CoB4C-2.

The monomeric unit thus consists of a MOF lattice in which Co^{2+} ions coordinate to two oxygens from the carboxyl groups of two $B4C^{4-}$ linkers. The other four positions are occupied by oxygens of water, giving each cobalt centre an octahedral geometry. The $B4C^{4-}$ linker exhibits a bridge bonding mode, creating one dimensional chains (Figure 4.4). Co exists in two chemical environments; that described above is Co_2 which is monodentate coordinated to two bridging $B4C^{4-}$ ligands in the equatorial positions and four oxygens from water in the equatorial-axial positions and Co_1 which is monodentate coordinated to six oxygens from water. Such $Co(H_2O)_6^{2+}$ moieties though uncommon in MOFs, have been reported before in literature [11,12].

The Co-O bond lengths are in the range 2.073(6) Å – 2.126(6) Å and the corresponding O-Co-O bond angles are in the range 86.62(17) ° – 93.38 ° or exactly 180.0 ° for the equatorial positions (Appendix B2, Table S5). This is similar to the ranges observed in other Co-H_4B4C complexes containing the cobalt hexaaqua cation [13].

Each unit cell contains two bridging B4C ligands each coordinated to two cobalt centres, two cobalt hexaaqua cations and sixteen solvated water molecules (Figure 4.4 A). CoB4C-2 crystallizes forming one-dimensional ribbons (Figure 4.4 B). Between the sheets are cobalt cations and guest waters. The one dimensional ribbons are held together forming a compact network stabilized by the combination of hydrogen bonds and interchain π---π stacking. Such network stabilization has been observed in other MOFs [14].

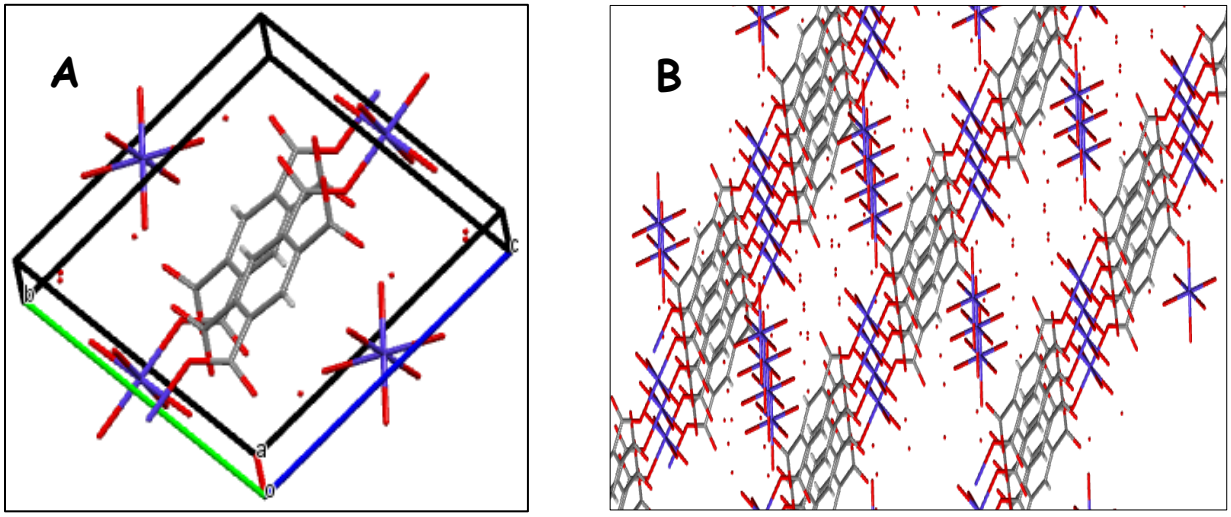

Figure 4. 4: Packing in CoB4C-2 unit cell, viewed along b axis (A) and 2-D sheets of CoB4C-2 (B). Hydrogen bonds not shown for clarity.

Table 4. 4: Crystallographic data for CoB4C-2.

	CoB4C-2
Empirical formula	$Co_2H_2C_{10}O_{26}$
Formula weight	655.98
Crystal system	Triclinic
Space group	P-1 (No. 2)
a /(Å)	6.8202(5)
b/ (Å)	9.9554(7)
c/(Å]	10.9025(8)
V /($Å^3$)	691.88(9)
Alpha	93.073(3)
Beta	104.512(3)
Gamma	103.500(3)
Z	1
D(calc) [g/cm^3]	1.574
μ (mm^{-1})	1.298
F(000)	324
Crystal Size [mm]	0.28 x 0.30 x 0.35
R(int)	0.000
Observed Data [I > 2.0 sigma(I)]	3190
R, wR2,	0.0755, 0.2104
S	1.23
Min. and Max. Resd. Dens. ($e/Å^{-3}$)	-0.92, 1.64

When searching the Cambridge Structural Database (Conquest version 1.2, 2018), no structures for a similar compound were found. Full SC-XRD data (ga113) is given in Appendix B2.

4.3 FTIR Spectra for CoBTC and CoB4C-2

The IR spectrum of CoBTC (Figure 4.5A) displays O-H bands centred at 3211 cm^{-1}. A sharp C=O asymmetric stretch is observed at 1675 cm^{-1} and the corresponding symmetric stretched at 1406 cm^{-1}. Both stretches have shifted to lower wavenumbers from H_3BTC to CoBTC; 1691 to 1675 cm^{-1} for the asymmetric stretch and 1457 to 1405 cm^{-1} for the symmetric stretch, which is characteristic of coordination. Removal of the Co metal's positive charge causes a shift of the electrons to the COπ* orbitals causing the C=O wavenumber to decrease [15,16].

A few weak sp^2 C-O stretches are observed between 1335 cm^{-1} and 1195 cm^{-1} [15]. Similar bands for coordinated carboxyl stretches were observed by Karmarkar and Oliver[17] in their CoBTC MOF. In this case, the Co was coordinated to one BTC^{3-} via a monodentate, bridging carboxyl group and to another via a bidentate coordination mode. The value for $\Delta[\nu_{as}(COO) - \nu_{sym}(COO)]$ in CoBTC is 269 cm^{-1} which is larger than the corresponding value in H_3BTC (234 cm^{-1}), indicating that the carboxylate groups behave as monodentate ligands in this complex [18]. The region between 1275 - 1000 cm^{-1} is characterized by higher C-H in-plane bends [19] whilst that between 880 - 800 cm^{-1} is characterized by aromatic sp^2 C-H bends (out-of plane bending) [15]. These are present in both H_3BTC and CoBTC.

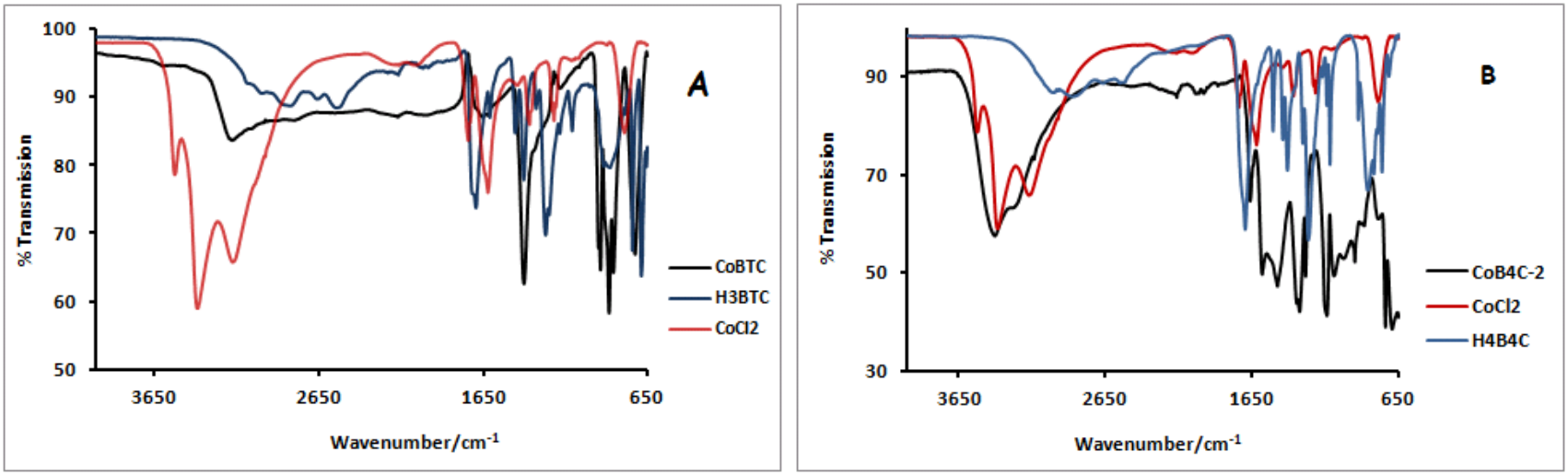

Figure 4. 5: FTIR spectra of CoBTC (A) and CoB4C-2 (B); and their respective starting materials.

In CoB4C-2 (Figure 4.5B) the band centred at 3400 cm^{-1} has been assigned as νOH (water) whilst that at 3159 cm^{-1} as νC-H stretches. The peaks at 1586 cm^{-1} and 1476 cm^{-1} have been assigned as C=C skeletal vibration bands[15]. The asymmetric C=O bands shifted to lower wavenumbers, 1700-1662 cm^{-1} and the symmetric stretches from 1408 cm^{-1} in H_4B4C to 1352 cm^{-1} in CoB4C-2 indicating that coordination occurred. The value for $\Delta v[\nu_{as}(COO) - \nu_s(COO)]$ in CoB4C-2 (310 cm^{-1}) is larger than the corresponding value in the ligand H_4B4C (292 cm^{-1}); indicating that the carboxylate groups behave as monodentate ligands in this MOF [18], as observed in the single crystal XRD. The absence of any strong bands around 1720 cm^{-1} in both complexes, suggests that the COOH groups are deprotonated in both CoBTC and CoB4C-2 [16,18]. The region between 1351-1099 cm^{-1} is characterized by sp^2 C-O stretches as well as strong C-H in-plane bending vibrations (1275-1000 cm^{-1}) [15,16]. The lower aromatic sp^2 C-H bands are observed between 905-850 cm^{-1}. In cobalt complexes, the region between 950-420 cm^{-1} is also characterized by Co-O vibrations [20–22]. However, the complexity of the fingerprint region limited specific assignments from being made. Such behaviour has been observed in other Co polycarboxylate complexes and the frequency, intensity and sharpness are attributed the strength of oxygen-hydrogen interactions and their environment [23].

4.4 Thermal analysis

Given that CoB4C-2 is an ionic MOF and would consequently represent a poor electrocatalytic comparison with CoBTC, it was not pursued further. The thermal behaviour of CoB4C has been reported before [7]. The thermal behaviour of CoBTC was investigated by means of TGA and DSC (Figure 4.6 and Table 4.5).

The TGA thermogram for CoBTC (Figure 4.6A) shows a multistep decomposition behaviour, with no obvious plateaus between decomposition steps. Such behaviour has been observed before in Co benzene polycarboxylates [24]. The first weight loss (calculated 12.99 weight %; observed 13.1 weight %) occurs between 82 – 132 °C. This is attributed to loss of lattice ammonia (TGA-1 and DSC-1) and is followed by a phase change (DSC-2) to accommodate the instability resulting from the loss of guests.

The second mass loss occurs between 132 - 147 °C (TGA-2 and DSC-3); (observed 18 weight %; calculated 9.45 weight % (for $4H_2O$), 17.28 weight % (for $8H_2O$)). The higher observed value suggests that during handling the MOF picked up an additional four waters, a possibility given the uptake capacity of the structure of upto twelve waters or fifteen ammonia molecules reported by Yaghi *et al* [6] . This is followed by a second phase change (DSC-4) to accommodate the instability resulting from the loss of water. Similar phase changes have been observed in other Co-BTC MOFs [25].

The loss of coordinated water results in the complete breakdown of the framework, with decarboxylation of the ligand [26]. From the TGA thermogram this is observed as a two step decomposition above 237 °C. The first BTC ligand is lost between 247 – 360 °C (TGA-3) (observed 24 weight %; calculated 24.83 weight %) in a multistep decarboxylation (broad endotherm DSC-5). The second BTC ligand is lost 360 – 414 °C (TGA-4) (observed 25 weight %; calculated 24.83 weight %) via a multistep decarboxylation (DSC-6).

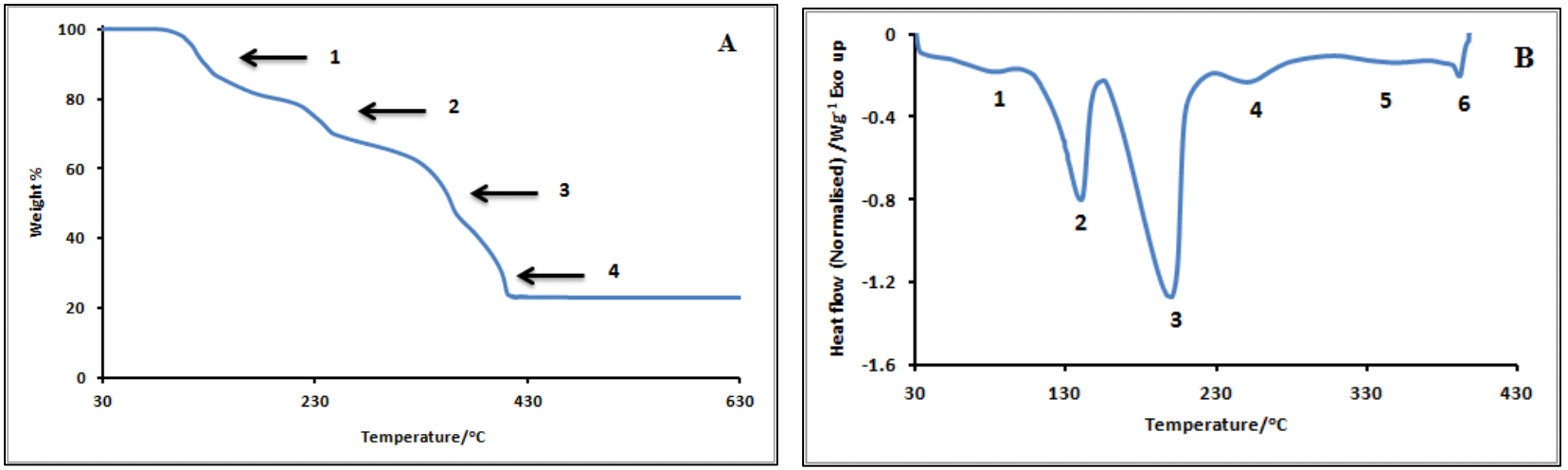

Figure 4. 6: TGA (A) and DSC (B) thermograms for CoBTC.

Table 4. 5: Thermal decomposition data of CoBTC.

DSC (T peak /°C)	TGA (T range/°C)	Mass loss (theor wt%/found wt%)	Molecules lost	Process
83 & 196 endotherms	82 - 132	12.99 / 13.1	$5.5NH_3$	Loss of guest & phase change
139 & 246 endotherms	132 - 247	17.28 / 18.0	$8H_2O$	Desolvation & phase change
336 endotherm	247 - 360	24.83/ 24.0	1 BTC^{3-}	Decomposition, (1^{st} BTC)
390 endotherm	360 - 414	24.83/ 25.0	1 BTC^{3-}	Decomposition, (2^{nd} BTC)

Above 430 °C no further mass loss or gain (the latter indicating oxidation) is observed. The final weight % of approximately 23 % indicates that the metal oxide formed is predominantly CoO[23] calculated (22%).

4.5 Electrochemical characterization of electrodes

Electrochemical characterization of the synthesized MOFs was done so as to determine their electrochemical properties. Of the three MOFs reported in this chapter, only CoBTC and CoB4C were investigated for their potential as electrochemical sensors with the aim of using them for electrocatalysis of L-cysteine. Due to its contamination and ionic nature, CoB4C-POM was not employed in electrocatalysis. Comparison was restricted to CoBTC and CoB4C. A GCE was modified with either CoBTC or CoB4C and named CoBTC-GCE and CoB4C-GCE respectively then characterized using cyclic voltammetry so as to evaluate their electrochemical behaviour. Specific details are reported in the following sections.

4.5.1 Cyclic Voltammetry

Figure 4.7A shows cyclic voltammograms for the modified and unmodified electrodes in 1 mM $Fe(CN)_6^{3-/4-}$ in 0.1 M KCl in the range -0.2 to 0.6 V. The peak potential separation (ΔE) for a reversible system such as $Fe(CN)_6^{3-/4-}$ is a good measure of the electron transfer ability of the electrode with lower values depicting a good electron transfer ability [27]. The cobalt polycarboxylate MOF modified electrodes showed good electron transfer abilities and follow the following order for ΔE : Bare GCE (0.066 V) < CoB4C-GCE (0.142 V) < CoBTC-GCE

(0.220 V) Table 4.6. From the obtained results, the Co-MOF modifications reduced the electrodes' electron transfer ability compared to that of the Bare GCE electrode. The ΔEp value for CoB4C-GCE is smaller than that for CoBTC-GCE suggesting the B4C ligand results in better electron transfer kinetics [28].

Table 4. 6: Electrochemical parameters for the electrodes.

GCE Modifier	ΔEp for $Fe(CN)_6^{3-/4-}$ in 0.1 M KCl	E/V (L-Cysteine) oxidation pH 4 buffer	Surface roughness	Eff. Area (cm^{-2})	Γ ($mol.cm^{-2}$)	Background corrected oxidation currents/μA in pH 4 buffer
Bare GCE	0.066	-	-	-	-	-
CoBTC-GCE	0.220	0.624	3.2312	0.234	2.46E2	29.967
CoB4C-GCE	0.142	0.624	8.4083	0.597	7.31E1	36.234

The surface roughness factors for the modified electrodes were determined by using the $[Fe(CN)_6]^{3-/4-}$ redox system and applying the Randles-Sevcik equation [29] (Eq. (1)) for reversible systems:

$$I_p = 2.69 \times 10^5 \, n^{3/2} \, ACD^{1/2} \, v^{1/2} \qquad (1)$$

where Ip, n, A, C, D and v are the peak current, the number of electrons involved, the electrode surface area, the concentration of $[Fe(CN)_6]^{3-/4-}$, the diffusion coefficient of $[Fe(CN)_6]^{3-/4-}$, and the scan rate, respectively.

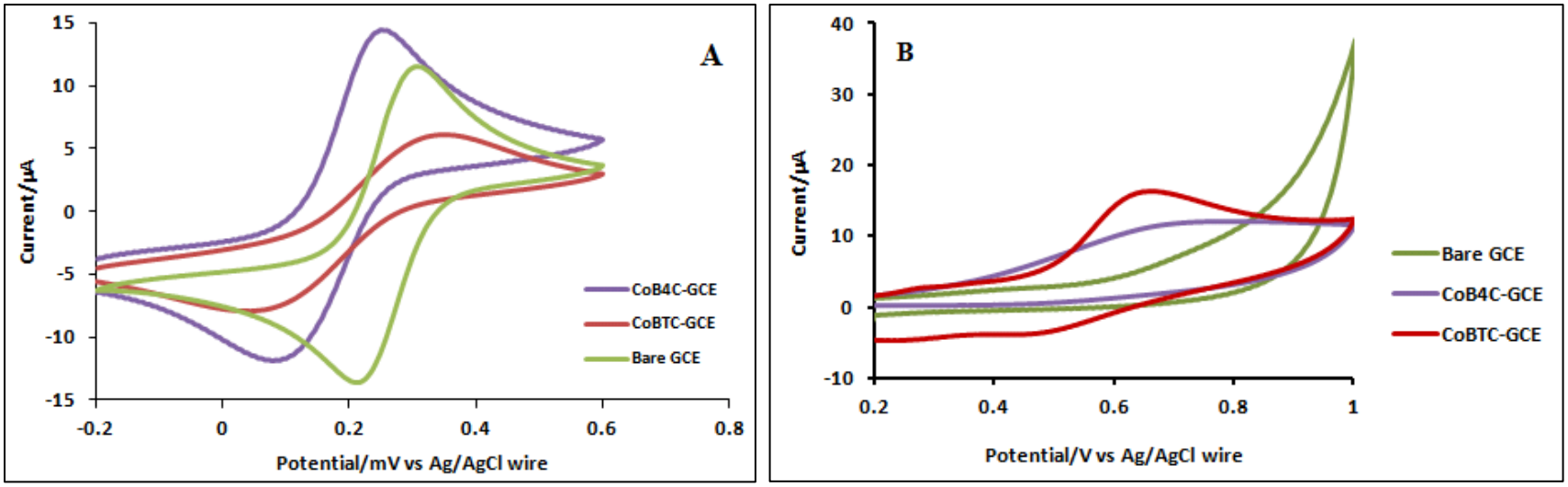

Figure 4. 7: Cyclic voltammograms of the electrodes in 1 mM $[Fe(CN)_6]^{3-/4-}$ (A) and in pH 4 buffer (B) at scan rate 100 mV/s.

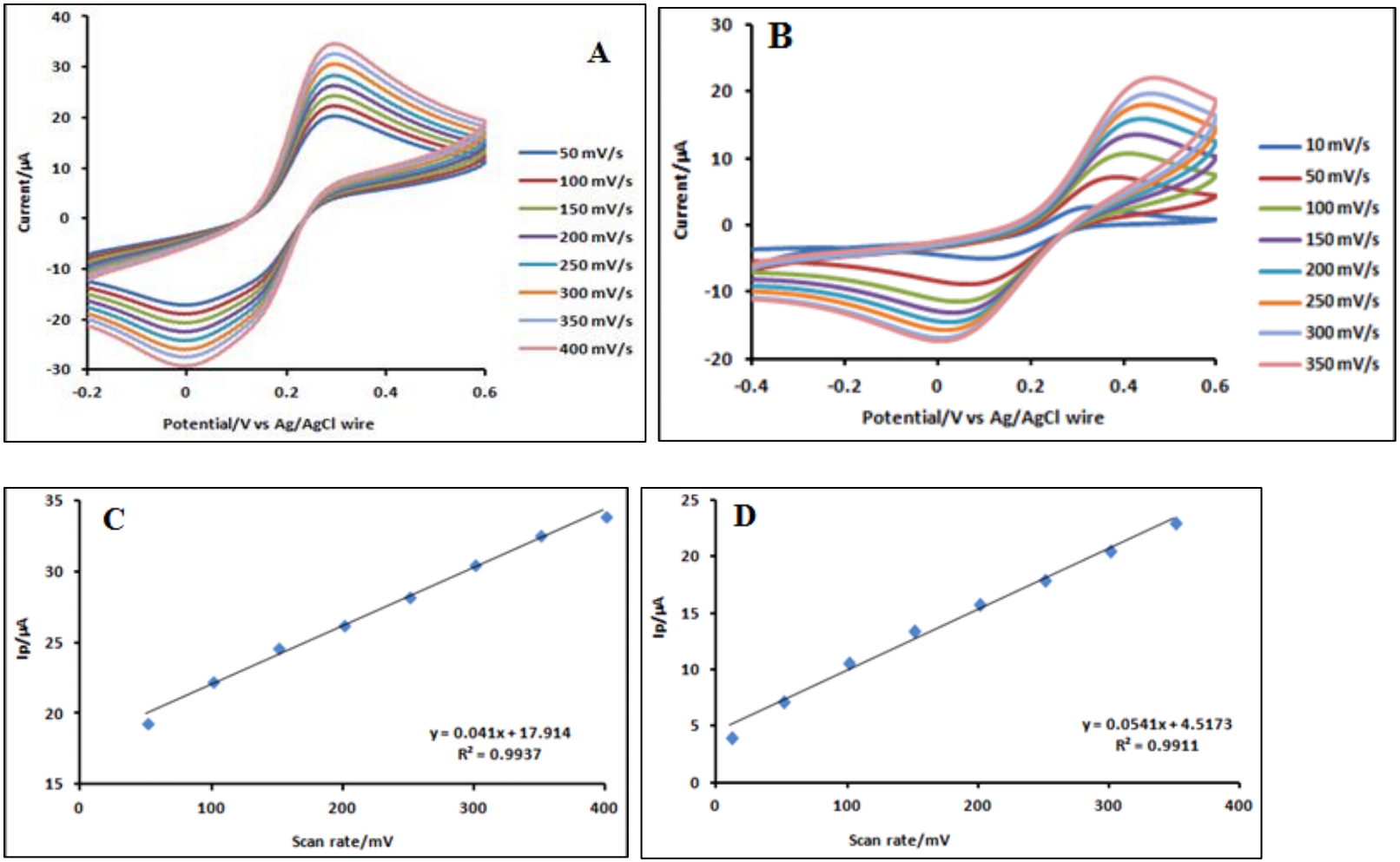

Figure 4. 8: Cyclic voltammograms at different scan rates and their corresponding plots of Ip_a vs. V for CoB4C-GCE (A,C) and for CoBTC-GCE (B,D) in 1 mM $[Fe(CN)_6]^{3-/4-}$ solution for the modified electrodes.

From the D value for $K_3[Fe(CN)_6]$ = 7.6 x 10^{-6} cm^2 s^{-1} and n = 1, the surface roughness factors (ratio of I_{pa} experimental/I_{pa} theoretical; shown in Table 4.8) were determined for all the probes and the corresponding effective electrode areas {roughness factor x theoretical surface area (0.071 cm^2)} were determined.

Equation (2) below was used for the calculation of surface coverage, Eq. (2) [30];

$$Ip_a = \frac{n^2F^2vA_{eff}\Gamma}{4RT} \quad (2)$$

where m (the gradient) is given by;

$$m = \frac{n^2F^2A_{eff}\Gamma}{4RT} \quad (3)$$

A plot of Ip_a vs v (Figure 4.8) gives the gradient, m, and by substituting for A_{eff} (effective electrode area) and other scientific terms (n is the number of transferred electrons, F is the Faraday constant, R is the universal gas constant and T is temperature), this relationship can be used to calculate the film surface coverage (Γ). The surface coverage follows the order CoBTC-GCE > CoB4C-GCE (Table 4.6). The effective area improved three fold and eight fold in CoBTC-GCE and CoB4C-GCE respectively.

In pH 4 buffer solutions the bare GCE does not conduct (Figure 4.7B). Once modified with the MOFs, well resolved oxidation peaks are observed at around 0.64 V for the CoBTC-GCE (16.14 μA), suggesting better electron transfer than the poorly resolved peak for CoB4C-GCE with a current of 11.60 μA at the same potential.

4.5.2 L-cysteine detection

Both electrodes modified with the cobalt MOFs displayed electrocatalytic activity for L-cysteine, with good signal strengths whilst the bare GCE showed no activity (Figure 4.9 and Table 4.6). Since the bare GCE does not exhibit a peak in the presence of L-cysteine, it can be concluded that modification resulted in the development of an electrode with the potential to detect L-cysteine. The oxidation peaks for CoBTC-GCE and CoB4C-GCE were observed at 0.624 V with signals of 32.36 μA and 46.69 μA respectively. This oxidation potential is characteristic of L-cysteine oxidation [32,33]. In the presence of the blank, both CoBTC-GCE and CoB4C-GCE displayed peaks with currents of 16.14 μA and 11.60 μA respectively. Since the bare GCE did not display a peak, the presence of a signal on the modified electrodes suggests that modification results in better electron transfer between the electrode and the analyte [31]. The increase in signal strength from the blank solutions (in pH 4 buffer) to L-cysteine suggests that these peaks are due to L-cysteine.

From the electrochemical behaviour, it is suggested that L-cysteine is oxidized to cystine [34,35]. The proposed mechanism involves the Co^{2+}/Co^{1+} couple. Electro-reduction is not observed possibly because of the slow speed and high energy demands of the process. This behaviour has been observed before with Cu MOFs [32], however much lower signals of 1.5 μA only were observed before modification of the MOF with nanoparticles. The current study is an example of a scenario when the MOF without any modification, post-synthetic or otherwise, is able to show good detection abilities with very high signals. This confirms that the field of MOFs in electrochemistry is still largely unexplored [36,37].

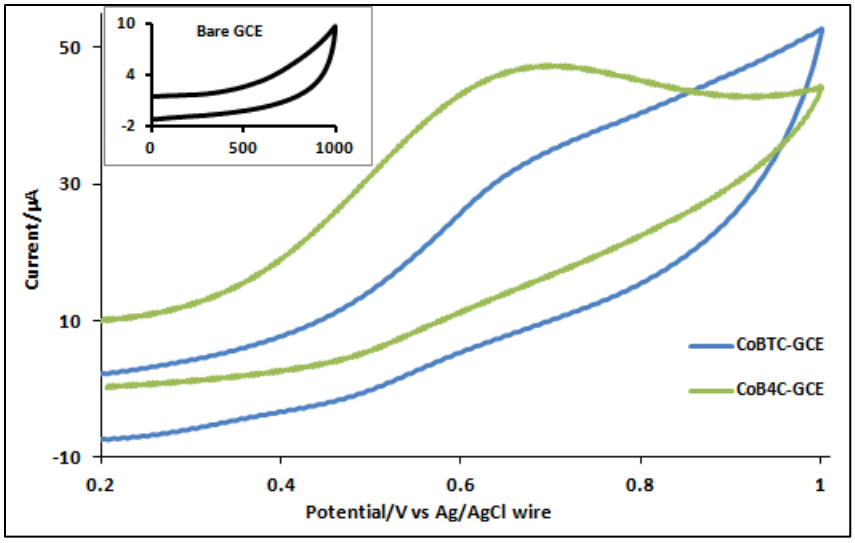

Figure 4. 9: Cyclic voltammograms of the modified electrodes (and Bare GCE (insert)) in 10 mM L-cysteine at 100 mV/s scan rate, pH 4 buffer.

Electrode stability was investigated by running 10 successive cyclic voltammograms in 10 mM L-cysteine (Figure 4.10). The modified electrodes were found to be fairly stable with good signal strength after 10 cycles, with CoBTC-GCE showing excellent stability. Stability was also expressed in terms of percentage current drop between the first and second cycles. The drops were found to be 2,4% and 8.2% for CoBTC-GCE and CoB4C-GCE respectively. These values are much lower than those found in literature showing that the electrodes have a very high resistance to fouling.

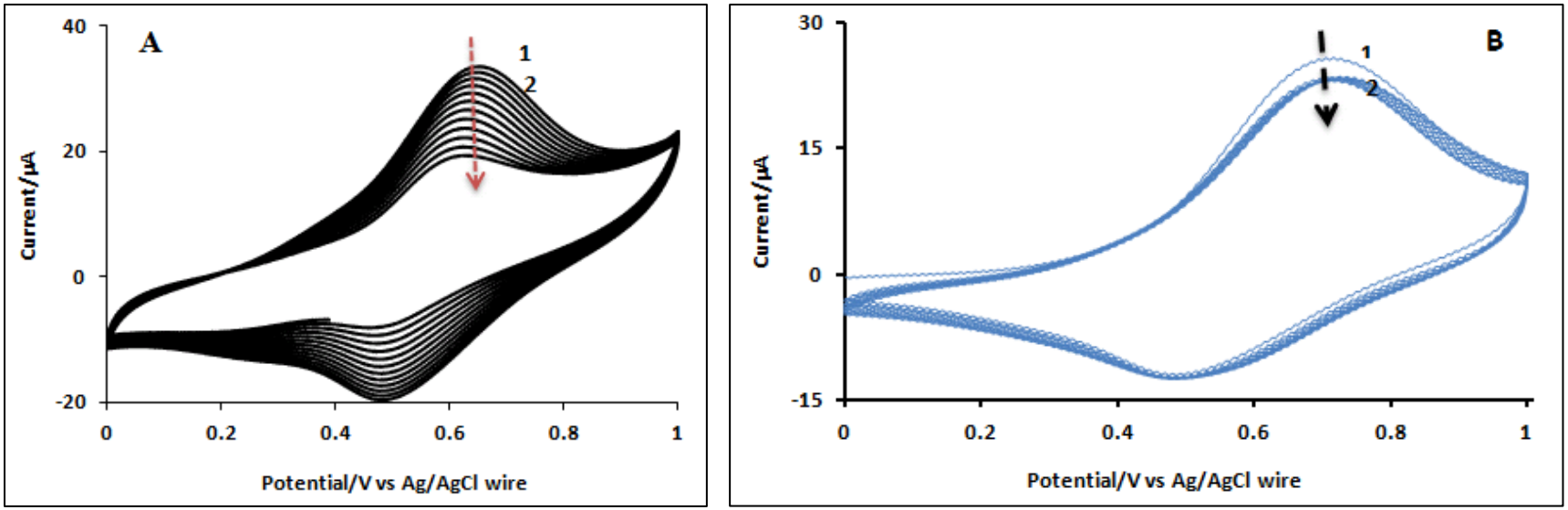

Figure 4. 10: Cyclic voltammogrammes (10 successive scans) of CoBTC-GCE (A) and CoB4C-GCE (B) in 10 mM L-cysteine. Scan rate of 100 mV/s, pH = 4 buffer.

4.5.3 Kinetic studies

The effect of scan rates on the modified electrodes was investigated in L-cysteine. For all the modified electrodes, the change in the scan rate is accompanied by a shift in peak potential which is suggestive of an irreversible reaction during oxidation of L-cysteine on the modified electrode surface (Figure 4.11). The relationship between oxidation peak potential and log of scan rate, Figure 4.11, for an irreversible diffusion-controlled process is given by Eq. (5) [38],

$$E_p = \frac{2.303RT}{2(1-\alpha)n_\alpha F}\log v + K \qquad (5)$$

where α is the transfer coefficient, n_α is the number of electrons involved in the rate determining step, *v* is the scan rate, K is a constant, R is the universal gas constant and T is the temperature (298 K).

From Figure 4.11, peak height increases linearly with the square root of scan rate ($v^{1/2}$) suggesting that the electrochemical processes are diffusion controlled rather than surface controlled [39], in the presence of sufficient overpotential, for all the modified electrodes. Diffusion limited reactions are those whose rate of reaction is determined by the rate of transport of reactants through the medium via diffusion [40]. Diffusion rate through solutions is affected by various factors such as particle size, solution density and temperature of the system [41]. Using the Randles-Sevcik equation [42] (Eq. 1), the diffusion coefficients for CoBTC-GCE and CoB4C-GCE in 10 mM L-cysteine were calculated and found to be 2.6 x 10^{-8} cm^2 s^{-1} and 1.9 x 10^{-8} cm^2 s^{-1} respectively. Both are lower than the diffusion coefficient for 1mM $K_3[Fe(CN)_6]$ which is 7.6 x 10^{-6} cm^2 s^{-1} [30]. This is line with literature which suggests that the diffusion coefficients for reactions in certain media (eg.

in L-cysteine) are expected to lower than those in ferricyanide due to the higher density of molecules (buffer and 10 mM L-cysteine vs 1mM $[Fe(CN)_6]^{3-/4-}$), which in turn reduces mobility by increasing resistance and lowers the rate of diffusion [42].

Tafel slopes and corresponding data were obtained using the equation (6) below;

$$E_{pa} = \frac{b}{2} logv + k \qquad (6)$$

where ν is the scan rate and b is the Tafel slope.

The plots of Ep versus log ν for both CoB4C-GCE and CoBTC-GCE gave linear relationships (Figure 4.11). The Tafel slope for CoB4C-GCE gave a value of 98.6 mV/decade which is within the normal range (60 – 120 mV/decade). The Tafel slope for CoBTC-GCE on the other hand gave a very high value (613.4 mV/decade). Such a high value indicates to adsorption complications which can be caused by the presence of either the products or intermediates on the modified electrode surface [30].

Information on the rate determining step was also obtained from the relationship $a_a n_a$, where (where a_a is the anodic transfer coefficient and n_a is the number of electrons involved in the rate determining step) for the electrocatalytic oxidation of L-cysteine. The anodic transfer coefficients values were found to be 0.1115 and 0.1065 for CoBTC-GCE and CoB4C-GCE, respectively. The corresponding calculated values of $a_a n_a$ were 0.112 and 0.107, assuming that a one-electron transfer process is the rate determining step [29].

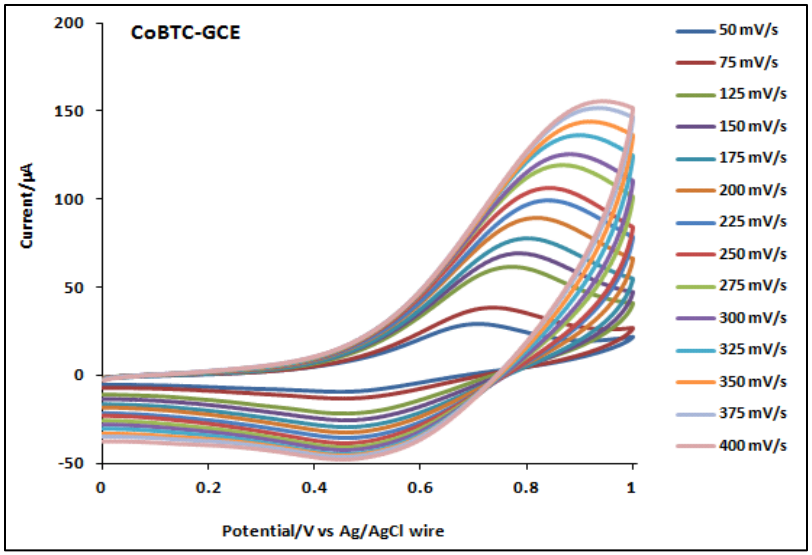

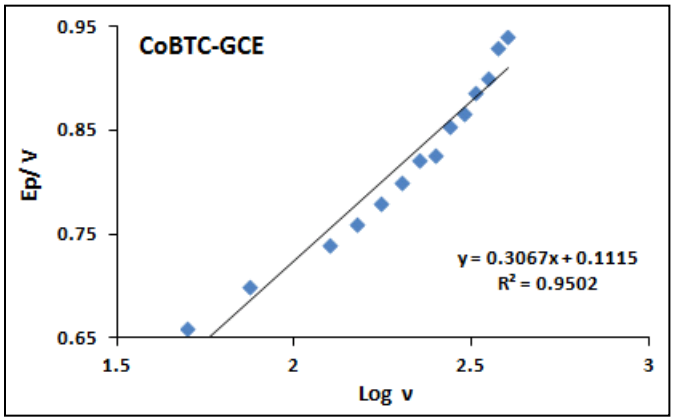

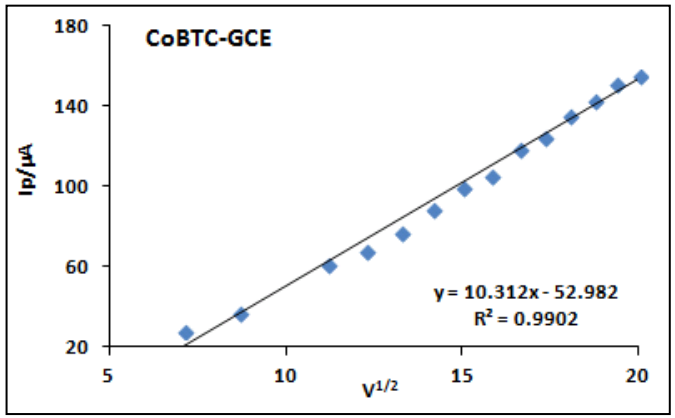

Figure 4. 11: Cyclic voltammograms of the detection of L-cysteine at different scan rates, their corresponding plots of oxidation Ep vs. log v and of oxidation Ip vs. $v^{1/2}$ in 10 mM L-cysteine and pH 4 buffer using the different electrodes (continued to the next page).

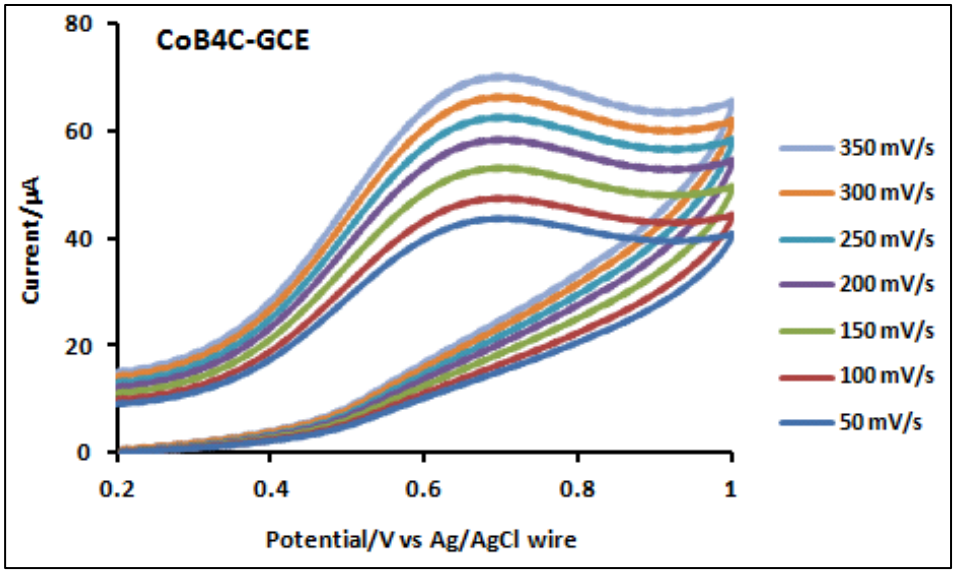
CoB4C-GCE
Current/µA
Potential/V vs Ag/AgCl wire
350 mV/s
300 mV/s
250 mV/s
200 mV/s
150 mV/s
100 mV/s
50 mV/s

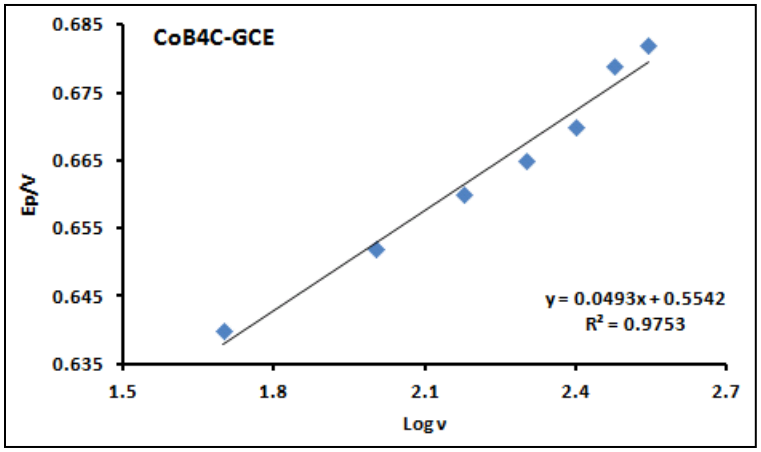
CoB4C-GCE
Ep/V
Log v
y = 0.0493x + 0.5542
R² = 0.9753

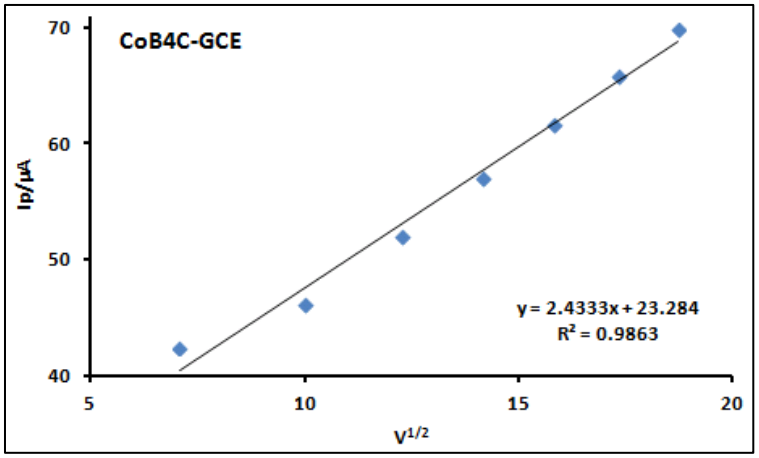
CoB4C-GCE
Ip/µA
V1/2
y = 2.4333x + 23.284
R² = 0.9863

4.5.4 Chronoamperometry

Due to the adsorption complications observed with the CoBTC-GCE, chronoamperometry was used to determine the nanoprobes sensitivity, rate constants and the detection limits for CoBTC-GCE. Chronoamperometry is a square wave pulsed voltammetric technique which generates high charging currents, which decay exponentially with time. This helps prevent fouling of the electrode by L-cysteine and its oxidation products, resulting in a good signal to noise ratio [43]. Within the first five seconds (on average), the catalytic current is dominated by electro oxidation of L-cysteine (Figure 4.12) before it reaches steady-state. The sensitivity of the probe was found from the calibration curves, which was 0.1159 $\mu A/\mu M$ (Figure 4.12) for CoBTC-GCE.

The rate constant was evaluated using Eq. (7) below;

$$\frac{I_{cat}}{I_{buf}} = \gamma^{\frac{1}{2}} \pi^{\frac{1}{2}} = \pi^{\frac{1}{2}} (k C_o t)^{\frac{1}{2}} \qquad (7)$$

where k is the catalytic rate constant, C_o is the bulk concentration of L-cysteine and t is time elapsed in seconds.

Figure 4.12 shows the plots of I_{cat}/I_{buf} vs $t^{1/2}$ (Eq. 7) for L-cysteine oxidation. The relationship between the slopes of these plots squared vs their corresponding concentrations was then used to calculate the rate constant and is represented by equation (8).

$$y = 0.049[\text{L-cysteine}](\frac{s^{-1}}{mM}) - 0.7023 s^{-1},\ R^2 = 0.9663 \qquad (8)$$

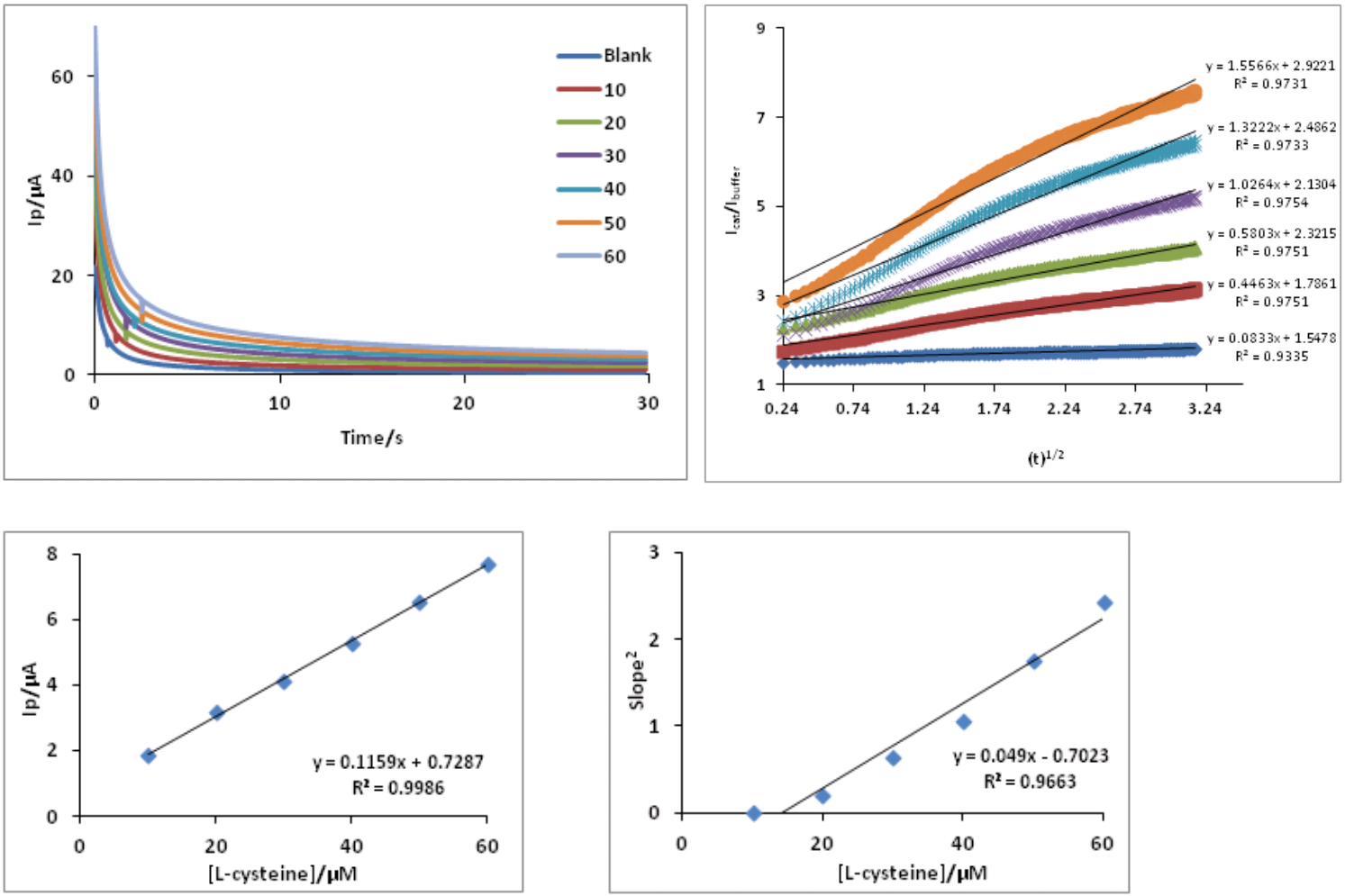

Figure 4. 12: Chronoamperograms, plots of I_{cat}/I_{buf} versus $t^{1/2}$, calibration curve and slope^2 vs [L-cysteine] (10 µM, 20 µM, 30 µM, 40 µM, 50 µM and at 60 µM) determined using chronoamperometry for the CoBTC-GCE.

The slope obtained from the latter plot is equal to πk where k is the rate constant. Using this relationship, the rate constant was found to be 1.56 x 10^4 M^{-1} s^{-1}. The electrocatalytic oxidation peak current of L-cysteine showed a linear dependence on the L-cysteine concentration obtained in the range 0 - 6.0 x 10^{-5} M. Using the 3δ notation ($3S_b/m$; where S_b is the standard deviation of the blank signal and m is the slope of the calibration graph), the limit of detection was found to be 3.92 x 10^{-6} M. This value is comparable to that of other electrodes in literature (Table 4.7).

4.5.5 Differential pulse voltammetry (DPV)

The normal Tafel value of CoB4C-GCE is indicative a better electrode surface that is more resistant to passivation. Due to this DPV was used to determine the nanoprobe sensitivity and the detection limits for CoB4C-GCE. DPV is a very sensitive technique which can be used with very small analyte concentrations [44]. It reduces the interferences due to non-faradaic processes. The electrode showed well resolved peaks in the concentration range 0-60 μM. The sensitivity of the probe was found from the calibration curve to be 0.720 μA/μM for CoB4C-GCE (Figure 4.13). This is comparable with other electrodes in literature (Table 4.7).

Kinetic data was generated by running multiple scans at a constant scanrate but with varying concentrations. It was observed that the peak current increases as concentration increases, showing the dependence of the oxidation rate, d[L-cysteine]/dt, on the bulk L-cysteine concentration. This suggests that the reaction

is pseudo first order with respect to L-cysteine [45]. The limit of detection was calculated using the 3σ notation and found to be 6.85 x 10^{-6}M for CoB4C-GCE.

Table 4. 7: Comparative LODs for electrochemical oxidation of L-cysteine using different catalytic systems.

Electrode	pH	LOD	Reference
CoBTC-GCE	4	3.92 x 10^{-6} M	This work
CoB4C-GCE	4	6.85 x 10^{-6} M	This work
Boron-doped CNT-GCE	7.4	2.6x10^{-7}M	[28]
Pt-CNT	7.4	3.0x10^{-7}	[33]
Ferrocenedicarboxylic acid-CPE	8	2.6X10^{-5}M	[46]

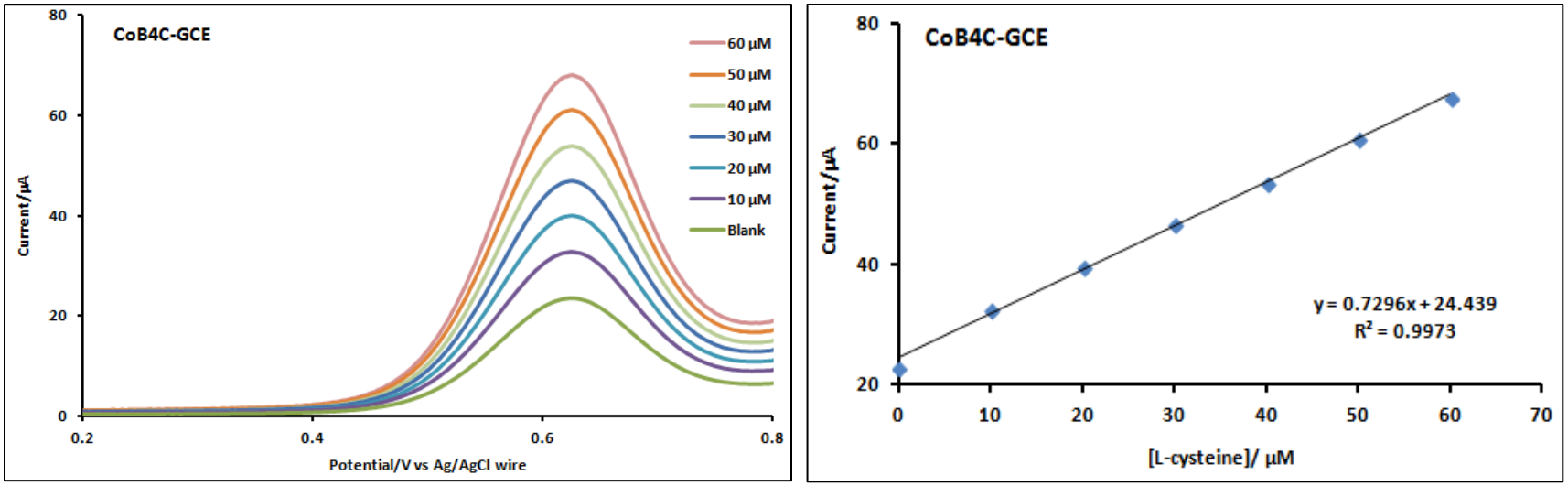

Figure 4. 13: Voltammograms and calibration curves determined using DPV for the CoB4C-GCE .

4.5.6 Electrochemical impedence spectroscopy (EIS)

EIS was employed to investigate the charge transfer resistance (R_{CT}) and electron transfer kinetics [47]. Typical R_{CT} values range from a few ohms for very fast reaction kinetics to greater than 10 Giga ohms for very slow reaction kinetics at the electrode surface. The Nyquist presentation shown in Figure 4.14A is a plot of the real component (Z") vs the imaginary component (Z'). Table 4.8 gives comparative R_{CT} values obtained from the Nyquist plot. The EIS parameters were obtained by fitting the Randles equivalent circuit (Figure 4.14C) to the experimental data and performing complex nonlinear least-squares procedures available in EIS data fitting computer programme. The model circuit has four elements; R_S (Solution resistance), C_P (Capacitor), Z_W (Warburg impedance) and R_{CT} (charge transfer resistor). Instead of R_{CT} some circuits have R_P, which is the polarization resistance and behaves like a resistor.

The R_{CT} values were determined to be 82.2 KΩ for the Bare-GCE, 51.2 KΩ for CoB4C-GCE and 41.8 KΩ for CoBTC-GCE. EIS data shows that there was a relatively large decrease in R_{CT} for the Co MOF-modified electrodes compared to the bare GCE, showing improved electron transfer rates and good conductivity [38,48] for the Co MOF modified electrodes. The electrodes R_{CT} values follow the order CoBTC-GCE < CoB4C-GCE showing that there is a slight decrease in conductivity with the CoB4C-GCE (Table 4.8).

When looking at the impedence Nyquist plot (Figure 4.14A), it is observed that the semicircular regions are relatively well defined for all electrodes. Due to this we

were able to approximate the R_{CT} values by extrapolating the diameters of the semicircles and obtaining the corresponding frequencies. If the chemical system is kinetically rather sluggish, it will show a large R_{CT} (> 10 GΩ), and may display only a very limited-frequency region where mass transfer is a significant factor [41].

Table 4. 8: Summary of R_{CT} (kΩ), n and K_{app} (cms^{-1}) values for the different surfaces in 10 mM L-cysteine, pH 4 buffer.

	R_{CT} (kΩ)	K_{app} (cms^{-1})
Bare GCE	82.6	3.22E-6
CoBTC-GCE	41.8	6.37E-6
CoB4C-GCE	51.2	5.11E-6

Our results show R_{CT} values that are small by comparison to the ohmic resistance and the Warburg impedance. This indicates that the catalytic reaction at the electrode surfaces is mass transfer or diffusion controlled as predicted earlier by results of the plot of Ip vs. $\nu^{1/2}$ (Figure 4.11) which is linear and confirms that the system is kinetically facile and mass transfer plays a major role [38].

A plot of phase-shift vs. log frequency (Figure 4.14B) provides extra information on frequency which cannot be obtained from the Nyquist plot. The phase angle values for all the electrode surfaces studied in this work are less than the ideal 90° for a true capacitor. Upon modification, all the surfaces' phase angles shifted towards lower frequencies indicating better catalytic efficiency.

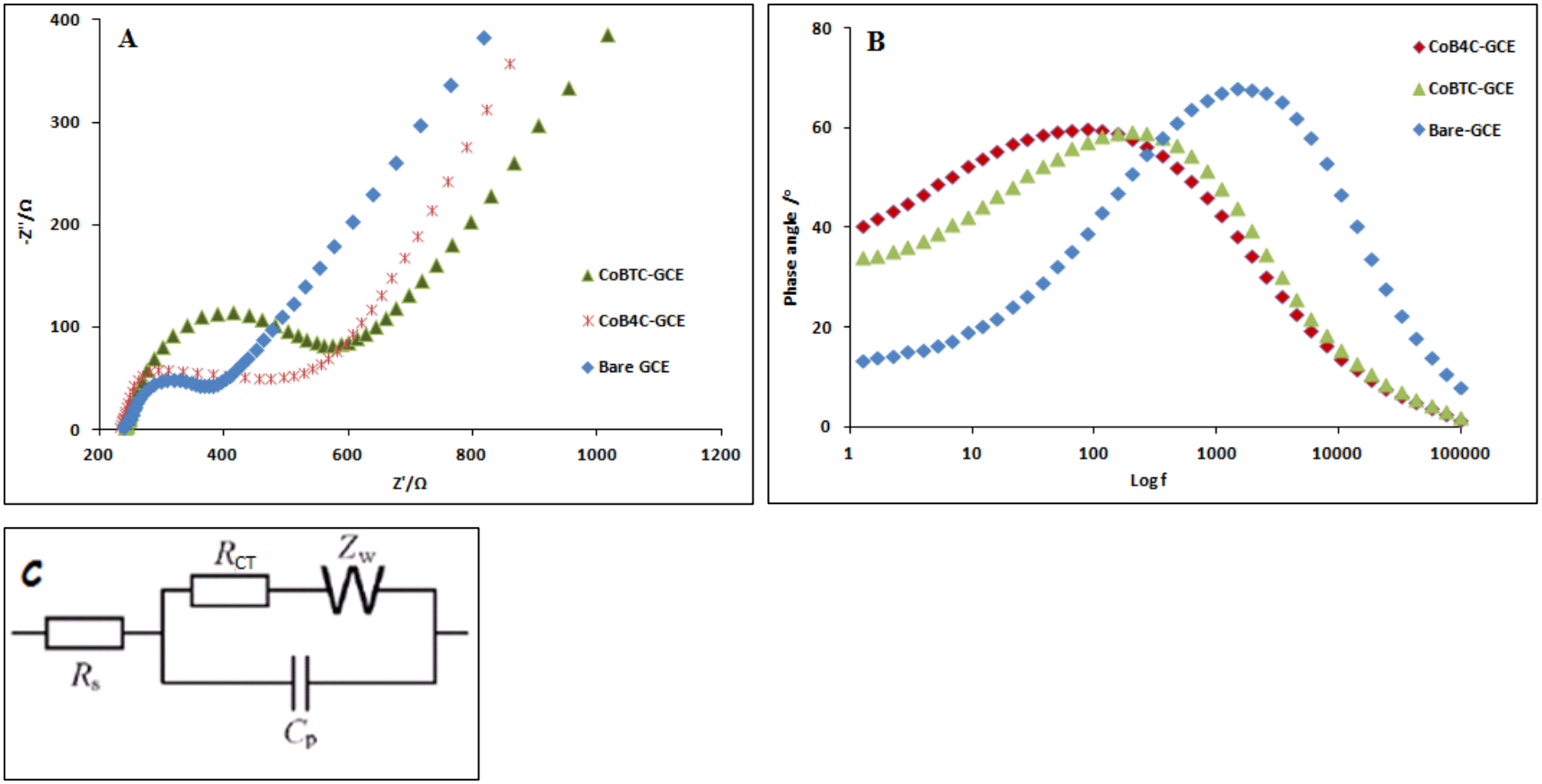

Figure 4. 14: Nyquist plots (A) and Bode plots (B) for the bare GCE and MOF-modified electrodes; as well as the circuit used to fit EIS parameters (C).

The CoBTC–GCE surface gave a lower phase angle of 58.76° compared to that of CoB4C-GCE (59.80°). The bare GCE had the highest phase angle of 67.80° showing that this surface had the lowest catalytic activity towards L-cysteine. Such changes in phase angles and frequencies are indicative of the structural differences of the surfaces, and that oxidation of the analyte occurred at the modified surfaces rather than on the bare GCE [38]. These results show that all modified surfaces have non-capacitative features and the surfaces were acting as conductors. This also serves to explain the differences in the catalytic activity observed from the other techniques explained in sections above.

The apparent electron transfer rate constants (k_{app}) were calculated, using Eq. (9) [49], for the different electrode surfaces towards oxidation of L-cysteine to cystine.

$$K_{app}=RT/F^2R_{CT}C \qquad (9)$$

where C = [L-cysteine] i.e. (1 mM) and with R, T and F taking their normal scientific meaning.

These K_{app} values are shown in Table 4.8. The sizes of these values (R_{CT} and K_{app}) for the modified electrodes compare well with those in literature [50,51]. By applying the Butler-Volmer equation [52] (Eq. 10) below, the exchange current densities were calculated. well with those in literature [42,43].

$$R_{CT}=\frac{RT}{nFi_o} \qquad (10)$$

where i_o is the exchange current densities and all the other values take their normal scientific meaning.

These were found to be 3.11 x 10^{-4}, 6.14 x 10^{-4} and 5.01 x 10^{-4} for the Bare-GCE, CoBTC-GCE and CoB4C-GCE respectively. The exchange current density is a reflection of the intrinsic rate of electron transfer (net current=0) between the analyte (L-cysteine) and the electrode surface, with a higher value indicating better electrocatalytic properties [41]. From the obtained results, the CoBTC-GCE is the best Nerstian sensor material.

4.6 Conclusions

A series of Co coordination compounds were synthesized using either H_3BTC or H_4B4C as ligands. Two of the products, CoBTC and CoB4C have been reported before in literature whilst the third, CoB4C-2 is new. Two compounds (CoBTC-GCE and CoB4C-GCE) were employed for the electrocatalytic detection of L-cysteine and gave good detection signals. CoBTC-GCE had the least non-capacitative surface (phase angle 58.8°), a higher resistance to electrode fouling and better LOD (3.92 x 10^{-6}), making it the better candidate for electrocatalytic detection of L-cysteine.

References

[1] J. Gu, M. Wen, X. Liang, Z. Shi, M. Kirillova, A. Kirillov, *Crystals* **2018**, *8*, 83.

[2] W. Lu, Z. Wei, Z. Y. Gu, T. F. Liu, J. Park, J. Park, J. Tian, M. Zhang, Q. Zhang, T. Gentle, et al., *Chem. Soc. Rev.* **2014**, *43*, 5561–5593.

[3] S. Kitagawa, R. Matsuda, *Coord. Chem. Rev.* **2007**, *251*, 2490–2509.

[4] S. Bureekaew, S. Shimomura, S. Kitagawa, *Sci. Technol. Adv. Mater.* **2008**, *9:1*, 12pp.

[5] P. Kumar, A. Deep, K.-H. Kim, *Trends Anal. Chem.* **2015**, *73*, 39–53.

[6] O. M. Yaghi, H. Li, T. L. Groy, *J. Am. Chem. Soc.* **1996**, *118*, 9096–9101.

[7] O. Fabelo, J. Pasan, L. Canadillas-Delgado, F. S. Delgado, A. Labrador, F. Lloret, M. Julve, C. Ruiz-Perez, *Cryst. Growth Des.* **2008**, *8*, 3984–3992.

[8] M. Camara, M. Tine, C. Daiguebonne, O. Guillou, T. Roisnel, *Acta Cryst.* **2014**, *E69*, m680–m681.

[9] C. Giacovazzo, *Fundamentals of Crystallography*, Oxford University Press, 2002, **2002**.

[10] D. E. Sands, *Introduction to Crystallography*, Dover Publications, **2012**.

[11] V. Stavila, I. Bulimestru, A. Gulea, A. C. Colson, K. H. Whitmire, *Acta Crystallogr. Sect. C Cryst. Struct. Commun.* **2011**, *67*, DOI 10.1107/S0108270110053497.

[12] J. Y. Zou, W. Shi, J. Y. Zhang, Y. F. He, H. L. Gao, J. Z. Cui, P. Cheng, *CrystEngComm* **2014**, *16*, 7133–7140.

[13] D. Ward, D. C. Luehrs, *Acta Cryst.* **1983**, *C39*, 1370–1372.

[14] G. Mehlana, S. A. Bourne, G. Ramon, *CrystEngComm* **2014**, *16*, 8160.

[15] B. H. Stuart, in *Infrared Spectrosc. Fundam. Appl.* (Ed.: D.J. Ando), **2004**, pp. 15–45.

[16] K. Nakamoto, in *Infrared Raman Spectra Inorg. Coord. Compd.*, John Wiley & Sons, Inc., **2008**, pp. 1–273.

[17] A. Karmakar, C. L. Oliver, *Z.Kristallogr.* **2013**, *288*, 330–334.

[18] A. Majumder, V. Gramlich, G. M. Rosair, S. R. Batten, J. D. Masuda, M. S. El Fallah, J. Ribas, J.-P. Sutter, C. Desplanches, S. Mitra, *Cryst. Growth Des.* **2006**, *6*, 2355–2368.

[19] C.-L. Ming, Y.-N. Zhao, B.-Y. Yu, K. Van Hecke, G.-H. Cui, *Bull. Korean Chem. Soc* **2014**, *35*, 3349–3352.

[20] S. Kundu, M. D. Mukadam, S. M. Yusuf, M. Jayachandran, *CrystEngComm* **2013**, *15*, 482–497.

[21] D. Danset, L. Manceron, *Phys. Chem. Chem. Phys.* **2005**, *7*, 583–591.

[22] K. Ghasemi, A. R. Rezvani, A. Shokrollahi, R. Mendoza-Meron, A. Moghimi, S. Gavahi, S. Garcia-Granda, *Comptes Rendus Chim.* **2014**, *17*, 1221–1229.

[23] Y.-G. Li, N. Hao, E.-B. Wang, Y. Lu, C.-W. Hu, L. Xu, *Eur. J. Inorg. Chem.* **2003**, *3*, 2567–2571.

[24] P. Song, B. Liu, Y. Li, J. Yang, Z. Wang, X. Li, *CrystEngComm* **2012**, *14*, 2296–2301.

[25] S. Vairam, S. Govindarajan, *Thermochim. Acta* **2004**, *414*, 263–270.

[26] E. Lamprecht, G. M. Watkins, M. E. Brown, *Thermochim. Acta* **2006**, *446*, 91–100.

[27] B. Yuan, J. Zhang, R. Zhang, H. Shi, X. Guo, Y. Guo, X. Guo, S. Cai, D. Zhang, *Int. J. Electrochem. Sci* **2015**, *10*, 4899–4910.

[28] C. Deng, J. Chen, X. Chen, M. Wang, Z. Nie, S. Yao, *Electrochim. Acta* **2009**, *54*, 3298–3302.

[29] J. Raoof, R. Ojani, Z. Mohammadpour, *Int. J. Electrochem. Sci.* **2010**, *5*, 177–188.

[30] M. Shumba, T. Nyokong, *Electrochim. Acta* **2016**, *196*, 457–469.

[31] Y. Wang, H. Ge, G. Ye, H. Chen, X. Hu, *J. Mater. Chem. B* **2015**, *3*, 3747–3753.

[32] H. Hosseini, H. Ahmar, A. Dehghani, A. Bagheri, A. Tadjarodi, A. Reza, *Biosens. Bioelectron.* **2013**, *42*, 426–429.

[33] S. Fei, J. Chen, S. Yao, G. Deng, D. He, Y. Kuang, *Anal. Biochem.* **2005**, *339*, 29–35.

[34] R. Shanmugam, P. Barathi, J.-M. Zen, A. K. Senthil, *Electrochim. Acta* **2016**, *187*, 34–45.

[35] C. Xiao, J. Chen, B. Liu, X. Chu, L. Wu, S. Yao, *Phys. Chem. Chem. Phys* **2011**, *13*, 1568–1574.

[36] K. F. Babu, M. A. Kulandainathan, I. Katsounaros, L. Rassaei, A. D. Burrows, P. R. Raithby, F. Marken, *Electrochem. Commun.* **2010**, *12*, 632–635.

[37] L. Yang, S. Kinoshita, T. Yamada, S. Kanda, H. Kitagawa, M. Tokunaga, T. Ishimoto, T. Ogura, R. Nagumo, A. Miyamoto, et al., *Angew. Chem. Int. Ed* **2010**, *49*, 5348–5351.

[38] S. Nyoni, T. Mugadza, T. Nyokong, *Electrochim. Acta* **2014**, *128*, 32–40.

[39] M. Mazloum-Ardakani, H. Rajabi, H. Beitollahi, B. Bi, F. Mirjalili, A. Akbari, N. Taghavinia, *Int. J. Electrochem. Sci* **2010**, *5*, 147–157.

[40] C. Gabrielli, F. Huet, M. Keddam, *J. Chem. Phys.* **1993**, *99*, 7232–7239.

[41] A. J. Bard, L. R. Faulkner, *Eectrochemical Methods; Fundamentals and Applications*, John Wiley & Sons, Inc., New York, **2001**.

[42] P. Zanello, *Inorganic Electrochemistry Theory,Practice and Application*, **2003**.

[43] P. N. Jiang, *Electroanalytical Chemistry Research Developments*, Nova Science Publishers, New York, New York, **2007**.

[44] C. T. P. da Silva, F. R. Veregue, L. W. Aguiar, J. G. Meneguin, M. P. Moises, S. L. Favaro, E. Radovanovic, E. M. Girotto, A. W. Rinaldi, *New J. Chem.* **2016**, *40*, 8872–8877.

[45] I. Ali, S. Omanovic, *Int. J. Electrochem. Sci.* **2013**, *8*, 4283–4304.

[46] J. B. Raoof, R. Ojani, H. Beitollahi, *Electroanalysis* **2007**, *19*, 1822–1830.

[47] S. P. J. Higson, *Biosensors for Medical Applications*, **2012**.

[48] Y.-R. Kim, B. Sungyool, K. M. Rakesh, K. Hasuck, *Biosens. Bioelectron.* **2010**, *25*, 2366–2369.

[49] R. K. Mendes, R. S. Freire, C. P. Fonseca, S. Neves, L. T. Kubota, *J. Braz. Chem. Soc.* **2004**, *15*, 849–855.

[50] E. Sabatani, I. Rubinstein, R. Maoz, J. Sagiv, *J. Electroanal. Chem.* **1987**, *219*, 365–371.

[51] D. Nkosi, J. Pillay, K. I. Ozoemena, K. Nouneh, M. Oyama, *Phys. Chem. Chem. Phys.* **2010**, *12*, 604–13.

[52] W. Dreyer, C. Guhlke, R. Müller, *Phys. Chem. Chem. Phys.* **2016**, *18*, 24966–24983.

Chapter Five

In this chapter two structures were assembled from either Co(II) ions or Cu(II) ions with 2,6-pyridinedicarboxylic acid. The synthetic procedures are described. The synthesized products were characterized using SC-XRD, FTIR, TGA and DSC. Their potential as electrocatalysts in oxidative detection of L-cysteine was then investigated using various electrochemical techniques.

5. Compounds of Co,Cu and 2,6-pydc

This chapter describes the attempted synthesis of two structures from either Co(II) ions or Cu(II) ions with 2,6-pyridinedicarboxylic acid as the ligand. The reaction with Co(II) yielded a MOF whereas that with Cu(II) produced a complex. The synthetic procedures and characterization techniques (SC-XRD, FTIR, TGA and DSC) are described. Their potential as electrocatalysts in oxidative detection of L-cysteine was then investigated using various electrochemical techniques.

5.1 Synthesis

5.1.1 Synthesis of Co2,6Py

0.6 g (2,5 mmols) of cobalt chloride hexahydrate was dissolved in 10 mL of distilled water. A mass of 0.4 g (2,42 mmols) of 2, 6-pyridinedicarboxylate was dissolved in 10 mL of pyridine in a separate beaker. The two solutions were combined with stirring and the resulting solution was kept at room temperature for about 2 weeks at which time purple rhombic crystals (herein referred to as Co2,6Py) were obtained. (Yield: 1.26 g, 74% based on Co). $CoH_{20}C_{26}O_{13}N_4$ (Mr. 655.39)

5.1.2 Synthesis of CuPy (Attempted synthesis of Cu2,6Py)

About 0.8 g (0.97 mmols) of copper chloride hexahydrate was dissolved in 10 mL of distilled water. A mass of 0.4 g of 2, 6-pyridinedicarboxylate was dissolved in 10 mL of pyridine in a separate beaker. The two solutions were combined with stirring and the resulting solution was kept at room temperature for about 2 weeks at which time blue needle-like crystals (herein referred to as CuPy) were obtained. (Yield: 0.75 g, 78% based on Cu) $C_{10}H_{10}Cl_2CuN_2$ (Mr. 292.65).

5.2 SC-XRD and microanalysis

5.2.1 SC-XRD for Co2,6Py

Co2,6Py is a new cobalt MOF, pyridinium 2,6-pyridinehydrogendicarboxylato2,6-pyridinedicarboxylatocobaltate(ll)·2,6-pyridinedicarboxylic acid·1 water, which was formed by the self assembly of cobalt(ll) ions and 2,6-pyridinedicarboxylic acid. Single crystal X-ray diffraction revealed that the compound crystallizes in the triclinic space group P-1 (number 2). The coordination environment of the compound is depicted in Figure 5.1. The asymmetric unit contains 1 cobalt cation coordinated to one hydrogen2,6-pyridinedicarboxylato ion and one 2,6-pyridinedicarboxylate ion via the nitrogen and oxygen molecules, as well as containing one free dihydrogen2,6-pyridinedicarboxylate molecule and one free pyridinium ion, both interacting with the cobalt complex through hydrogen bonding to its ligands. Each cobalt centre is bound to two ligands; two Co-N (from the heterocyclic ring) bonds occupy axial positions and four Co-O (from the carboxylate groups) bonds occupy the equatorial positions. The coordinated 2,6-pyridinedicarboxylate units exhibit two bonding modes (through the carboxylate groups) as shown in Scheme 5.1. The corresponding bond lengths are in the range 2.1094(10) Å – 2.1500(10) Å for Co-O and 2.0321 Å – 2,0342 Å for the Co-N bond (Appendix C1, Table S5).

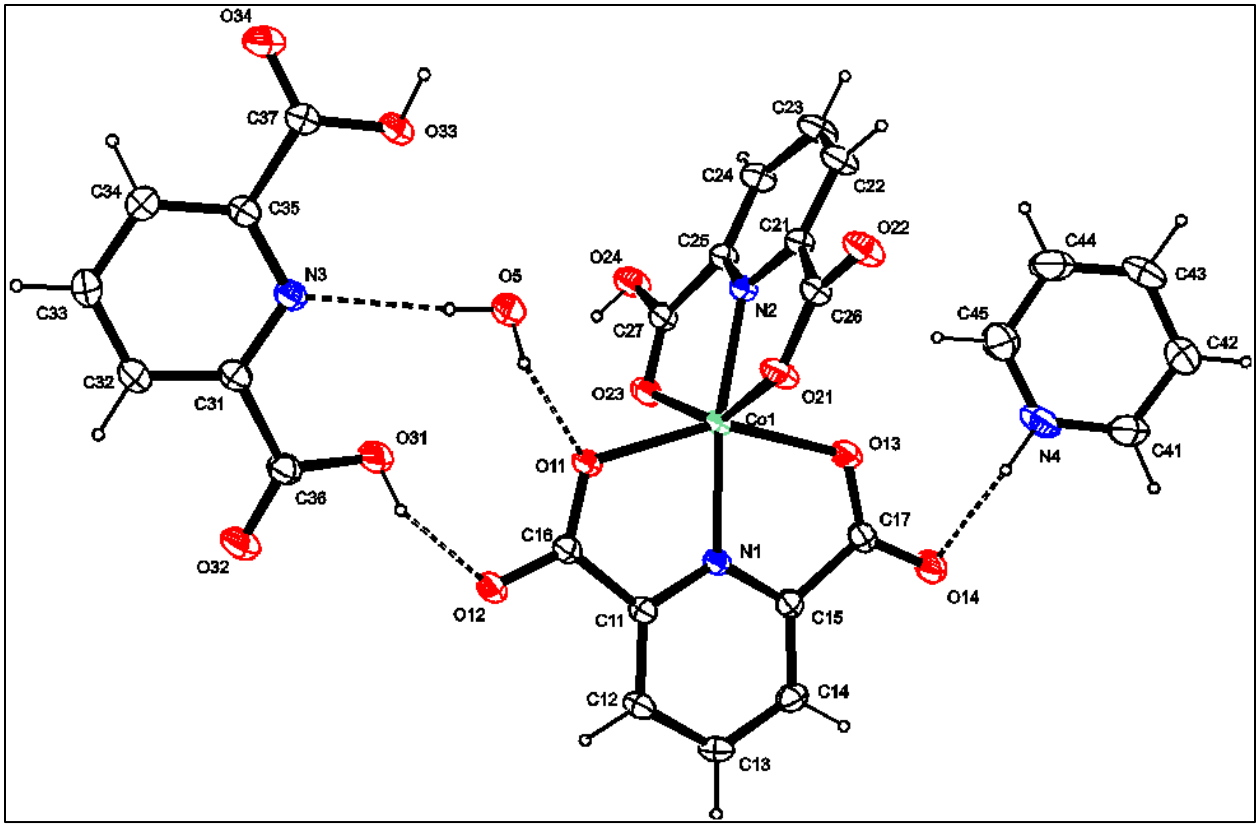

Figure 5. 1: Coordination environment of the Co(II) centre with atomic labels for Co2,6Py.

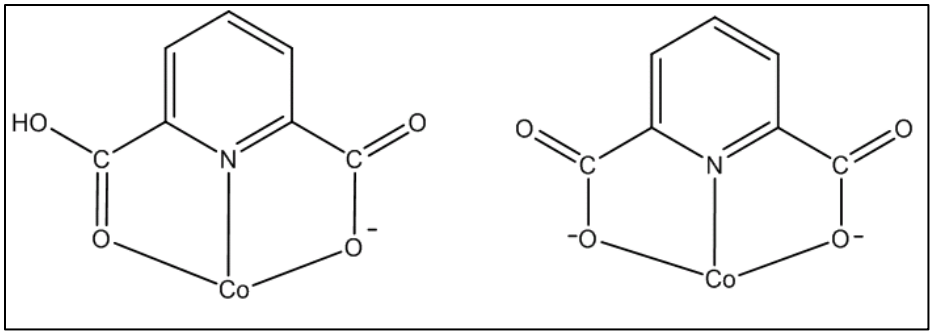

Scheme 5. 1: Coordination bonding modes of the 2,6-pyridinedicarboxylate moieties in Co2,6Py.

The O-Co-O coordination angles are around 152° and 93-95° for the equatorial and axial oxygens respectively. All O-Co-N coordination angles are axial-equatorial and range from 75.84(4)° to 119.46(4)°. The two N are coordinated to the metal by a coordination angle of 161.67(4)°. Full crystallographic data is given in Table S6 of the Appendix C1. The overall structure of a cobalt centre is a distorted octahedron.

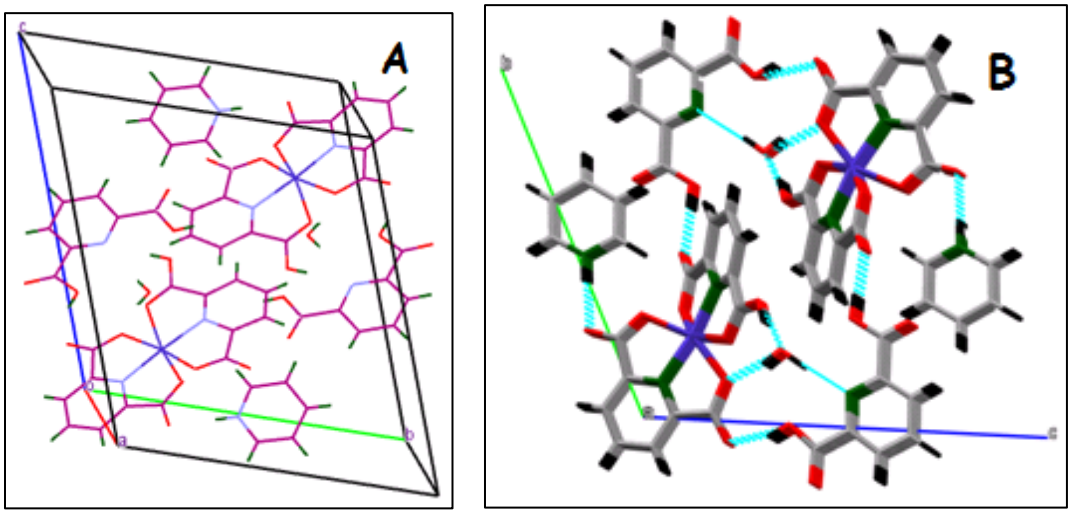

Figure 5. 2: Packing in Co2,6Py (A) and when repeat unit is viewed along a-axis (B). Interchain H-bonding is depicted by dashed lines.

The packing diagram depicts two molecules of Co2,6Py associated with two molecules of 2,6 pyridinedicarboxylic acid, two pyridinium ions and two water molecules per unit cell (Figure 5.2 A). The repeat unit forms 1D chains by laying the aromatic ring of one unit under the next, forming doubly stacked chains (Figure 5.2 B). The 2 rings of the ligands are held together by π---π stacking interactions. These chains are then held together by hydrogen bonding (N—H and O—H) of adjacent units. Such behaviour has been exhibited by other supramolecular structures [1,2].

The inter-chain space between adjacent chains is occupied by pyridinium ions and 2,6-pyridinedicarboxylic acid, which are themselves held by hydrogen bonding and π---π stacking. The various interactions result in lattice stabilization [2] despite the absence of coordination bonds. The structure of Co2,6Py is very similar to that previously reported for $[OPDH]_2[Co(dipic)_2]\cdot H_2O$ in that both Co centres are bound to 2,6-pyridinedicarboxylic acid ions in a tridentate manner [3]. However, in $[OPDH]_2[Co(dipic)_2]\cdot H_2O$, both 2,6-pyridinedicarboxylate ligands are fully deprotonated whilst in Co2,6Py, only one ligand is fully deprotonated. The presence of the proton in Co2,6Py (Co_1-O_{23}) results in a slight reduction in bond strength evidenced by the higher contact distance of 2.3130 (10) Å whilst the other Co_1-O bond distances are in the range 2.1094(10) - 2.1500(10) Å (Appendix C1, Table S5 and S8).

Table 5. 1: Crystallographic data for Compound Co2,6Py.

Empirical formula	$CoH_{20}C_{26}O_{13}N_4$
Formula weight	655.39
Crystal system	Triclinic
Space group	P-1 (No. 2)
a /(Å)	7.1103(2)
b/ (Å)	13.8259(4)
c /(Å]	14.7599(5)
V /($Å^3$)	1289.65(7)
Alpha	114.034(1)
Beta	93.170(2)
Gamma	100.454(1)
Z	2
D(calc) [g/cm^3]	1.688
μ (mm^{-1})	0.748
F(000)	670
Crystal Size [mm]	0.28 x 0.40 x 0.50
R(int)	0.017
Observed Data [I > 2.0 sigma(I)]	5922
R, wR2,	0.0259, 0.0703
S	1.03
Number of distance and angle restraints	3
Number of least-squares restraints	3
Number of unrefined Donor-H atoms	3
Min. and Max. Resd. Dens. (e/ $Å^{-3}$)	-0.38, 0.40

When searching the Cambridge Structural Database (version 5.35, May 2014), several structures with the similar compound were found.

Albeit not exactly the same structure as the one reported here, there are five papers that present similar dipicolinic acid coordination compounds with Co(II). In all the cases the Co-O distances are similar to the complex reported here (Table 5.2). $(C_6H_9N_2)[Co(C_7H_3NO_4)(C_7H_4NO_4)]\cdot C_7H_5NO_4\cdot 3H_2O$ (WABPOG) is the most similar with the single difference being the existence of a phenylhydrazinium cation [4], where as we report a pyridinium cation. The other four structures are different in terms of coordination (bridged bis-dipicolinic acid [5] ; tris-dipicolinic acid [6]) and in exhibiting either diprotonation [7] or the lack of protonation [5,7,8] of the 2,6-pyridine dicarboxylic acid ligand around the Co centre, as well as in the nature of the guest moieties [5–8]. Full SC-XRD (ga081) data is given in Appendix C1.

Table 5. 2: Comparison of Co-O bond distances.

Structure	Co-O bond distance /Å	Reference
AWORIO	2.1363 - 2.2037(8)	[5]
BODJEL	2.1040(13) - 2.2270(13)	[6]
TEHFIX	2.1260(13) - 2.1970(14)	[8]
UGORIR	2.1080(2) - 2.2220(3)	[7]
WABPOG	2.0900(2) - 2.2810(2)	[4]
Co2,6Py	2.1094(10) – 2.3130(10)	This work

The microanalysis showed a close agreement between the observed and theoretical results (Table 5.3).

Table 5. 3: Microanalysis for Co2,6Py: $CoH_{20}C_{26}O_{13}N_4$.

Element	Expected	Observed	Difference	% Error
Carbon	47.65	48.04	+0.39	0.818
Hydrogen	3.07	2.88	-0.19	6.189
Nitrogen	8.55	8.55	0	0

5.2.2 SC-XRD for CuPy

Single crystal X-ray diffraction revealed that the compound crystallizes in the monoclinic space group P-21/n (number 14). The coordination environment of the compound is depicted in Figure 5.3. The asymmetric unit contains one copper cation coordinated to one pyridine unit and one chloride ion. Each Cu centre unit is coordinated to two pyridine ligands via the nitrogen groups and two chloride ions. Each pyridine molecule allows for monodentate bonding. The Cu-N bonds occupy the equatorial positions whilst the axial positions are occupied by Cu-Cl bonds.

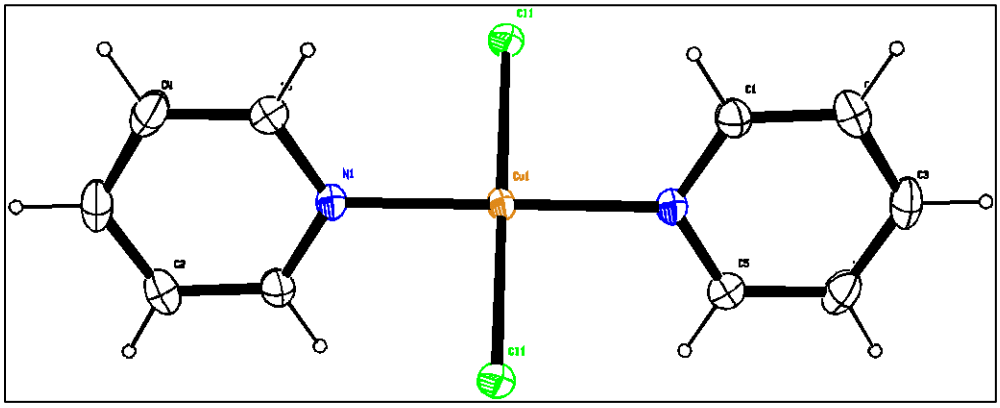

Figure 5. 3: Coordination environment of CuPy.

The observed bond distances for Cu-N and Cu-Cl were 2.0091(11) Å and 2.3024(3) Å respectively. The Cl-Cu-Cl and N-Cu-N bond angles are 180 ° whilst the Cl-Cu-N bond angles are in the range 89.56(3) ° – 120.05(9) °. Full SC-XRD data (ga085) is given in appendix C2. Several similar structures have been reported with the main variation being the coordination around the metal node. Most compounds are six coordinate around the copper centre[9–11] whilst in this work, it is displays a square planer coordination, a feature often found when the ligand is a pyridine derivative [12] or larger halides like iodine are coordinated [13].

When pyridine is used as a solvent with $CuCl_2$, various products with the general formula $CuCl_2(py)_n$ can result. An interesting example of this is Czugler *et al* 's[9] bis(pyridinium)tetrachlorocuprate(ll) complexes. Cu and Cl formed discrete $CuCl_4^{2-}$ polyhedral with isolated pyridinium cations. The Cl-Cu-Cl bond angles ranged between 97.83(2) and 132.05(2)°, showing a geometry intermediate between square planar and tetrahedral coordination due to steric hinderance from the pyridinium ions. The Cu-Cl bond lengths were 2.233(1) and 2.251(1) Å which is shorter than for most complexes. When 2 chlorides are replaced with 2 pyridine ligands as is the case with $CuCl_2(py)_2$, the geometry becomes an almost perfect square planar molecule as is shown by our CuPy. The Cu-Cl bond lengths become slightly larger (2.2 vs 2.3 Å) possibly due to interactions with the bulky, strongly bound pyridine moieties (Cu-N bond length 2.0 Å).

$CuCl_2(py)_2$ was first reported by Kabalkina [14] in 1956. Meervelt [15] made and refined the crystal structure of the same complex (Table 5.4).

Table 5. 4: Comparison of SC-XRD data for $CuCl_x(py)_y$ complexes.

Formula	$C_{10}H_{10}Cl_2CuN_2$ (CuPy)	$C_{10}H_{10}Cl_2CuN_2$ [16]	$(C_5H_5NH)_2[CuCl_4]$[10]
Formula weight	292.65	292.65	365.57
Crystal system	Monoclinic		Monoclinic
Space group	P21/n (number 14)	P21/n (number 14)	C2/c (number 15)
a/Å	3.8160(1)	3.7911(2)	7.980(1)
b/Å	8.5281(3)	8.5205(3)	13.818(1)
c/Å	16.9743(6)	16.9910(7)	13.523(1)
V/Å^3	552.08(3)	548.5	1485.9(2)
Alpha/°	90	-	-
Beta/°	91.948	91.973(3)	94.81(1)
Gamma/°	90	-	-
Z	2	2	4
D(calc) [g/cm^3]	1.760	-	1.634
μ (MoKa) [mm^{-1}]	2.426	70 cm^{-1}	2.2
F(000)	294	-	-
Crystal size [mm]	0.24 x 0.34 x 0.34	0.10 x 0.10 x 0.30	0.25 x 0.30 x 0.40
Rint	0.015	-	0.023
Observed data [1>2.0 sigma(I)]	1312	1010	1725
R, wR2	0.0169; 0.0457	0.033; 0.086	0.0385; 0.1018
S	1.12	-	0.93
Min and Max Resd	-0.28	-	-0.47
Density (e/Å^{-3})	0.32	-	0.71

A six coordinate geometry around the Cu centre is often observed in systems where water occupies the axial positions. Based on its wide reporting in literature [15,16], extensive characterization was not pursued and microanalysis and SC-XRD were deemed sufficient confirmation.

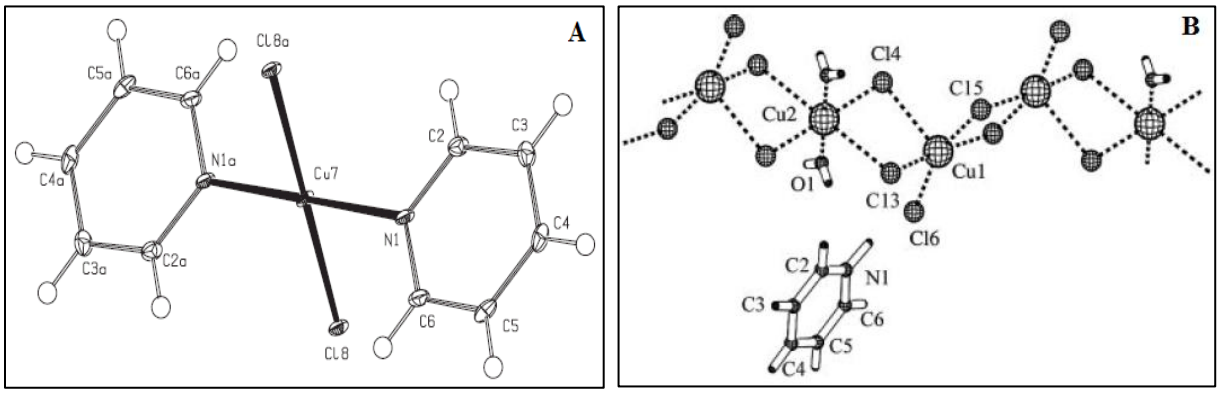

Figure 5. 4: Illustrations of $CuCl_x(py)_y$ complexes made by Meervelt (A) and Czugler (B).

The microanalysis showed a close agreement between the observed and theoretical results (Table 5.5).

Table 5. 5: Microanalysis for CuPy: $CuH_{10}C_{10}Cl_2N_2$

Element	Expected	Observed	Difference	% Error
Carbon	41.04	40.94	-0.10	0.24
Hydrogen	3.44	3.68	+0.24	6.97
Nitrogen	9.57	9.45	-0.12	1.25

5.3. FTIR Spectra

The IR spectrum of compound Co2,6Py (Figure 5.5A) displays a broad water band centered at around 3375cm^{-1}. A sharp secondary amine N-H stretch is also visible in both Co2,6Py (3100 cm^{-1}) and the free ligand (3064 cm^{-1}) possibly due to protonation of the uncoordinated pyridinium ion in the former, and strong hydrogen bonding in the latter, as is seen in the crystal structure. Such behaviour has been observed in other pyridinium salts and the frequency, intensity and sharpness are attributed the strength of nitrogen-hydrogen interactions and their environment [17]. Co2,6Py also displays very sharp bands in the region 1717 to 1428 cm^{-1} which is characteristic of CO symmetric and asymmetric stretches of aromatic carboxylates [2].

It's important to note that comparing these bands with those in 2,6-pyridinedicarboxylic acid, the asymmetric carboxyl stretch shows both a shift to lower and a shift to higher wavenumbers reflecting differing coordination environments; the higher shift (1698 to 1717 cm^{-1}) suggests coordination occurred with an increase in bond strength and that the carboxylic bond strength is the result of the anionic form of the ligand, rather than suggesting back bonding by the metal into the C=O antibonding orbital. The symmetric stretches display similar behavior, with strong bands at 1387 cm^{-1}, which is characteristic of pyridine-2,6-dicarboxylate complexes [3]. The value of $\Delta[V_{as}-V_{sym}]$ is much larger than that in pyridine-2,6-dicarboxylic acid, suggesting monochelation of the carboxyl group to the metal [2,3]. The region from 1370 to 1000 cm^{-1} is characterized by multiple sharp bands which are representative of N-C ring

stretches and the higher C-H in plane bends [18] as well as in-plane hydrogen-deformations of pyridinium ions [17]. The region from 730-770 cm^{-1} displays the lower sp^2 C-H bends of the aromatic in plane and out of plane vibrations. These are present in both the ligand and Co2,6Py.

Similar bands have been observed in other pyridinium ions and N heterocyclic rings [2,3]. Ghasemi *et al* [3] previously assigned the metal ligand vibrations as follows: 585 cm^{-1} and 522 cm^{-1} (vCo–O), 453 cm^{-1}, 434 cm^{-1}, and 420 cm^{-1} (vCo–N). The spectrum of Co2,6Py exhibits all but the band at 453 cm^{-1}. Given that vCo–N for octahedral complexes involving the pyridine nitrogen lie below 250 cm^{-1} [19,20], and given the presence of internal ligand vibrations within this region (Figure 5.5B), the following assignments were made; 601 cm^{-1} pyridine ring in-plane vibration (mode 6a); 588 cm^{-1} v_a(Co–O); 526 cm^{-1} δO=C–O (in-plane) vibration; 434 cm^{-1} v_s(Co–O); 420 cm^{-1} pyridine ring out-of-plane vibration (mode 16b). The vCo–N lie below 250 cm^{-1}.

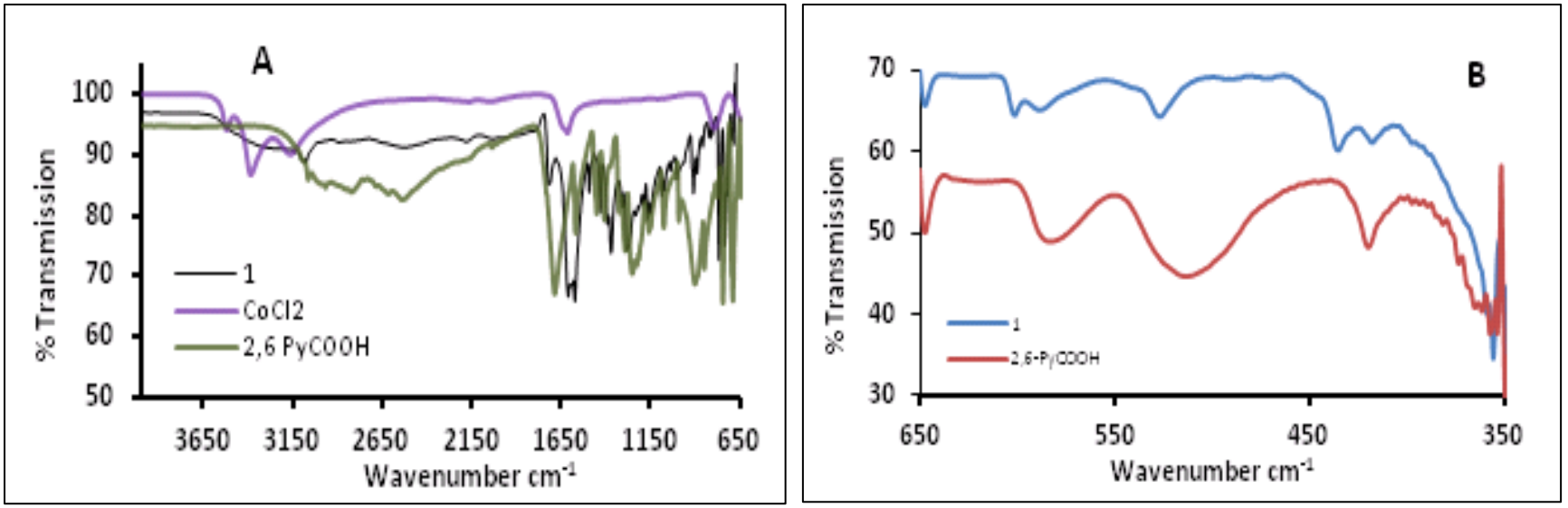

Figure 5. 5: Mid IR spectra of compound Co2,6Py and starting materials (A) with ATR attachment and (B) as nujol mulls on KBR discs.

5.4 Thermal Analysis

The thermal behaviour of Co2,6Py was investigated by use of TGA and DSC. The TGA curve shows a multistep decomposition (Figure 5.6). The first weight loss (calculated 2.75 weight %) occurs in a two step loss (DSC-1 and -2) between 60 and 120 °C (TGA-1), and is due to the loss of uncoordinated water. The second weight loss (56 weight %) is attributed to partial breakdown of the framework due to the loss of the pyridine solvate (calculated 12.1 weight %), the loss of the 2,6-pyridinedicarboxylate solvate (calculated weight 21.8%) and the loss of one 2,6-pyridine dicarboxylate ligand (calculated 21.8 weight %) (TGA-2). This occurs in three interconnected steps between 170 and 290 °C (DSC-3, -4 and -5). The last decomposition (32 weight %) occurs between 430 and 600 °C and is due to the decomposition of the last 2,6-pyridinedicarboxylate (TGA-3). The high temperatures result in formation of Co oxides (TGA-4). The final weight at 900 °C is approximately 9.4 % suggesting the predominance of Co_3O_4 (calculated weight 9.2%).

The DSC thermogram shows five exothermic peaks (Figure 5.6 insert). The first peak (74 °C) corresponds to desolvation and starts at the same temperature as shown in the TGA. After loss of ½ water, a phase change occurs in the crystal resulting in the remaining water being lost from a different environment, shown by the second exothermic peak (96 °C). The third and fourth peaks (198 and 224 °C) signify the loss of the pyridine and the pyridinedicarboxylic acid solvates respectively. The last exothermic peak (253 °C) represents the loss of one of the ligands.

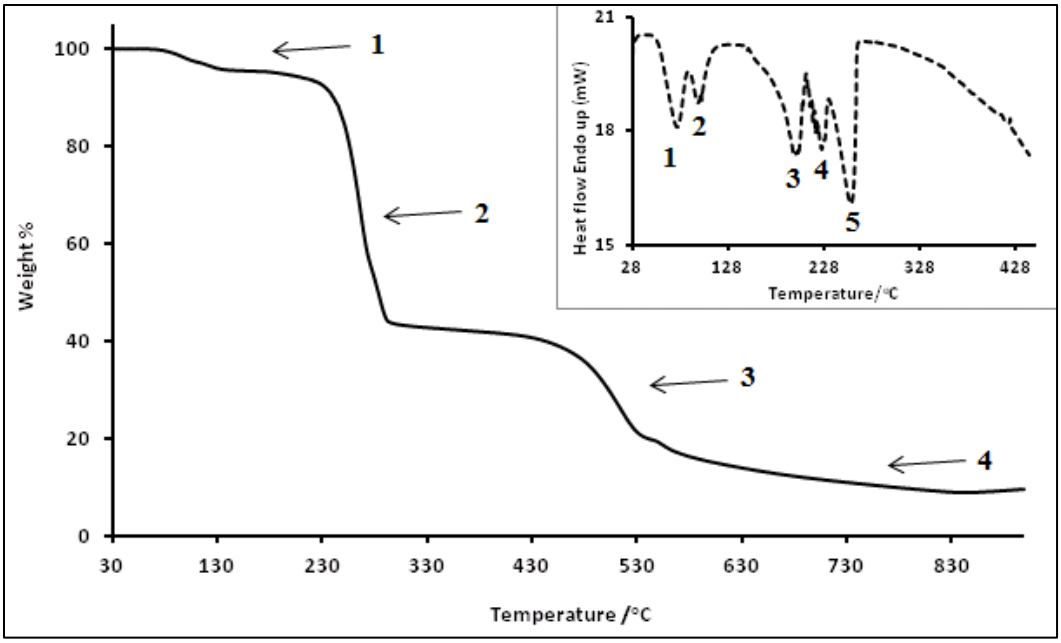

Figure 5. 6: TGA and DSC (insert) thermograms for the Co2,6Py MOF.

5.5 Electrochemical characterization of modified electrodes

Electrochemical characterization of the synthesized MOF and complex was done so as to determine their electrochemical properties and determine the effects if any of the different structures. Both Co2,6Py and CuPy were used to modify a GCE with the aim of determining their properties. The aim was to investigate their potential as electrochemical sensors for electrocatalysis of L-cysteine. A glassy carbon electrode was modified with 2 mg/mL of either Co2,6Py or CuPy in DMF using the dip-dry method and the electrodes named Co2,6Py-GCE and CuPy-GCE respectively. These electrodes were then characterized using cyclic voltammetry so as to evaluate their electrochemical behaviour. Specific details are reported in the following sections

5.5.1 Cyclic Voltammetry

Figure 5.7A shows cyclic voltammograms for the electrodes in 1 mM $Fe(CN)_6^{3-/4-}$ in 0.1 M KCl over the range -0.3 to 0.5 V. The peak potential separation (ΔE_p) for a reversible system such as $Fe(CN)_6^{3-/4-}$ is a good measure of the electron transfer ability of the electrode with lower values depicting a good electron transfer ability. All electrodes showed good electron transfer ability (Table 5.6), though modification seems to slightly reduce this ability. The surface roughness factor for the modified electrodes was determined by using $[Fe(CN)_6]^{3-/4-}$ redox system and applying the Equation (1) [21] for reversible systems:

$$I_p=2.69x10^5n^{3/2}ACD^{1/2}v^{1/2} \quad (1)$$

where I_p, n, A, C, D and v are the peak current, the number of electrons involved, the electrode surface area, the concentration of $[Fe(CN)_6]^{3-/4-}$, the diffusion coefficient of $[Fe(CN)_6]^{3-/4-}$, and the scan rate, respectively.

From the D value for $K_3[Fe(CN)_6]$ = 7.6 x 10^{-6} cm^2 s^{-1} and n = 1, the surface roughness factor (ratio of I_{pa} experimental/I_{pa} theoretical; shown in Table 5.6) and the corresponding effective electrode area {roughness factor x theoretical surface area (0.071 cm^2)} were determined and used for the calculation of surface coverage, Eq. (2) [21].

$$\Gamma=\frac{Q}{nFA} \quad (2)$$

where: Γ is the film surface coverage, Q is the charge under the oxidation peak in the supporting electrolyte, n is the number of transferred electrons, F is the Faraday constant, and A is the effective area of the electrode.

The effective area improved twenty-one fold (21.08) for Co2,6Py-GCE and almost twenty fold (19.67) for CuPy-GCE.

Table 5. 6: Electrochemical parameters for electrodes.

GCE Modifier	ΔEp for $Fe(CN)_6^{3-/4-}$ in 0.1 M KCl	E/V (L-cysteine) oxidation pH 4 buffer	Surface roughness factor	Effective area	Γ ($mol.cm^{-2}$)	Background corrected oxidation
Bare GCE	0.066	-	-	-	-	-
Co2,6Py-GCE	0.088	0.623	21.08	1.497	4.707E-11	72.80
CuPy-GCE	0.084	0.612	19.68	1.397	4.599E-11	47.55

In pH 4 buffer solutions, the bare GCE and CuPy-GCE both do not conduct (Figure 5.7 B). When modified with Co2,6Py-GCE however, it shows a well resolved reduction peak at -689 mV with a signal of -9.34 μA. This reduction peak is characteristic of a Co^{II}/Co^{I} red^{ox} couple and is usually weak and often difficult to observe [22]. The fact that it appears as a well defined peak in Co-GCE means the modifier has enhanced electron transfer ability.

Comparing with the previously discussed electrodes, in chapters three (series 1: HKUST-1-GCE, Mo1-GCE and Mo2-GCE) and four (series 2: CoBTC-GCE and CoB4C-GCE), Co2,6Py-GCE and CuPy-GCE (series 3) generally display the lowest ΔEp values and surface coverages, followed by the POM-MOFs, Co-BTC/B4C MOFs and lastly HKUST-1. This suggests that the heterocyclic ligands result in better electron transfer properties. It is interesting to note that CuPy is a coordination complex (not a MOF) also displays enhanced electron transfer abilities.

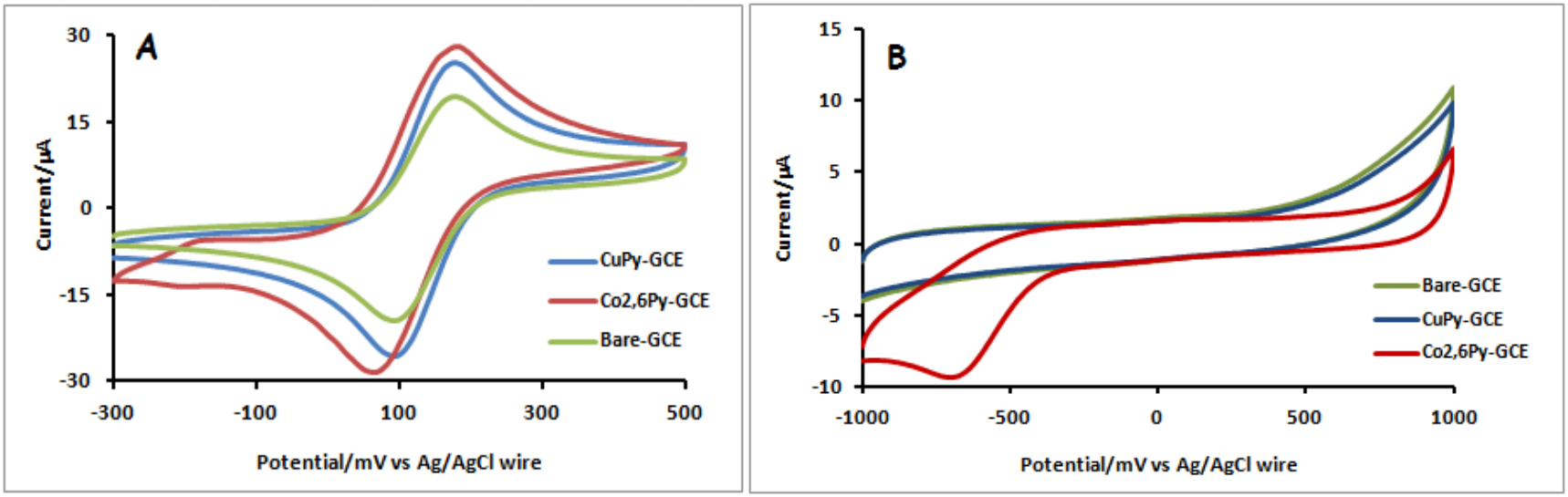

Figure 5. 7: Cyclic voltammograms of the electrodes (A) in 1 mM $[Fe(CN)_6]^{3-/4-}$ and (B) in pH 4 buffer at scan rate 100 mV/s.

5.5.2 L-cysteine detection via cyclic voltammetry

After electrochemical characterization, the bare and modified electrodes were applied to the electrocatalytic detection of L-cysteine. Both the modified electrodes exhibited electrocatalytic oxidation of L-cysteine with good signal strengths whilst the bare GCE showed no activity (Figure 5.8 and Table 5.6). The observed oxidation peak potential was between 0.610 - 0.623 V, which is characteristic for L-cysteine oxidation and is comparable to literature values [23,24]. Since the bare GCE did not exhibit a peak, it can be concluded that modification with both heterocyclic coordination compounds resulted in the development of an electrodes with the potential to detect L-cysteine.

This behaviour has been mirrored by the series 1 and 2 MOFs employed in previous chapters. All three Co MOFs oxidized L-cysteine at the same potential suggesting that the Co centre is actively involved in the oxidation; Co2,6Py-GCE (0.623 V, 72.80 μA), CoB4C-GCE (0.624 V, 36.23 μA) and CoBTC-GCE (0.624 V, 29.97 μA). Despite the similar potential, the higher current signal exhibited by Co2,6Py-GCE suggests that it has better catalytic properties. CuPy-GCE and HKUST-1-GCE displayed peaks at 0.612 V/47.55 μA and 0.283V/39.75 μA respectively. This suggests that the overpotential required with HKUST-1-GCE (CuBTC) is less than that required for CuPy-GCE. The higher signal however, shows that the Cu – pyridine combination works better for electrocatalysis of Lcysteine than the Cu – BTC combination. The POM-MOFs Mo1-GCE and Mo2-GCE displayed peaks at 0.205 V/31.40 μA and 0.328 V/58.60 μA respectively. This suggests that though the encapsulated POM results in less overpotential, the encorporated POM results in a much higher signal (almost twice that of Mo1-GCE).

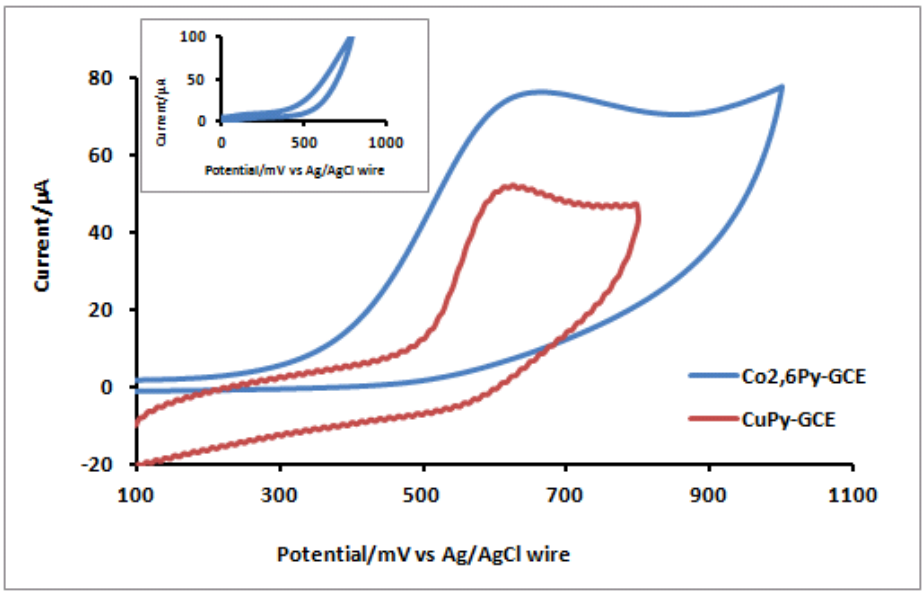

Figure 5. 8: Cyclic voltammograms of the modified electrodes (and Bare GCE (insert)) in 10 mM L-cysteine at 100 mV/s scan rate, pH 4 buffer.

The variations in electrocatalytic performance of the compounds demonstrates the importance of selection of PBU and SBU's in development of a good electrocatalyst. L-cysteine can be oxidized to cystine via the following reaction (Eq. 3) [25,26];

$$2RSH \Leftrightarrow RSSR + 2H^{+} + 2e^{-} \quad (3)$$

$$Co^{2+} + e^{-} \leftrightarrow Co^{+} \quad (4)$$

$$Cu^{2+} + e^{-} \leftrightarrow Cu^{+} \quad (5)$$

It is proposed that during L-cysteine oxidation, the mechanisms involve reduction of the Co^{2+}/Co^{+} and Cu^{2+}/Cu^{+} couples (Eq. 4 and 5), since Co^{2+} and Cu^{2+} are strong oxidizing agents [27]. Similar behaviour has been observed whilst investigating the electrochemical properties of Cu [28,29] and Co[28] complexes. The reversibility of the reaction depends on the speed of the reaction at the electrode surface, the

slower the reaction, the more irreversible the reaction becomes. Electro-reduction of L-cysteine is difficult to observe possibly because of the high energy levels required to oxidize Co^{+} back Co^{2+} and Cu^{+} to Cu^{2+} [30].

Electrode stability was investigated by running 20 successive cyclic voltammograms in 10 mM L-cysteine (Figure 5.9). Both electrodes appear to be fairly stable and continue to detect L-cysteine, with good signal strength after 20 cycles. Stability was also expressed as percentage current drop between the first and second cycles. The drops were found to be 8.8% and 7.5% for Co2,6Py-GCE and CuPy-GCE respectively. These values are much lower than those found for other MOFs in literature and indicate that electrodes have a very high resistance to passivation by the analyte [31,32].

Generally, series 2 and 3 have very comparable stabilities with % drops in the range 2.5 to 8.8%. With series 1 however, HKUST-1-GCE and Mo2-GCE are both relatively stable whilst Mo2-GCE losses its stability and ability to detect after 10 cycles. This suggests that encorporation results in a stable POM-MOF whilst encapsulation reduces this stability. In this study, stability of the MOFs and POM-MOFs appears to lead to better electrocatalysts.

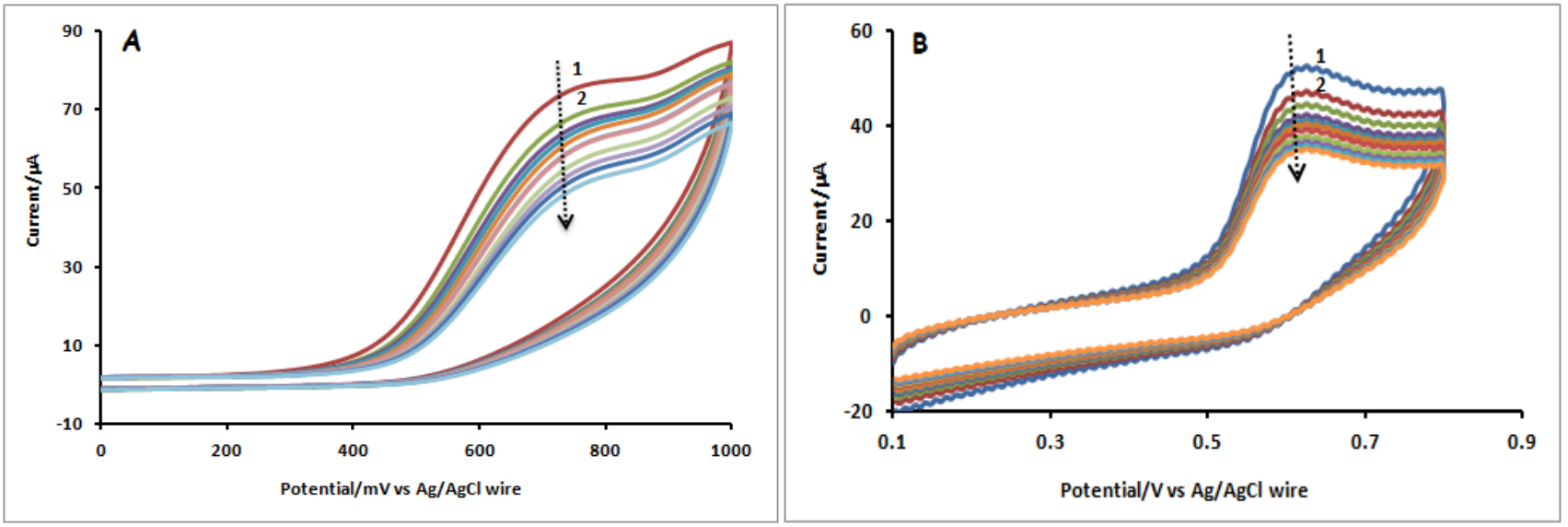

Figure 5. 9: Cyclic votammogrammes (20 successive scans) of Co2,6Py-GCE (A) and CuPy-GCE (B) in 10 mM L-cysteine. Scan rate of 100 mV/s. pH 4 buffer.

5.6 Chronoamperometry

The sensitivity, rate constants and limits of detection were calculated from chronoamperometry. Within the first five seconds (on average), the catalytic current is dominated by electro-oxidation of L-cysteine (Fig. 5.10) before it reaches steady-state. The sensitivity of the probes was found from the calibration curves (Fig 5.10), which were 0.0032 *μA/μM* for Co2,6Py-GCE and 0.0047 *μA/μM* for CuPy-GCE. These values were compared with a variety of other modified carbon nanotube electrodes in literature (Table 5.7) and found to be considerably lower [33-37]. In this work, the sensitivity follows the order series 1 < series 2 < series 3. All the modified electrodes displayed sensitivities in the range 0.0047 to 25.3290 μA/μM.

The rate constants were evaluated using Eq. 6 below;

$$\frac{I_{cat}}{I_{buf}} = \gamma^{\frac{1}{2}}\pi^{\frac{1}{2}} = \pi^{\frac{1}{2}}(kC_o t)^{\frac{1}{2}} \qquad (6)$$

where k is the catalytic rate constant, C_o is the bulk concentration of L-cysteine and t is time elapsed in seconds.

Figure 5.10 shows the plots of I_{cat}/I_{buf} vs $t^{1/2}$ (Eq. 6) for L-cysteine oxidation. The relationship between the slopes of these plots squared and their respective concentrations were used to calculate the rate constants and are represented by equations (7) and (8) for Co2,6Py-GCE and CuPy-GCE respectively.

$$y=0.002[\text{L-cysteine}](\frac{s^{-1}}{\mu M})-0.311s^{-1}, \quad R^2=0.9811 \qquad (7)$$

$$y=0.0234[\text{L-cysteine}](\frac{s^{-1}}{\mu M})-0.6451s^{-1},\ R^2=0.9833 \quad (8)$$

The slope is equal to πk where k is the rate constant.

Using this relationship, the rate constants were found to be 6.37 x 10^1 M^{-1} s^{-1} for Co2,6Py-GCE and 7.45 x 10^3 M^{-1} s^{-1} for CuPy-GCE. This showed that the reaction was occurring much faster at the CuPy-GCE surface than it was at the Co2,6Py-GCE surface. The rate constants for series 1 and 2 are in the range 5.8 to 1.56x10^4 $M^{-1}s^{-1}$, with the upper limit being CoBTC-GCE. This shows that reaction occurred fastest at the CuPy-GCE and CoBTC-GCE surfaces.

The electrocatalytic oxidation peak current of L-cysteine showed a linear dependence on the L-cysteine concentration obtained in the range 0 – 1.2 x 10^{-6} M for both electrodes. Using the 3δ notation ($3S_b/m$; where S_b is the standard deviation of the blank signal and m is the slope of the calibration graph), the limits of detection were found to be 1.85 x 10^{-6} M and 2.73 x 10^{-6} M for Co2,6Py-GCE and CuPy-GCE respectively. These values compare well with others in literature (table 5.5) and are within the range often found in biological fluids (0.5-680 μM) such as urine and plasma [24] making the probes promising L-cysteine sensor platforms.

Selectivity of L-cysteine detection on other electrodes has been shown to be affected by the presence of sulphur containing amino acids like Methionine. However, this occurs when the oxidation potentials are in the same range [35,38] and concentrations of interferences are very high (above 200-fold) [39,40]. With the Co2,6Py-GCE and CuPy-GCE, the oxidation potentials are at 0.623 V and 0.612 V

respectively whilst that for Methionine, under optimum conditions on a similar modified Co/Cu-GCE, was found to be at 0.810 V [41]. Given the difference in potentials, no interference is expected under these conditions. Other non-sulphur amino acids like L-serine, L-histidine, D-glutamic acid and L-alanine have also been reported to have very little interference [36]. Amongst compounds like glucose, citric acid, urea, oxalic acid and ascorbic acid which often exist in the biological matrix, only ascorbic acid has been known to cause interference when in concentrations of at least 200 fold that of L-cysteine [36,40].

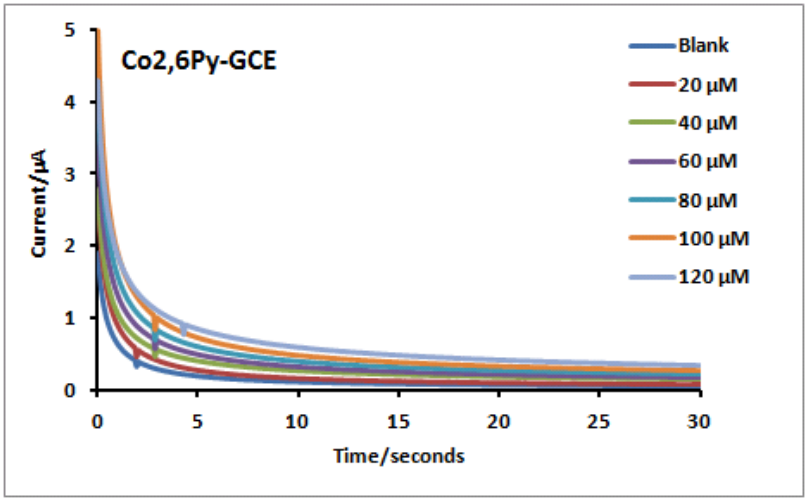

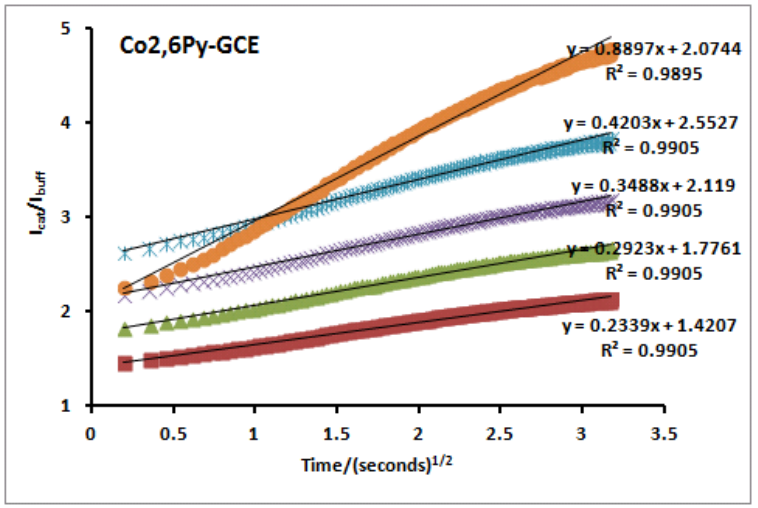

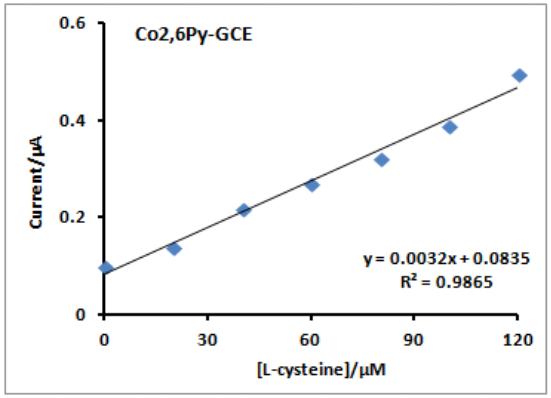

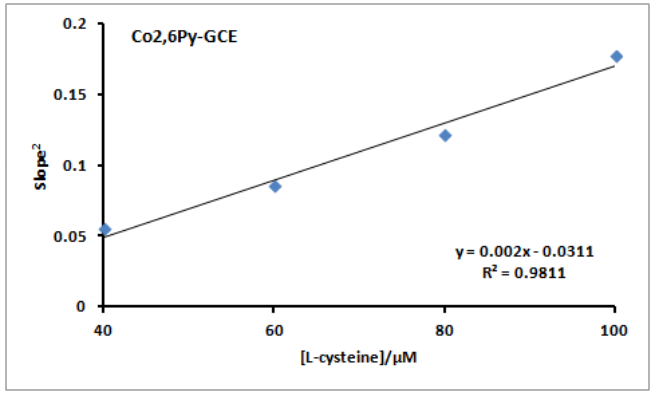

Figure 5. 10: Chronoamperograms, plots of I_{cat}/I_{buf} versus $t^{1/2}$, calibration curve and slope^2 vs [L-cysteine] determined using chronoamperometry for the Co2,6Py-GCE and CuPy-GCE (continued on next page).

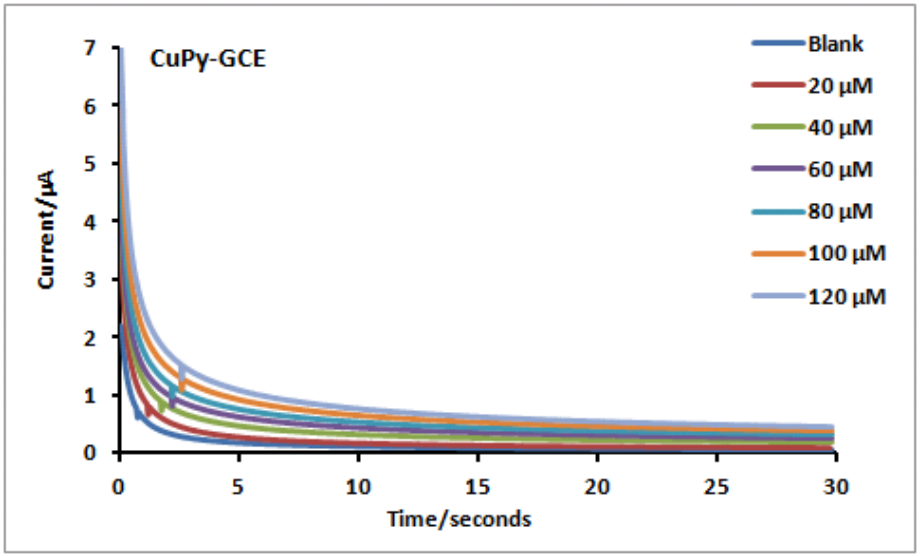
CuPy-GCE
Blank
20 µM
40 µM
60 µM
80 µM
100 µM
120 µM
Current/µA
Time/seconds

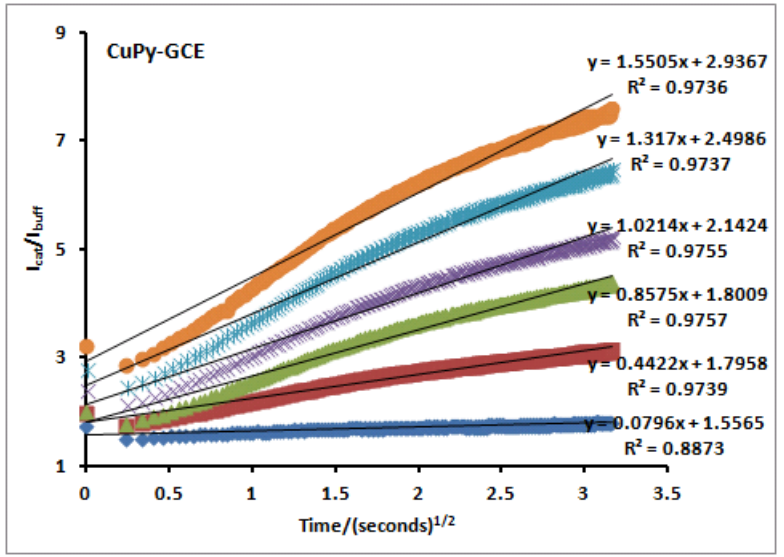
CuPy-GCE
y = 1.5505x + 2.9367
R² = 0.9736
y = 1.317x + 2.4986
R² = 0.9737
y = 1.0214x + 2.1424
R² = 0.9755
y = 0.8575x + 1.8009
R² = 0.9757
y = 0.4422x + 1.7958
R² = 0.9739
y = 0.0796x + 1.5565
R² = 0.8873
Icat/Ibuff
Time/(seconds)1/2

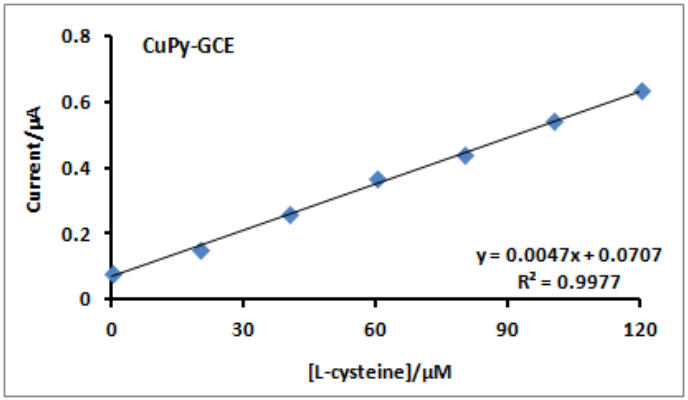
CuPy-GCE
y = 0.0047x + 0.0707
R² = 0.9977
Current/µA
[L-cysteine]/µM

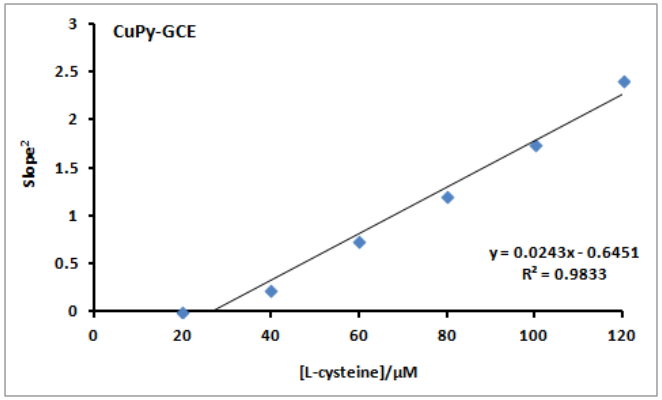
CuPy-GCE
y = 0.0243x - 0.6451
R² = 0.9833
Slope2
[L-cysteine]/µM

Table 5. 7: Comparative LODs for electrochemical oxidation of L-cysteine using different catalytic systems.

Electrode	LOD	Sensitivity	pH	Reference
Ferrocene dicarboxylic acid-CPE	2.60×10^{-5} M	8.1 µA/mM	8	[33]
GCE/MWCNT@PTZ-biQ	1.10×10^{-7} M	3.6 µA/mM	7	[34]
Pt/CNT	3.00×10^{-7} M	-	7.4	[35]
Boron-doped CNT-GCE	2.60×10^{-7} M	25.1 nA/mM	7.4	[36]
CoMSal-CPE	2.00×10^{-7} M	35 µA/M	5	[37]
Co2,6Py-GCE	1.85×10^{-6} M	0.0032 µA/µM	4	This work
CuPy-GCE	2.73×10^{-6} M	0.0047 µA/µM	4	This work
CoBTC-GCE	3.92×10^{-6} M	0.1159 µA/µM	4	This work
CoB4C-GCE	6.85×10^{-6} M	0.7200 µA/µM	4	This work
HKUST-1-GCE	3.03×10^{-7} M	6.1439 µA/µM	4	This work
Mo1-GCE	3.07×10^{-7} M	4.4919 µA/µM	4	This work
Mo2-GCE	3.47×10^{-7} M	25.3290 µA/µM	4	This work

5.7 Conclusion

A new coordination compound Co2,6Py, a cobalt 2-6-pyridinedicarboxylate MOF, was synthesized by slow evaporation techniques. Attempts to make the Cu analogue resulted in the formation of CuPy (a $CuCl_2(C_5H_5N)_2$ complex). Co2,6Py and CuPy were both employed for the electrocatalytic detection of L-cysteine and gave good detection signals with high resistance to fouling. The probes were effective upto low concentrations (LODs of 1.85 µM and 2.73 µM) with very fast response times of approximately 5 seconds. The hydrogen bonded MOF displayed better electrocatalytic properties compared to the complex possibly due to the larger surface areas associated with MOFs. However, both coordination compounds performed well when compared with other electrodes in literature, suggesting that they could serve as promising platforms for L-cysteine sensing.

References

[1] K. Uemura, R. Matsuda, S. Kitagawa, *J. Solid State Chem.* **2005**, *178*, 2420–2429.

[2] A. Majumder, V. Gramlich, G. M. Rosair, S. R. Batten, J. D. Masuda, M. S. El Fallah, J. Ribas, J.-P. Sutter, C. Desplanches, S. Mitra, *Cryst. Growth Des.* **2006**, *6*, 2355–2368.

[3] K. Ghasemi, A. R. Rezvani, A. Shokrollahi, R. Mendoza-Meron, A. Moghimi, S. Gavahi, S. Garcia-Granda, *Comptes Rendus Chim.* **2014**, *17*, 1221–1229.

[4] C. Yuste, M. R. Silva, M. Ghadermazi, F. Feizib, E. Motieiyan, *Acta Crystallogr.* **2010**, *E66*, m1643–m1644.

[5] S. Yousuf, A. S. Johnson, S. A. Kazmi, M. Hemamalinic, H.-K. Func, *Acta Crystallogr.* **2011**, *E67*, m1105–m1106.

[6] M. Mirzaei, H. Eshtiagh-Hosseini, Z. Karrabi, K. Molčanov, E. Eydizadeh, J. T. Mague, A. Bauzád, A. Frontera, *CrystEngComm* **2014**, *16*, 5352–5363.

[7] L. Yang, D. C. Crans, S. M. Miller, A. la Cour, O. P. Anderson, P. M. Kaszynski, M. E. Godzala, L. D. Austin, G. R. Willsky, *Inorg. Chem.* **2002**, *41*, 4859–4871.

[8] Z. Derikvand, N. Dorosti, F. Hassanzadeh, A. Shokrollahi, Z. Mohammadpour, A. Azadbakht, *Polyhedron* **2015**, *43*, 140–152.

[9] M. Czugler, L. Kótai, B. Sreedhar, A. Rockenbauer, I. Gács, S. Holly, *Eur. J. Inorg. Chem.* **2002**, *8*, 3298.

[10] B. B. Koleva, E. N. Trendafilova, M. G. Arnaudov, W. S. Sheldrick, H. Mayer-Figge, *Transit. Met. Chem.* **2006**, *31*, 866–873.

[11] G. Bowmaker, C. Di Nicola, C. Pettinari, B. W. Skelton, N. Somers, A. H. White, *Dalton Trans.* **2011**, *40*, 5102–5115.

[12] R. A. Ahmadi, F. Hasanvand, G. Bruno, H. A. Rudbari, S. Amani, *ISRN Inorg. Chem.* **2013**, *2013:42671*, 7pp.

[13] A. D. Mighell, C. W. Reimann, A. Santoro, *Acta Crystallogr.* **1972**, *28*, 126–134.

[14] S. S. Kabalkina, *Dolk. Akad. Nauk. SSSR.* **1956**, *110*, 1013–1014.

[15] L. Van Meervelt, A. Pacco, K. Binnemans, *Zeitschrift für Krist. New Cryst. Struct.* **2003**, *218*, 197–198.

[16] B. Morosin, *Acta Crystallogr.* **1975**, *8*, 632–634.

[17] D. Cook, *Can. J. Chem.* **1961**, *39*, 2009–2024.

[18] C.-L. Ming, Y.-N. Zhao, B.-Y. Yu, K. Van Hecke, G.-H. Cui, *Bull. Korean Chem. Soc* **2014**, *35*, 3349–3352.

[19] D. A. Thornton, *Coord. Chem. Rev.* **1990**, *104*, 251–295.

[20] D. A. Thornton, P. F. M. Verhoeven, H. O. Desseyn, H. Hofmans, *Thermochim. Acta* **1987**, *113*, 161–169.

[21] M. Shumba, T. Nyokong, *Electrochim. Acta* **2016**, *196*, 457–469.

[22] X. Liu, C. Shi, C. Zhai, M. Cheng, Q. Liu, G. Wang, *Appl. Mater. Interfaces* **2016**, *8*, 4585–4591.

[23] H. Hosseini, H. Ahmar, A. Dehghani, A. Bagheri, A. Tadjarodi, A. Reza, *Biosens. Bioelectron.* **2013**, *42*, 426–429.

[24] C. Xiao, J. Chen, B. Liu, X. Chu, L. Wu, S. Yao, *Phys. Chem. Chem. Phys.* **2011**, *13*, 1568–1574.

[25] A. Eid, O. Benlounes, H. S. Hilal, S. Hocine, C. Rabia, *Adv. Chem. Eng. Sci.* **2013**, *3*, 82–92.

[26] L. H. Wang, W. S. Huang, *Sensors* **2012**, *12*, 3562–3577.

[27] E. S. Wiedner, J. A. S. Roberts, W. G. Dougherty, W. S. Kassel, D. L. Dubois, R. M. Bullock, *Inorg. Chem.* **2013**, *52*, 9975–9988.

[28] I. Uçar, B. Karabulut, A. Bulut, O. Büyükgüngör, *J. Mol. Struct.* **2007**, *834–836*, 336–344.

[29] K. M. Lincoln, E. O. Michael, T. D. Hayden, R. E. Saunders, K. N. Green, *Inorg. Chem.* **2013**, *53*, 1406–1416.

[30] S. Nyoni, T. Mugadza, T. Nyokong, *Electrochim. Acta* **2014**, *128*, 32–40.

[31] T. Mugadza, T. Nyokong, *Polyhedron* **2011**, *30*, 1820–1829.

[32] H. Dejmkova, C. Dag, J. Barek, J. Zima, *Cent. Eur. J. Chem.* **2012**, *10*, 1310–1317.

[33] J. B. Raoof, R. Ojani, H. Beitollahi, *Electroanalysis* **2007**, *19*, 1822–1830.

[34] R. Shanmugam, P. Barathi, J.-M. Zen, A. K. Senthil, *Electrochim. Acta* **2016**, *187*, 34–45.

[35] S. Fei, J. Chen, S. Yao, G. Deng, D. He, Y. Kuang, *Anal. Biochem.* **2005**, *339*, 29–35.

[36] C. Deng, J. Chen, X. Chen, M. Wang, Z. Nie, S. Yao, *Electrochim. Acta* **2009**, *54*, 3298–3302.

[37] S. Shahrokhian, M. Karimi, *Electrochim. Acta* **2004**, *50*, 77–84.

[38] X.-Q. Wu, J.-G. Ma, H. Li, D.-M. Chen, W. Gu, G.-M. Yang, P. Cheng, *Chem. Commun.* **2015**, *51*, 9161–9164.

[39] A. Nezamzadeh-Ejhieh, H.-S. Hashemi, *Talanta* **2012**, *88*, 201–208.

[40] Y. Wang, H. Ge, G. Ye, H. Chen, X. Hu, *J. Mater. Chem. B* **2015**, *3*, 3747–3753.

[41] A. Abbaspour, A. Ghaffarinejad, *Electrochim. Acta* **2008**, *53*, 6643–6650.

Chapter Six

This chapter contains the summary conclusions of the thesis. It compares the various groups of compounds in terms of observed physical characteristics as well as the electrocatalytic behaviour towards L-cysteine.

6. Final conclusions

6.1 Summary

For the past two decades, MOFs have been received a great deal of attention, due to their diverse properties and correspondingly wide range of possible applications [1–3]. The work in this thesis focused on the preparation, characterization and potential in catalytic applications of MOFs. Cu, Co and Mo POMs were used as the metal nodes and 1,3,5-benzenetricarboxylate, 1,2,4,5-benzenetetracarboxylate and 2,6-pyridinedicarboxylate were employed as the various linkers. These combinations gave rise to both 2D and 3D structures with interesting properties.

The MOFs were characterized using various techniques such as Fourier transform infrared spectroscopy, thermogravimetric analysis and differential scanning calorimetry. Surface morphology was studied by means of scanning electron microscopy. Structural elucidation was done by means of single crystal X-ray diffraction. In the absence of single crystals, chemical formulae were proposed based on elemental analysis and inductively coupled plasma-optical emission spectroscopy. Evaluation of electrocatalytic activity was done using cyclic voltammetry, differential pulse voltammetry, electrochemical impedence spectroscopy and chronoamperometry techniques for the detection of L-cysteine. Important parameters such as sensitivity, limits of detection and rate constants were calculated. The behaviour of these MOFs was compared to that of similar compounds in literature to gain an understanding of the importance of the work in the relevant fields.

6.2 Compounds of Cu, Mo and H_3BTC

Two compounds were generated based on the MOF, HKUST-1. The compound Mo1 was made by post synthetic modification of HKUST-1 whilst Mo2 was generated using a one-step solvothermal approach. Mo1 displayed a slightly distorted HKUST-1 crystal structure whilst Mo2 formed rod like crystals. This proved that the modification approach resulted in totally different compounds, despite using exactly the same starting materials. The electrocatalytic behaviour of both Mo doped compounds was evaluated against that of HKUST-1. The encapsulated Mo1-GCE had lower a LOD and was more sensitive than HK-GCE, whilst the encorporated Mo2-GCE displayed larger values. In terms of signal strengths however, both Mo1-GCE and Mo2-GCE had higher signal strengths than HK-GCE, with Mo2-GCE having almost twice the signal strength of the other two electrodes. In terms of stability, Mo2-GCE was the most stable followed by HK-GCE and Mo1-GCE. The lower stability of Mo1-GCE is a characteristic often associated with POM loading [4,5].

6.3 Compounds of Co, H_3BTC and H_4B4C

Using solvothermal techniques, three compounds were produced from Co combined with either H_3BTC or H_4BTC ligands; CoBTC, CoB4C and CoB4C-2. Both B4C compounds were suitable for SC-XRD. Literature revealed that only one of the compounds (CoB4C-2) had not been made before. Of the three compounds, the two non-ionic MOFs were employed in electrocatalytic oxidation of L-cysteine. The signal observed for CoB4C-GCE was higher than that for CoBTC-GCE, showing that better conductivity of Co when coordinated to this ligand. In terms of stability however, the CoBTC-GCE is considerably more stable than the CoB4C-GCE (2,4% vs

8.2% drop). Sensitivities for both electrodes were in the μA/μM range, with that for CoBTC-GCE being approximately six times lower that for CoB4C-GCE. Limits of detection showed similar trends with that for CoBTC-GCE being approximately half that of CoB4C-GCE. Both LODs were also in the micromolar range.

Electrochemical impedence confirmed the good conductivity exhibited by both Co electrodes, evidenced by low R_{CT} values in the Kilo-ohms range, showing fast reaction kinetics at the electrode surface [6]. Phase angles below 90 ° showed the deviation from behaviour of an ideal capacitor [7]. The phase angles for both CoB4C-GCE and CoBTC-GCE are lower than that for the bare GCE by almost 10 ° showing how modification improved conductivity. Exchange current densities were found to be 3.11E-4, 6.14E-4 and 5.01E-4 for the Bare-GCE, CoBTC-GCE and CoB4C-GCE respectively, indicating the better electrocatalytic properties of CoBTC-GCE. The behaviour confirms that the different ligands not only result in structural differences [8] but also behavioural differences of the two electrodes. In this case, there was an improvement in most electrochemical parameters when H_3BTC was employed as the ligand.

6.4 Compounds of Co, Cu and 2,6-pydc.

Two compounds were synthesized using slow evaporation techniques, with 2,6-pyridinedicarboxylate employed as the ligand and pyridine as the solvent. A new MOF, pyridinium 2,6-pyridinehydrogendicarboxylato2,6-pyridine dicarboxylatocobaltate(II)·2,6-pyridinedicarboxylic acid·1 water, was produced via

self assembly of the reactants. The system containing Cu however resulted in the formation of a simple copper(II) chloride pyridine complex, that has already been reported in literature [9,10]. Co2,6Py was characterized by microanalysis, FTIR, TGA, DSC and SC-XRD. Both compounds potential as electrocatalytic platforms for the detection of L-cysteine was investigated by modifying a GCE with the complexes. Though both compounds showed electrocatalytic activity, the Co2,6Py-GCE displayed superior electrochemical abilities in terms of signal strength (72.80 μA vs 47.55 μA) and electrode sensitivity (0.0032 μA/μM vs 0.0047 μA/μM). In terms of stability however, the CuPy-GCE was more stable, showing its resistance to fouling in the analyte [11].

Rate constants for both systems were comparable to literature with that for CuPy-GCE being times a hundred fold (1.2 $x10^2$) that for Co2,6Py-GCE, showing that the rates of reaction were relatively fast. Limits of detection were in the micromolar range for both electrodes with that for CuPy-GCE being almost half that for Co2,6Py-GCE (2.73 x 10^{-6} M vs 4.23 $x10^{-6}$ M). From these results it can be seen that choice of metal centre and ligand had unforeseen effects on the performance of the electrodes. The Co system resulted in better electron transfer abilities evidenced by the higher signals and sensitivities [12]. The Cu system on the other hand resulted in more stable electrode with lower detection limits and higher rate constants.

Overally, the Co2,6Py-GCE system performed better than the other modified electrodes, giving a better detection signal, lower LOD and sensitivity (Table 6.1). It is interesting to note that CuPy-GCE, though not a MOF, also displays enhanced

electron transfer abilities. Co2,6Py-GCE and CuPy-GCE (series 3) generally display the lowest ΔEp values and surface coverages, followed by the POM-MOFs (series 1; Mo1-GCE and Mo2-GCE), Co-BTC/B4C-GCE MOFs (series 2) and lastly HKUST-1-GCE.This leads us to conclude that the use of 2,6-pydc as a linker in series 3, greatly improved the electrocatalytic activity in both the Co and Cu coordination compounds.

Table 6. 1: Comparative LODs for electrochemical oxidation of L-cysteine using different catalytic systems (continued to next page).

Electrode	LOD	Sensitivity	pH	Reference
Ferrocene dicarboxylic acid-CPE	2.60 x 10^{-5} M	8.1 μA/mM	8	[13]
GCE/MWCNT@PTZ-biQ	1.10 x10^{-7} M	3.6 μA/mM	7	[14]
Pt/CNT	3.00 x 10^{-7} M	-	7.4	[11]
Boron-doped CNT-GCE	2.60 x 10^{-7} M	25.1 nA/mM	7.4	[15]
CoMSal-CPE	2.00 x 10^{-7} M	35 μA/M	5	[16]
Co2,6Py-GCE	1.85 x 10^{-6} M	0.0032 μA/μM	4	This work
CuPy-GCE	2.73 x 10^{-6} M	0.0047 μA/μM	4	This work
CoBTC-GCE	3.92 x 10^{-6} M	0.1159 μA/μM	4	This work
CoB4C-GCE	6.85 x 10^{-6} M	0.7200 μA/μM	4	This work

HKUST-1-GCE	3.03 x 10^{-7} M	6.1439 μA/μM	4	This work
Mo1-GCE	3.07 x 10^{-7} M	4.4919 μA/μM	4	This work
Mo2-GCE	3.47 x 10^{-7} M	25.3290 μA/μM	4	This work

6.5 Thermal stability

All compounds showed relatively high thermal stability. The pyridine compounds, CuPy and Co2,6Py were the least stable with framework decompositions starting around 170 °C. These were followed by the Mo modified compounds and CoBTC whose frameworks start to breakdown at 250 °C. The temperature at which the framework breaksdown can be taken as the catalytic temperature limit for these compounds. Though this work was carried out at ambient temperatures for electrocatalysis, the high thermal stabilities make it possible for other catalytic systems which require higher temperatures (like desulphurization) to be investigated in future.

6.6 Electrocatalytic behaviour

L-cysteine is an important amino acid in most biological systems [17]. Its role involves various protein and enzyme synthesis mechanisms as well as antioxidant defense systems [18]. Deficiency of it can lead to a number of clinical situations such as poor healing, muscle production and metabolism [19]. For this reason it is necessary to monitor its levels in biological environments. Electrochemical methods are fast and easy whilst offering low detection limits [13,20]. All compounds were

evaluated for their electrocatalytic activity and they all displayed activity towards the electrooxidation of L-cysteine. It was observed that post-synthetic modification of the Cu MOF, HKUST-1, with Mo POMs resulted in an improvement in activity in terms of both sensitivity and LODs. There was also a reduction in the overpotential required for the reaction. When the metal centre was changed to Co, the same trend was observed for overpotential required for the reaction, as with HK-Mo electrodes. There was however a marked improvement in sensitivity, from μA/mM for HK-Mos to μA/μM for the Co electrodes. There was also a noticeable increase in overpotential from 0.2-0,3 V for HK-Mo electrodes to 0.624 V for both CoB4C-GCE and CoBTC, suggesting that the Co centre is actively involved in the reaction. Signal strength, however, reduced from a best of 58 μA observed with Mo2-GCE to almost half that value 36 μA, for CoB4C-GCE and even lower with CoBTC (30 μA,) When the ligand was changed to pyridine, the signal increased to 48 μA and upon changing to 2,6-pyridine dicarboxylate, the signal observed increased to 72.80 μA, showing the positive effect the carboxyl groups had on electron transfer abilities. In terms of electrode stabilities, the observed trends indicate that Cu systems are the most stable, followed by Co then lastly the Mo containing complexes.

Selectivity of L-cysteine detection on other electrodes has been shown to be affected by the presence of sulphur containing amino acids like Methionine. However, this occurs when the oxidation potentials are in the same range [14,16] and concentrations of interferences are very high (above 200-fold) [21,22]. Series 1, 2 and 3 oxidation potentials are in the range 0.205 -0.328 V, 0.624 V and 0.612-

0.623 V, respectively whilst that for Methionine, under optimum conditions on a similar modified Co/Cu-GCE, was found to be at 0.810 V [23]. Given the difference in potentials, no interference is expected under these conditions. Other non-sulphur amino acids like L-serine, L-histidine, D-glutamic acid and L-alanine have also been reported to have very little interference [11]. Amongst compounds like glucose, citric acid, urea, oxalic acid and ascorbic acid which often exist in the biological matrix, only ascorbic acid has been known to cause interference when in concentrations of at least 200 fold that of L-cysteine [11,22].

6.7 Future work

The primary objectives as presented in chapter one were all achieved. A series of MOF compounds were synthesized with some of the structures (CuPy, CoB4C, CoB4C-2 and Co2,6Py) confirmed by single crystal XRD. A selection of the compounds synthesized were examined for their electrocatalytic activity towards the oxidation of L-cysteine to investigate some of the factors that may be definitive. In future, it would be interesting to see if the compounds can also show electrocatalytic activity towards other physiological molecules like glucose, whose detection is also very important.

Future work can also include the synthesis of additional compounds with mixed ligand systems. A combination of benzenepolycarboxylates and pyridine polycarboxylates promises better properties due to the combination of compounds with different strengths. Such studies would have to extend the pH range

investigated over the full biological range (pH 4 for lysosomes to 7.5 for cerebral fluid).

This study can additionally be extended by completing the circle that incentivized the work, namely the desulphurization of fuels using MOFs as hydrodesulphurization catalysts, particularly POM-MOFs. The first requirement in this regard would be establishing methods to successfully create additional Co MOFs modified by Mo POMs and to fully characterize their structures and electrocatalytic activity.

6.8 Final comments

The application of MOFs in electrocatalysis is still relatively unexplored and holds promise for new and exciting discoveries. The work presented here is important to the body of MOFs as it touches on the relatively new field of POM-MOFs and the application of MOFs in electrocatalysis [24]. The effects of different ligands and metal centres on electrocatalytic abilities was investigated. This behaviour is important for the development of new electrocatalysts and their application in various environments.

References

[1] J. Lei, R. Qian, P. Ling, L. Cui, H. Ju, *Trends Anal. Chem.* **2014**, *58*, 71–78.

[2] R. J. Kuppler, D. J. Timmons, Q.-R. Fang, J.-R. Li, T. A. Makal, M. D. Young, D.-Q. Yuan, D. Zhao, W.-J. Zhuang, H.-C. Zhou, *Coord. Chem. Rev.* **2009**, *253*, 3042–3066.

[3] R. F. Mendes, F. A. A. Paz, *Inorg. Chem. Front.* **2015**, *2*, 495–509.

[4] X. Hu, Y. Lu, F. Dai, C. Liu, Y. Liu, *Micropor. Mesopor. Mat.* **2013**, *170*, 36–44.

[5] J. Juan-Alcaniz, M. G. Goesten, E. V Ramos-fernandez, J. Gascon, F. Kapteijn, *New J. Chem.* **2012**, *36*, 977–987.

[6] R. K. Mendes, R. S. Freire, C. P. Fonseca, S. Neves, L. T. Kubota, *J. Braz. Chem. Soc.* **2004**, *15*, 849–855.

[7] P. C. Banerjee, D. E. Lobo, R. Middag, W. K. Ng, M. E. Shaibani, M. Majumder, *Appl. Mater. Interfaces* **2015**, *7*, 3655–3664.

[8] A. Béziau, S. A. Baudron, D. Rasoloarison, M. W. Hosseini, *CrystEngComm* **2014**, *16*, 4973–4980.

[9] Y. Krysiak, L. Fink, T. Bernert, J. Glinnemann, M. Kapuscinski, H. Zhao, E. Alig, M. U. Schmidt, *Zeit. Anorg. Allgem. Chem.* **2014**, *640*, 3190–3196.

[10] M. Czugler, L. Kótai, B. Sreedhar, A. Rockenbauer, I. Gács, S. Holly, *Eur. J. Inorg. Chem.* **2002**, *8*, 3298.

[11] S. Fei, J. Chen, S. Yao, G. Deng, D. He, Y. Kuang, *Anal. Biochem.* **2005**, *339*, 29–35.

[12] K. Ozoemena, P. Westbroek, T. Nyokong, *Electrochem. Commun.* **2001**, *3*, 529–534.

[13] J. B. Raoof, R. Ojani, H. Beitollahi, *Electroanalysis* **2007**, *19*, 1822–1830.

[14] R. Shanmugam, P. Barathi, J.-M. Zen, A. K. Senthil, *Electrochim. Acta* **2016**, *187*, 34–45.

[15] C. Deng, J. Chen, X. Chen, M. Wang, Z. Nie, S. Yao, *Electrochim. Acta* **2009**, *54*, 3298–3302.

[16] S. Shahrokhian, M. Karimi, *Electrochim. Acta* **2004**, *50*, 77–84.

[17] Y. Di Zhao, W. De Zhang, H. Chen, Q. M. Luo, *Sensors Actuators, B Chem.* **2003**, *92*, 279–285.

[18] H. Hosseini, H. Ahmar, A. Dehghani, A. Bagheri, A. Tadjarodi, A. Reza, *Biosens. Bioelectron.* **2013**, *42*, 426–429.

[19] J. Yin, W. Ren, G. Yang, J. Duan, X. Huang, R. Fang, C. Li, T. Li, Y. Yin, Y. Hou, et al., *Mol. Nutr. Food Res.* **2015**, *0*, 1–13.

[20] C. Xiao, J. Chen, B. Liu, X. Chu, L. Wu, S. Yao, *Phys. Chem. Chem. Phys.* **2011**, *13*, 1568–1574.

[21] X.-Q. Wu, J.-G. Ma, H. Li, D.-M. Chen, W. Gu, G.-M. Yang, P. Cheng, *Chem. Commun.* **2015**, *51*, 9161–9164.

[22] A. Nezamzadeh-Ejhieh, H.-S. Hashemi, *Talanta* **2012**, *88*, 201–208.

[23] Y. Wang, H. Ge, G. Ye, H. Chen, X. Hu, *J. Mater. Chem. B* **2015**, *3*, 3747–3753.

[24] K. F. Babu, M. A. Kulandainathan, I. Katsounaros, L. Rassaei, A. D. Burrows, P. R. Raithby, F. Marken, *Electrochem. Commun.* **2010**, *12*, 632–635.

Appendices

Appendix A: Elemental analysis (ICP-OES) for Mo and Cu.

Appendix B1: Supplementary crystallographic information for CoB4C (ga280).

Appendix B2: Supplementary crystallographic information for CoB4C-2 (ga113); microanalysis and thermal analysis for CoB4C-POM.

Appendix C1: Supplementary crystallographic information for Co2,6Py (ga081).

Appendix C2: Supplementary crystallographic information for CuPy (ga085).

The following files are attached for each crystal structure:

.mercury : Crystallographic information files

.sup : Crystallographic data and refinements

.hkl : Reflection data

.pdf : CheckCIF report

.jpeg : Crystal pictures

Simple Sample Report

Author:

Published: 28/06/2014 16:58:10

Notes:

Blank

Acquire Date: 23/06/2014 15:57:05 Sample Type: Standard

Method Name: taffy-mo1 Method Revision: 1

Analyst Name: admin

Elem	Flags	Avg	Units	Stddev	%RSD
Mo2045		-14.02	Cts/S	1.027	7.328
Mo2816		-55.83	Cts/S	14.07	25.20

CalibStd-1

Acquire Date: 23/06/2014 16:00:09 Sample Type: Standard

Method Name: taffy-mo1 Method Revision: 1

Analyst Name: admin

Elem	Flags	Avg	Units	Stddev	%RSD
Mo2045		3,373	Cts/S	21.13	0.6266
Mo2816		19,530	Cts/S	455.8	2.334

CalibStd-2

Acquire Date: 23/06/2014 16:03:14 Sample Type: Standard

Method Name: taffy-mo1 Method Revision: 1

Analyst Name: admin

Elem	Flags	Avg	Units	Stddev	%RSD
Mo2045		7,468	Cts/S	81.50	1.091
Mo2816		42,150	Cts/S	2,811	6.670

CalibStd-3

Acquire Date: 23/06/2014 16:06:24 Sample Type: Standard

Method Name: taffy-mo1 Method Revision: 1

Analyst Name: admin

Elem	Flags	Avg	Units	Stddev	%RSD
Mo2045		11,710	Cts/S	71.37	0.6092
Mo2816		68,680	Cts/S	560.1	0.8155

CalibStd-4

Acquire Date: 23/06/2014 16:09:33 Sample Type: Standard

Method Name: taffy-mo1 Method Revision: 1

Analyst Name: admin

Elem	Flags	Avg	Units	Stddev	%RSD
Mo2045		16,290	Cts/S	23.28	0.1429
Mo2816		97,200	Cts/S	326.4	0.3358

CalibStd-5

Acquire Date: 23/06/2014 16:12:56 Sample Type: Standard

Method Name: taffy-mo1 Method Revision: 1

Analyst Name: admin

Elem	Flags	Avg	Units	Stddev	%RSD
Mo2045		20,290	Cts/S	177.6	0.8753

CalibStd-5

Acquire Date:	23/06/2014 16:12:56	Sample Type:	Standard
Method Name:	taffy-mo1	Method Revision:	1
Analyst Name:	admin		

Elem	Flags	Avg	Units	Stddev	%RSD
Mo2816		122,600	Cts/S	1,379	1.124

MO-BTC1

Acquire Date:	23/06/2014 16:17:33	Sample Type:	Unknown
Method Name:	taffy-mo1	Method Revision:	1
Analyst Name:	admin		

Elem	Flags	Avg	Units	Stddev	%RSD
Mo2045		24.07	ppm	0.1132	0.4703
Mo2816		24.52	ppm	0.1322	0.5392

Search Overview

Search:	search1
Date/Time done:	Thu Nov 24 11:50:34 2016
Database(s):	CSD version 5.37 updates (Nov 2015) CSD version 5.37 (November 2015) CSD version 5.37 (November 2015) CSD version 5.37 updates (Feb 2016) CSD version 5.37 updates (May 2016)
Restriction Info:	No refcode restrictions applied
Filters:	None
Percentage Completed:	100%
Number of Hits:	23

Single query used. Search found structures that:

match

Query 1

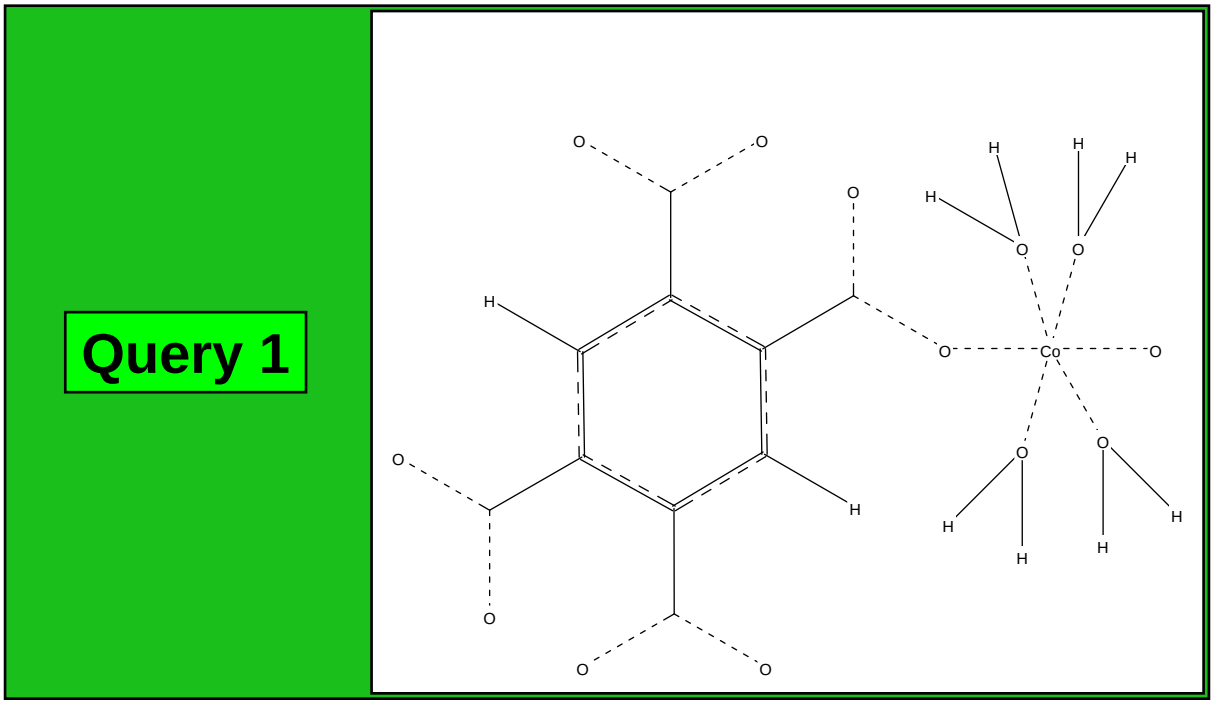

Search: search1 (Thu Nov 24 11:50:34 2016): Hit 1

BANGED

Reference: Deping Cheng, M.A.Khan, R.P.Houser (2002)
Cryst.Growth Des. ,**2,**415

Formula: $(C_5 H_{14} N_2)^{2+}2n,n(C_{20} H_{36} Co_4 O_{32}),n(C_{20} H_{20} Co_2 O_{24})^{4-},22n(H_2 O_1)$

Compound Name: catena-(bis(Homopiperazonium) (bis(μ_4-1,2,4,5-benzenetetracarboxylato)-hexadeca-aqua-tetra-cobalt)-(bis(μ_2-1,2,4,5-benzenetetracarboxylato)-octa-aqua-di-cobalt(ii)) hydrate)

Space Group:	P-1	***Cell:***	***a***	9.823(4)	***b***	11.587(4)	***c***	20.385(7)
Space Group No.:	2	***(Å,°)***	α	95.10(2)	β	92.42(1)	γ	98.90(2)
R-Factor (%):	7.13	***Temperature(K):***	173	***Density(g/cm^3):***	1.739			

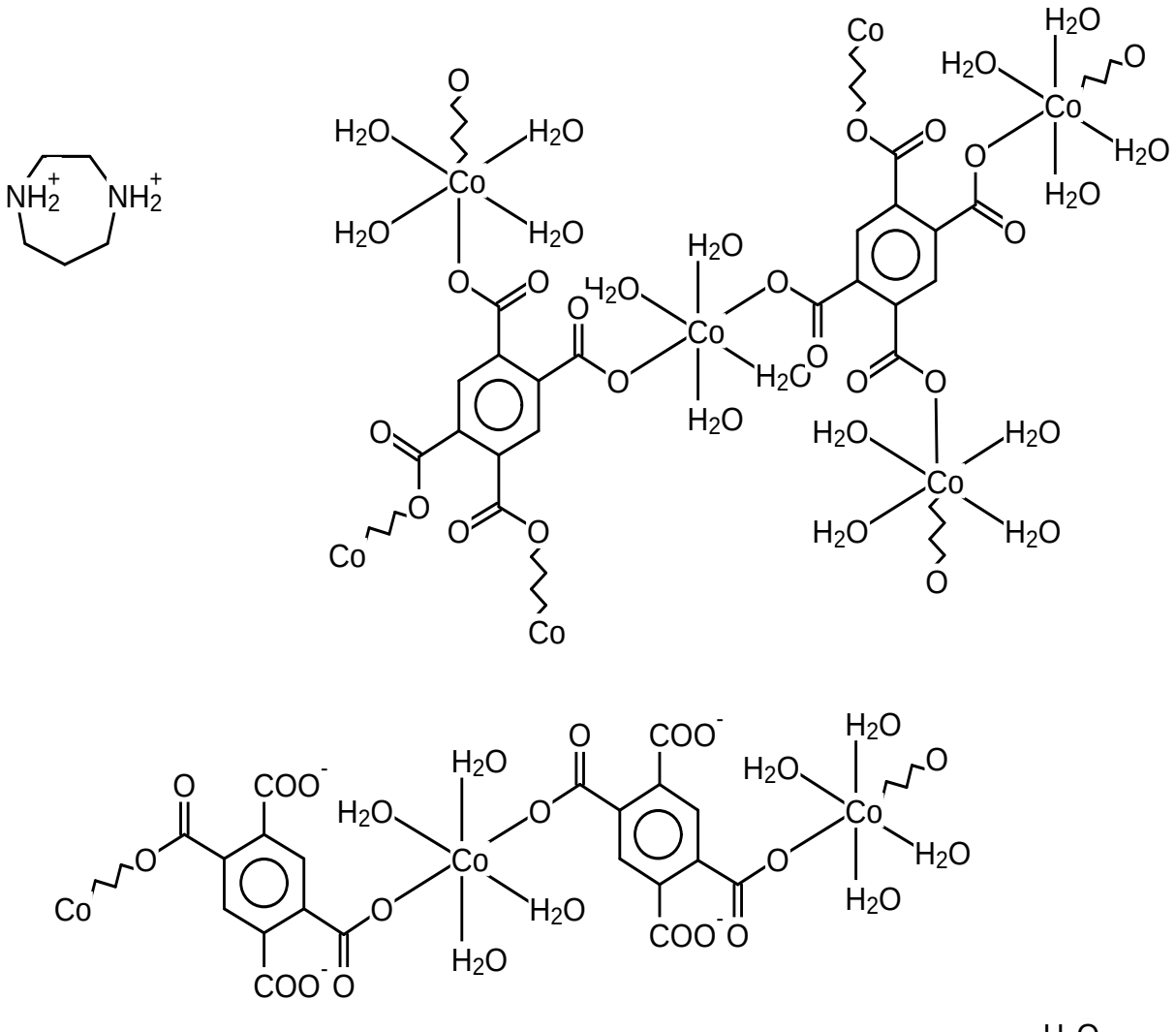

Search: search1 (Thu Nov 24 11:50:34 2016): Hit 2

BANGIH

Reference:	Deping Cheng, M.A.Khan, R.P.Houser (2002) *Cryst.Growth Des.* ,**2,**415
Formula:	$(C_5 H_{14} N_2 ^{2+})2n,n(C_{20} H_{16} Co_2 O_{22} ^{4-}),6n(H_2 O_1)$
Compound Name:	catena-(bis(Homopiperazonium) (μ_4-1,2,4,5-benzenetetracarboxylato)-(μ_2-1,2,4,5-benzenetetracarboxylato)-hexa-aqua-di-cobalt(ii) hexahydrate)

Space Group:	P-1	***Cell:***	***a***	9.776(1)	***b***	11.208(3)	***c***	11.224(2)
Space Group No.:	2	***(Å,°)***	α	60.30(1)	β	73.69(1)	γ	84.31(1)
R-Factor (%):	4.73	***Temperature(K):***	173		***Density(g/cm^3):***	1.684		

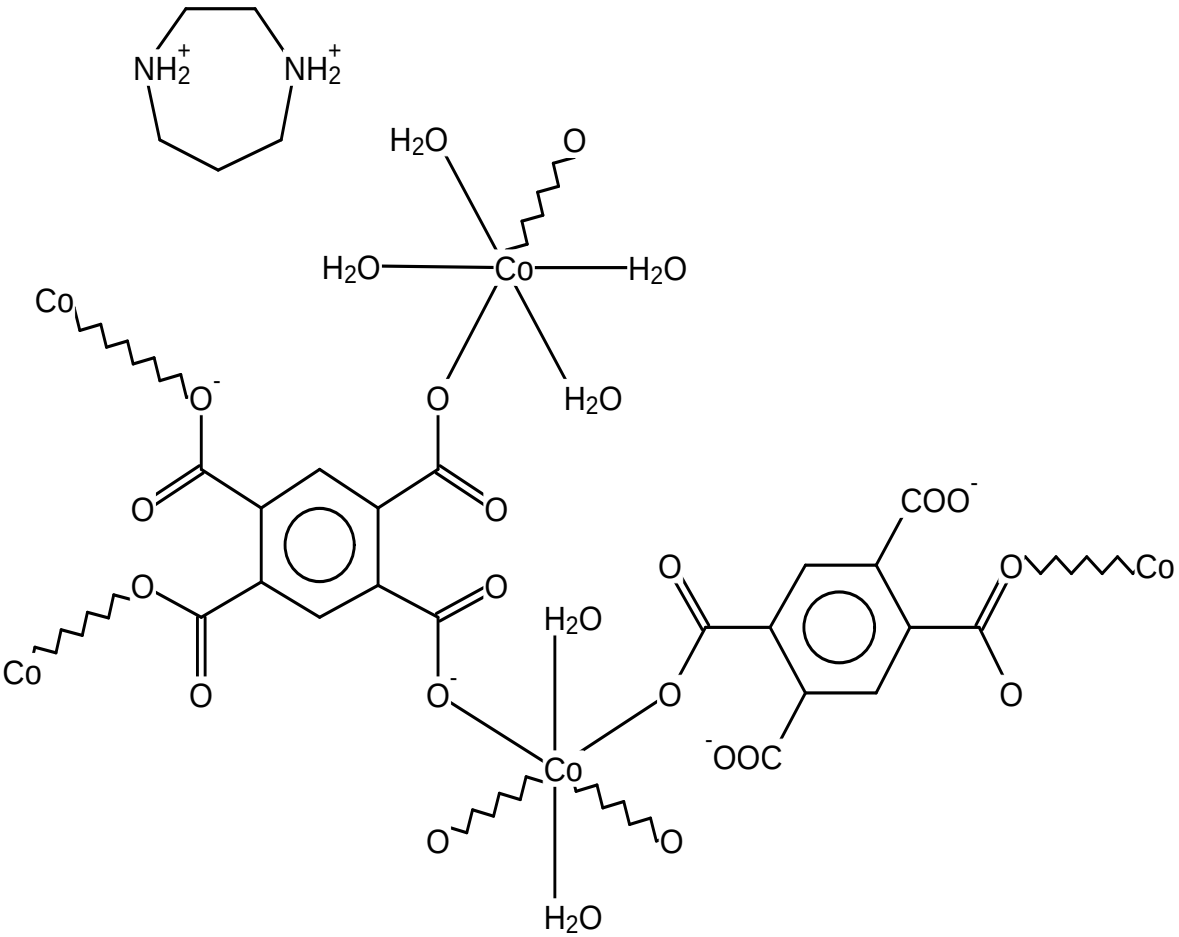

H_2O

Search: search1 (Thu Nov 24 11:50:34 2016): Hit 3

CIQGUG

Reference:	M.Camara, M.Tine, C.Daiguebonne, O.Guillou, T.Roisnel (2013) *Acta Crystallogr.,Sect.E:Struct.Rep.Online ,***69,**m680
Formula:	$(C_{10}\ H_{18}\ Co_2\ O_{16})n,8n(H_2\ O_1)$
Compound Name:	catena-((μ_4-Benzene-1,2,4,5-tetracarboxylato)-octaaqua-di-cobalt(ii) octahydrate)

Space Group:	P-1	***Cell:***	***a***	5.437(0)	***b***	9.850(0)	***c*** 10.256(0)
Space Group No.:	2	***(Å,°)***	α	96.45(0)	β	91.23(0)	γ 91.33(0)

R-Factor (%):	4.80	***Temperature(K):***	298	***Density(g/cm^3):***	1.998

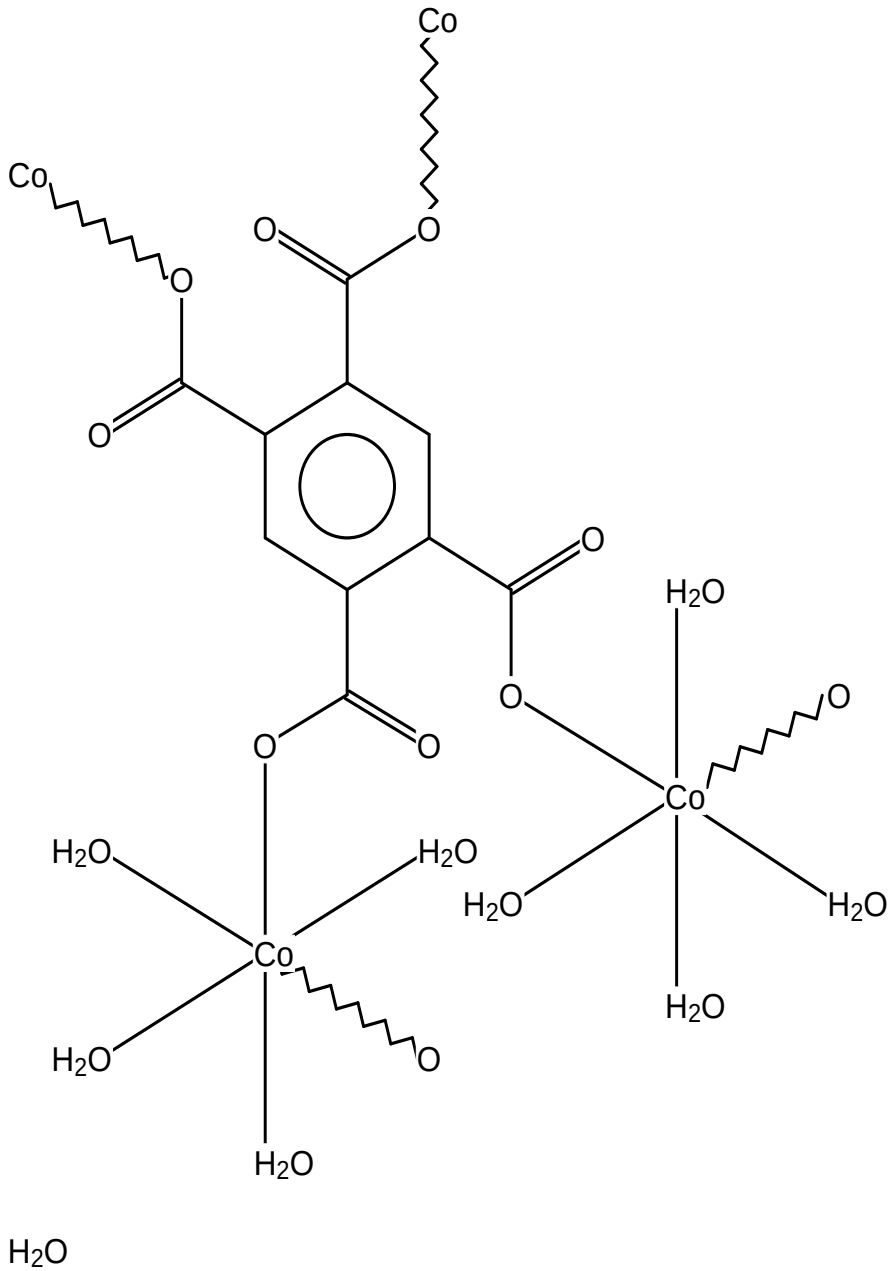

Search: search1 (Thu Nov 24 11:50:34 2016): Hit 4

HUWWAY

Reference: O.Fabelo, L.Canadillas-Delgado, J.Pasan, F.S.Delgado, F.Lloret, J.Cano, M.Julve, C.Ruiz-Perez (2009) *Inorg.Chem.* ,**48,**11342

Formula: $(C_{20}\ H_{28}\ Co_4\ O_{28})n,4n(H_2\ O_1)$

Compound Name: catena-[(μ_4-Benzene-1,2,4,5-tetracarboxylato-O,O,O',O'',O''')-(μ_4-benzene-1,2,4,5-tetracarboxylato-O,O',O'',O''')-bis(μ_2-aqua)-deca-aqua-tetra-cobalt(ii) tetrahydrate]

Space Group:	P-1	***Cell:***	***a***	6.779(0)	***b***	8.068(0)	***c*** 16.651(0)
Space Group No.:	2	***(Å,°)***	α	102.10(0)	β	92.02(0)	γ 93.51(0)
R-Factor (%):	1.93	***Temperature(K):***	293		***Density(g/cm^3):***		1.916

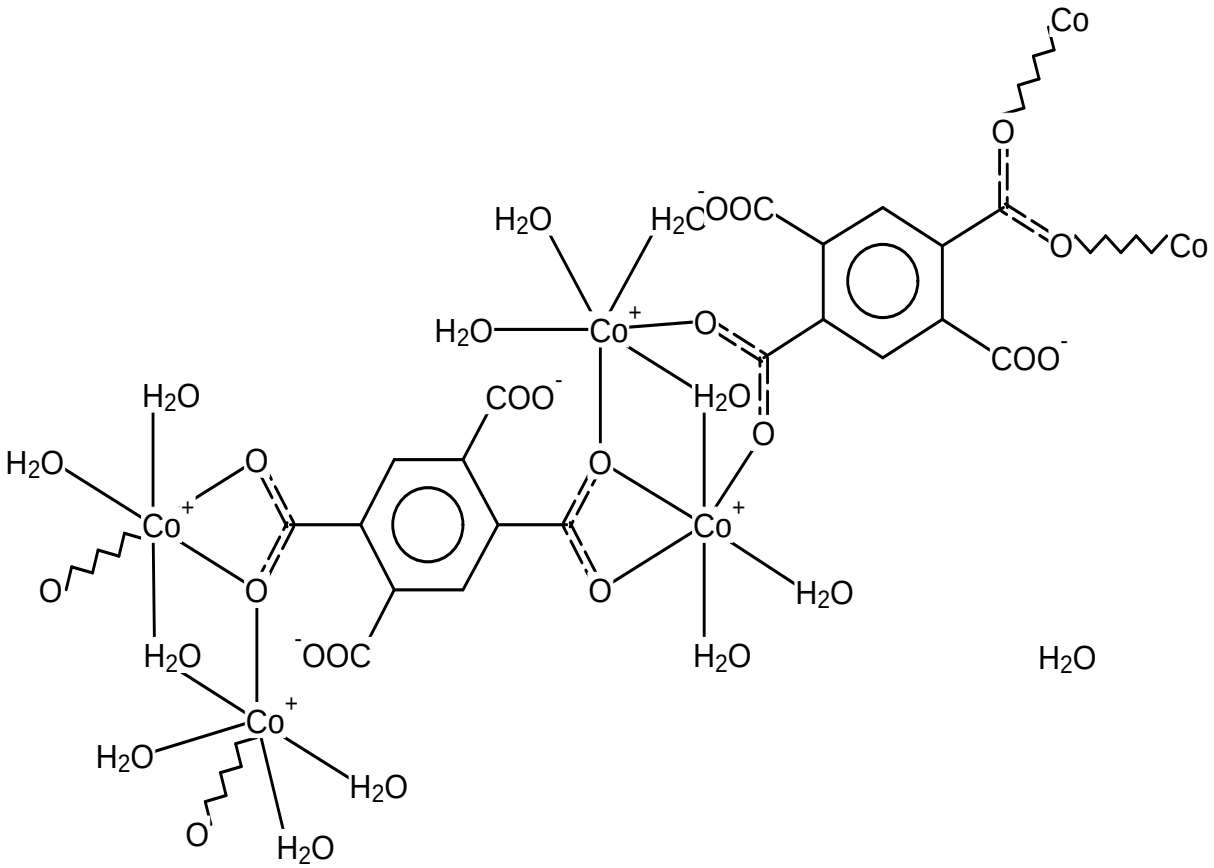

Search: search1 (Thu Nov 24 11:50:34 2016): Hit 5

IGAHED03

Reference: O.Fabelo, J.Pasan, L.Canadillis-Delgado, F.S.Delgado, F.Lloret, M.Julve, C.Ruiz-Perez (2008) *Inorg.Chem. ,***47,**8053

Formula: $(C_{10}\ H_{10}\ Co_2\ O_{12})n,2n(H_2\ O_1)$

Compound Name: catena-((μ_6-Benzene-1,2,4,5-tetracarboxylato)-bis(μ_2-aqua)-diaqua-di-cobalt(ii) dihydrate)

Space Group:	P2/n	***Cell:***	***a***	9.486(0)	***b***	6.046(0)	***c*** 14.113(0)
Space Group No.:	13	***(Å,°)***	α	90.00	β	104.90(0)	γ 90.00
R-Factor (%):	2.89	***Temperature(K):***	100		***Density(g/cm^3):***		2.021

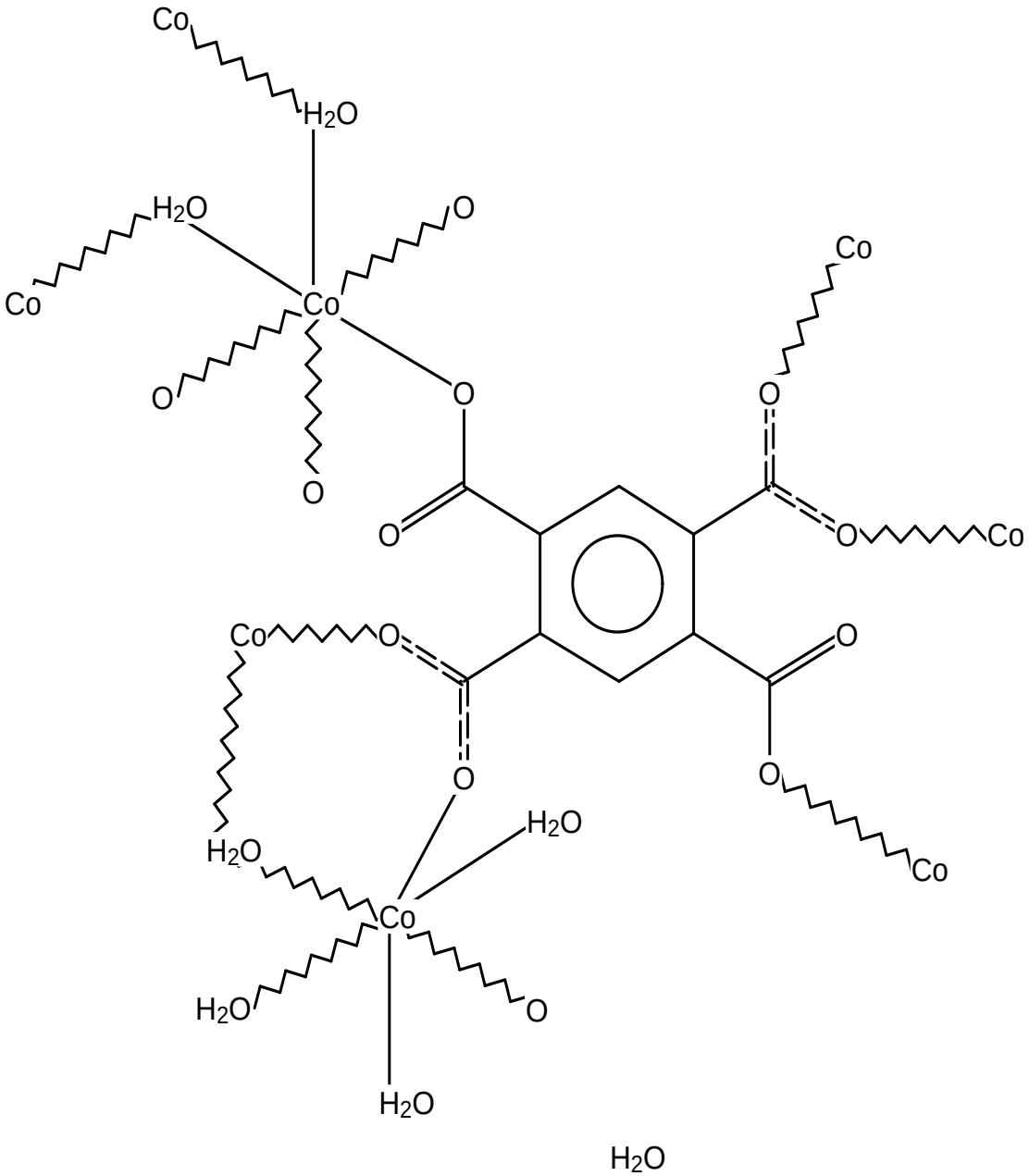

Search: search1 (Thu Nov 24 11:50:34 2016): Hit 6

LUJPOW

Reference: Miao-Tzu Ding, Jing-Yun Wu, Yen-Hsiang Liu, Juang-Lieh Lu (2009) *Inorg.Chem. ,***48,**7457

Formula: $C_{10}\,H_{22}\,Co_2\,O_{18},H_2\,O_1$

Compound Name: (μ_2-Benzene-1,2,4,5-tetracarboxylato)-decaaqua-di-cobalt(ii) monohydrate

Space Group:	P-1	***Cell:***	***a***	9.406(1)	***b***	10.215(2)	***c***	11.096(2)
Space Group No.:	2	***(Å,°)***	α	87.82(3)	β	77.29(3)	γ	70.21(3)
R-Factor (%):	2.95	***Temperature(K):***	293		***Density(g/cm^3):***	1.923		

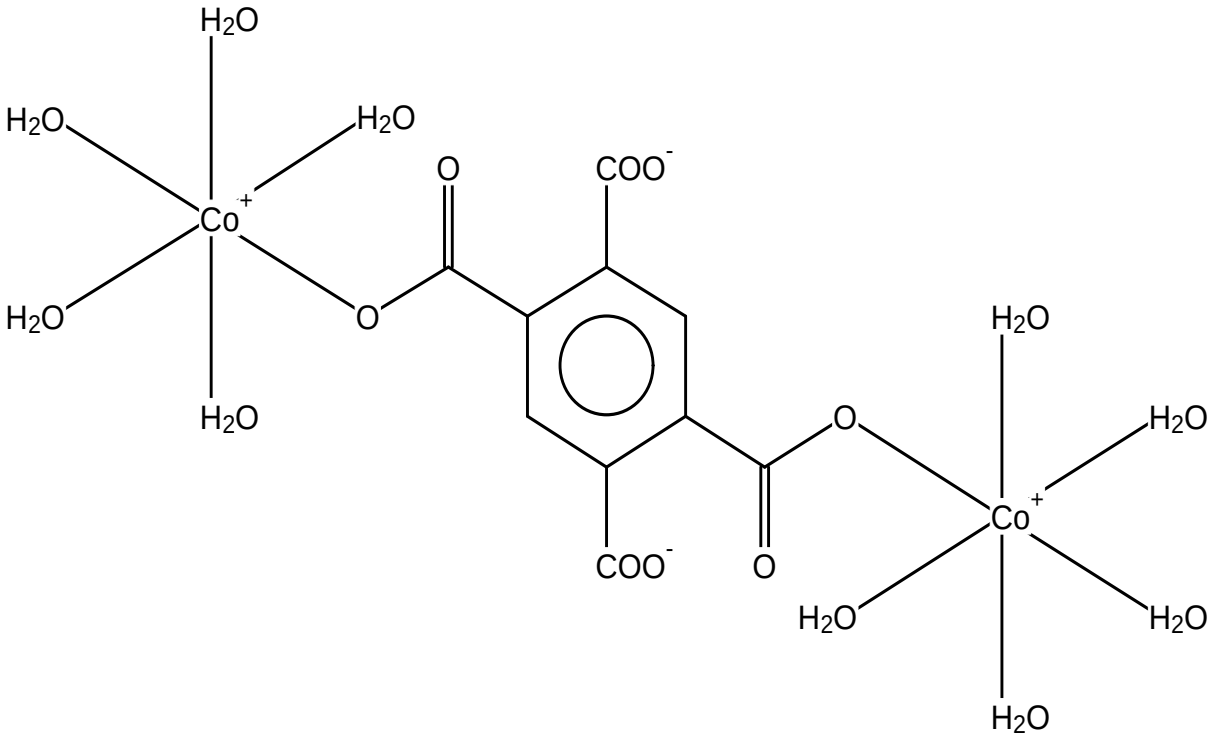

H_2O

Search: search1 (Thu Nov 24 11:50:34 2016): Hit 7

METQOR

Reference: R.Murugavel, D.Krishnamurthy, M.Sathiyendiran (2002) *J.Chem.Soc.,Dalton Trans.* ,34

Formula: $(C_4 H_{12} N_2 ^{2+})n,n(C_{10} H_{10} Co_1 O_{12} ^{2-}),4n(H_2 O_1)$

Compound Name: catena-(Piperazinedi-ium (μ_2-1,2,4,5-benzenetetracarboxylato-O,O')-tetra-aqua-cobalt tetrahydrate)

Space Group:	P-1	***Cell:***	***a***	6.867(1)	***b***	9.114(1)	***c*** 9.698(1)
Space Group No.:	2	***(Å,°)***	α	104.63(3)	β	98.04(3)	γ 109.66(3)
R-Factor (%):	4.37	***Temperature(K):***	213	***Density(g/cm^3):***	1.677		

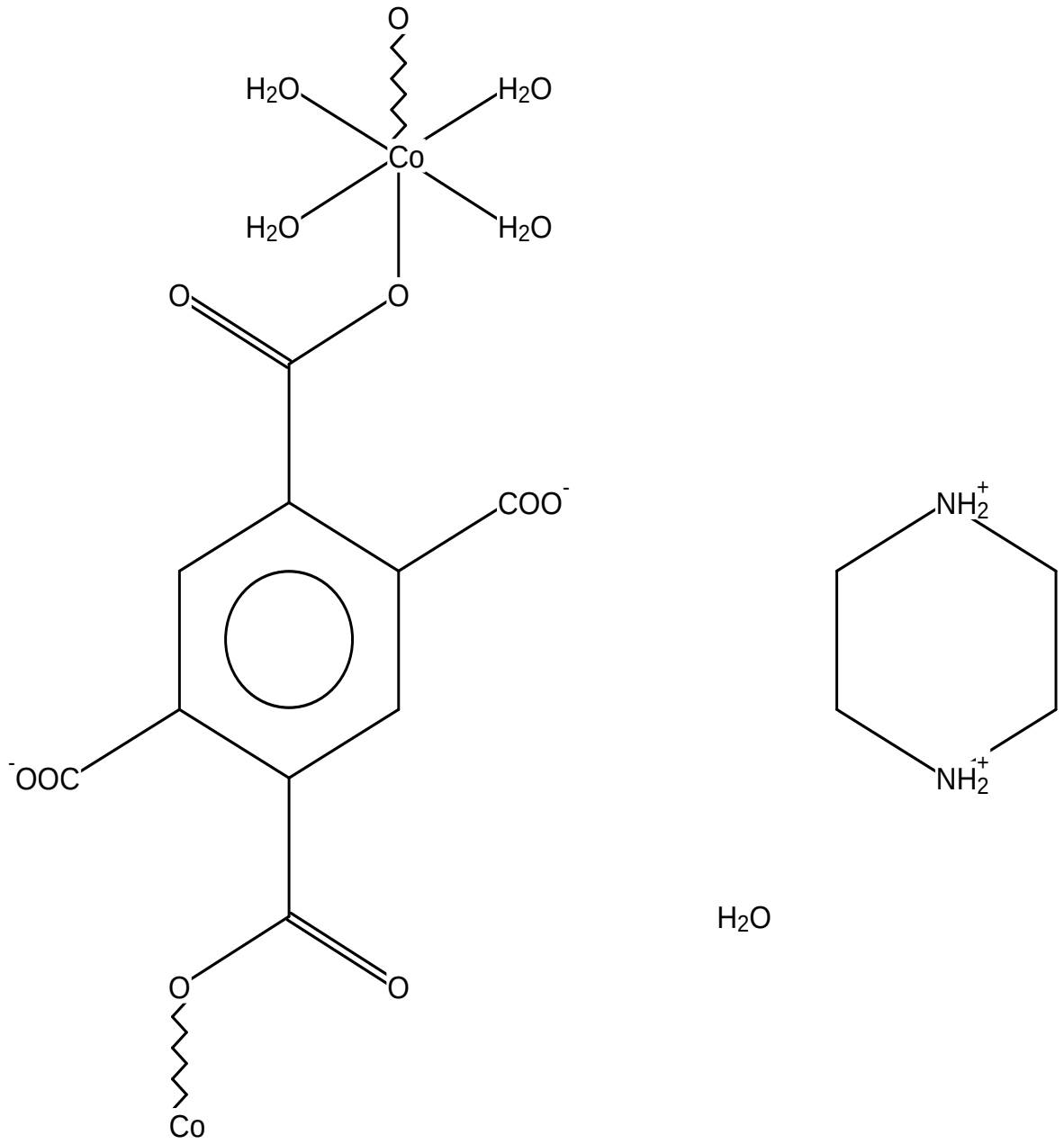

Search: search1 (Thu Nov 24 11:50:34 2016): Hit 8

METQOR01

Reference:	H.Aghabozorg, F.Mahfoozi, M.A.Sharif, A.Shokrollahi, S.Derki, M.Shamsipur, H.R.Khavasi (2010) *J.Iran.Chem.Soc. ,***7,**727
Formula:	$(C_{10}\ H_{10}\ Co_1\ O_{12}\ ^{2-})n,n(C_4\ H_{12}\ N_2\ ^{2+}),4n(H_2\ O_1)$
Compound Name:	catena-(Piperazinedi-ium (μ_2-benzene-1,2,4,5-tetracarboxylato)-tetra-aqua-cobalt tetrahydrate)

Space Group:	P-1	***Cell:***	***a***	6.891(0)	***b***	9.133(0)	***c***	9.723(1)
Space Group No.:	2	***(Å,°)***	α	104.85(0)	β	98.15(0)	γ	109.65(0)

R-Factor (%):	3.30	***Temperature(K):***	293	***Density(g/cm^3):***	1.667

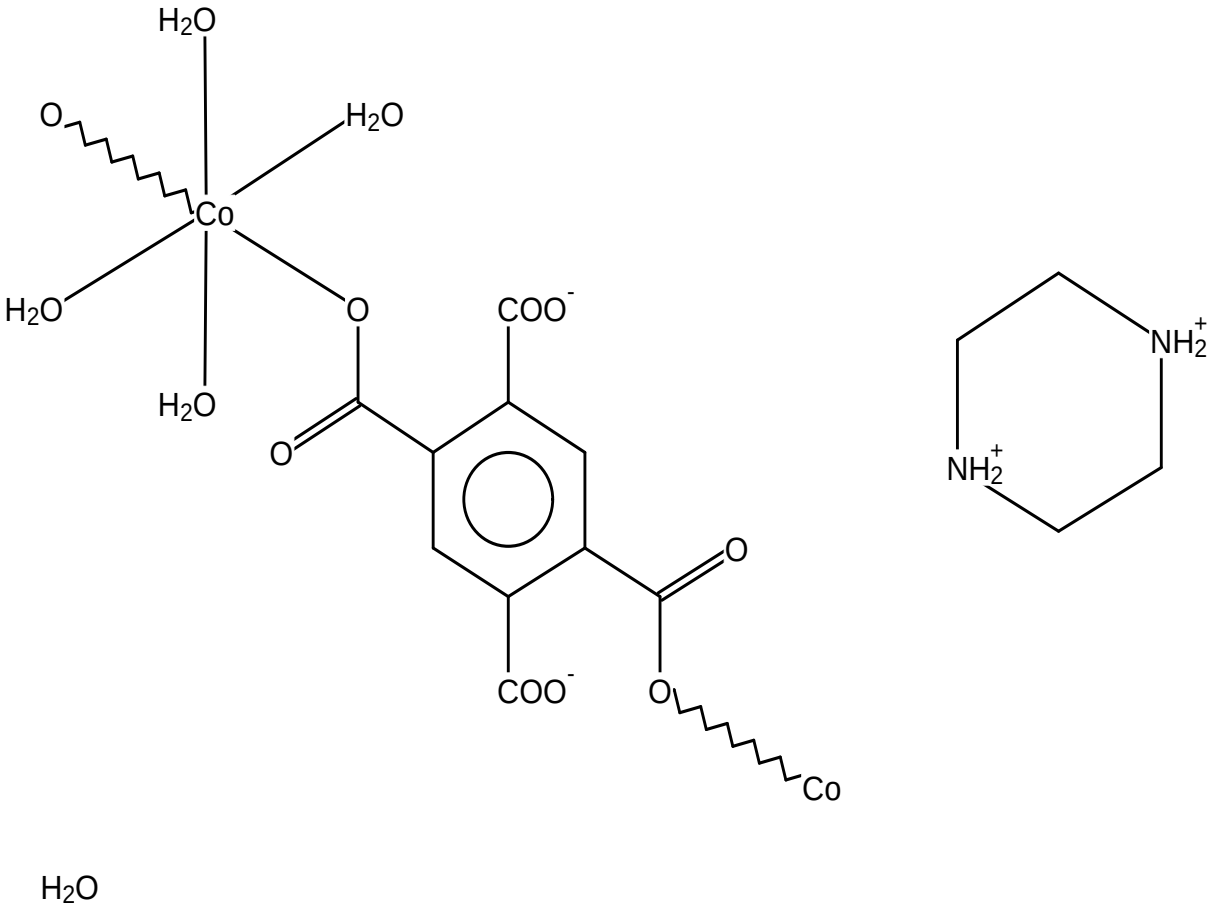

H_2O

Search: search1 (Thu Nov 24 11:50:34 2016): Hit 9

QORDIK

Reference: F.D.Rochon, G.Massarweh (2001) *Inorg.Chim.Acta* ,**314,** 163

Formula: $C_{10}\ H_{22}\ Co_2\ O_{18}$,6($H_2\ O_1$)

Compound Name: (μ_2-Benzene-1,4-dicarboxylato-2,5-dicarboxylate-O,O')-deca-aqua-di-cobalt(ii) hexahydrate

Space Group:	C2/c	***Cell:***	***a***	17.845(7)	***b***	7.440(2)	***c***	19.064(5)
Space Group No.:	15	***(Å,°)***	α	90.00	β	91.94(2)	γ	90.00

R-Factor (%): 3.57 ***Temperature(K):*** 295 ***Density(g/cm^3):*** 1.723

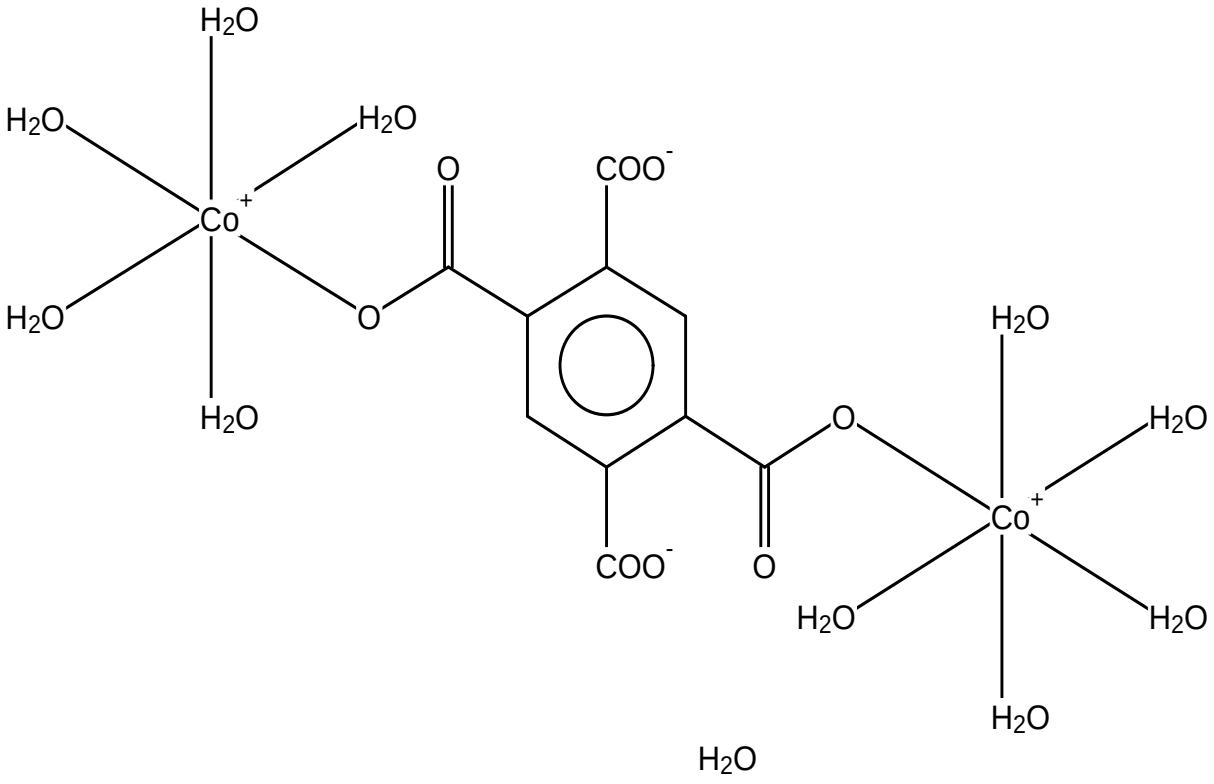

Search: search1 (Thu Nov 24 11:50:34 2016): Hit 10

QORDUW

Reference: F.D.Rochon, G.Massarweh (2001) *Inorg.Chim.Acta* ,**314,** 163

Formula: $C_{10}H_{22}Mn_2O_{18},C_{10}H_{22}Co_2O_{18},2(H_2O_1)$

Compound Name: (μ_2-Benzene-1,4-dicarboxylato-2,5-dicarboxylate-O,O')-deca-aqua-di-cobalt(ii) (μ_2-benzene-1,4-dicarboxylato-2,5-dicarboxylate-O,O')-deca-aqua-di-manganese(ii) dihydrate

Space Group:	P-1	***Cell:***	***a***	9.453(2)	***b***	10.268(2)	***c***	11.192(2)
Space Group No.:	2	***(Å,°)***	α	87.66(1)	β	77.53(1)	γ	70.09(2)

R-Factor (%): 4.27 ***Temperature(K):*** 295 ***Density(g/cm^3):*** 1.873

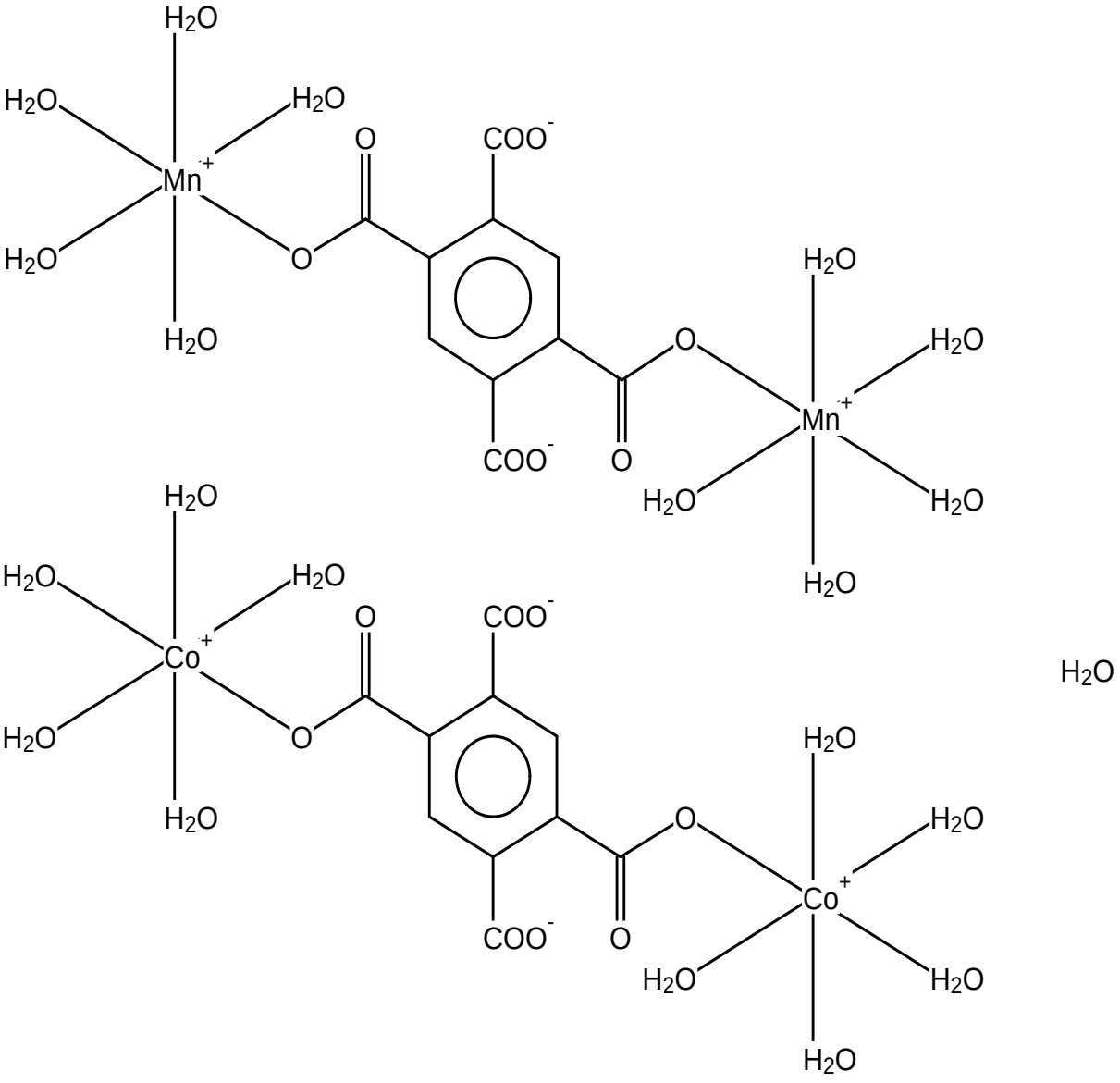

Search: search1 (Thu Nov 24 11:50:34 2016): Hit 11

QOYMEX

Reference:	Jing-Yun Wu, Miao-Tzu Ding, Yuh-Sheng Wen, Yen-Hsiang Liu, Kuang-Lieh Lu (2009) *Chem.-Eur.J. ,***15,**3604
Formula:	$(Cs_1{}^{1+})2n,n(C_{10}H_{10}Co_1O_{12}{}^{2-}),2n(H_2O_1)$
Compound Name:	catena-(Di-cesium (μ_2-benzene-1,2,4,5-tetracarboxylato)-tetraaqua-cobalt(ii) dihydrate)

Space Group:	C2/c	***Cell:***	***a***	15.270(3)	***b***	6.703(1)	***c***	18.718(4)
Space Group No.:	15	***(Å,°)***	α	90.00	β	105.53(3)	γ	90.00
R-Factor (%):	2.66	***Temperature(K):***		293	***Density(g/cm^3):***			2.458

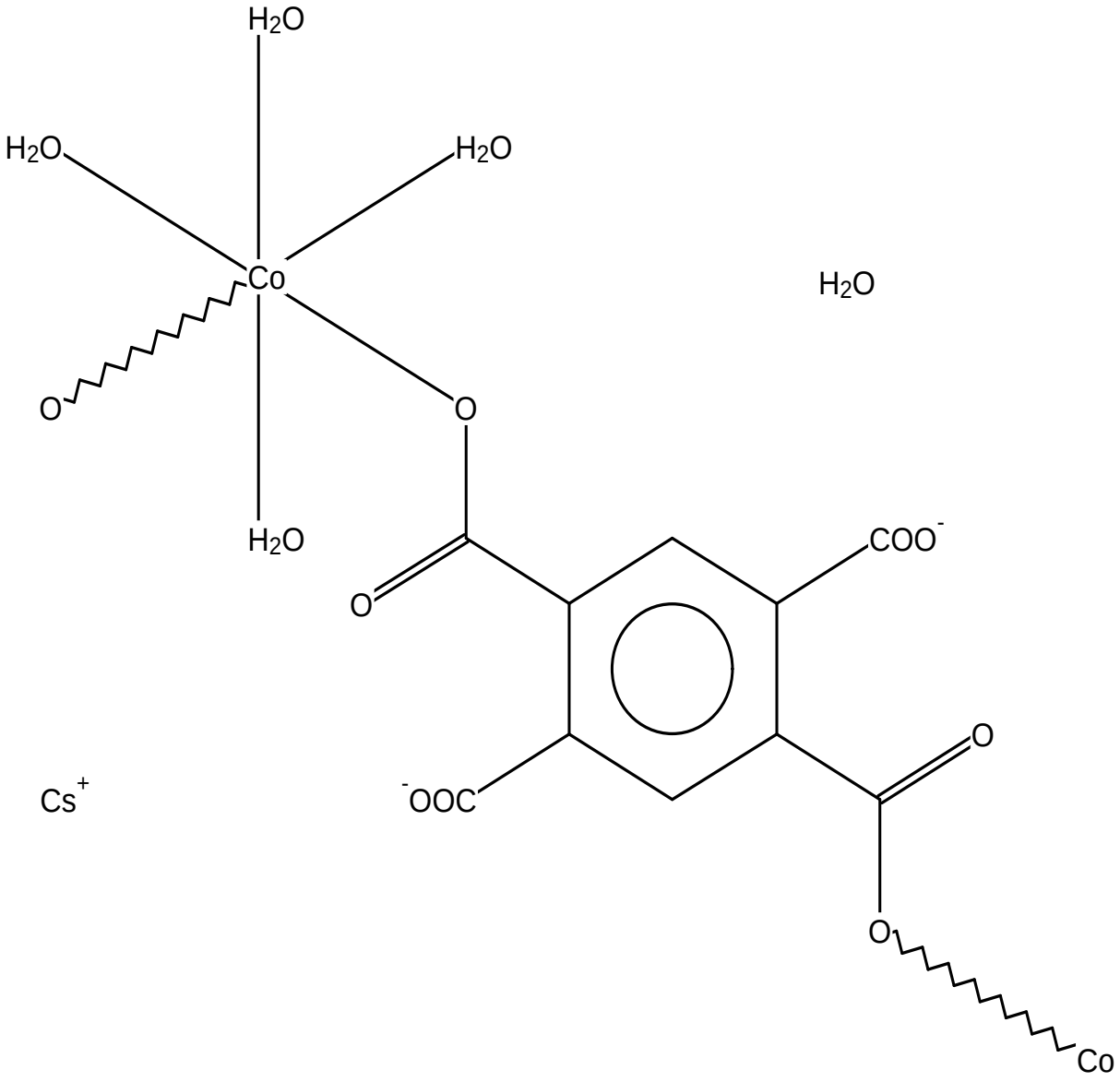

Search: search1 (Thu Nov 24 11:50:34 2016): Hit 12

RUPYEH

Reference:	L.K.Sposato, R.L.LaDuca (2009) *Acta Crystallogr.,Sect.E:Struct.Rep.Online* ,**65,**m1709
Formula:	$(C_{16}\ H_{22}\ N_4\ ^{2+})n,n(C_{10}\ H_{10}\ Co_1\ O_{12}\ ^{2-}),2n(H_2\ O_1)$
Compound Name:	catena-(1,4-bis(pyridin-4-ylmethyl)piperazinediium (μ_2-benzene-1,2,4,5-tetracarboxylato-1κO^1:2κO^4)-tetra-aqua-di-cobaltate dihydrate)
Synonym:	catena-(1,4-bis(4-pyridylmethyl)piperazinediium (μ_2-pyromellitato)-tetra-aqua-cobalt(ii) dihydrate)

Space Group:	P-1	***Cell:***	***a***	7.278(2)	***b***	9.752(3)	***c*** 11.257(3)
Space Group No.:	2	***(Å,°)***	α	66.73(0)	β	75.17(0)	γ 83.36(0)

R-Factor (%):	5.03	***Temperature(K):***	173	***Density(g/cm^3):***	1.609

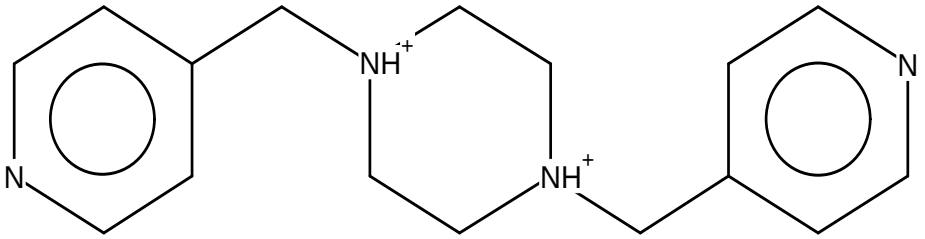

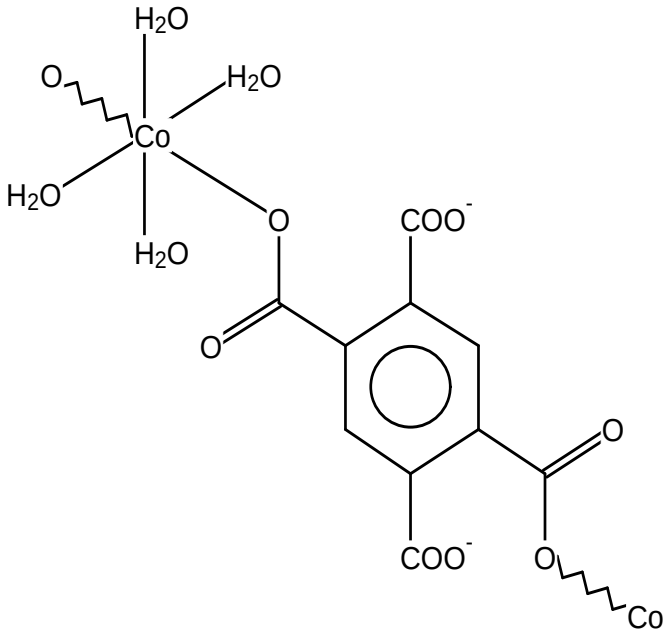

H_2O

Search: search1 (Thu Nov 24 11:50:34 2016): Hit 13

SIJJUR

Reference: O.Fabelo, J.Pasan, F.Lloret, M.Julve, C.Ruiz-Perez (2007) *CrystEngComm* ,**9,**815

Formula: $C_{30}\ H_{34}\ Co_2\ N_4\ O_{20}$,4($H_2\ O_1$)

Compound Name: (μ_2-benzene-1,2,4,5-tetracarboxylato)-octa-aqua-bis(4,4'-bipyridine 1,1'-dioxide)-di-cobalt(ii) tetrahydrate

Space Group:	P-1	***Cell:***	***a***	8.412(1)	***b***	8.530(0)	***c***	13.321(3)
Space Group No.:	2	***(Å,°)***	α	85.33(1)	β	76.03(1)	γ	80.49(1)

R-Factor (%): 3.68 ***Temperature(K):*** 293 ***Density(g/cm^3):*** 1.745

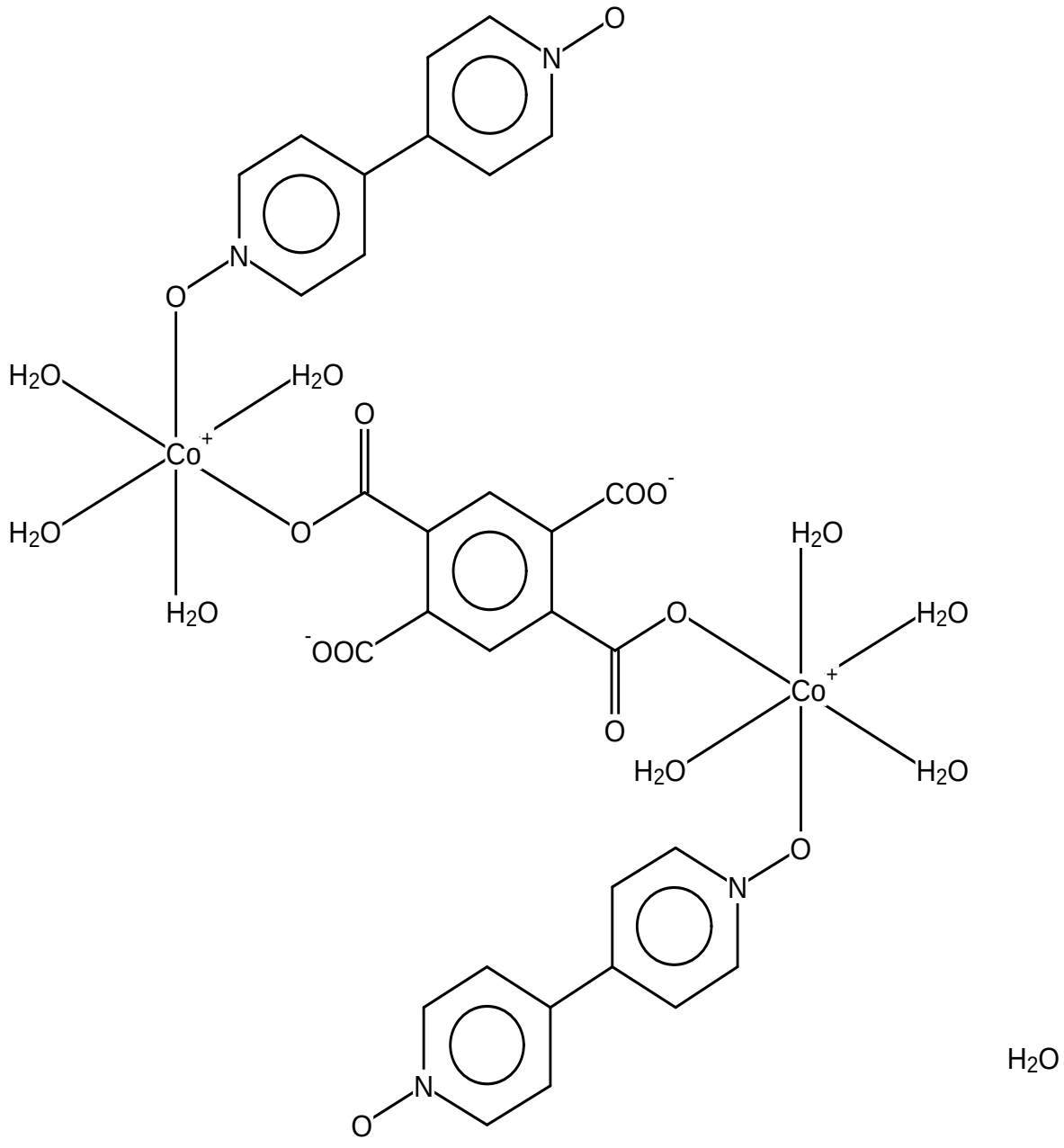

Search: search1 (Thu Nov 24 11:50:34 2016): Hit 14

VAWXAS

Reference:	D.Poleti, Lj.Karanovic (1989) *Acta Crystallogr.,Sect.C:Cryst.Struct.Commun. ,* **45,**1716
Formula:	$(C_{10}\ H_{10}\ Co_1\ O_{12}\ ^{2-})n,n(H_{12}\ Co_1\ O_6\ ^{2+}),7.36n(H_2\ O_1)$
Compound Name:	catena(Hexa-aqua-cobalt(ii) tetra-aqua-(μ_2-1,2,4,5-benzenecarboxylato-O,O')-cobalt(ii) hydrate)

Space Group:	P-1	***Cell:***	***a***	9.972(4)	***b*** 10.921(4)	***c***	6.852(2)
Space Group No.:	2	***(Å,°)***	α	104.89(2)	β 103.63(2)	γ	93.00(2)

R-Factor (%):	5.10	***Temperature(K):***	295	***Density(g/cm^3):***	1.625

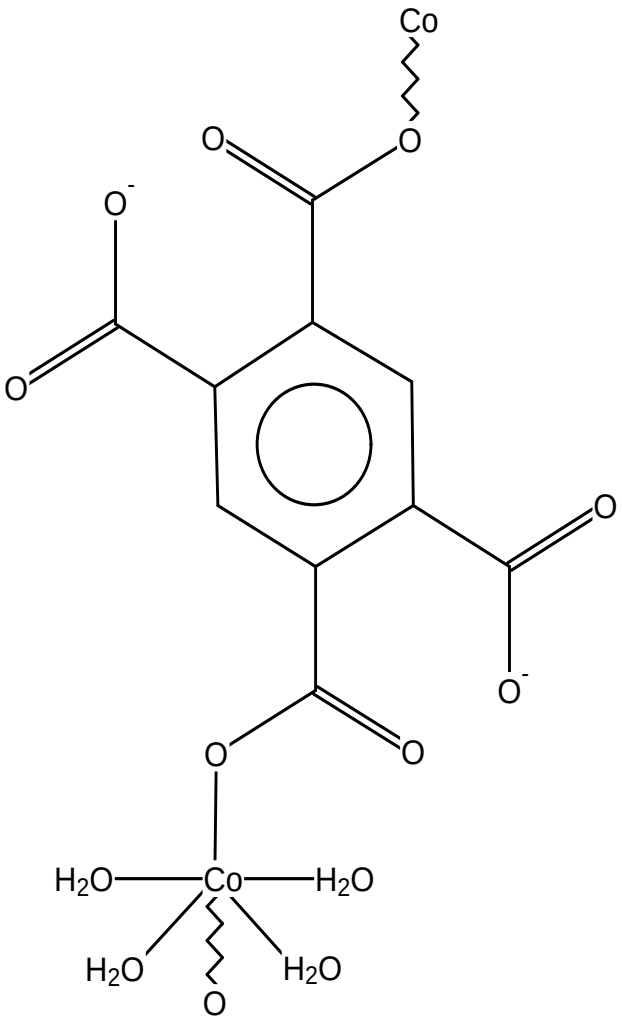

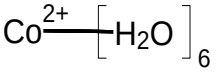

H_2O

Search: search1 (Thu Nov 24 11:50:34 2016): Hit 15

VAWXAS01

Reference: C.Robl, S.Hentschel (1991) *Mater.Res.Bull.* ,**26,**1355

Formula: $(C_{10}\ H_{10}\ Co_1\ O_{12}\ ^{2-})n,n(H_{12}\ Co_1\ O_6\ ^{2+}),8n(H_2\ O_1)$

Compound Name: catena((μ$_2$-Pyromellitato)-tetra-aqua-cobalt hexa-aqua-cobalt octahydrate)

Space Group:	P-1	***Cell:***	***a***	6.864(1)	***b***	10.000(20)	***c*** 10.932(2)
Space Group No.:	2	***(Å,°)***	α	93.00(2)	β	104.86(1)	γ 103.59(1)

R-Factor (%): 3.35 ***Temperature(K):*** 295 ***Density(g/cm^3):*** 1.642

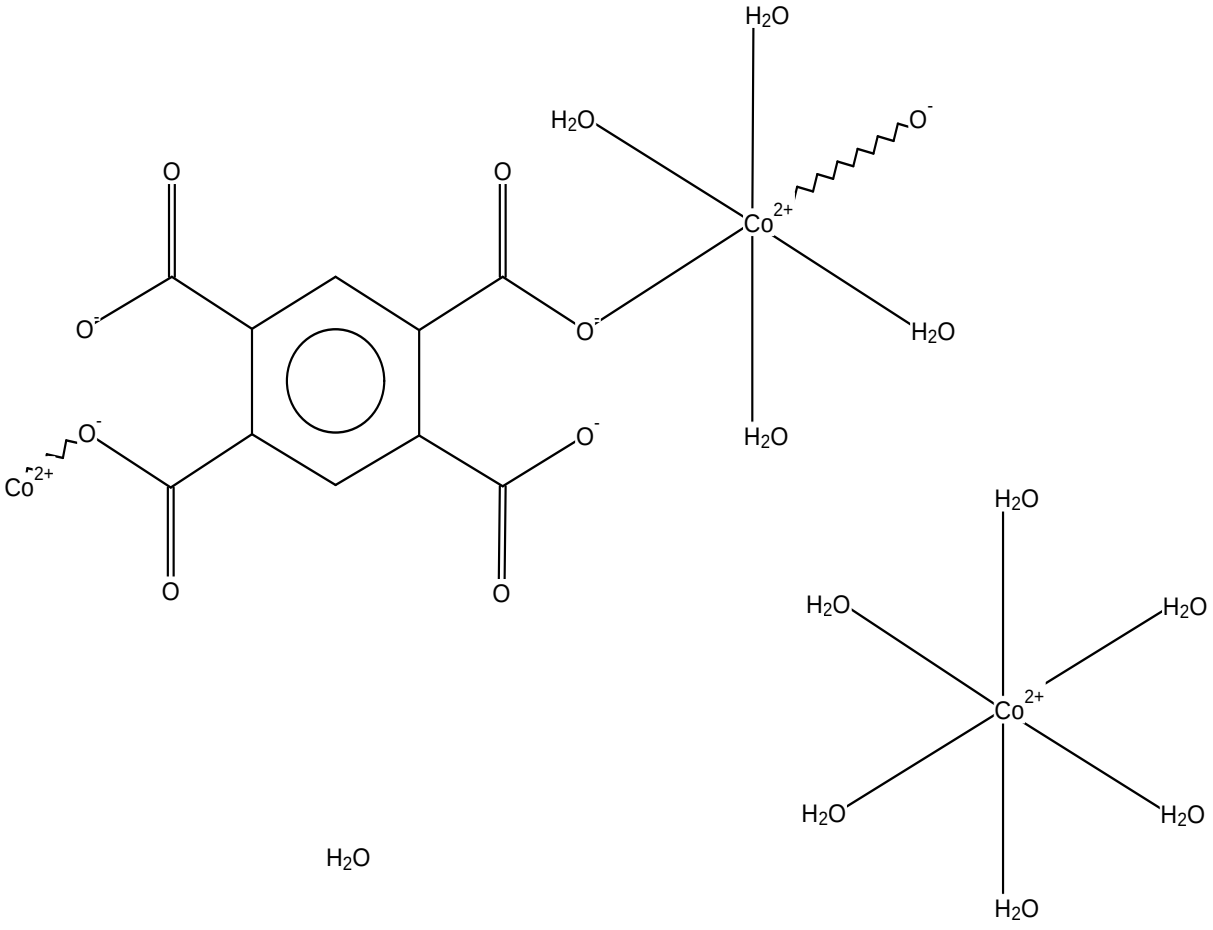

Search: search1 (Thu Nov 24 11:50:34 2016): Hit 16

VAWXAS02

Reference:	M.Zeller, A.R.Chema, P.S.Szalay, A.D.Hunter (2005) *J.Chem.Cryst. ,***35,**433
Formula:	$(C_{10}\ H_{10}\ Co_1\ O_{12}\ ^{1-})n,n(H_{12}\ Co_1\ O_6\ ^{1+}),7.7n(H_2\ O_1)$
Compound Name:	catena-(Hexa-aqua-cobalt(ii) (μ_2-benzenetetracarboxylato-O,O')-tetra-aqua-cobalt(ii) hydrate)

Space Group:	P-1	***Cell:***	***a***	6.859(0)	***b***	9.969(1)	***c*** 10.923(1)
Space Group No.:	2	***(Å,°)***	α	93.02(0)	β	104.88(0)	γ 103.70(0)

R-Factor (%):	3.86	***Temperature(K):***	293	***Density(g/cm^3):***	1.638

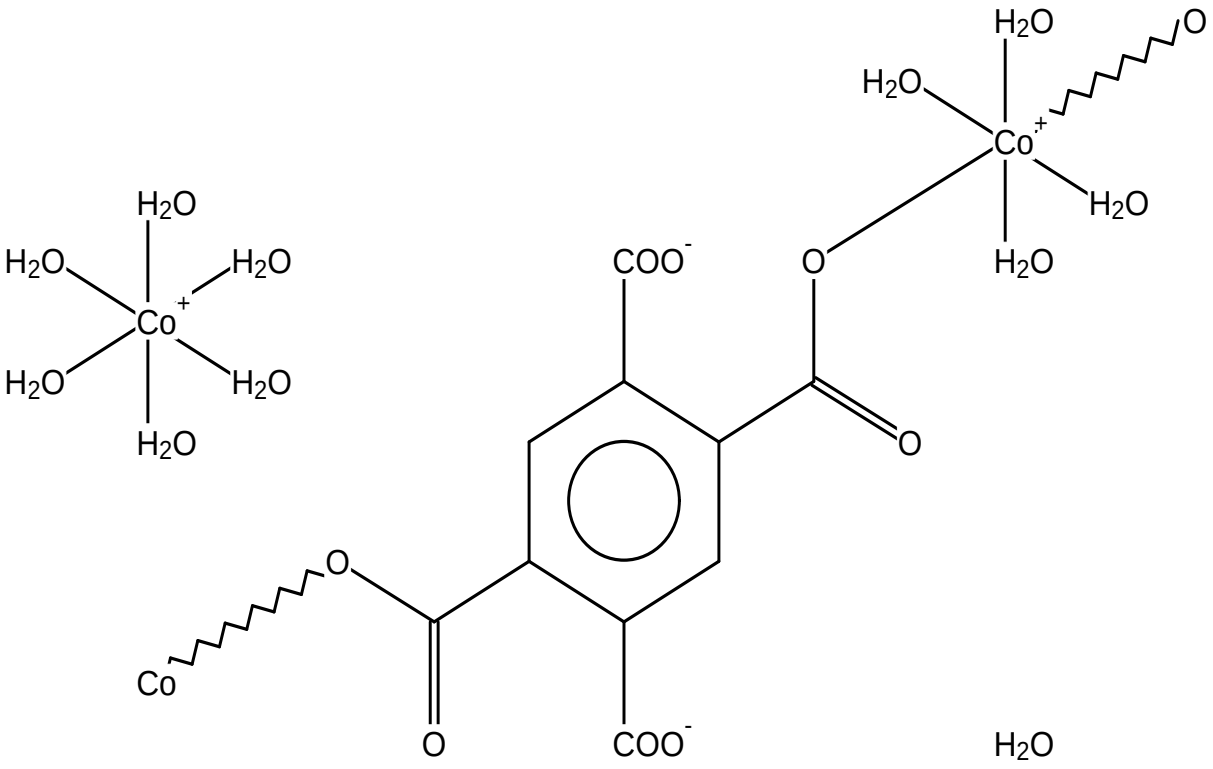

Search: search1 (Thu Nov 24 11:50:34 2016): Hit 17

VAWXAS03

Reference:	A.M.Atria, M.T.Garland, R.Baggio (2013) *J.Chil.Chem.Soc.* ,**58,**1576
Formula:	$(C_{10}\ H_{10}\ Co_1\ O_{12}\ ^{2-})n,n(H_{12}\ Co_1\ O_6\ ^{2+}),8n(H_2\ O_1)$
Compound Name:	catena-[hexa-aqua-cobalt (μ_2-benzene-1,2,4,5-tetracarboxylato)-tetra-aqua-cobalt octahydrate]

Space Group:	P-1	***Cell:***	***a***	10.664(4)	***b***	11.309(4)	***c*** 13.321(3)
Space Group No.:	2	***(Å,°)***	α	109.03(3)	β	111.72(1)	γ 93.16(4)
R-Factor (%):	3.68	***Temperature(K):***	150	***Density(g/cm^3):***	1.663		

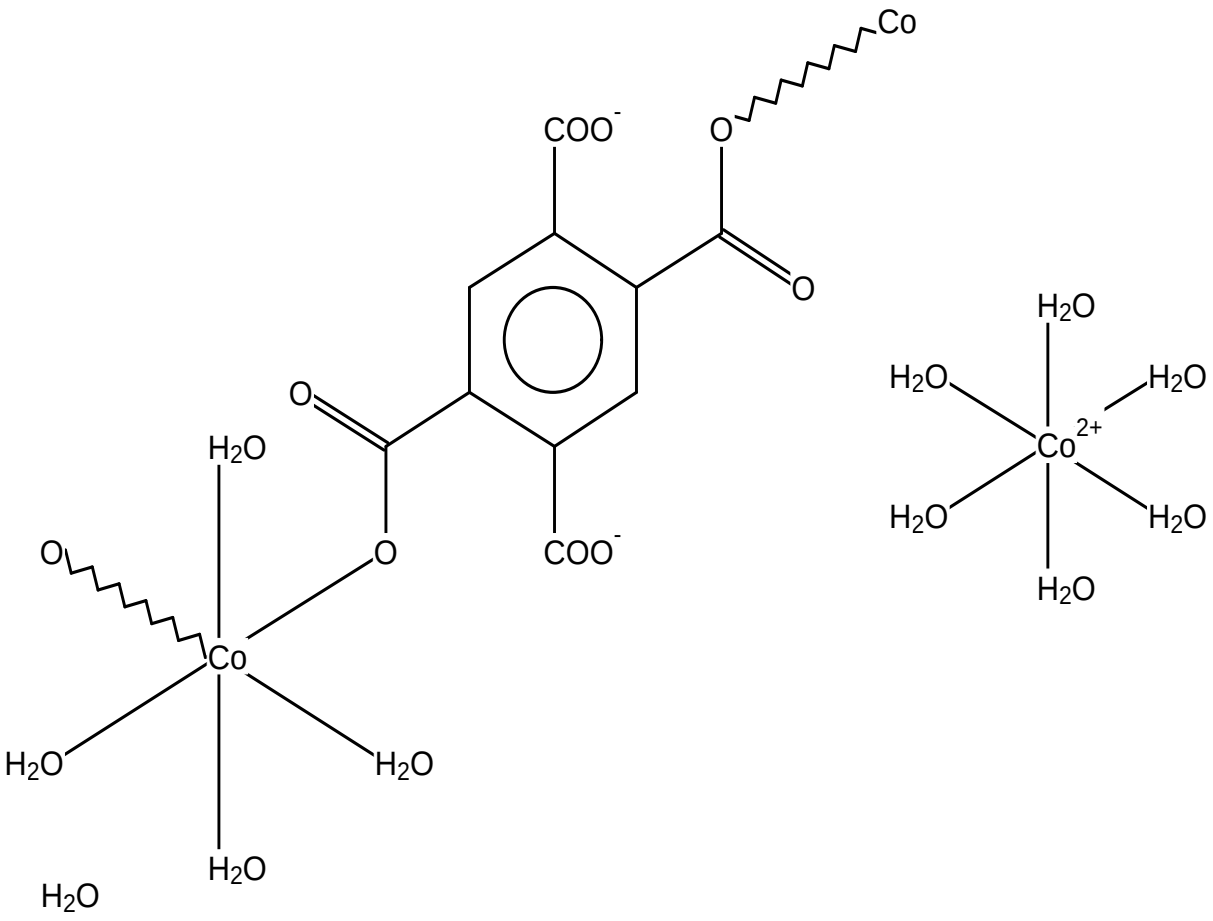

Search: search1 (Thu Nov 24 11:50:34 2016): Hit 18

XESSIY

Reference: A.Majumder, V.Gramlich, G.M.Rosair, S.R.Batten, J.D.Masuda, M.S.El Fallah, J.Ribas, J.-P.Sutter, C.Desplanches, S.Mitra (2006) *Cryst.Growth Des.* ,**6,**2355

Formula: $(C_{10}\ H_{12}\ Co_1\ O_{12})n,2n(C_5\ H_6\ N_2),2n(H_2\ O_1)$

Compound Name: catena-((μ_2-Dihydrogen 1,2,4,5-benzenetetracarboxylato-O,O')-tetra-aqua-cobalt(ii) bis(4-aminopyridine) dihydrate)

Space Group:	P-1	***Cell:***	***a***	7.272(6)	***b***	9.361(6)	***c*** 10.642(9)
Space Group No.:	2	***(Å,°)***	α	115.08(5)	β	105.96(6)	γ 95.38(6)

R-Factor (%): 4.15 ***Temperature(K):*** 293 ***Density(g/cm^3):*** 1.648

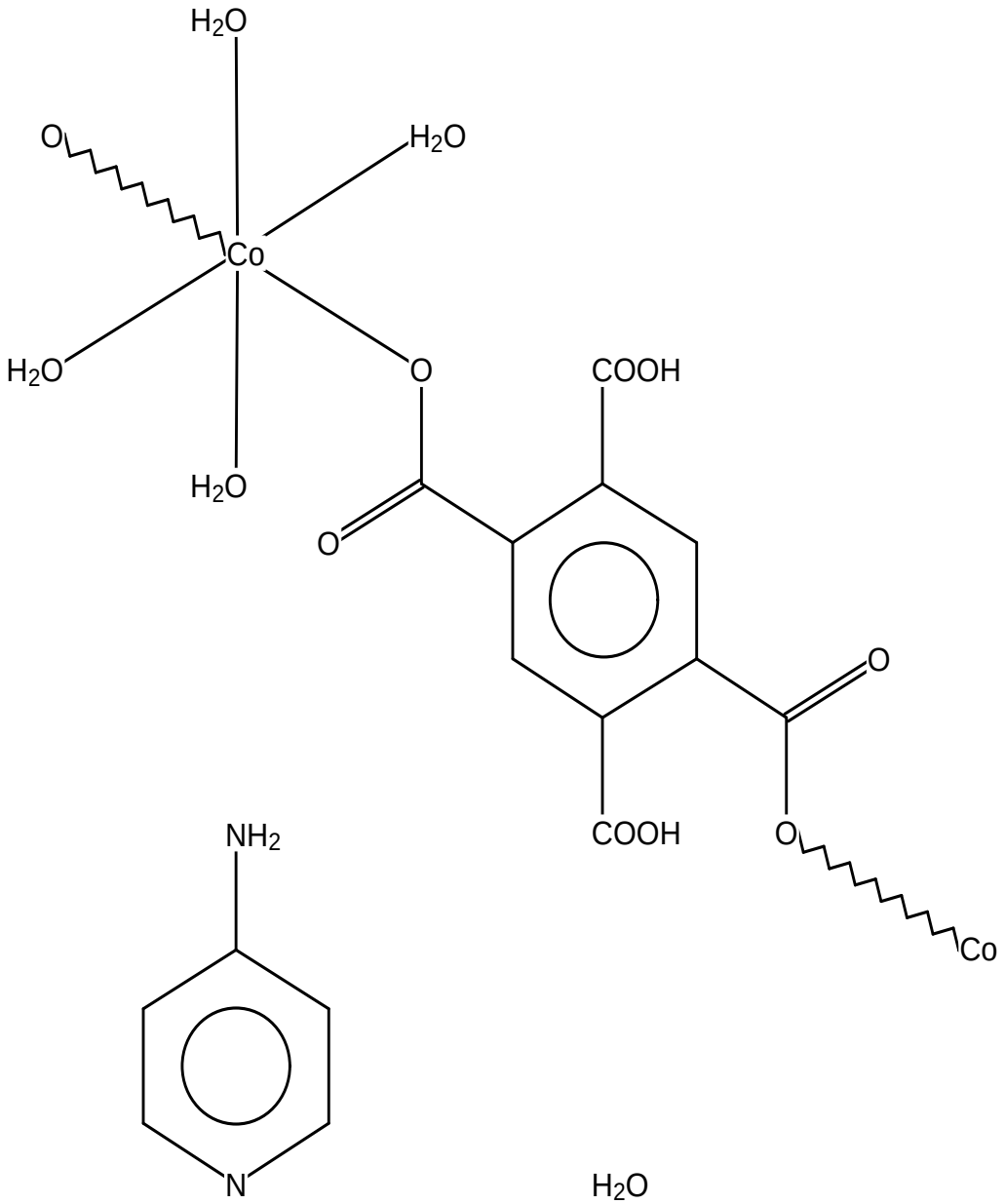

Search: search1 (Thu Nov 24 11:50:34 2016): Hit 19

XOJMAL

Reference: O.Fabelo, J.Pasan, L.Canadillas-Delgado, F.S.Delgado, A.Labrador, F.Lloret, M.Julve, C.Ruiz-Perez (2008) *Cryst.Growth Des.* , **8,**3984

Formula: $(C_{10}\ H_{18}\ Co_2\ O_{16})n,4n(H_2\ O_1)$

Compound Name: catena-((μ_4-Benzene-1,2,4,5-tetracarboxylato-O,O',O'',O''')-octa-aqua-di-cobalt(ii) tetrahydrate)

Space Group:	P-1	***Cell:***	***a***	5.429(1)	***b***	9.829(1)	***c*** 10.230(3)
Space Group No.:	2	***(Å,°)***	α	96.45(1)	β	91.23(2)	γ 91.34(1)

R-Factor (%): 7.74 ***Temperature(K):*** 293 ***Density(g/cm^3):*** 1.789

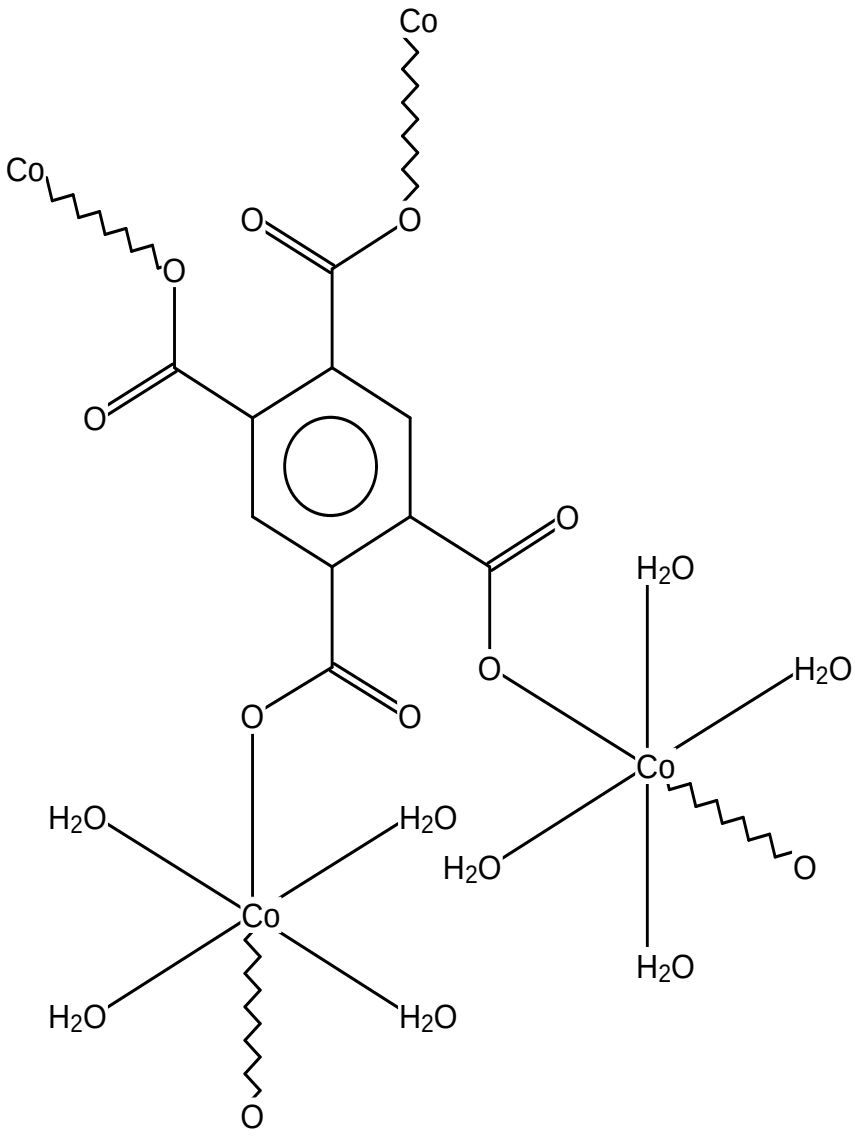

H_2O

Search: search1 (Thu Nov 24 11:50:34 2016): Hit 20

XOJMAL01

Reference: O.Fabelo, J.Pasan, L.Canadillas-Delgado, F.S.Delgado, A.Labrador, F.Lloret, M.Julve, C.Ruiz-Perez (2008) *Cryst.Growth Des.* , **8,**3984

Formula: $(C_{10}\ H_{18}\ Co_2\ O_{16})n,4n(H_2\ O_1)$

Compound Name: catena-((μ_4-Benzene-1,2,4,5-tetracarboxylato-O,O',O'',O''')-octa-aqua-di-cobalt(ii) tetrahydrate)

Space Group:	P-1	***Cell:***	***a***	10.847(2)	***b***	11.107(2)	***c***	11.483(2)
Space Group No.:	2	***(Å,°)***	α	82.93(3)	β	63.02(3)	γ	62.12(3)

R-Factor (%): 3.24 ***Temperature(K):*** 100 ***Density(g/cm^3):*** 1.792

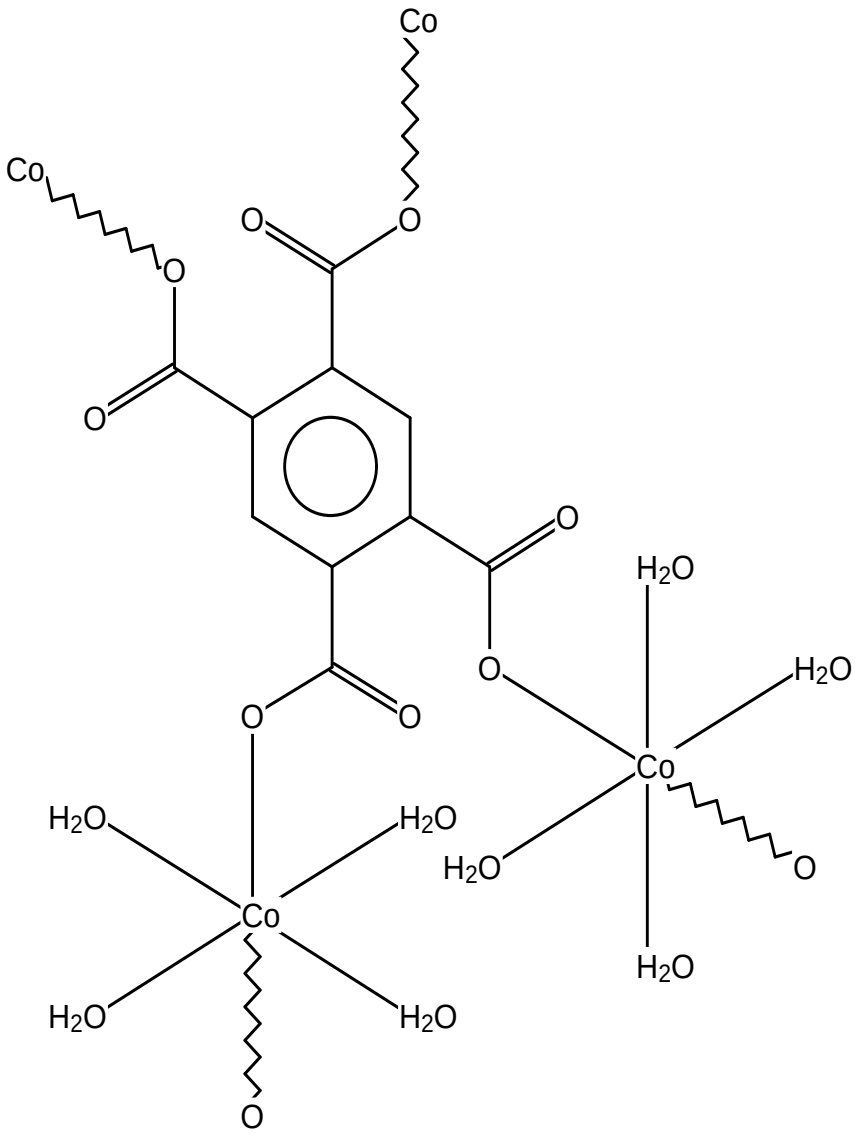

H_2O

Search: search1 (Thu Nov 24 11:50:34 2016): Hit 21

XOJMAL02

Reference: Xia Feng, Shu-Guang Zhang, Yun-Long Feng, You-Zhao Lan, Yi-Hang Wen (2008) *Jiegou Huaxue(Chin.J.Struct.Chem.)* ,**27,**1445

Formula: $(C_{10}\ H_{18}\ Co_2\ O_{16})n,4n(H_2\ O_1)$

Compound Name: catena-((μ_4-Benzene-1,2,4,5-tetracarboxylato)-octaaqua-di-cobalt(ii) tetrahydrate)

Space Group:	P-1	***Cell:***	***a***	10.876(0)	***b***	11.141(0)	***c***	11.508(0)
Space Group No.:	2	***(Å,°)***	α	82.90(0)	β	63.01(0)	γ	62.15(0)

R-Factor (%): 5.78 ***Temperature(K):*** 173 ***Density(g/cm^3):*** 1.777

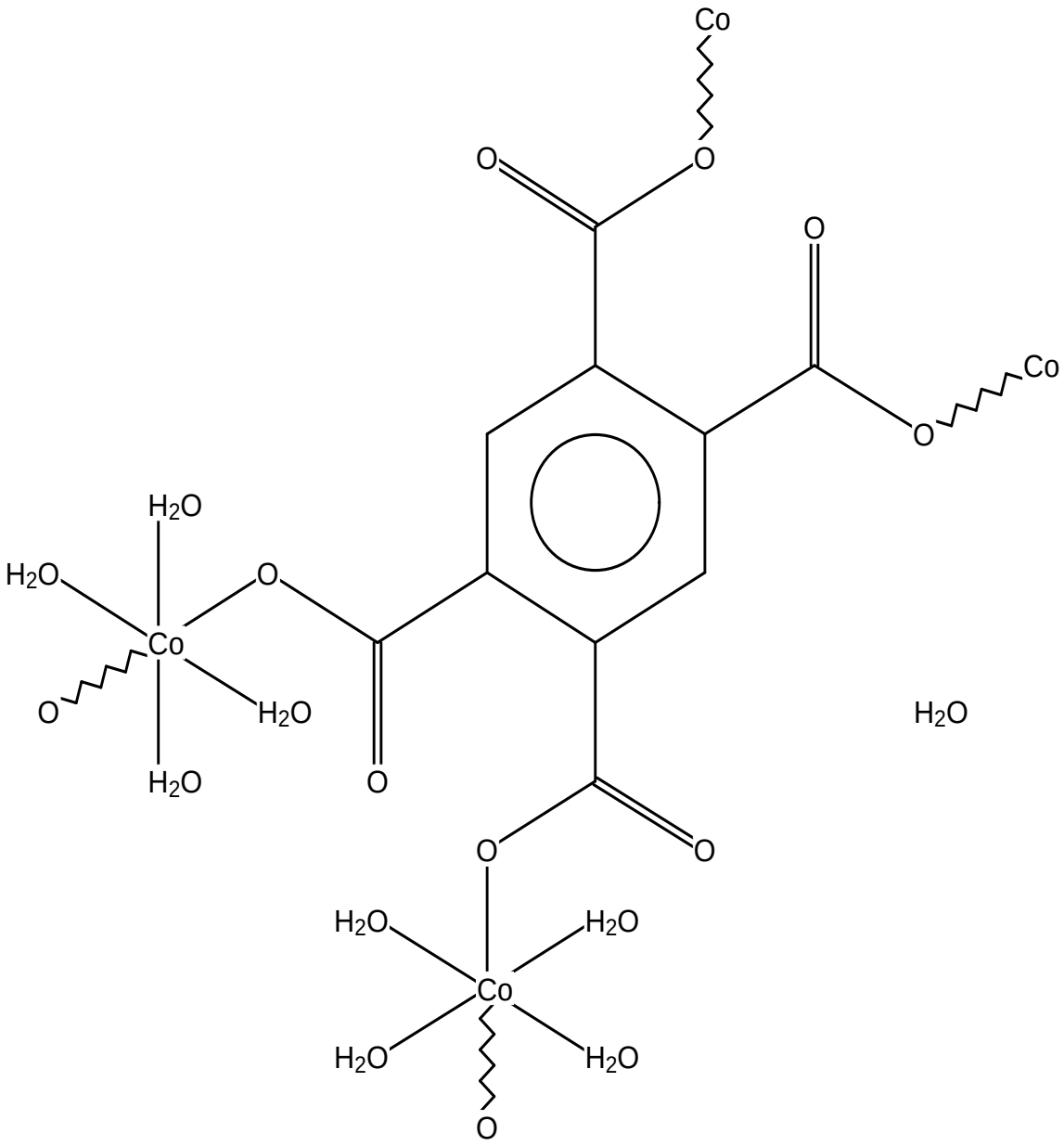

Search: search1 (Thu Nov 24 11:50:34 2016): Hit 22

XOJMAL03

Reference: O.Fabelo, J.Pasan, L.Canadillas-Delgado, F.S.Delgado, A.Labrador, F.Lloret, M.Julve, C.Ruiz-Perez (2008) *CrystEngComm* , **10,**1743

Formula: $(C_{10}\ H_{18}\ Co_2\ O_{16})n,4n(H_2\ O_1)$

Compound Name: catena-((μ_4-benzene-1,2,4,5-tetracarboxylato)-octaaqua-di-cobalt(ii) tetrahydrate)

Space Group:	P-1	***Cell:***	***a***	10.847(2)	***b*** 11.107(2)	***c***	11.483(2)
Space Group No.:	2	***(Å,°)***	α	82.93(3)	β 63.02(3)	γ	62.12(3)

R-Factor (%): 3.24 ***Temperature(K):*** 100 ***Density(g/cm^3):*** 1.792

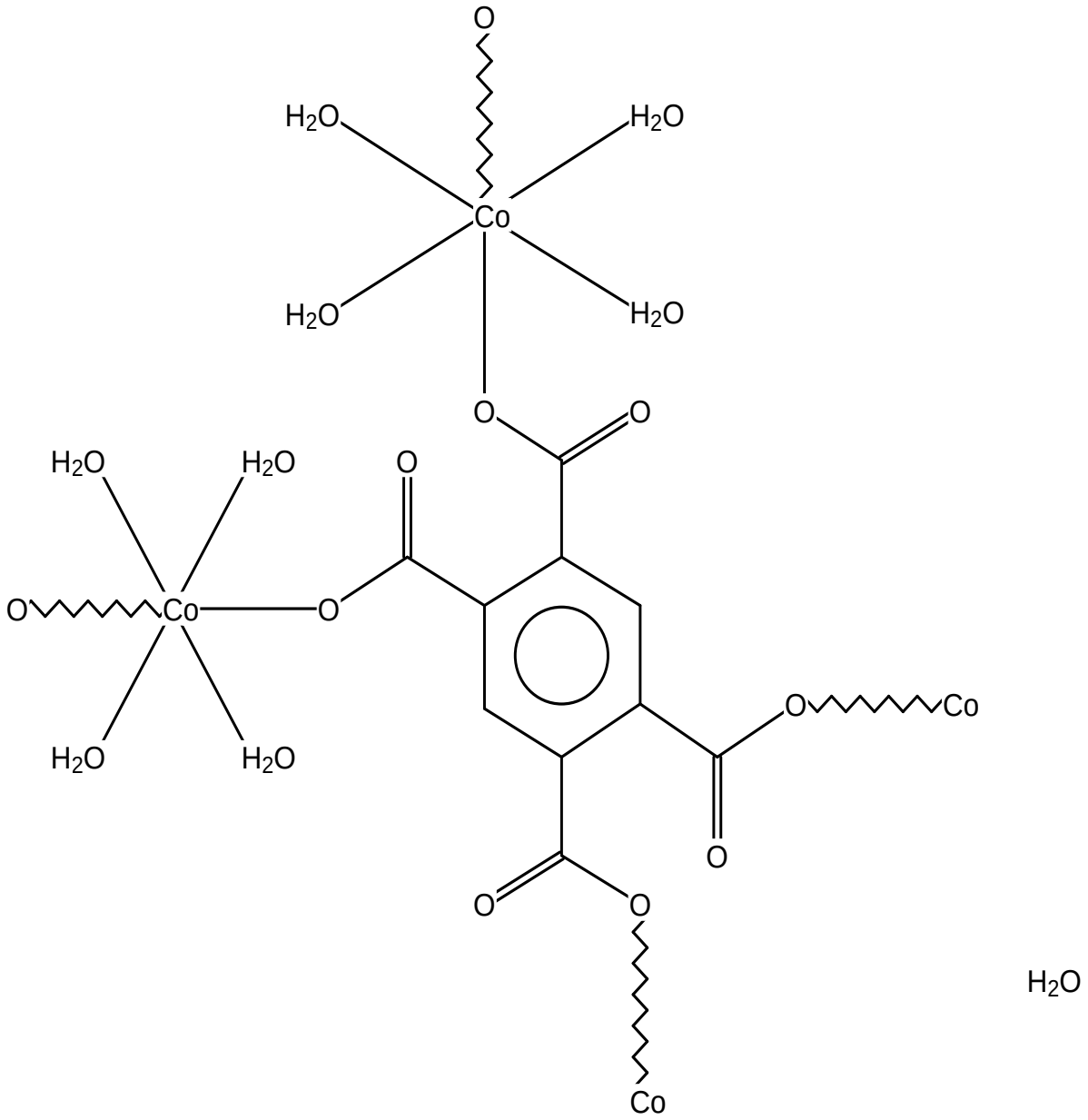

Search: search1 (Thu Nov 24 11:50:34 2016): Hit 23

XOJMEP

Reference: O.Fabelo, J.Pasan, L.Canadillas-Delgado, F.S.Delgado, A.Labrador, F.Lloret, M.Julve, C.Ruiz-Perez (2008) *Cryst.Growth Des.* , **8,**3984

Formula: $(C_{10}\ H_{18}\ Co_2\ O_{16})n,n(C_{10}\ H_{18}\ Co_2\ O_{16}),4n(H_2\ O_1)$

Compound Name: catena-(bis(μ_4-Benzene-1,2,4,5-tetracarboxylato-O,O',O'',O''')-octa-aqua-di-cobalt(ii) tetrahydrate)

Space Group:	C2/c	***Cell:***	***a***	18.083(0)	***b*** 13.541(0)	***c***	18.064(0)
Space Group No.:	15	***(Å,°)***	α	90.00	β 113.41(0)	γ	90.00

R-Factor (%): 5.50 ***Temperature(K):*** 293 ***Density(g/cm^3):*** 1.794

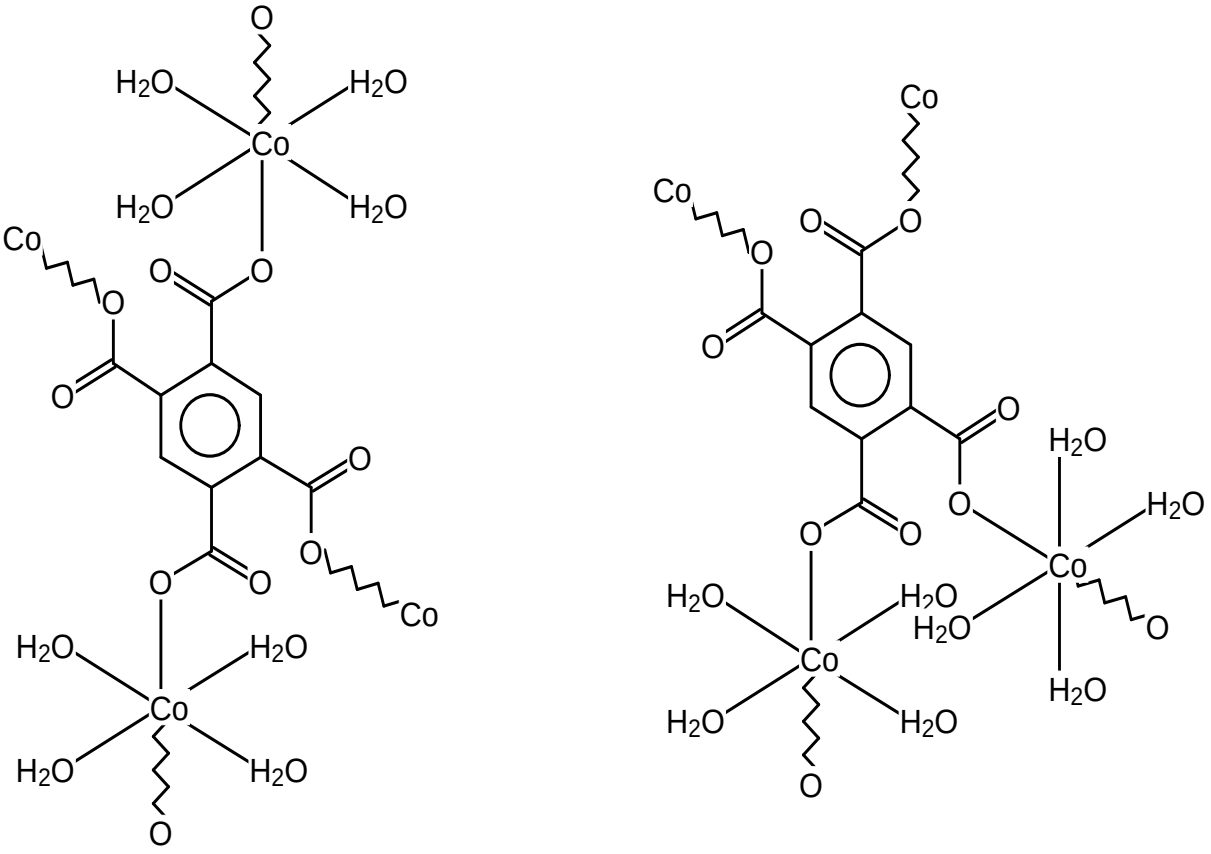

H_2O

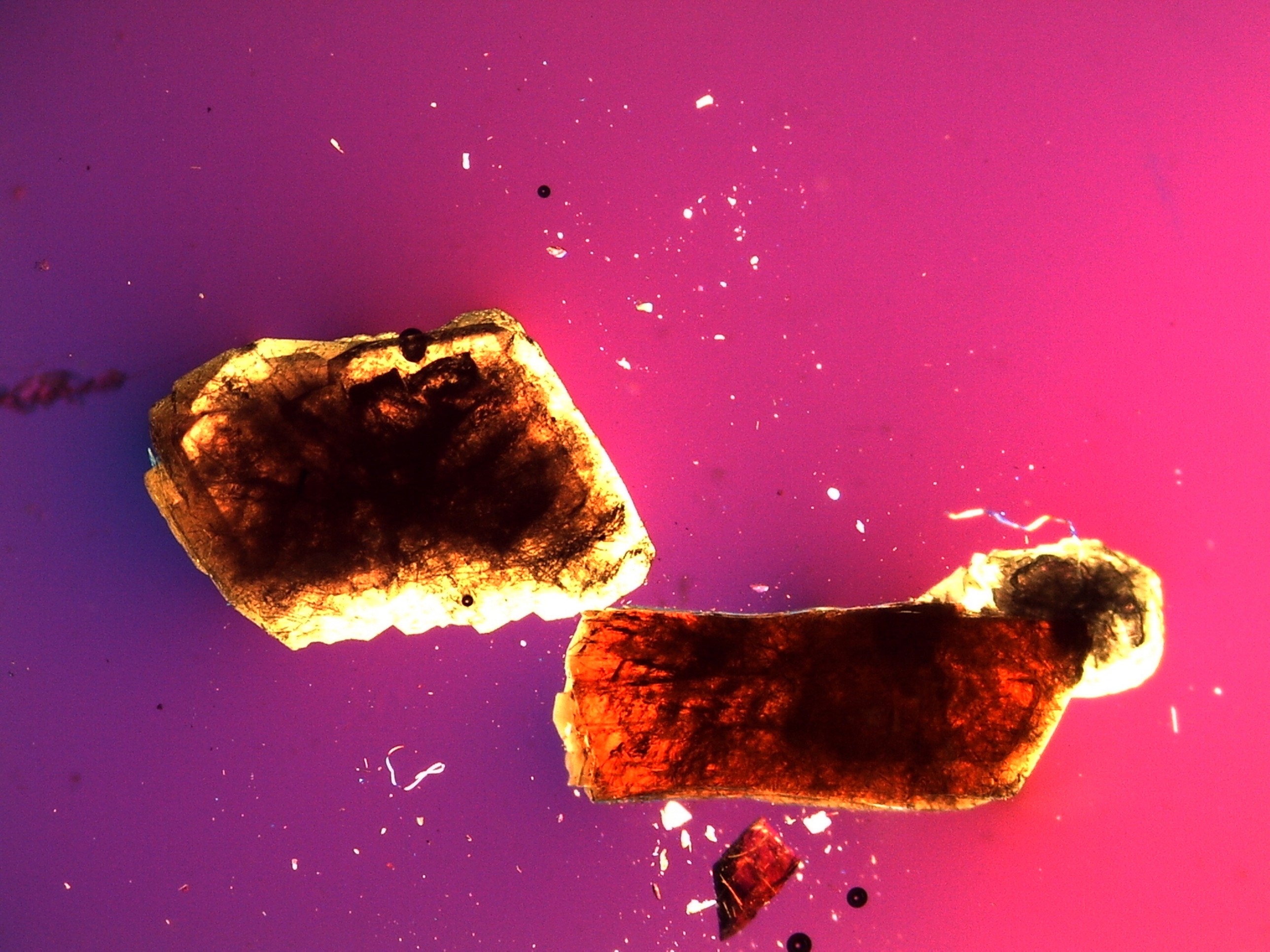

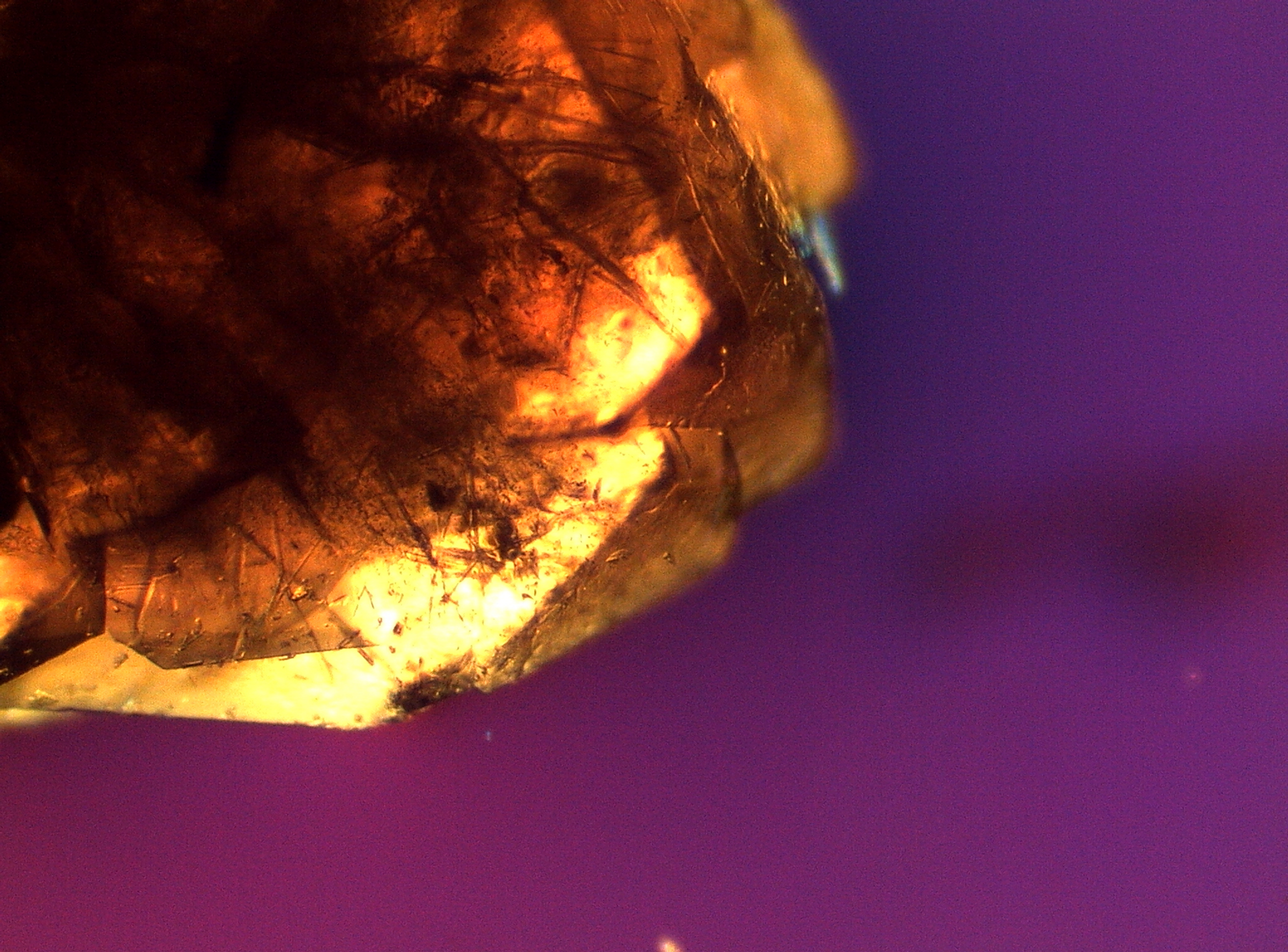

CoB4C-POM Thermal analysis and microanalysis

Table B1: Microanalysis of CoB4C-POM:proposed $(NH_4)_2Mo_2O_4Co_2(B_4C)_2H_2O$[1].

Element	Expected %	Obtained %	Difference	% Error
Carbon	17.256	17.250	-0.006	-0.035
Hydrogen	2.027	2.071	+0.044	+0.022
Cobalt	16.864	16.900	+0.036	+0.213
Nitrogen	4.025	4.084	0.060	+1.489

1. M. Hong, Chinese Journal of Structural Chemistry, 1985, 34-38

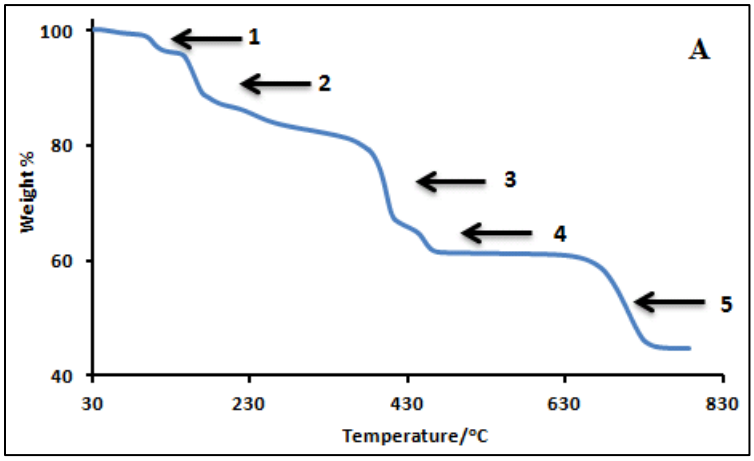

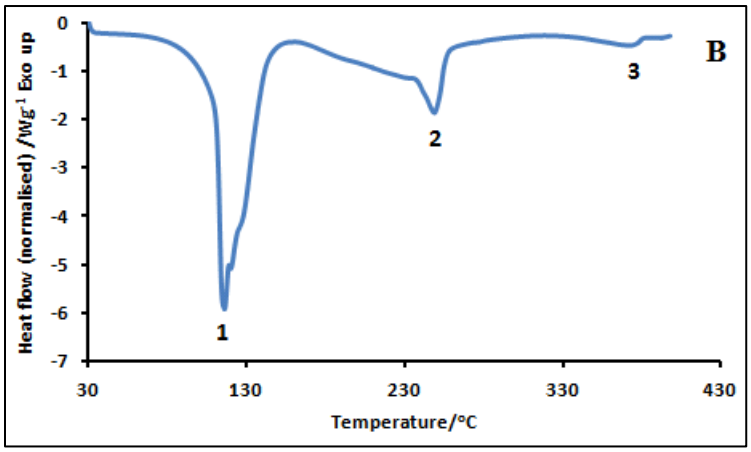

Figure B1: TGA (A) and DSC (B) thermograms for CoB4C-POM.

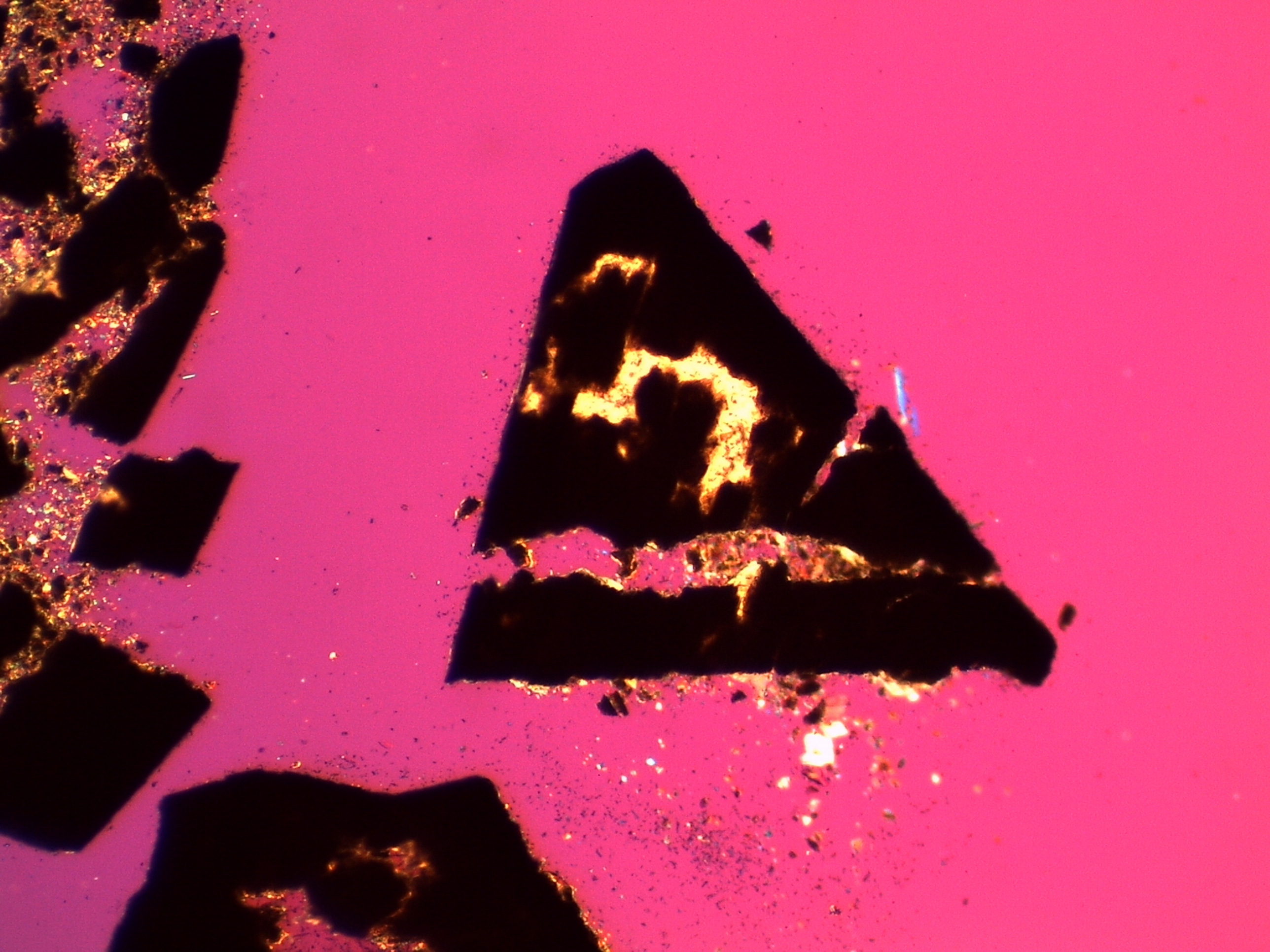

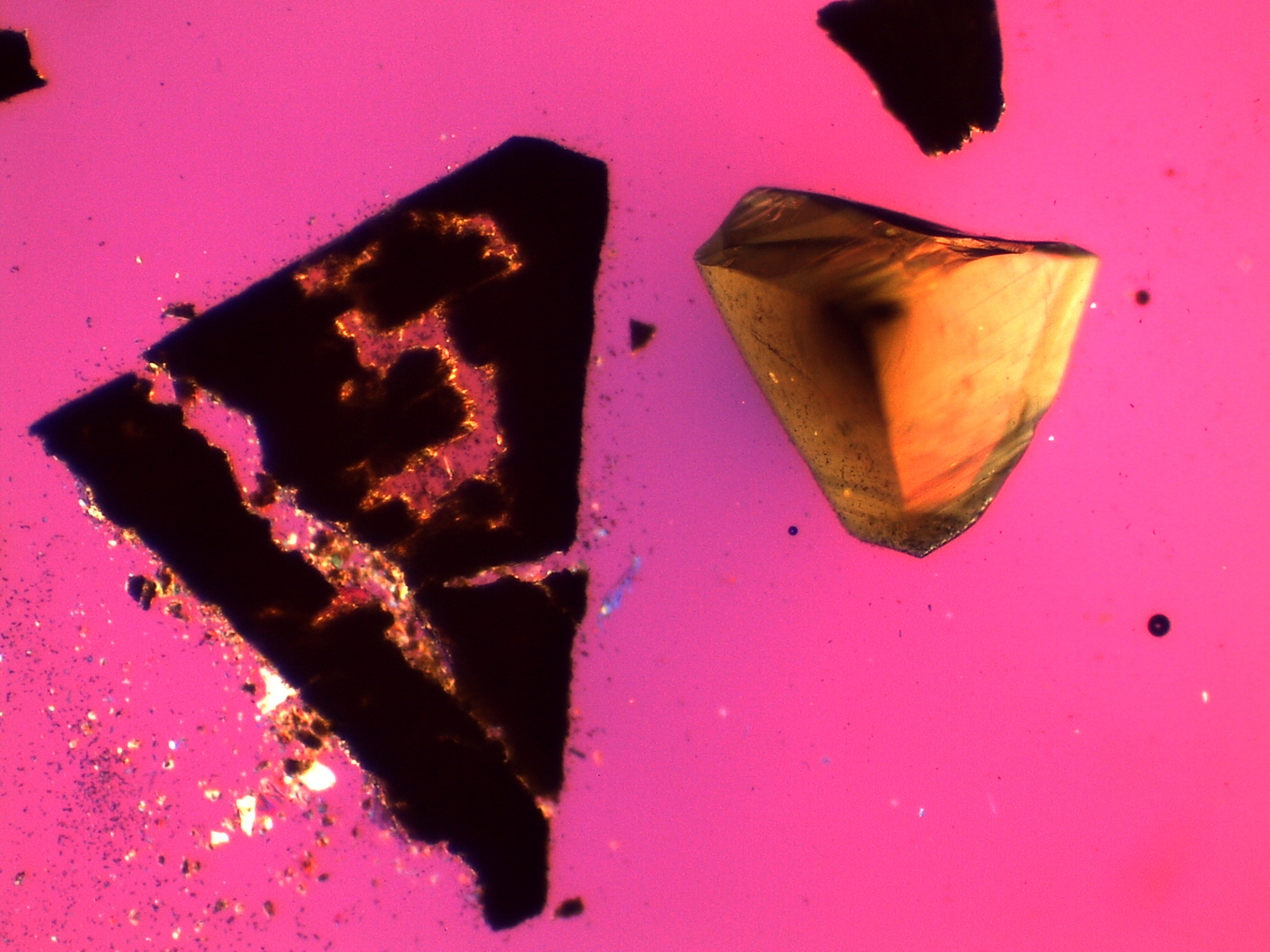

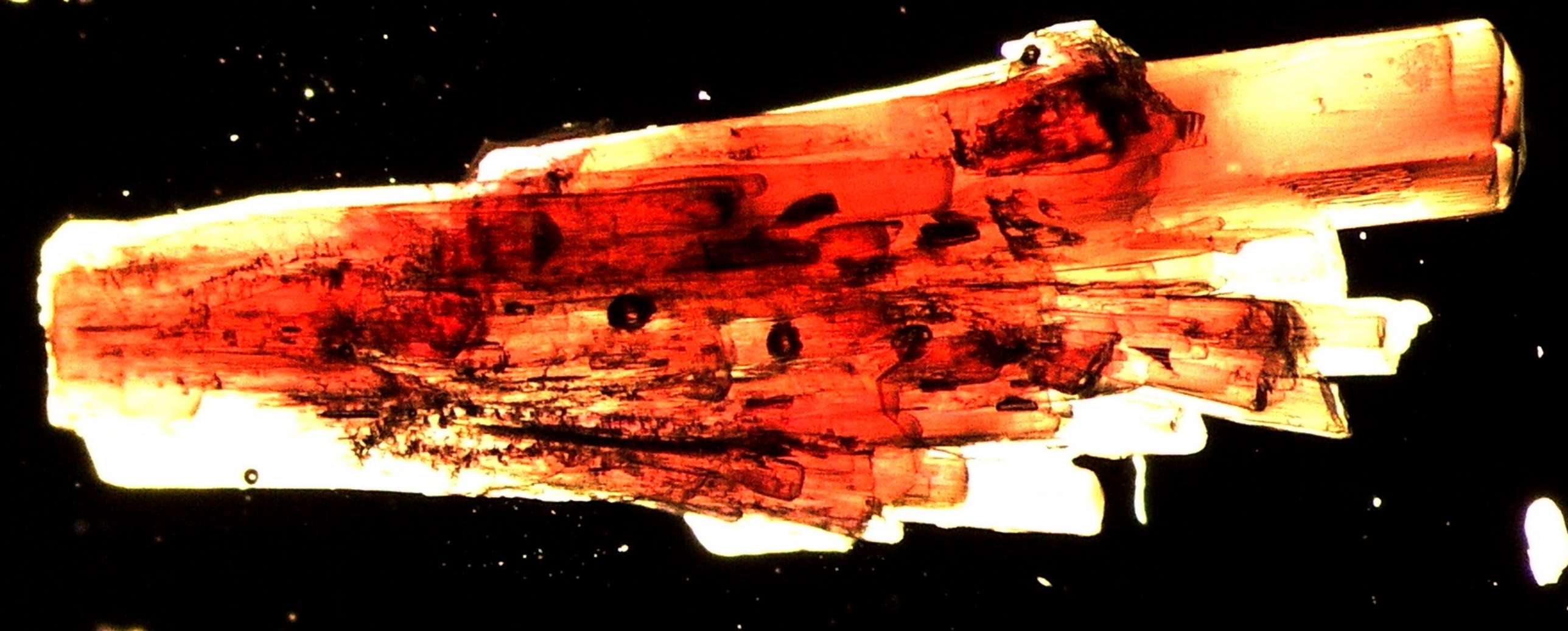

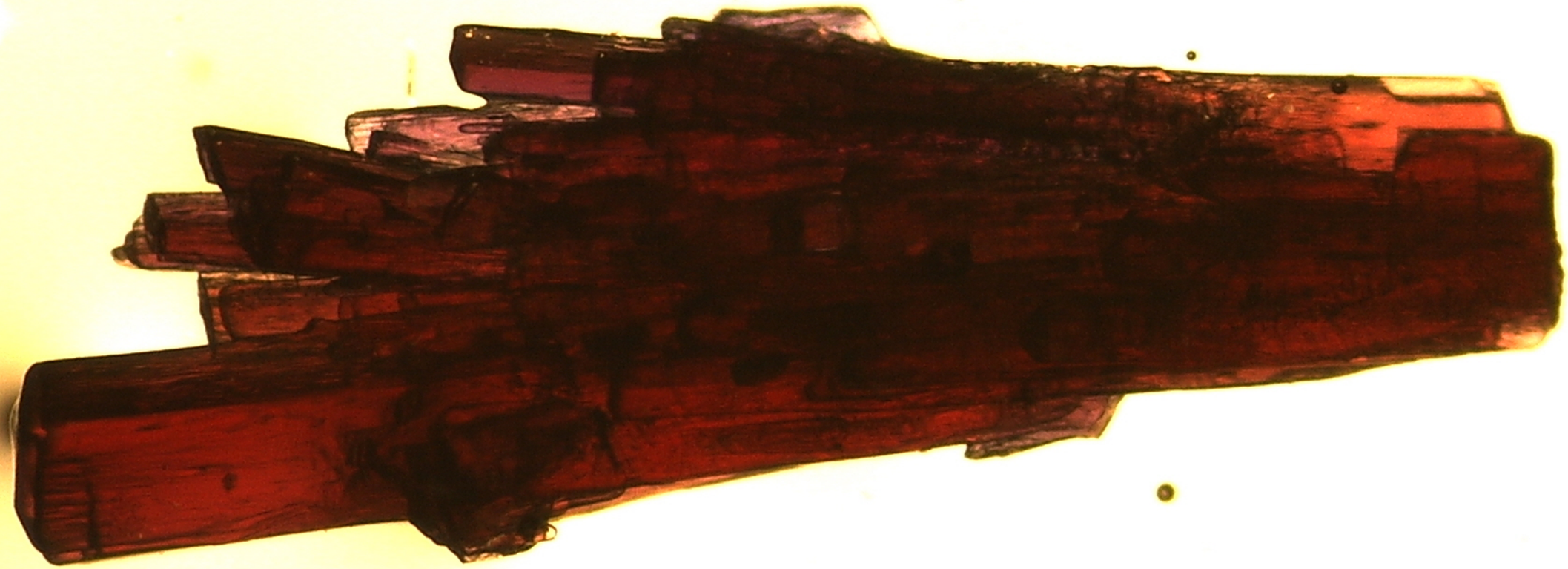

Search Overview

Search:	search3
Date/Time done:	Thu Mar 17 10:49:28 2016
Database(s):	CSD version 5.37 updates (Nov 2015) CSD version 5.37 (November 2015) CSD version 5.37 (November 2015) CSD version 5.37 updates (Feb 2016)
Restriction Info:	No refcode restrictions applied
Filters:	None
Percentage Completed:	100%
Number of Hits:	6

Single query used. Search found structures that:

match

Query 1

Query 1

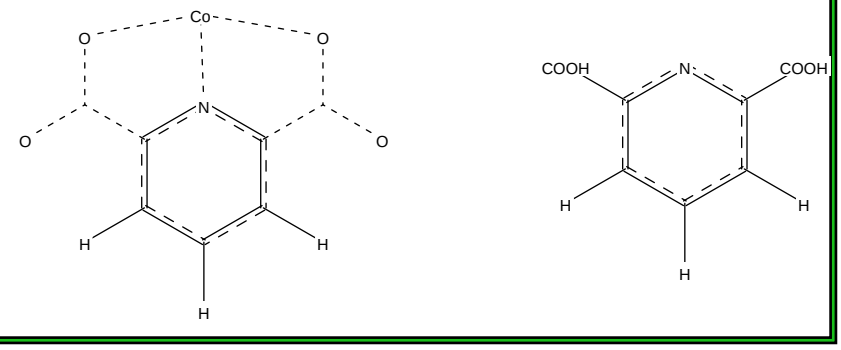

Search: search3 (Thu Mar 17 10:49:28 2016): Hit 1

AWORIO

Reference:	S.Yousuf, A.S.Johnson, S.A.Kazmi, M.Hemamalini, H.-K.Fun (2011) *Acta Crystallogr.,Sect.E:Struct.Rep.Online ,* **67,**m1105
Formula:	$C_2\ H_6\ N_5\ ^{1+}$,$C_{14}\ H_6\ Co_1\ N_2\ O_8\ ^{2-}$,$C_7\ H_5\ N_1\ O_4$,$H_2\ O_1$,$H_3\ O_1\ ^{1+}$
Compound Name:	3,5-Diamino-4H-1,2,4-triazol-1-ium oxonium bis(pyridine-2,6-dicarboxylato-N,O,O')-cobalt(ii) pyridine-2,6-dicarboxylic acid monohydrate

Space Group:	P-1	***Cell:***	***a***	8.021(0)	***b***	9.203(0)	***c*** 18.700(0)
Space Group No.:	2	***(Å,°)***	α	98.54(0)	β	96.72(0)	γ 100.52(0)
R-Factor (%):	2.69	***Temperature(K):***	100		***Density(g/cm^3):***	1.735	

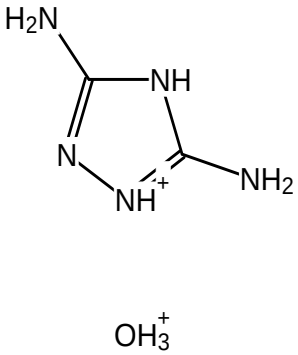

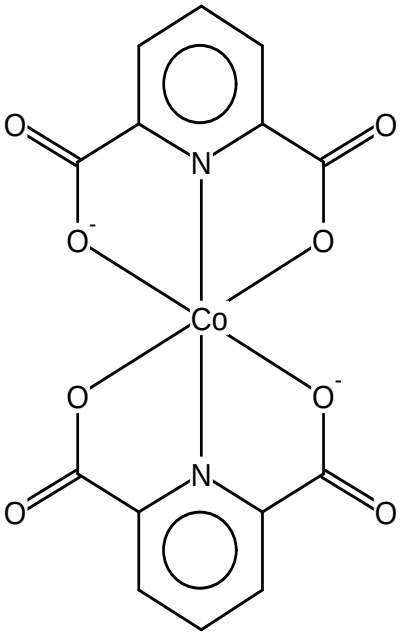

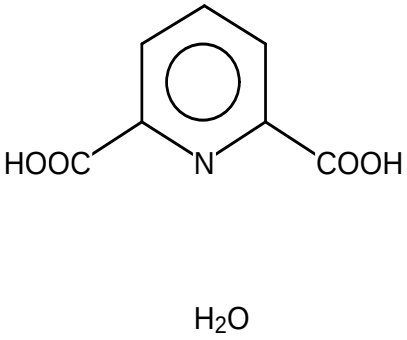

Search: search3 (Thu Mar 17 10:49:28 2016): Hit 2

BODJEL

Reference: M.Mirzaei, H.Eshtiagh-Hosseini, Z.Karrabi, K.Molcanov, E.Eydizadeh, J.T.Mague, A.Bauza, A.Frontera (2014) *CrystEngComm* , **16,**5352

Formula: $C_{14}\ H_8\ Co_1\ N_2\ O_8,3(H_2\ O_1)$

Compound Name: (Pyridine-2,6-dicarboxylato)-(pyridine-2,6-dicarboxylic acid)-cobalt trihydrate

Space Group:	P21/c	***Cell:***	***a***	13.804(0)	***b*** 10.043(0)	***c***	13.651(0)
Space Group No.:	14	***(Å,°)***	α	90.00	β 115.77(0)	γ	90.00

R-Factor (%): 3.72 ***Temperature(K):*** 200 ***Density(g/cm^3):*** 1.735

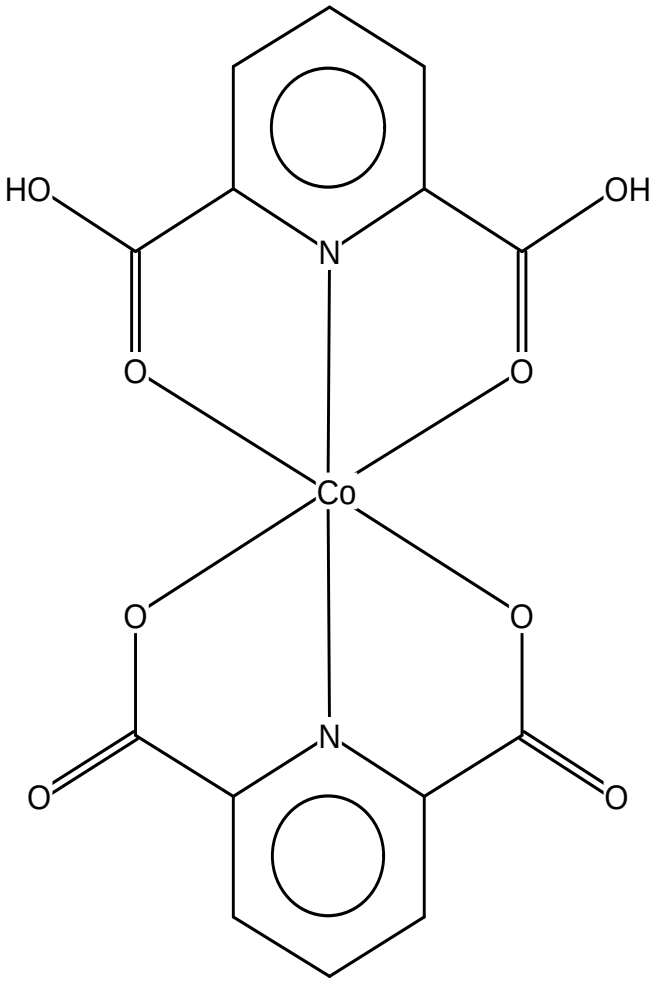

H_2O

Search: search3 (Thu Mar 17 10:49:28 2016): Hit 3

REFNOG

Reference: Hong Su, Yi-Hang Wen, Yun-Long Feng (2005)
*Z.Kristallogr.-New Cryst.Struct. ,***220,**560

Formula: $C_{19}\ H_{13}\ Co_1\ N_3\ O_5, C_7\ H_5\ N_1\ O_4, 4(H_2\ O_1)$

Compound Name: Aqua-(1,10-phenanthroline)-(pyridine-2,6-dicarboxylato)-cobalt(ii) (pyridine-2,6-dicarboxylic acid) solvate tetrahydrate

Space Group:	P-1	***Cell:***	***a*** 9.837(0)	***b*** 11.603(0)	***c*** 12.907(0)
Space Group No.:	2	***(Å,°)***	α 76.61(0)	β 82.22(0)	γ 77.62(0)

R-Factor (%): 7.48 ***Temperature(K):*** 298 ***Density(g/cm^3):*** 1.576

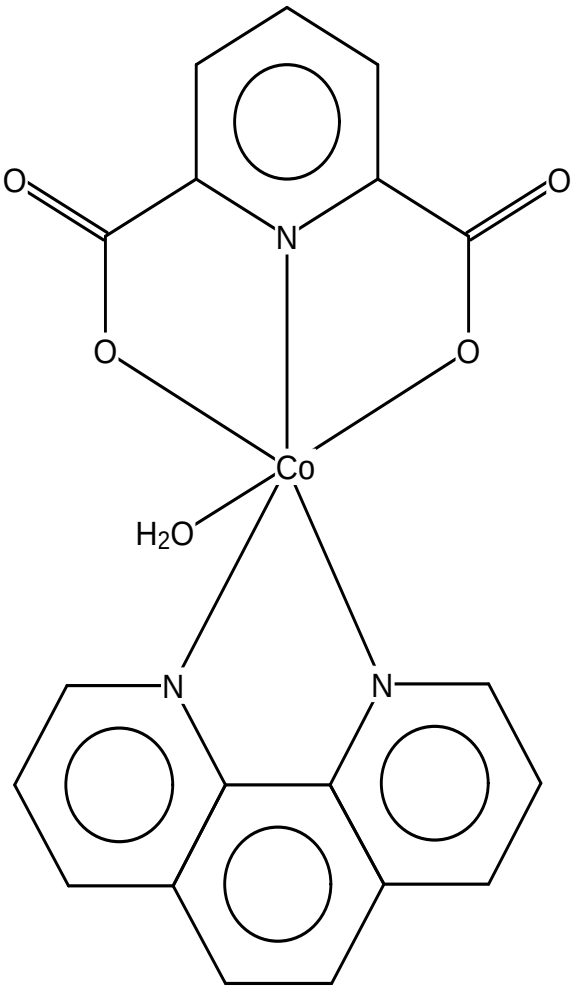

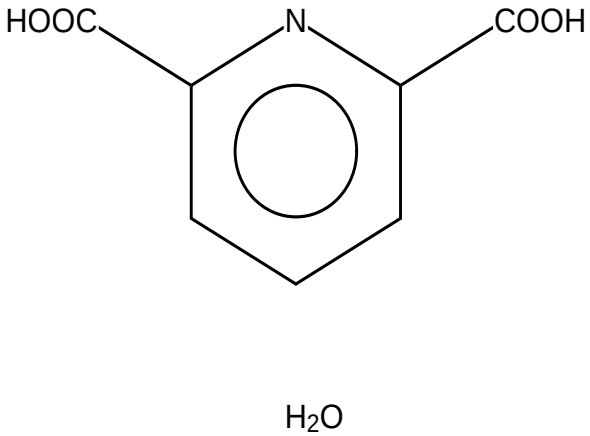

H_2O

Search: search3 (Thu Mar 17 10:49:28 2016): Hit 4

TEHFIX

Reference:	Z.Derikvand, N.Dorosti, F.Hassanzadeh, A.Shokrollahi, Z.Mohammadpour, A.Azadbakht (2012) *Polyhedron ,***43,**140
Formula:	$C_{14}\ H_6\ Co_1\ N_2\ O_8\ ^{2-}$,$C_7\ H_5\ N_1\ O_4$,$C_5\ H_9\ N_3\ ^{2+}$,4($H_2\ O_1$)
Compound Name:	4-Amino-3-ammoniopyridinium bis(pyridine-2,6-dicarboxylato)-cobalt(ii) pyridine-2,6-dicarboxylic acid tetrahydrate

Space Group:	P-1	***Cell:***	***a***	8.580(0)	***b***	13.243(0)	***c***	14.247(0)
Space Group No.:	2	***(Å,°)***	α	74.62(0)	β	79.49(0)	γ	78.72(0)

R-Factor (%):	4.09	***Temperature(K):***	120	***Density(g/cm^3):***	1.620

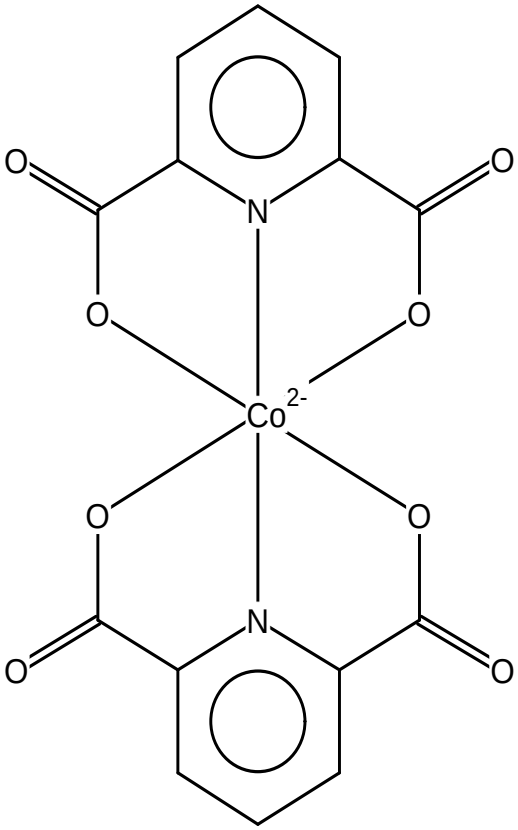

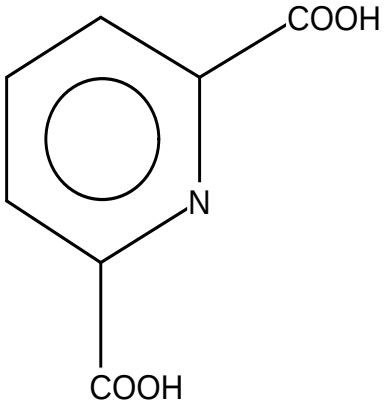

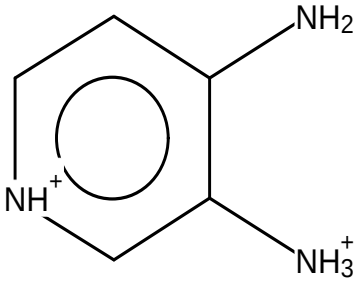

H_2O

Search: search3 (Thu Mar 17 10:49:28 2016): Hit 5

UGORIR

Reference: Luqin Yang, D.C.Crans, S.M.Miller, A.la Cour, O.P.Anderson, P.M.Kaszynski, M.E.Godzala III, L.D.Austin, G.R.Willsky (2002) *Inorg.Chem. ,***41,**4859

Formula: $C_{14}\ H_8\ Co_1\ N_2\ O_8,3(H_2\ O_1)$

Compound Name: (Pyridine-2,6-dicarboxylic acid)-(pyridine-2,6-dicarboxylato)-cobalt(ii) trihydrate

Space Group:	P21/c	***Cell:***	***a***	13.806(3)	***b*** 10.036(2)	***c***	13.646(3)
Space Group No.:	14	***(Å,°)***	α	90.00	β 115.81(3)	γ	90.00

R-Factor (%): 4.97 ***Temperature(K):*** 293 ***Density(g/cm^3):*** 1.737

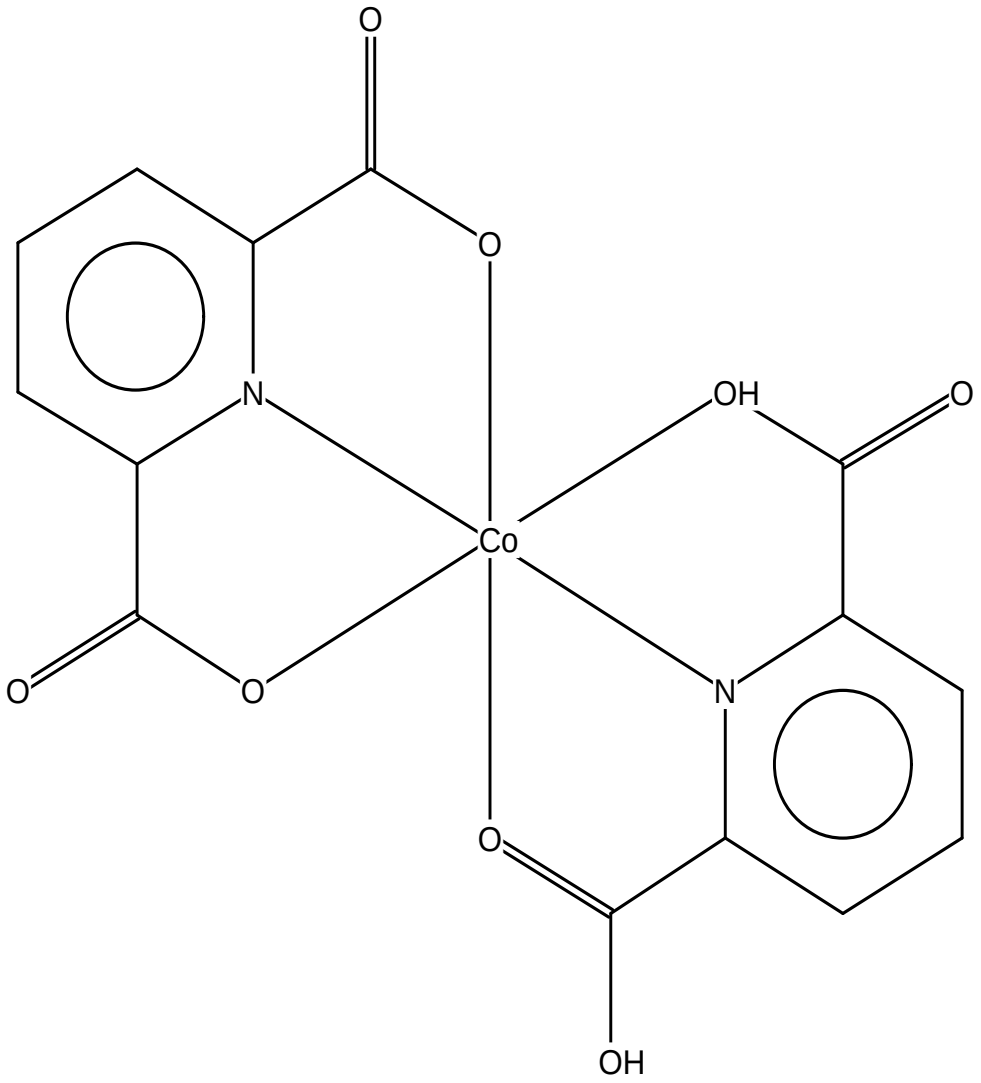

H_2O

Search: search3 (Thu Mar 17 10:49:28 2016): Hit 6

WABPOG

Reference:	C.Yuste, M.R.Silva, M.Ghadermazi, F.Feizi, E.Motieiyan (2010) *Acta Crystallogr.,Sect.E:Struct.Rep.Online ,***66,**m1643
Formula:	$C_{14}\ H_7\ Co_1\ N_2\ O_8\ ^{1-}$,$C_7\ H_5\ N_1\ O_4$,$C_6\ H_9\ N_2\ ^{1+}$,3($H_2\ O_1$)
Compound Name:	Phenylhydrazinium (6-carboxypyridine-2-carboxylato)-(pyridine-2,6-dicarboxylato)-cobalt(ii) pyridine-2,6-dicarboxylic acid trihydrate

Space Group:	P-1	***Cell:***	***a***	8.802(0)	***b***	12.238(0)	***c***	14.656(0)
Space Group No.:	2	***(Å,°)***	α	101.08(0)	β	91.35(0)	γ	98.75(0)

R-Factor (%):	4.27	***Temperature(K):***	293	***Density(g/cm^3):***	1.565

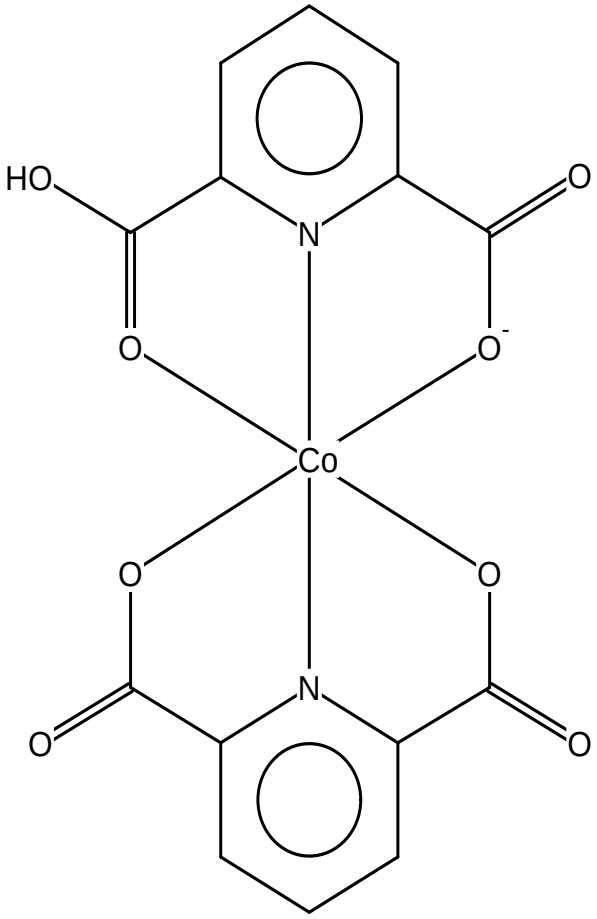

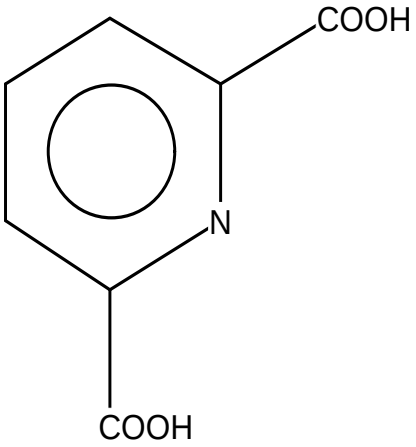

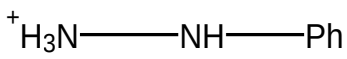

H_2O